Omzetting van bio-ethanol naar koolwaterstoffen:
van laboratorium tot industriële schaal

Bioethanol Conversion to Hydrocarbons:
from Laboratory to Industrial Scale

Kristof Van der Borght

UNIVERSITEIT
GENT

Promotoren:

dr. Vladimir V. Galvita   Universiteit Gent

prof. dr. ir. Guy B. Marin   Universiteit Gent

Examencommissie:

prof. dr. ir. Patrick De Baets, voorzitter   Universiteit Gent

prof. dr. ir. An Verberckmoes   Universiteit Gent

prof. dr. Marie-Françoise Reyniers   Universiteit Gent

prof. dr. ir. Joris W. Thybaut   Universiteit Gent

prof. dr. Pascal Van Der Voort, secretaris   Universiteit Gent

prof. dr. Andrei Khodakov   Université Lille

Universiteit Gent

Faculteit Ingenieurswetenschappen en Architectuur

Vakgroep Chemische Proceskunde en Technische Chemie

Laboratorium voor Chemische Technologie

Technologiepark 914

B-9052 Gent

België

Tel: +32 (0)9 331 17 57

Fax: +32 (0)9 331 17 59

http:// www.lct.ugent.be

Dankwoord

Acknowledgments

Na zes jaar werken aan mijn doctoraat is nu een nieuw hoofdstuk in mijn leven aangebroken. Het was een periode waarin ik mij zowel op wetenschappelijk als persoonlijk vlak heb kunnen ontplooien. Vooraleer ik begin aan mijn volgende uitdaging, had ik graag even stilgestaan bij een aantal personen die ik wil bedanken voor hun bijdrage – direct of indirect - aan het tot stand komen van dit werk.

Allereerst wil ik professor Guy B. Marin bedanken om mij de kans te bieden om aan het LCT te doctoreren. De wetenschappelijke discussies en de (vele) correcties van mijn manuscripten waren van onschatbare waarde om mijn werk nog te verbeteren. *I would like to thank dr. Vladimir Galvita for all his efforts he has put into my research. I think I would not have been able to come to this result without your input and enthusiasm. Good luck with your future career! I would also like to express my gratitude to the members of my examination committee. Thanks for all your valuable comments and suggestions on the PhD dissertation which definitely improved the quality of this work.*

Een speciale vermelding gaat uit naar prof. Joris Thybaut. Hij sprak mij als eerste aan over de mogelijkheid tot het behalen van een doctoraat waarvoor ik hem nog steeds dankbaar ben. Bedankt ook om mij te betrekken bij de CaRE groep zodanig dat ik mijn modellering *skills* kon verbeteren. Ik wil je ook bedanken voor de fijne momenten tijdens het vakoverschrijdend project, de workshops van 'Glaasje vol' en naast het werk.

Ik wil ook alle andere onderzoekers bedanken die betrokken geweest zijn in het onderzoek over de omzetting van alcoholen over zeolieten. Prof. Marie-Françoise Reyniers, ik denk dat sommige van onze (veelal levendige) discussies mij altijd zullen bij blijven. *Kostas, thank you for your help with the modelling of ethanol dehydration and the many discussion that we had, good luck in the future!* Ik wil ook Matthew John, Dieter Gunst en Rakesh Batchu vermelden voor hun fijne samenwerking.

Hilde, bedankt om mij onder te dompelen in de wereld van katalysatorkarakterisering en synchrotrons. Ik zal de trips naar Grenoble en Parijs met het busje en de trein niet snel vergeten. Ook de vele reisverhalen waren steeds een bron van inspiratie voor mijn volgende vakantiebestemming. Je rabarber op het einde van de zomer zal ik nu jammer genoeg moeten missen.

Ook wil ik prof. Geraldine Heynderickx bedanken voor de fijne samenwerking aan het ingenieursproject voor de 1ste bachelor studenten: ik denk dat we er in geslaagd zijn heel wat studenten te overtuigen om voor chemische technologie te kiezen. Ook je humor – alhoewel niet door iedereen even goed begrepen – zal mij bijblijven.

Ik wil ook mijn thesisstudenten van de afgelopen jaren bedanken die elk op hun manier een steentje bijgedragen hebben aan dit werk: Stefaan Stevens, Brecht Laforce, Bjorn De Vleesschauwer, Anton De Vylder en Hannelore Poelvoorde. Ik wil ook het technisch en administratief personeel van het LCT bedanken voor hun ondersteuning wanneer er iets mis liep. Bert, Brecht, Marcel voor zijn relativisme en positivisme, Georges, Wim en Michael voor wanneer de GC weer eens lastig deed, bedankt! Petra, Sarah en Kim van het secretariaat mogen hier natuurlijk ook niet ontbreken!

Ik wil alle collega's van het LCT bedanken voor de fijne tijd aan het labo. In het bijzonder denk ik aan Kenneth Toch waarmee ik op allerlei vlakken heb mogen samenwerken: wetenschappelijk, de workshops, het doctoraatssymposium,… Ook wanneer mijn onderzoek niet ging zoals het hoort, stond je klaar met raad waarvoor nogmaals mijn dank. Ook wil ik Jeroen, Bart, Jonas en Jolien bedankt voor de fijne middagpauzes. Ik wil ook mijn collega's van mijn bureau in 914 bedanken en mij nogmaals verontschuldigen voor al die keren dat mijn muziek te hard stond. Hier wil ik ook mijn studiegenoten van weleer, Pieter, Carl en Thomas, vermelden: de ritjes met *den Twingo* blijven legendarisch!

Tenslotte wil ik mijn ouders en mijn zus bedanken voor de kansen die zij mij hebben geboden om verder te studeren en tot dit punt te komen. Alhoewel ik steeds vaag was over wat ik nu exact deed, hoop ik dat mijn werk dat ik de afgelopen jaren uitgevoerd heb tijdens mijn doctoraat nu wat duidelijker is.

En, *last but not least,* Leen! Zijn er voldoende woorden beschikbaar om te beschrijven wat jij voor mij betekent? Bedankt om er altijd voor mij te zijn. Bedankt om mij te steunen wanneer het eens wat minder ging en ik slechtgezind thuiskwam. Bedankt voor de goeie zorgen voor onze twee schatten van kinderen, Thomas en Simon. Ik hoop dat we hen dezelfde kansen en meer kunnen bieden als wij gekregen hebben. Bedank voor al hetgeen wat we reeds tot hiertoe meegemaakt hebben en wat er nog op ons pad zal volgen!

Kristof

September 2016

Table of contents

Chapter 6 Ethanol to higher hydrocarbons over Ni, Ga, Fe-modified ZSM-5: effect of metal content   139

Chapter 7 First-principles based simulation of a fixed bed reactor for ethanol dehydration   165

x

List of figures

List of tables

Nomenclature

Roman symbols

a_s	specific surface area	[m² kg^{-1}]
A_i	GC area of component *i*	[-]
A_f	Arrhenius pre-exponential factor	[variable]
A_r	surface area of the cross-section of the reactor	[m^2]
A_{BET}	BET surface area	[m² kg^{-1}]
b_i	parameter	[variable]
b	bed dilution	[-]
c_p	specific heat capacity	[J kg^{-1} K^{-1}]
C_i	concentration of component *i* in the pellet	[mol kg^{-1}]
C_t	acid site concentration	[mol$_{H+}$ kg^{-1}]
CN_i	amount of carbon atoms in component *i*	[-]
Ca	Carberry number	[-]
CF	correction factor	[-]
d	diameter	[m]
d	mean crystallite size	[m]
D_i	diffusion coefficient of component *i*	[m² s^{-1}]
$D_{e,i}$	effective diffusion coefficient of component *i*	[m² s^{-1}]
E_a	activation energy	[J mol^{-1}]
f	friction factor	[-]
F_i	molar flow rate of gas phase component *i*	[mol s^{-1}]
F_{regres}	F-value resulting for the significance test	[-]
G	mass flow rate	[kg s^{-1}]
ΔG_r	Gibbs free energy of reaction	[J mol^{-1}]
h	Planck constant = $6.63 \cdot 10^{-34}$	[m² kg s^{-1}]
h	height	[m]
j	counter	[-]
ΔH_r	enthalpy of reaction	[J mol^{-1}]

k_B	Boltzmann constant = $1.38 \cdot 10^{-23}$	[m^2 kg s^{-2} K^{-1}]
k_j	rate constant of elementary step j	[variable]
k_{fi}	external mass transfer coefficient of component i	[m s^{-1}]
K	equilibrium coefficient	[variable]
K	dimensionless shape factor in Scherrer equation	[-]
L	length	[m]
M	molecular mass	[kg mol^{-1}]
M	metal content	[%]
n	apparent order of reaction	[-]
n	number of chiral atoms	[-]
n_{comp}	number of components	[-]
n_e	number of single-events	[-]
N_i	molar flux of i with respect to a fixed plane	[mol m^{-2} s^{-1}]
Q_{ads}	amount of N_2 adsorbed	[mol kg^{-1}]
Q_c	reaction quotient	[variable]
p_i	partial pressure of component i	[Pa]
p_t	total reactor pressure	[Pa]
u_s	superficial velocity	[m s^{-1}]
r	radius of the catalyst pellet	[m]
r_j	turnover frequency of elementary step j	[s^{-1}]
R	universal gas constant = 8.31	[J mol^{-1} K^{-1}]
R_i	specific production rate of component i	[mol kg^{-1} s^{-1}]
Re	Reynolds number	[-]
S_i	selectivity of component I	[mol mol^{-1}]
S	sum of squares	[-]
ΔS_r	entropy of reaction	[J mol^{-1} K^{-1}]
t	time	[s]
t	t-value	[-]
T	temperarature	[K]
T_M	maximum desorption temperature	[K]
u_s	superficial velocity	[m s^{-1}]
v	stoichiometric coefficient	[-]

V	volume	[m³]
V(b)	(co-)variance of parameter vector b_i	[variable]
W	catalyst mass	[kg]
w_i	weighing factor for response i	[-]
x	factor	[-]
x	axial reactor coordinate	[m]
x_i	mass fraction of component i	[-]
X_i	conversion of component i	[mol mol^{-1}]
y	output variable	[variable]
y_i	molar fraction of component i in the gas phase	[mol mol^{-1}]
Y_i	yield of component i	[mol mol^{-1}]

Greek symbols

α	heat transfer coefficient	[W m^{-2} K^{-1}]
α	reaction order	[-]
β	full width at half maximum	[-]
β	heating rate	[K s^{-1}]
β	real parameter vector	[-]
ε	porosity	[-]
η	catalyst effectiveness	[-]
μ	dynamic viscosity	[Pa s]
ρ	density	[kg m^{-3}]
$\rho_{i,j}$	binary correlation coefficients between parameter i and j	[-]
ξ	dimensionless distance	[-]
θ_k	fractional coverage of surface species k	[-]
θ	Bragg angle	[°]
λ_p	pellet thermal conductivity	[W m^{-1} K^{-1}]
λ	wavelength	[m]
σ	symmetry number	[-]
ϕ	Thiele modulus	[-]
Φ	Weisz modulus	[-]
τ	tortuosity	[-]

Subscripts

°	inlet
‡	transition state
alk	alkylation
b	catalyst bed
b	bulk
bs	β-scission
c	crystallite
cap	capillary
C2	combined ethanol and ethene
C2H4	ethene
C3H6	propene
d	desorption
elem	elementary steps
eth	ethylation
EtOH	ethanol
exp	experimental
f	formation
f	fluid
g	gas
glob	global
i	gas phase species
id	internal diameter
isom	isomerization
eq	equilibrium
j	elementary step
k	surface species
K	Knudsen
l	liquid
m	molecular
max	maximum
min	minimum

oxy   oxygenates

p   catalyst pellet

p   protonation

par   parameters

pore   pore

m   mixture

r   reaction

r   reactor

r   reactant

r   responses

s   surface

v   volumetric

t   total

Superscripts

$^{-}$ average

$\sim$ single-event

$\ddagger$ activation

°   standard

*   adsorbed

intr   intrinisic

ncomp number of components

ngrid   number of grid points

obs   observed

Abbreviations

Al   Aluminium

BEA   Beta

C2H4   ethene

C3H6   propene

C4H8   butene isomers

C5H10 pentene isomers

C6H12   hexene isomers

CH4   methane

DEE   diethyl ether

DHA   Detailed Hydrocarbon Analyzer

EtOH   ethanol

FAU   faujasite

FER   ferrierite

FID   Flame Ionization Detector

MFI   pentasil

MOR   mordenite

MTBE   methyl tertiary butyl ether

MTO   methanol to olefins

OCP   olefin cracking process

PONA   Paraffin – Olefin – Naphthene – Aromatic

RGA   Refinery Gas Analyser

SEMK   Single-Event Microkinetic Modelling

Si   Silicon

TCD   Thermal Conductivity Detector

Glossary of terms

Acid strength	The ability or tendency of a functional group to lose a proton.
Activation energy	For an elementary step, the difference in internal energy between transition state and reactants. A measure for the temperature dependence of the rate coefficient.
Active site	Functional group at the surface of a solid support which is responsible for the catalytic activity.
Adsorption	The preferential concentration of a species at the interface between two phases. Adherence of the atoms, ions or molecules of a gas or liquid to the surface of another substance.
Alkene homologation	The cycle involving methylation and alkylation of lower carbon number compounds and cracking of higher carbon number compounds in Methanol-To-Olefins.
Arrhenius relation	Relationship that expresses the dependence of a rate coefficient k on the temperature T and activation energy, Ea: $k = A\exp(E_a/RT)$ with R is the universal gas constant, T the temperature and A the pre-exponential factor.
Catalyst	A source of active centers regenerated at the end of a closed reaction sequence.
Catalyst descriptor	Parameter in the kinetic model which specifically account for the effect of the catalyst properties on the kinetics.
Chemisorption	Also known as chemical adsorption. Adsorption in which the forces involved are valence forces of the same kind as those operating in the formation of chemical compounds. Chemisorption strongly depends on the surface and the sorptive, and only one layer of chemisorbed molecules is formed. Its energy of adsorption is the same order of magnitude as in chemical reactions, and the adsorption may be activated.

Confinement effect	Zeolites possess a highly curved internal surface resulting in non-covalent interactions between the zeolite framework host and the guest molecules located inside. These interactions are repulsive, Pauli type, in the short range and attractive, van der Waals type, in the long range. The term confinement effect encompasses all effects related to these interactions, such as shape selectivity, preferential adsorption, and enhanced diffusivity.
Conversion	Measure for the amount of a reactant that has been transformed into products as a result of a chemical reaction.
Deactivation	Measure for the amount of a reactant that has been transformed into products as a result of a chemical reaction.
Delplot technique	Method for reaction pathway analysis.
Effectiveness factor	Ratio of actual reaction rate for a porous catalyst to reaction rate that would be observed if the total surface area throughout the catalyst pellet interior were exposed to a fluid of the same composition and temperature as that found at the external surface of the pellet.
Elementary step	The irreducible act of reaction in which reactants are transformed into products directly, i.e., without passing through an intermediate that is susceptible to isolation.
Group contribution method	A technique to estimate and predict thermodynamic and other properties from molecular structures, i.e., atoms, atomic groups, bond type etc.
Hydrocarbon pool	The cycle involving polymethylbenzene as active centers involving methylation, deprotonation and dealkylation steps to produce light olefins.
Induction period	The time during which the progress of an autocatalytic reaction remains below experimental detection.
Internal diffusion	Also called intraparticle diffusion. Motion of atoms within the particles of a solid phase that has a sufficiently large porosity to

	allow this motion.
Intermediate	Is formed from a reactant and transform into a product during a chemical reaction. The intermediate is often an unstable species that cannot directly be detected during a reaction.
Kinetic descriptor	Parameter in the kinetic model which solely depend on the reaction mechanism.
Knudsen diffusion	Type of mass-transfer which is dominated by molecule-pore wall collision, as a result of large mean free path between collisions compared to the pore diameter. Prevails at low pressures and/or small pore diameters.
Lignocellulosic biomass	Non-edible biomass composed of carbohydrate polymers (cellulose, hemicellulose), and an aromatic polymer (lignin).
Nitrogen adsorption-desorption measurments	Experimental method to determine the specific surface, average pore size and pore size distribution of a porous solid material.
Objective function	Is a function used during optimization problems which have to be minimized or maximized by choosing the best set of variables which determines the values of this function.
Parameter estimation	Process of estimating the parameters of a relation between independent and dependent variables as to describe a chemical reaction as good as possible.
Parity diagram	A 2-dimensional scatter plot in which the model calculated values of the responses are displayed against the experimentally observed values.
Physisorption	Also known as physical adsorption. Adsorption in which the forces involved are intermolecular forces (van der Waals forces) of the same kind as those responsible for deviation from ideal gas behavior or real gases at the condensation of vapors, and which do not involve a significant change in the electronic orbital patterns of the species involved. Physisorption usually occurs at temperatures near the boiling point of adsorbate, and multilayer can occur.

Porosity	A measure of the void spaces in a material, expressed as the ratio of the volume of voids to the total volume of the material.
Pre-exponential factor	The temperature-independent factor of a rate, also called the frequency factor.
Reaction family	Classification of elementary reaction steps on the basis of same Features
Reaction mechanism	A sequence of elementary steps in which reactants are converted into products, through the formation of intermediates.
Specific reaction rate	The number of moles of a component created by a chemical reaction per unit of time and catalyst mass.
Selectivity	The selectivity towards a product i is defined as the number of moles of product i formed per mole of reactant converted.
Single-Event Microkinetics	A kinetic modeling concept in which elementary steps are grouped into reaction families mainly based on enthalpic/energetic considerations. By accounting for the symmetry effects of reactant and transition state a unique, single-event rate coefficient suffices per reaction family. As a result, the number of adjustable parameters is greatly reduced.
Site time	The site time is defined as the ratio of the number of moles of active sites and the molar feed flow rate.
Site time yield	The site time yield is defined as the number of moles of reactant converted per mole of active sites and per second.
Steady state	A system in steady-state has certain properties that are time independent.
Surface coverage	Ratio of the amount of adsorbed substance to the monolayer capacity (also, sometimes defined for metals as the ratio of the number of adsorbed atoms or groups to the number of metal surface atoms).
Transition state	Also called activated complex. The configuration of highest potential energy along the path of lowest energy between reactants and products.

Transition state theory	Theory to calculate the rate of an elementary reaction from a knowledge of the properties of the reacting components and their concentrations. Differs from collision theory in that it takes into account the internal structure of reactant components.
Turnover frequency	The number of molecules of a component reacting per active site and per unit of time.
Yield	The number of moles of *i* formed per mole of reactant fed.

Summary

Crude oil is the cornerstone of modern society as it forms the basis for fuels and plastics encountered in our daily life. Fluctuating oil prices, depleting fossil resources as well as increased environmental awareness, however, have triggered the quest towards sustainable alternatives. One of the most promising candidates of potentially viable routes for the production of fuels and chemicals is the catalysed conversion of alcohols. Most attention has been given to methanol as feed molecule but (bio)ethanol is gaining interest rapidly [1]. Ethanol is already utilized as fuel or as fuel-additive in several parts of the world such as the United States, Brazil and Europe, but it can also be a platform molecule from which a variety of key components for the chemical industry can be derived. Several catalysts can be employed for the conversion of ethanol but this work will focus on the zeolite catalysed conversion to hydrocarbons.

A multiscale approach is employed in this work which starts at the laboratory scale with catalyst synthesis, characterization and experimental performance testing using high-throughput technology, to industrial scale reactor simulations. The information-driven methodology presented is the running thread through the work and is depicted in Figure 1. This methodology focusses on catalytic testing of various catalysts as well as on detailed mechanistic investigation to gain insights in the reaction mechanism. Rather than increasing the performance or selectivity of the catalyst, the initial goal is to maximize the information extracted from the experimental testing. The acquired information can be combined into a suitable kinetic model, allowing for *in silico* catalyst screening, in which an ideal catalyst can be selected tailored to the operating conditions at which it will be used. Ideally speaking, high-throughput setups are employed for accelerated information extraction. The information extracted from these setups corresponds to so-called intrinsic kinetics, i.e. kinetics in the absence of phenomena such as transport limitations. Literature correlations or physical laws can be employed to account for the latter.
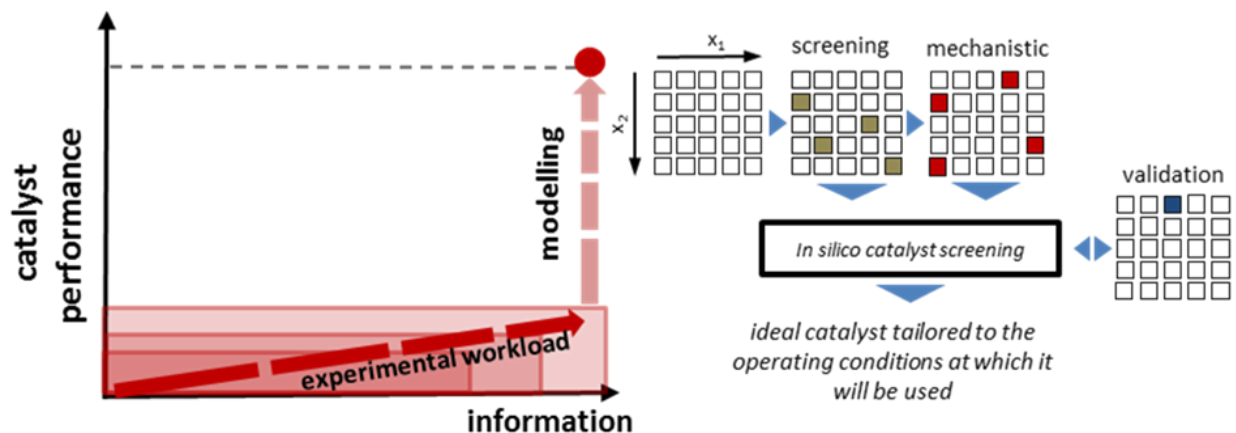
Figure 1: Information-driven catalyst design [2].

Two different processes can be identified during ethanol conversion on H-ZSM-5: ethanol dehydration and the production of higher hydrocarbons. Ethanol dehydration occurs either via monomolecular dehydration yielding ethene or via bimolecular dehydration resulting in diethyl ether. Diethyl ether can subsequently be converted into ethene and ethanol. The consecutive nature of ethanol dehydration and production of higher hydrocarbons is experimentally verified and can be explained using the results of microkinetic simulations based on quantum chemically obtained rate and equilibrium coefficients [3]. During ethanol dehydration, the catalyst surface is almost completely covered with adsorbed diethyl ether, so that no free sites are available for the production of higher hydrocarbons. Only when ethanol conversion is almost complete, higher hydrocarbons begin to form. In addition to that, an autocatalytic behaviour was observed for the production of higher hydrocarbons, as shown in Figure 2, which can only be partially attributed to the dehydration of ethanol.

The mechanism of the production of higher hydrocarbons is still a matter of debate in literature: a pure acid catalysed mechanism [4], a radical mechanism [5] and an aromatic-assisted mechanism [6] have been proposed. This aromatic-assisted mechanism is typically referred to as the hydrocarbon pool mechanism in the methanol-to-olefins process [7] and considers aromatics formed inside the catalyst pores to form new catalytic centres. Here, it has been found that ethanol is much more active on H-ZSM-5 than methanol. Conducting the same experiments but using ethene as feed shows the same autocatalytic behaviour as ethanol conversion and no

differences in product distribution are observed. The autocatalytic behaviour was already observed for methanol [8] but not yet for ethanol/ethene conversion. Propene is found to be much more reactive than the other considered feeds.
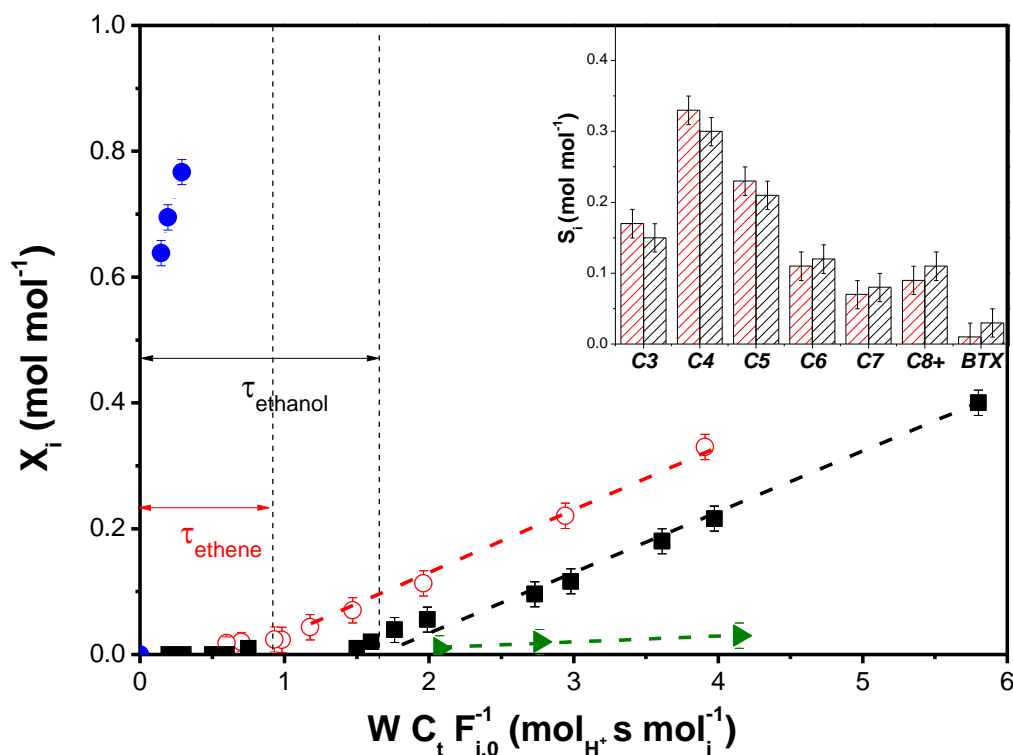
Figure 2: Conversion of different feeds: ethanol (C$_2$-conversion as defined in paragraph 2.4.2, ■, black), ethene (○, red), propene (●, blue) and methanol (▶, green) as a function of site time. Inset: selectivity towards higher hydrocarbons (C$_3$ to C$_{8+}$) and aromatics (Benzene-Toluene-Xylenes) at X$_{C2}$ = 0.2 for an ethene feed (red) and an ethanol feed (black) (T = 573 K, p$_{EtOH,MeOH,0}$= 30 kPa, p$_{ethene,propene,0}$ = 27 kPa). Lines are to guide the eye.

Via Temporal Analysis of Products experiments [9] using ethene as reactant, it has been found that all olefinic products are formed from the first pulse onwards. Aromatics are only observed at a later stage. This indicates that the dimerization of ethene to 1-butene is the slowest step in this reaction sequence. Examination of the spent catalyst showed a gradual darkening of the catalyst along the reactor axis: near the entrance of the reactor, the catalyst remains white, which corresponds to the dehydration of ethanol in which no higher hydrocarbons are being formed but it gradually turns into grey, while moving away from the inlet. UV/VIS spectroscopy showed that different types of aromatic species are formed inside the pores.

Ultimately, this results in the reaction mechanism as shown in Figure 3, in which the consecutive character of ethanol dehydration and C_{3+} hydrocarbon production is shown. Different types of surface species can be distinguished: butene which is formed via the dimerization of ethene and responsible for the autocatalytic behaviour, short-lived species labelled as aliphatic and long-lived species labelled aromatics. Isotopic labelling experiments using $^{13}C_2H_4$ have indicated that the involvement of long-lived surface species only contributes to 5% of the propene production.
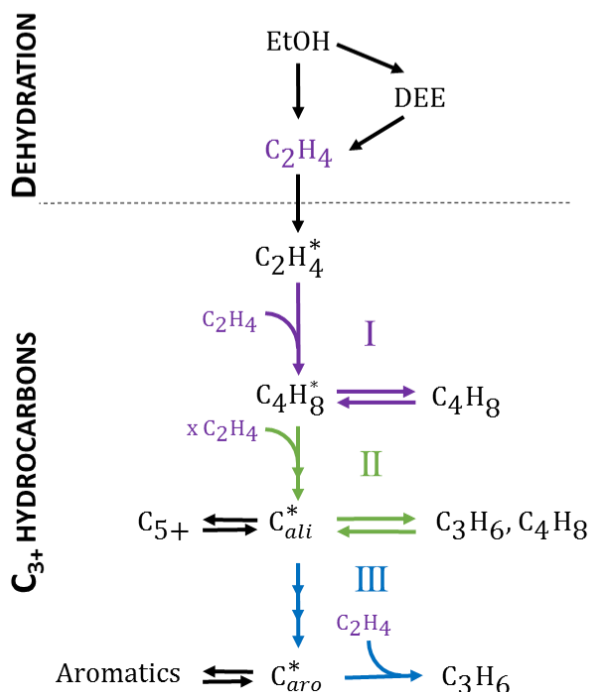
Figure 3: Reaction mechanism for the conversion of ethanol to hydrocarbons with: EtOH: ethanol, DEE: diethyl ether, C_2H_4: ethene, C_3H_6: propene, C_4H_8: butene, C_{5+}: olefinic hydrocarbons containing more than 5 carbon atoms, aromatics: hydrocarbons containing one or more aromatic rings, $C_2H_4^*$: ethene surface species; $C_4H_8^*$: butene surface species; C_{ali}^*: aliphatic surface species, C_{aro}^*: aromatic surface species. Route I (violet): the dimerization of ethene to butene, Route II (green): formation of propene and butene via aliphatic surface intermediates, Route III (blue): formation of propene via aromatic surface intermediates.

A separate investigation of both processes, i.e. ethanol dehydration and production of C_{3+} hydrocarbons, has been conducted to gain more insight in the effect of process conditions. Ethanol dehydration has been studied at a lower temperature so that only the monomolecular and bimolecular dehydration are present and no unwanted side reactions such as higher hydrocarbon formation. High conversion and temperature is found to favour ethene yield. A good agreement between the catalytic ethanol dehydration experiments and the results from

microkinetic simulations using ab initio obtained rate and equilibrium coefficients [3] has been obtained. Several other industrially relevant zeolites have been evaluated for ethanol dehydration. H-MOR and H-FER exhibit the highest initial ethene selectivity. A structure-activity relationship between the activity and ethene selectivity of the different zeolites and the ammonia desorption energy is observed.

A reaction network for the production of C_{3+} hydrocarbons has been generated, considering the acid catalysed elementary steps of ethylation, alkylation and β-scission. The single-event methodology [10] has subsequently been applied for reducing the number of adjustable parameters. The kinetic and catalyst descriptors that were determined via model regression to experimental data are found to have a physical meaning as well as to be statistically significant. Rate analysis shows that the dimerization of ethene to 1-butene is the step responsible for the autocatalytic behaviour of the reaction.

Catalyst optimization for the production of higher hydrocarbons has been attempted via post-synthesis introduction of gallium, nickel or iron into the zeolite. The effect of metal content on catalyst properties has been studied by comparing unmodified H-ZSM-5 and 0.5-7 wt.% Ga, Fe and Ni modified H-ZSM-5. Low metal amounts (< 1 wt.%) have a slight positive effect on the C_2 conversion. Increasing the amount of metal leads to a decreased production of these hydrocarbons, which is attributed to bulky metal clusters formation. These clusters decrease the accessibility of the acid sites due to pore blockage. For the first time, catalyst performance in ethanol conversion has been assessed at similar conditions, i.e. same C_2 conversion, showing that the selectivity towards the various product classes is not altered by the metal introduction.

The step towards new economically viable chemical processes often lies in translating the observed lab scale phenomena into a full industrial scale reactor. In this work, a reactor model is presented for an ethanol dehydration unit using ab initio obtained rate and equilibrium coefficients. Heat and mass transfer limitations for the design case have been assessed via literature correlations. Good agreement between the simulations and a literature design case

have been obtained as can be seen in Figure 4. The industrial reactor model can be used as a tool to improve the performance of existing and to design new process units, e.g. by varying the water content as exemplified in this work. A high water content is favourable for the activity and selectivity to ethene as it reduces the temperature drop along the reactor axis.
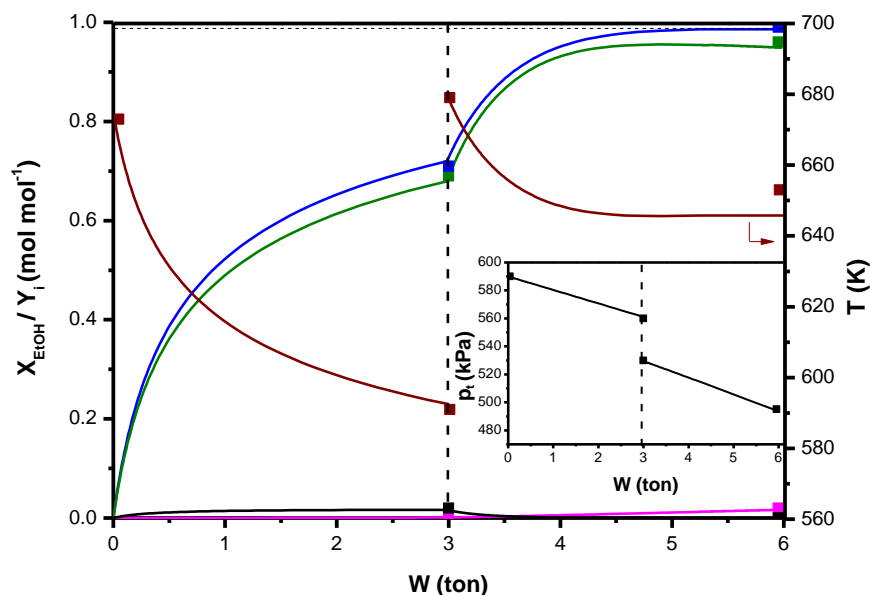
Figure 4: Ethanol conversion (X_{EtOH}, blue), ethene, diethyl ether and butene yield (green: Y_{C2H4}; black: Y_{DEE}; magenta; Y_{C4H8}) and temperature profiles (T) as a function of catalyst mass. Inset shows the pressure drop (p_t) as a function of catalyst mass.

Concluding, the ethanol conversion to hydrocarbons has been studied using a multiscale approach. This work has focused on a detailed understanding of the reaction mechanism of ethanol dehydration on the one hand and the subsequent conversion to higher hydrocarbons on the other hand. In the near future, additional insights can be acquired via co-feeding of aromatics and olefins, combined with isotopic labelling experiments using e.g. a SSITKA setup. Expanding the microkinetic model with the data extracted from high-throughput experimentation on e.g. other types of zeolites, can result in *in silico* determined structure-activity relationships [11]. Such relationships can be examined in more detail using quantum chemical calculations. Tailoring the product distribution via post-synthesis modification methods can be attempted via dealumination, desilication [12] and metal atomic layer deposition [13].

References

[1] J. Sun, Y. Wang, Recent Advances in Catalytic Conversion of Ethanol to Chemicals, ACS Catalysis, 4 (2014) 1078-1090.

[2] K. Van der Borght, K. Toch, V.V. Galvita, J.W. Thybaut, G.B. Marin, Information-Driven Catalyst Design Based on High-Throughput Intrinsic Kinetics, Catalysts, 5 (2015) 1948-1968.

[3] K. Alexopoulos, M. John, K. Van der Borght, V. Galvita, M.-F. Reyniers, G.B. Marin, DFT-based microkinetic modeling of ethanol dehydration in H-ZSM-5, Journal of Catalysis, 339 (2016) 173-185.

[4] A.G. Gayubo, A.M. Tarrío, A.T. Aguayo, M. Olazar, J. Bilbao, Kinetic Modelling of the Transformation of Aqueous Ethanol into Hydrocarbons on a HZSM-5 Zeolite, Industrial & Engineering Chemistry Research, 40 (2001) 3467-3474.

[5] F.F. Madeira, N.S. Gnep, P. Magnoux, H. Vezin, S. Maury, N. Cadran, Mechanistic insights on the ethanol transformation into hydrocarbons over HZSM-5 zeolite, Chemical Engineering Journal, 161 (2010) 403-408.

[6] R. Johansson, S.L. Hruby, J. Rass-Hansen, C.H. Christensen, The Hydrocarbon Pool in Ethanol-to-Gasoline over HZSM-5 Catalysts, Catalysis Letters, 127 (2009) 1-6.

[7] U. Olsbye, S. Svelle, M. Bjorgen, P. Beato, T.V.W. Janssens, F. Joensen, S. Bordiga, K.P. Lillerud, Conversion of Methanol to Hydrocarbons: How Zeolite Cavity and Pore Size Controls Product Selectivity, Angewandte Chemie-International Edition, 51 (2012) 5810-5831.

[8] X. Sun, S. Mueller, Y. Liu, H. Shi, G.L. Haller, M. Sanchez-Sanchez, A.C. van Veen, J.A. Lercher, On reaction pathways in the conversion of methanol to hydrocarbons on HZSM-5, Journal of Catalysis, 317 (2014) 185-197.

[9] J.T. Gleaves, G. Yablonsky, X.L. Zheng, R. Fushimi, P.L. Mills, Temporal analysis of products (TAP)-Recent advances in technology for kinetic analysis of multi-component catalysts, Journal of Molecular Catalysis a-Chemical, 315 (2010) 108-134.

[10] J.W. Thybaut, G.B. Marin, Single-Event MicroKinetics: Catalyst design for complex reaction networks, Journal of Catalysis, 308 (2013) 352-362.

[11] F.R. Ribeiro, F. Alvarez, C. Henriques, F. Lemos, J.M. Lopes, M.F. Ribeiro, Structure-Activity Relationship in Zeolites, Journal of Molecular Catalysis a-Chemical, 96 (1995) 245-270.

[12] H. Xin, X. Li, Y. Fang, X. Yi, W. Hu, Y. Chu, F. Zhang, A. Zheng, H. Zhang, X. Li, Catalytic dehydration of ethanol over post-treated ZSM-5 zeolites, Journal of Catalysis, 312 (2014) 204-215.

[13] B.D. Vandegehuchte, J.W. Thybaut, C. Detavernier, D. Deduytsche, J. Dendooven, J.A. Martens, S.P. Sree, T.I. Korányi, G.B. Marin, A Single-Event MicroKinetic assessment of n-alkane hydroconversion on ultrastable Y zeolites after Atomic Layer Deposition of alumina, Journal of Catalysis, 311 (2014) 433-446.

Samenvatting

Ruwe aardolie vormt de hoeksteen van onze moderne maatschappij aangezien het de basis is voor onze brandstoffen en olie-afgeleide producten zoals kunststoffen. Zowel wisselende olieprijzen, slinkende reserves van fossiele grondstoffen als een groeiend milieubewustzijn stimuleren de zoektocht naar duurzame alternatieven. Eén van de meest veelbelovende productieroutes voor zowel brandstoffen als chemicaliën is de gekatalyseerde omzetting van alcoholen. Tot nu toe werd de meeste aandacht aan methanol gegeven maar de interesse voor (bio)ethanol stijgt snel [1]. Ethanol wordt in verschillende delen van de wereld, zoals de Verenigde Staten, Brazilië en Europa, reeds als brandstof of als toevoeging aan brandstof gebruikt maar het kan ook als platformmolecule dienen voor de productie van een aantal sleutelcomponenten voor de chemische industrie. Verschillende katalysatoren kunnen hiervoor gebruikt worden maar in dit werk zal de klemtoon liggen op de zuur gekatalyseerde omzetting naar koolwaterstoffen.

Er zal in dit proefschrift gebruik gemaakt worden van een multischaal aanpak die begint op laboschaal met de synthese, karakterisering en het testen van verschillende katalysatoren tot en met industriële reactor simulaties. De informatie gedreven methodologie die wordt voorgesteld is de rode draad doorheen het werk en wordt weergeven in Figuur 1. Deze methodologie legt de nadruk op zowel het testen van verschillende katalysatoren als een gedetailleerd onderzoek naar het reactiemechanisme. In plaats van enkel de activiteit of de selectiviteit van de katalysator te verhogen, wordt er gestreefd naar het verkrijgen van maximale informatie uit de experimenten. De verkregen informatie kan vervolgens gecombineerd worden in een kinetisch model waarbij katalysatoren *in silico* getest en vergeleken worden. Het resultaat is een katalysator geoptimaliseerd voor de toepassing en de werkingsvoorwaarden. Idealerwijs worden hiervoor hoge doorvoeropstellingen gebruikt en is de verkregen informatie zogenaamde intrinsieke kinetiek, d.w.z. kinetiek in de afwezigheid van fenomenen zoals transportlimiteringen die via correlaties uit de literatuur of fysische wetmatigheden in rekening gebracht worden.
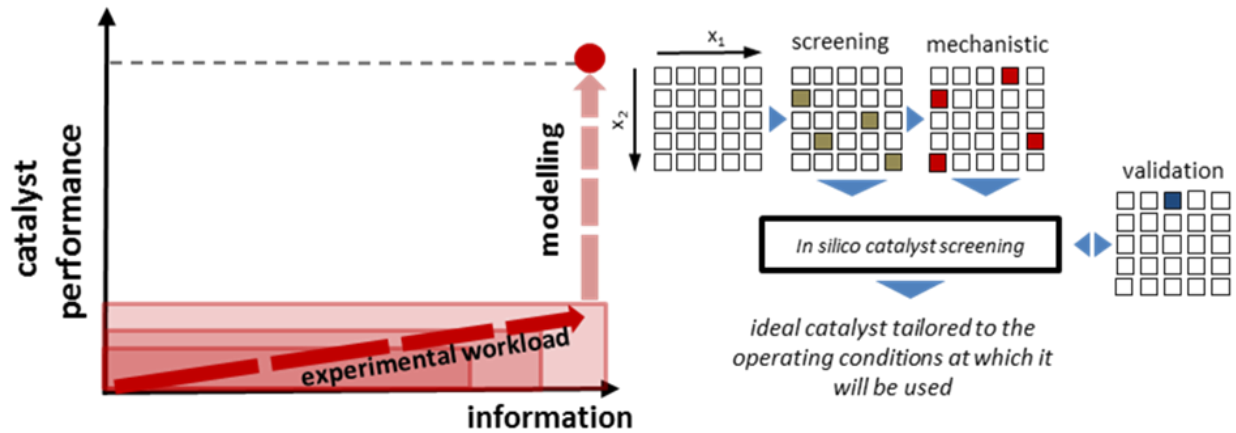
Figuur 1: Informatie gedreven katalysator ontwerp [2].

Twee verschillende processen kunnen geïdentificeerd worden tijdens de omzetting van ethanol op H-ZSM-5: ethanol dehydratie en de productie van hogere koolwaterstoffen. Ethanol dehydratie gebeurt ofwel via monomoleculaire dehydratie met ethene als product of de bimoleculaire dehydratie die di-ethylether oplevert. Di-ethylether kan vervolgens omgezet worden in ethene en ethanol. Het consecutieve karakter van ethanol dehydratie en de productie van hogere koolwater werd experimenteel vastgesteld en kon verklaard worden aan de hand van de resultaten van microkinetische simulaties gebaseerd op snelheid- en evenwichtscoëfficiënten die verkregen werden op basis van kwantumchemische berekeningen [3]. Tijdens ethanol dehydratie is het katalysatoroppervlak zo goed als volledig bezet met geadsorbeerd di-ethylether zodanig dat er geen vrije centra aanwezig zijn voor de productie van hogere koolwaterstoffen. Enkel wanneer de ethanol omzetting compleet is, beginnen er zich hogere koolwaterstoffen te vormen. Bovendien werd een autokatalytisch gedrag vastgesteld voor de productie van hogere koolwaterstoffen, zoals getoond in Figuur 2, dat slechts gedeeltelijk kan gewijd worden aan de dehydratie van ethanol.

Het mechanisme voor de productie van hogere koolwaterstoffen is nog steeds een punt van discussie in de wetenschappelijke literatuur: zowel een zuur gekatalyseerd mechanisme [4], een radicalair mechanisme [5] als een mechanisme waarin aromatische koolwaterstoffen een belangrijke rol spelen [6] werden reeds voorgesteld. Het mechanisme waarin aromaten een rol spelen wordt, is afkomstig uit het methanol omzettingsproces [7]. Hierbij worden aromatische

koolwaterstoffen die zich in de katalysatorporiën bevinden, beschouwd als nieuwe katalytisch centra. In dit werk werd vastgesteld dat ethanol veel actiever is op H-ZSM-5 dan methanol. De omzetting van etheen vertoonde hetzelfde autokatalytisch gedrag. Bovendien werden er geen verschillen in productdistributie waargenomen. Het autokatalytisch gedrag werd reeds opgemerkt voor methanol omzetting maar nog niet voor ethanol en ethene omzetting [8]. Propeen toonde zich in vergelijking tot de andere moleculen beschouwd in dit werk veel reactiever.
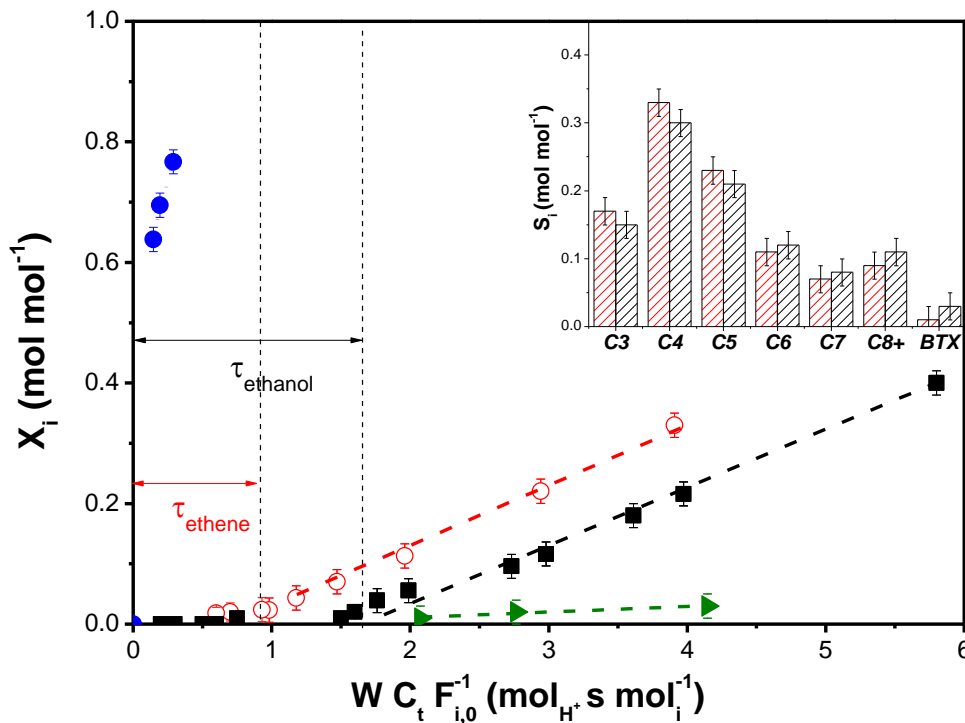
Figuur 2: Omzetting van verschillende voedingen: ethanol (C_2-omzetting zoals gedefinieerd in paragraaf 2.4.2, ■, zwart), etheen (○, rood), propeen (●, blauw) en methanol (▶, groen) als functie van site tijd. Staafdiagram: selectiviteit naar hogere koolwaterstoffen en aromaten bij $X_{C2} = 0.2$ voor een etheen voeding (rood) en een ethanol voeding (zwart) (T = 573 K, $p_{EtOH,MeOH,0}$ = 30 kPa, $p_{etheen,propeen,0}$ = 27 kPa).

Gebruik makend van temporale product analyse [9] met etheen als reactant werd gevonden dat alle olefinen reeds in de eerste stap gevormd worden. Aromaten worden pas waargenomen in een later stadium. Dit toont aan dat de dimerizatie van ethene naar 1-butene de traagste stap is in het reactie mechanisme. Een beoordeling van de kleur van de katalysator na reactie toont een graduele verkleuring: nabij de inlaat van de reactor blijft de katalysator wit, wat overeenkomt met de dehydratie van ethanol waarbij nog geen hogere koolwaterstoffen gevormd werden.

Verderop in de reactor wordt de katalysator grijs. UV/VIS spectroscopie toonde aan dat verschillende types van aromatische koolwaterstoffen gevormd worden in de poriën.

Uiteindelijk leidt dit tot het reactie mechanisme zoals voorgesteld in Figuur 3 waarbij het consecutieve karakter van de dehydratie en de productie van hogere koolwaterstoffen wordt getoond. Verschillende types van oppervlaktespecies kunnen onderscheiden worden: buteen gevormd door de dimerizatie van ethene en verantwoordelijk voor het autokatalytisch gedrag en intermediairen met een korte en lange levensduur op het oppervlak, namelijk alifatische en aromatische species. Experimenten met isotopisch gemerkte ethene hebben aangetoond dat de betrokkenheid van deze aromatische intermediaren slechts voor 5 % bijdraagt bij de productie van propeen.
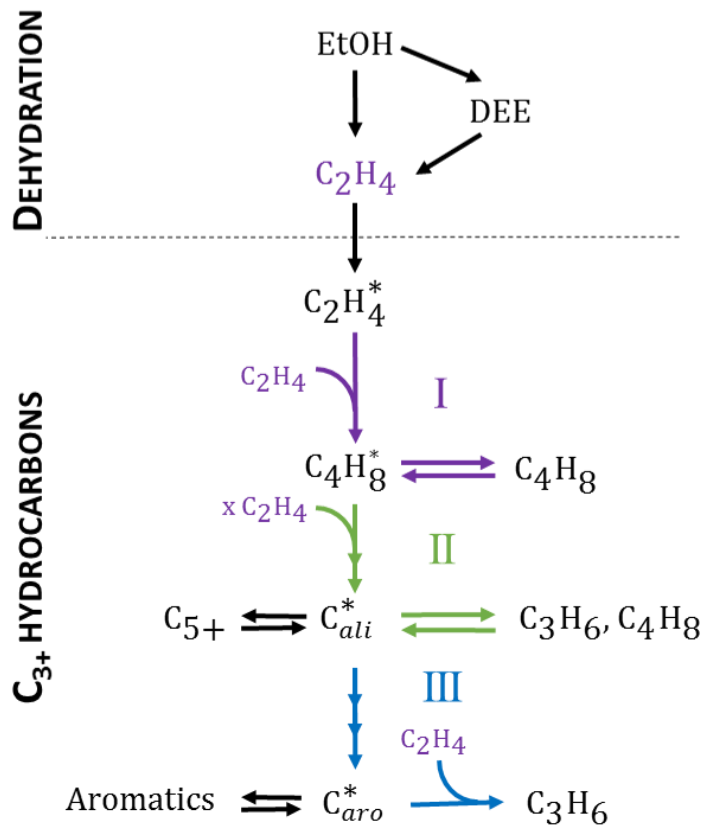
Figuur 3: Reactie mechanisme voor de omzetting van ethanol naar koolwaterstoffen met: EtOH: ethanol, DEE: di-ethylether, C_2H_6: etheen, C_3H_6: propeen, C_4H_8: buteen, C_{5+}: olefines met meer dan 5 koolstofatomen, aromaten: koolwaterstoffen met één of meer aromatische ringen, $C_2H_4^*$: etheen oppervlakte intermediair; $C_4H_8^*$: buteen oppervlakte intermediair; C_{ali}^*: alifatische oppervlakte intermediair, C_{aro}^*: aromatisch oppervlakte intermediair. Route I (paars): dimerizatie van etheen naar buteen, Route II (groen): vorming van propeen en buteen via alifatische oppervlakte intermediairen, Route III (blauw):vorming van propeen via aromatische oppervlakte intermediairen.

Vervolgens werd een aparte studie uitgevoerd naar de ethanol dehydratie en de productie van hogere koolwaterstoffen om meer inzicht te krijgen in het effect van werkingsvoorwaarden. Ethanol dehydratie werd bestudeerd bij lagere temperatuur zodanig dat enkel de monomoleculaire en bimoleculaire dehydratie aanwezig waren en geen ongewenste nevenreacties zoals hogere koolwaterstofvorming. Hoge omzetting en temperatuur zijn gunstig voor de etheenopbrengst. Een goede overeenkomst tussen de ethanol dehydratie experimenten en de resultaten van microkinetische simulaties gebaseerd op *ab initio* verkregen snelheids- en evenwichtscoefficiënten werd waargenomen [3]. Verschillende andere industrieel relevante zeolieten werden geëvalueerd voor ethanol. H-MOR en H-FER toonde een hogere initiële etheen selectiviteit. Een structuur-activiteitsverband tussen de activiteit en de etheen selectiviteit en de ammoniak desorptie energie werd vastgesteld.

Een reactienetwerk voor de productie van C_{3+} koolwaterstoffen werd opgesteld waarbij zuur gekatalyseerde stappen zoals ethylatie, alkylatie and β-scissie in rekening werden gebracht. De 'single-event' methodologie [10] werd vervolgens toegepast voor het reduceren van het aantal aanpasbare parameters. De kinetische en katalysator descriptoren die bepaald werden via modelregressie aan de experimentele data waren zowel statistisch significant als fysische zinvol. Een snelheidsanalyse toonde aan dat de dimerizatie van etheen naar 1-buteen verantwoordelijk is voor het autokatalytisch gedrag van de reactie.

Via post-synthese wijziging van H-ZSM-5 met metalen zoals gallium, nikkel en ijzer werd getracht een meer performante katalysator te vinden voor de productie van hogere koolwaterstoffen. Het effect van metaalinhoud op de katalysator eigenschappen werd bestudeerd door het vergelijken van ongewijzigde H-ZSM-5 met 0.5 – 7 wt.% Ga, Fe en Ni gewijzigde H-ZSM-5. Lage metaalbelading had een licht positief effect op de C_2 omzetting. Verhoging van het metaalgehalte zorgde voor het verlaagde productie van hogere koolwaterstoffen wat te wijten is aan de vorming van metaalclusters. Deze clusters verlagen de bereikbaarheid van zure centra door een blokkering van de katalysatorporiën. Voor de eerste keer werden de verschillende katalysatoren vergeleken bij gelijke C_2 omzetting maar de selectiviteit naar de verschillende producten ongewijzigd bleef.

De stap naar nieuwe economisch haalbare chemische processen ligt vaak in het vertalen van waargenomen effecten op laboschaal naar een industriële reactor. In dit werk wordt een multischaal reactor model voor ethanol dehydratie voorgesteld waarbij de kinetiek gebaseerd is op *ab initio* verkregen snelheids- en evenwichtscoëfficiënten. Warmte- en massatransportlimiteringen werden beoordeeld via correlaties uit de literatuur. Goede overeenkomst tussen de simulaties en data opgenomen op een pilootschaal eenheid [11] werd waargenomen zoals te zien in Figuur 4. Dit reactor model kan nu gebruikt worden als hulpmiddel bij het ontwerpen en optimaliseren van ethanol dehydratie eenheden. Dit werd geïllustreerd met een studie naar het effect van water: een hoog water gehalte is aangewezen voor een hoge activiteit en selectiviteit naar etheen aangezien het o.a. de temperatuursdaling in de reactor beperkt.
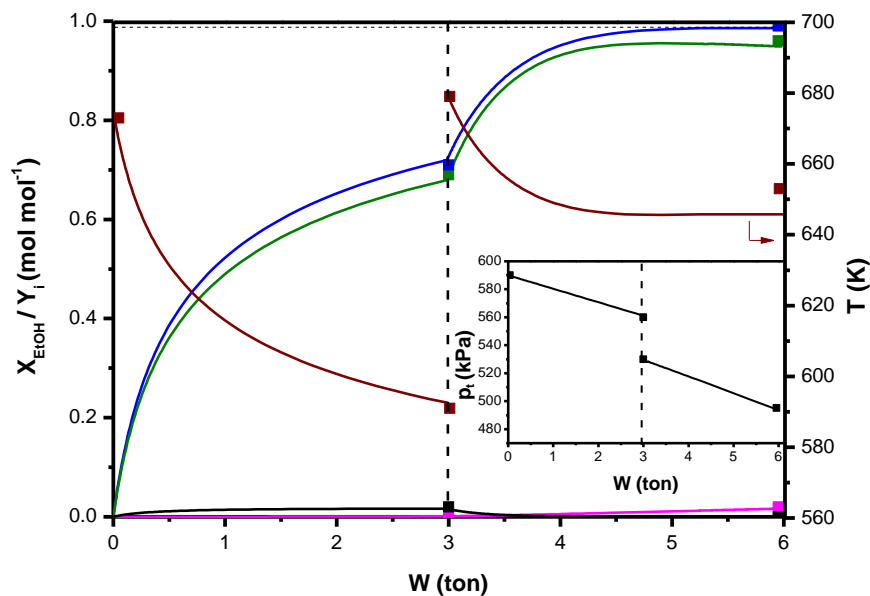
Figuur 4: Ethanol omzetting (X_{EtOH}, blauw), etheen, di-ethylether en buteen opbrengst (groen: Y_{C2H4}; zwart: Y_{DEE}; magenta; Y_{C4H8}) en temperatuursprofiel (T) als functie van de katalysatormassa. Grafiek getoond als inzet toont de drukval (p_t) als functie van de katalysatormassa. Punten tonen de experimentele data [11]

In dit werk werd de omzetting van ethanol naar koolwaterstoffen op zeolieten bestudeerd gebruik makend van een multischaal aanpak. De klemtoon lag op een gedetailleerd begrip van het reactiemechanisme van ethanol dehydratie aan de ene kant en de verdere omzetting naar koolwaterstoffen aan de andere kant. Bijkomende inzichten kunnen in de toekomst verkregen

worden via het co-voeden van aromaten en olefinen, eventueel gecombineerd met experimenten met isotopisch gemerkte componenten in bv. een SSITKA-opstelling. Het uitbreiden van het microkinetisch model met data verkregen uit hoge doorvoer experimenten met verschillende zeolieten, kan resulteren in *in silico* bepaalde structuur-activiteitsverbanden [12]. Zulke verbanden kunnen in meer detail bekeken worden via kwantum chemische berekeningen. Het wijzigen van de productdistributie kan overwegen worden via post-synthese methoden zoals dealuminatie, desilicatie [13] en metaal laag depositie [14].

Referenties

[1] J. Sun, Y. Wang, Recent Advances in Catalytic Conversion of Ethanol to Chemicals, ACS Catalysis, 4 (2014) 1078-1090.

[2] K. Van der Borght, K. Toch, V.V. Galvita, J.W. Thybaut, G.B. Marin, Information-Driven Catalyst Design Based on High-Throughput Intrinsic Kinetics, Catalysts, 5 (2015) 1948-1968.

[3] K. Alexopoulos, M. John, K. Van der Borght, V. Galvita, M.-F. Reyniers, G.B. Marin, DFT-based microkinetic modeling of ethanol dehydration in H-ZSM-5, Journal of Catalysis, 339 (2016) 173-185.

[4] A.G. Gayubo, A.M. Tarrío, A.T. Aguayo, M. Olazar, J. Bilbao, Kinetic Modelling of the Transformation of Aqueous Ethanol into Hydrocarbons on a HZSM-5 Zeolite, Industrial & Engineering Chemistry Research, 40 (2001) 3467-3474.

[5] F.F. Madeira, N.S. Gnep, P. Magnoux, H. Vezin, S. Maury, N. Cadran, Mechanistic insights on the ethanol transformation into hydrocarbons over HZSM-5 zeolite, Chemical Engineering Journal, 161 (2010) 403-408.

[6] R. Johansson, S.L. Hruby, J. Rass-Hansen, C.H. Christensen, The Hydrocarbon Pool in Ethanol-to-Gasoline over HZSM-5 Catalysts, Catalysis Letters, 127 (2009) 1-6.

[7] U. Olsbye, S. Svelle, M. Bjorgen, P. Beato, T.V.W. Janssens, F. Joensen, S. Bordiga, K.P. Lillerud, Conversion of Methanol to Hydrocarbons: How Zeolite Cavity and Pore Size Controls Product Selectivity, Angewandte Chemie-International Edition, 51 (2012) 5810-5831.

[8] X. Sun, S. Mueller, Y. Liu, H. Shi, G.L. Haller, M. Sanchez-Sanchez, A.C. van Veen, J.A. Lercher, On reaction pathways in the conversion of methanol to hydrocarbons on HZSM-5, Journal of Catalysis, 317 (2014) 185-197.

[9] J.T. Gleaves, G. Yablonsky, X.L. Zheng, R. Fushimi, P.L. Mills, Temporal analysis of products (TAP)-Recent advances in technology for kinetic analysis of multi-component catalysts, Journal of Molecular Catalysis a-Chemical, 315 (2010) 108-134.

[10] J.W. Thybaut, G.B. Marin, Single-Event MicroKinetics: Catalyst design for complex reaction networks, Journal of Catalysis, 308 (2013) 352-362.

[11] V. Coupard, N. Touchais, S. Fleurier, H.G. Penas, P. De Smedt, W. Vermeiren, C. Adam, D. Minoux, Process for dehydration of dilute ethanol into ethylene with low energy consumption without recycling of water, in, US 20130090510 A1, 2013.

[12] F.R. Ribeiro, F. Alvarez, C. Henriques, F. Lemos, J.M. Lopes, M.F. Ribeiro, Structure-Activity Relationship in Zeolites, Journal of Molecular Catalysis a-Chemical, 96 (1995) 245-270.

[13] H. Xin, X. Li, Y. Fang, X. Yi, W. Hu, Y. Chu, F. Zhang, A. Zheng, H. Zhang, X. Li, Catalytic dehydration of ethanol over post-treated ZSM-5 zeolites, Journal of Catalysis, 312 (2014) 204-215.

[14] B.D. Vandegehuchte, J.W. Thybaut, C. Detavernier, D. Deduytsche, J. Dendooven, J.A. Martens, S.P. Sree, T.I. Korányi, G.B. Marin, A Single-Event MicroKinetic assessment of n-alkane hydroconversion on ultrastable Y zeolites after Atomic Layer Deposition of alumina, Journal of Catalysis, 311 (2014) 433-446.

Chapter 1

Introduction

Crude oil is the key feedstock for the production of motor fuels and chemicals. Through refining, chemical building blocks, such as ethene and propene, are produced which serve as monomers for the production of polyethene and polypropene. However, since the beginning of the twenty-first century, crude oil prices have risen from 30 USD per barrel up to almost 140 USD per barrel in June of 2008 as shown in Figure 1-1 [1]. Afterwards the price has dropped dramatically due the economic crisis. A recovery of the oil price was accomplished but due to the increase in supply by the United States, Iraq and Iran and the economic slowdown in China, prices are again historically low.
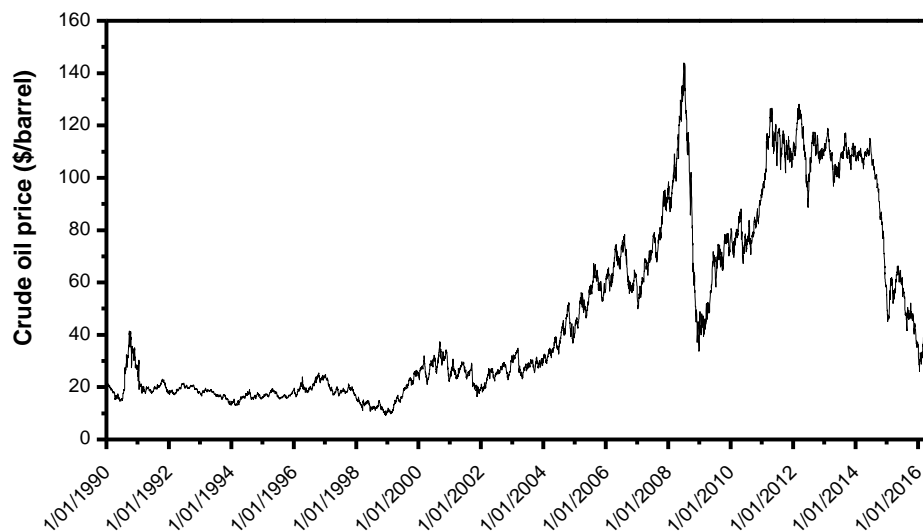
Figure 1-1: Evolution of the Brent crude oil price from 1990 to 2016 [1].

Climate change, public opinion and stringent legislation are incentives that accelerate the quest for alternatives. Many attention is given to solar cells and wind turbines for power generation but the security of supply and the storage of electricity still remain important vulnerabilities. Several of these shortcomings can be satisfied by the use of biofuels. They have a renewable character, reduce greenhouse gases and provide security, also for the countries

1

that do not possess large reserves of crude oil. Some of the most well-known are bioethanol, biobutanol and biodiesel. Ethanol possesses several advantages in comparison to these other types of renewables: multiple feedstocks can be utilized for the production and the diversity of the possible applications. Starting materials range from sugar and starch crops to lignocellulosic biomass from agricultural residues or forest resources which are pretreated and fermented to form an aqueous ethanol solution [2]. When the water content in ethanol is reduced to less than 1 v%, it can be used as fuel or added as an additive in fuel for a classic internal combustion engine. Due to its high octane number, ethanol (RON = 108) can also be used as anti-knocking agent, It is also environmentally friendlier than alternatives such as methyl tertiary butyl ether (MTBE, RON = 117), due to its lower toxicity. The Ford model T designed by Henri Ford was designed to run on corn-derived ethanol with gasoline as an option [3]. However, the lower energy content of ethanol (26 MJ kg^{-1}), compared to gasoline (46 MJ kg^{-1}) [4] will require the volume of a car's fuel tank to be increased in order to maintain the same action radius. The use of ethanol in ethanol/gasoline blends is limited to 10 v% anhydrous ethanol: higher ethanol content requires modifications to the engine [5]. Despite these drawbacks, ethanol currently is the most widely used liquid biofuel for motor vehicles [6].

Renewable energy discussions focus primarily on securing our transportation needs but crude oil is also the source for the majority of key chemical intermediates. Any product obtained from crude oil can, in principle, be produced from ethanol which is illustrated in Figure 1-2. Depending on the process, the catalyst and reaction conditions, a wide array of products can be synthesized such as hydrogen, ethene, diethyl ether, 1,3-butadiene, acetaldehyde, acetic acid, ethene oxide and many more [7]. Posada et al. made a comparison of 12 different bioethanol-based products and concluded that 1,3-butadiene, diethyl ether, ethene and propene are economically the most promising derivatives [8]. In this chapter, the production routes of ethanol will discussed, followed by a short description of the acid catalyzed conversion of alcohol to hydrocarbons.
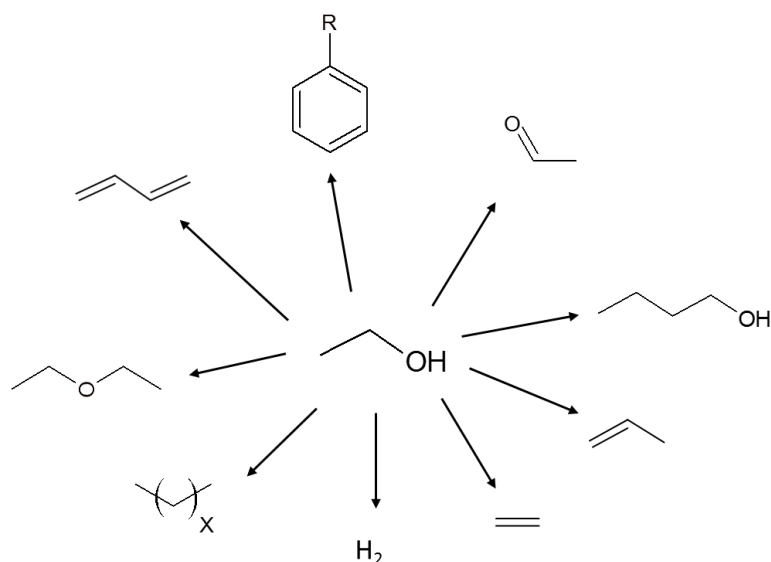
Figure 1-2: Possible pathways to utilize ethanol as a feedstock in the chemical industry.

1.1 Production of ethanol

The world annual ethanol production was 24 Mton in 2001, 31 Mton in 2006 and was almost 79 Mton in 2016 [9]. Brazil and the USA are the two major ethanol producers and account for 62% of the world production [10]. In Brazil, sugar cane is primarily used as feedstock [11, 12] while in the USA, corn is used [10, 13]. Three routes are available for the large scale production of ethanol.

1.1.1 Ethanol from ethene hydration

High purity ethanol can easily be produced from ethene coming from naphtha and ethane steam cracking facilities, by hydration with steam, typically performed between 550 K to 650 K at 5 to 8 MPa [14]:

$$C_2H_4 + H_2O \rightarrow C_2H_5OH \tag{1-1}$$

Synthetic production of ethanol from ethene was first commercialized by Union Carbide in 1930 using absorption of ethene in sulfuric acid and subsequent hydrolytic cleavage. In 1948, Shell introduced the direct catalytic hydration of ethene with an acid catalyst, of which only phosphoric acid catalysts are of industrial importance [15]. However, this process can definitely not be depicted as renewable.

3

1.1.2 Ethanol from syngas

Syngas is a mixture consisting of hydrogen and carbon monoxide and can be produced from gasification of biomass, among others. Gasification is a thermochemical process in which the feed reacts with a controlled amount of oxygen and steam. This feed is typically used for Fischer-Tropsch synthesis but by using an appropriate catalyst and H_2:CO ratio, ethanol can also be produced [16]:

$$n\,CO + 2n\,H_2 \rightarrow C_nH_{2n+1}OH + (n-1)\,H_2O \qquad (1\text{-}2)$$
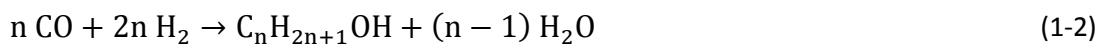
However, the catalysts used to produce ethanol from syngas typically also form methanol and higher alcohols as byproducts [17]. Further research is still required in this field and hence no commercial application exists yet.

1.1.3 Ethanol from biomass fermentation

Approximately 80% of the ethanol produced in the world is obtained from fermentation of biomass [2]. A typical flowchart of the production process to fuel grade quality ethanol is shown in Figure 1-3.
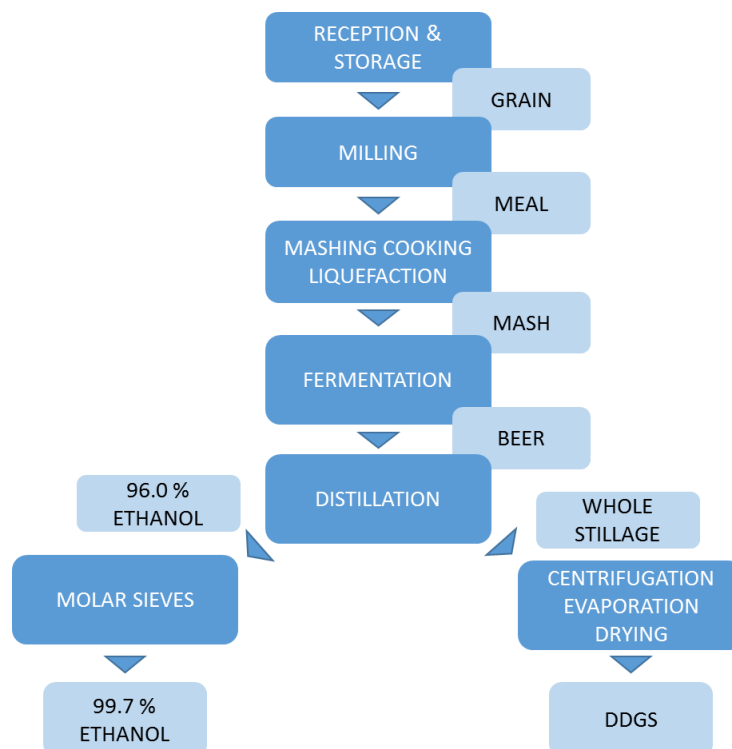
Figure 1-3: Overview of the production process of ethanol starting from corn. Adapted from [18].

Before the fermentation, several preparatory steps are required. In the case of corn, this consist of grounding and milling it into a coarse powder. Next, it is mixed with water and cooked. The steam breaks down the starch granules present inside the corn. The addition of an enzyme liquefies the mash by breaking down the starch into carbohydrates such as glucose and fructose.

Adding yeast to the sugar mixture at temperatures between 303 – 305 K in the absence of oxygen, will produce ethanol from glucose via the anaerobic digestion:

$$C_6H_{12}O_6 \rightarrow 2\ C_2H_5OH + 2\ CO_2 \hspace{3cm} (1\text{-}3)$$

If oxygen would be present, the glucose is oxidized to acetic acid which is subsequently transformed into carbon dioxide and water. However, the yield of ethanol in the fermentation process is lower than expected due to the formation of small amounts of byproducts, called fusel alcohol. The resulting product, i.e., an aqueous ethanol-water mixture, typically has an alcohol content of max. 18 v% and is called 'beer'. Efforts are undertaken at the moment in several industrial fermentation plants to prevent the release of carbon dioxide to the atmosphere. Distillation is subsequently performed to increase the ethanol concentration up to the azeotrope (96.0 w% ethanol). The fuel grade quality ethanol is obtained by removing the final water via membranes or molecular sieves. The remaining stillage is processed to cattle feed, called Distiller's Dried Grains with Solubles (DDGS), by centrifugation, to remove excess yeast, and evaporation [19].

Crops containing sugar or starch have been used for centuries as raw materials for the production of ethanol, mainly for beverages. At the moment, the majority of the produced ethanol is dedicated towards fuel applications. However, a growing awareness is rising about the conflict with food production [19]. Regardless of several ethical issues related to the latter, the competition for farm land for food crops will increase the price of bioethanol and hence reduce its economic viability [20]. The ethanol produced from fermentation of edible crops is typically referred to as first generation of ethanol.

Contrary to first generation biomass, second generation ethanol utilizes lignocellulosic material from agricultural residue or forest waste [21]. Ethanol produced from this second generation biomass is an interesting alternative since it avoids the competition between food and fuel from crops [13]. During World War II, several plants were built which produced

ethanol from cellulose [22]. After the war, competition from synthetically produced ethanol forced many of these plants to close. Recently, the demand for *green products* is bringing back the interest in lignocellulosic derived ethanol as chemical feedstock for many different products. Since 2004, a demonstration plant for the production of ethanol from lignocellulosic feedstocks is in operation in Canada [23].

Proven raw materials for the production of ethanol are hardwoods, softwoods, herbaceous biomass or paper waste [2]. It is reported that the total potential ethanol production from this lignocellulosic biomass can be up to 16 times higher than the current ethanol production from fermenting sugars or starch [10]. A disadvantage, however, is the necessity for extra pretreatment steps since the lignocellulosic biomass is made up of a matrix of cellulose and hemicellulose bound by lignin as shown in Figure 1-4. The cellulose matrix has to be broken in order to reduce the degree of crystallinity, making it more susceptible to hydrolysis [24, 25].
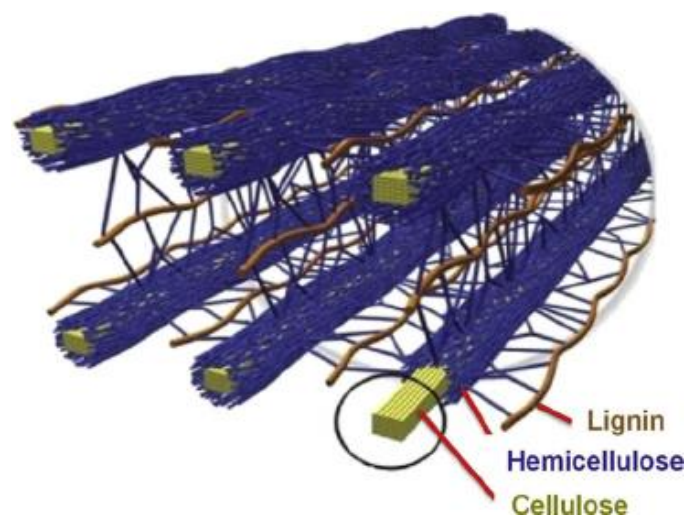
Figure 1-4: Structure of biomass: Cellulose strands surrounded by hemicellulose and lignin [26]

This hydrolysis reaction will produce sugars which can then be used in a classical fermentation process. Current research focuses on cost efficient abstraction of the sugars from lignocellulose biomass but still many process parameters need to be optimized for a successful industrial application [27].

1.2   Ethanol to hydrocarbons

Figure 1-5 presents an overview of the most important products derived from crude oil. In addition to motor fuels, six key base chemicals are produced via distillation, cracking and reforming. These chemicals can be transformed into a dozen commodity chemicals which are required for the plastics and other materials encountered in our daily lives. Using an acid catalyzed process, these key base chemicals can be produced from ethanol and via a drop-in strategy, no changes are required in the current refineries. The products can be classified as ethene on the one hand and higher hydrocarbons, i.e., C_{3+} hydrocarbons, on the other hand.
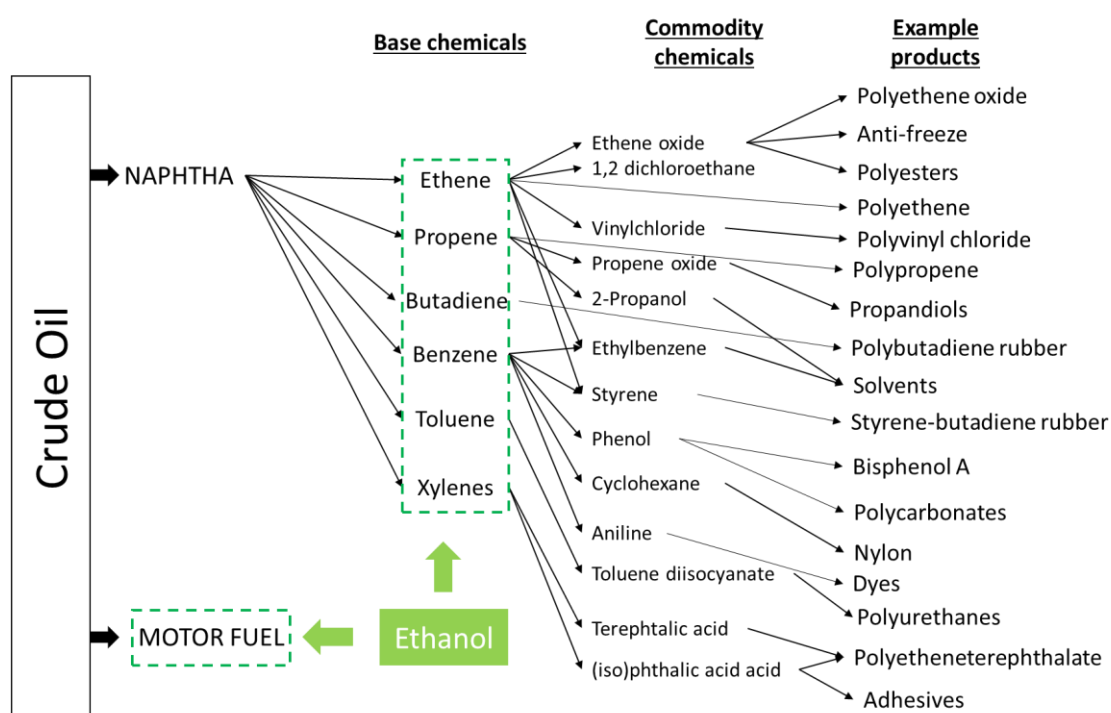
Figure 1-5: Simplified overview of the fossil resources derived chemical industry and the drop-in strategy of ethanol. Modified from [28].

1.2.1   Dehydration to ethene

With the advent of plastic industry in the beginning of the twentieth century, ethene became an essential raw material. In the thirties and forties of the previous century, several ethanol dehydration units were built which remained in operation until the sixties. Important advantages are the independence from crude oil and possibility to produce solely ethene in contrast to petrochemically derived ethene [4]. At the moment, around 150 Mton of ethene is produced per year, primarily from steam cracking.

Haro et al. [29] summarized and analyzed the techno-economic feasibility of different pathways for the dehydration of bioethanol. The results show that only Brazilian ethanol and ethanol via indirect synthesis from syngas enable the cost-competitive production of ethene at 2013 market prices. Alvarenga et al. [30] investigated the environmental benefits of either using Brazilian ethanol as a fuel or production of ethene. They concluded that if the yield of ethene is nearly 100%, the production of ethene from bioethanol consumes less fossil fuel energy and produces less green-house gas emissions than the route via steam cracking of naphtha. If the yield would drop below 96%, this would no longer be the case.

1.2.1.1 Supported phosphorus and alumina catalyzed ethanol dehydration process

Early technologies for ethanol dehydration were based on supported phosphoric acid but later activated alumina became the most commonly used catalyst in industry [31]. The first report published in literature about catalytic dehydration of ethanol to ethene already dates back to 1797 [32]. It was, however, not until 1913 that the first commercial plant was constructed to dehydrate ethanol by Elektrochemische Werke in Bitterfeld, Germany. This plant used an alumina catalyst to produce ethene, suited for the production of high purity ethane to use in refrigeration cycles [33]. From 1930 until the Second World War, ethanol dehydration plants were the unique source of ethene for manufacturing of mustard gas in Germany, Great Britain and the United States.

Until 1951, the process based on the supported phosphoric acid was the basis for all polyethene production in England. Despite the many disadvantages of this catalyst, such as low productivity, this catalyst was preferred based on the high purity of the ethene. The process with alumina catalyst was also used in Brazil and India until the 1960s, but all these plants were discontinued when low-cost feedstocks for steam cracking became readily available. Nowadays, one commercial plant is still running in India to produce ethene for ethene oxide [19]. In 2007 Braskem started the operation of a pilot plant in Brazil which is being used to make bio based ethene for high density and linear low density polyethene using silica-alumina catalyst [34].

1.2.1.2 Zeolite catalyzed ethanol dehydration process

The structure of a zeolite is interesting for catalysis because of their large internal surface area with the possibility of many catalytic sites. The high water content and impurities of these naturally occurring zeolites renders them practically unsuitable for catalytic reactions [35]. The invention of synthetic zeolites by Mobil in 1972 accelerated the research for application of zeolites in the petrochemical refinery units. A zeolite is composed of interconnected SiO_4 and AlO_4 tetrahedra with a shared oxygen atom. This connection produces a porous macromolecule with a distinctive 3-dimensional structure. This structure will be characteristic for the performance of the zeolite catalyst. Four different types of microporous systems are displayed in Figure 1-6. At the time of writing, 225 zeolite framework types are listed by the International Zeolite Association (IZA) [36].
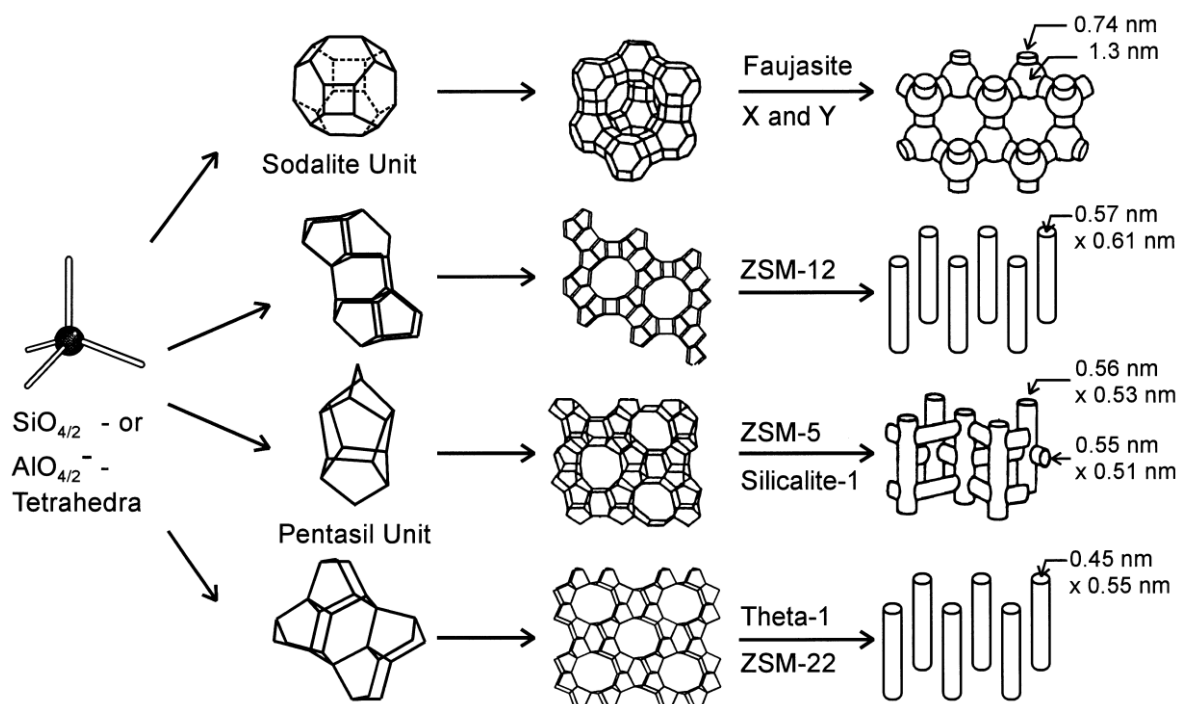
Figure 1-6: Structures of four important zeolites topologies and their microporous systems [35].

The general formula for a zeolite is given in (1-4):

$$A_{y/m}^{m+}\left[(SiO_2)_x.(AlO_2^-)_y\right].zH_2O$$

(1-4)

with A the cation (Na or H for example), (x+y) the amount of tetrahedra per crystallographic unit cell and x/y the ratio of silicon atoms over aluminium. It is clear that the net formula of a zeolite is $SiO_2.AlO_2^-$ with a net negative charge on each tetrahedron where a silicon atom is

substituted by an aluminum atom which is compensated by the cation A. The Si/Al ratio is a very important characteristic of the zeolite when the cation A is exchanged for a proton because it defines the Brønsted surface acidity of the catalyst. When this ratio is low, it leads to a high acid site density. However, more acid sites mean more AlO_4-tetrahedra as next nearest neighbors and thus a decrease in acid site strength. This illustrates the complex relationship between the Si/Al ratio and the Brønsted acidity of a zeolite. Lewis acid sites can also be present in zeolites, albeit at a lower concentration. These sites originate from non-framework aluminum species which can be formed by degradation of Brønsted-sites during severe thermal treatment [35].

Another important aspect of zeolites is the opportunity of shape selective catalysis [37]. Zeolite pores have dimensions comparable to molecule sizes which can result in different behaviour compared to an unconstrained environment. There are three categories of shape selectivity: reactant shape selectivity, product shape selectivity and transition state shape selectivity [38].

The zeolite based ethanol dehydration can either be operated in a fixed bed or a fluidized bed [39]. In the fixed bed process, the operating temperature is between 603 K and 693 K, and should be closely controlled. Typically, the ethanol conversion is between 98% and 99% and the ethene molar selectivity is between 95% and 99% [33]. The major byproduct is diethyl ether of which the formation is favored at low temperatures. Other reported by-products formed by side reactions, or obtained from ethanol contaminants are: acetic acid, methane, ethane, propene, butene isomers and hydrocarbons with 5 or more carbon atoms. The coking of the catalyst requires frequent regeneration. Depending on the process conditions and the catalyst, the regeneration procedure must be performed after 1 to 6 months.

A fluidized bed reactor allows for online catalyst regeneration which hence enables operation at temperatures between 673 K and 773 K. As a consequence, the ethanol conversion is higher than 99.5%, and the ethene molar selectivity reaches 99.9%. The endothermic heat of reaction is supplied by the hot feed and the recycle of the hot catalyst from the catalyst regeneration [33].

1.2.2 Production of higher hydrocarbons

After the invention of the H-ZSM-5 zeolite in 1972 and its application for the conversion of methanol-to-hydrocarbons (MTH), several laboratories explored the possibilities of this catalyst for the conversion of other alcohols such as ethanol [40, 41]. It was shown in 1978 that at temperatures between 573 K and 773 K, H-ZSM-5 is able to transform ethanol into a wide range of hydrocarbons [40].

The most widely explored zeolite for ethanol conversion is H-ZSM-5 for more than 40 years already. The initial focus was on obtaining ethene from ethanol and aqueous ethanol mixtures and reducing the amount of higher hydrocarbons [42, 43]. Due to cheap oil prices, the interest in ethanol as a feedstock for the production of higher hydrocarbons halted but after the year 2000, it regained new interest for the production of higher hydrocarbons [44]. Recently several reviews have appeared that highlight the most recent literature [45, 46]. No industrial application of this process exists at the moment. Most attention has been given to modification techniques but almost no mechanistic investigation has been performed.

1.2.3 Bioethanol conversion to hydrocarbons

Depending on the author, bioethanol can either refer to ethanol produced from renewable resources or to aqueous ethanol-water mixtures. In this work, the latter description will be employed. The fermentation broth typically contains 14 v% of ethanol, or can be distilled to form the azeotropic water/ethanol mixture containing 96 v% ethanol. It is thus interesting to see how the activity of the catalyst and the product distribution is affected when water is present in the feed.

Several authors [47-49] report a decrease in deactivation of the H-ZSM-5 when water is present due to attenuation of the acidic sites, but with the drawback that under very severe operating conditions, i.e., high temperature and high water content, irreversible dealumination of the catalyst may occur. This is also observed in MTO [50]. Talukdar et al. observed a rise in olefins when water is co-fed to ethanol, and a corresponding decrease in liquid hydrocarbons [51]. Shulz et al. observed a decrease in activity but attributed this to the dilution of the water causing a lower ethanol partial pressure [52]. It is clear that the effect of water is still a matter of discussion in ethanol conversion to hydrocarbons.

1.3   What have we learned from methanol conversion?

The process for converting methanol into gasoline was invented by Mobil on a H-ZSM-5 catalyst in 1977 [53]. In addition to H-ZSM-5, H-SAPO-34 is also currently used as catalyst in industrial scale MTO processes [54]. Shape selectivity is introduced by its chabazite (CHA) structure of large cavities connected by 8-rings, resulting in a selectivity to light olefins such as ethene and propene exceeding 80%. Moreover, conditions may be varied to change the propene versus ethene ratio. An importance difference between H-ZSM-5 and H-SAPO-34 is the faster coking on H-SAPO-34, which requires more frequent catalyst regeneration. This frequent regeneration requires an adapted reactor design, e.g. a fluidized bed reactor with online catalyst regeneration. Therefore, UOP developed the H-SAPO-34 based MTO process, applying a low-pressure fluidized-bed reactor designed to enable efficient temperature control and continuous regeneration. Further improvement of ethene versus propene selectivity was achieved by combining the UOP MTO process with an olefin cracking process (OCP) developed by Total Petrochemicals and UOP [55].
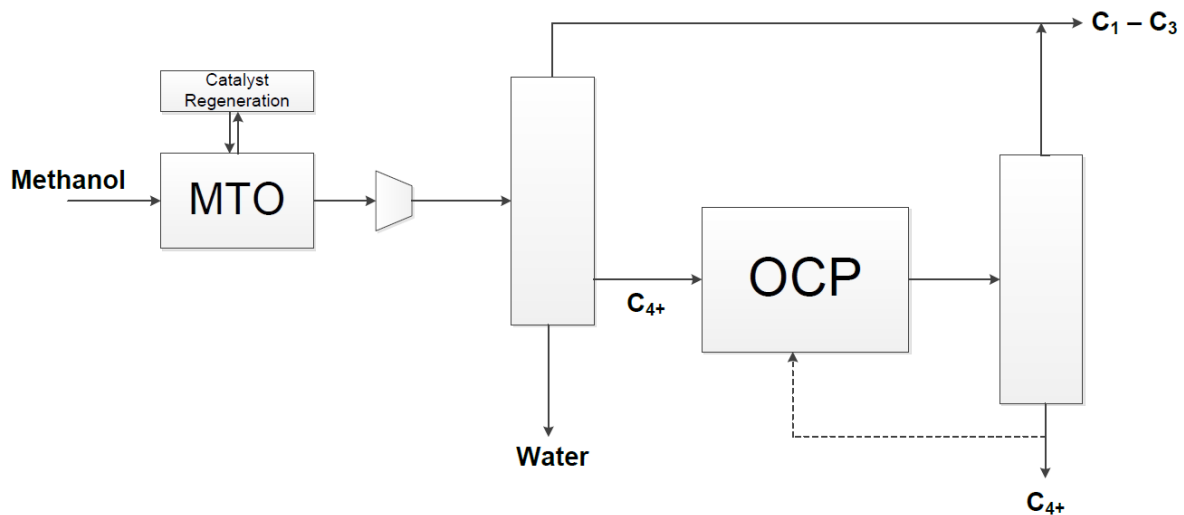
Figure 1-7: Fluidized bed H-SAPO-34 MTO process by UOP coupled with OCP by Total/UOP, for increased propene yield. Figure based on [55].

Figure 1-7 is a schematic representation of a fluidized bed MTO process coupled with OCP. Methanol is converted to olefins over H-SAPO-34 in the first reactor (MTO) and then sent to a first column which separates the water from the higher olefins. The C_1 to C_3 olefin fraction is sent over top of the column and the C_{4+}. The higher olefins are sent to a second reactor (OCP)

where they are cracked. Again, a column is in place to separate the C_1 to C_3 olefin fraction and the higher olefins.

The mechanism of converting methanol into hydrocarbons has been the subject of much research in the past decades [56]. One of the most discussed topics is explaining the first carbon-carbon coupling, for which more than 20 distinct mechanistic proposals exist.

1.3.1 Direct coupling of methanol

Many direct routes involving different types of intermediates have been proposed for the formation of the first carbon-carbon bond starting from methanol or dimethyl ether. Among them are oxonium ylides [57], carbocations [58], carbenes [59] and free radicals [60]. Via theoretical models it became clear that none of these direct mechanisms can lead to the formation of light olefins because of unstable intermediates and/or too high activation energies [56, 61].

1.3.2 Autocatalytic nature of methanol conversion

The methanol to hydrocarbon reaction is found to be autocatalytic in nature [55, 58, 62]: a small amount of product present leads a higher conversion. Due to this accelerating effect, an induction period exists in the early stages of reaction, and a sigmoidal activity curve is obtained as displayed in Figure 1-8.
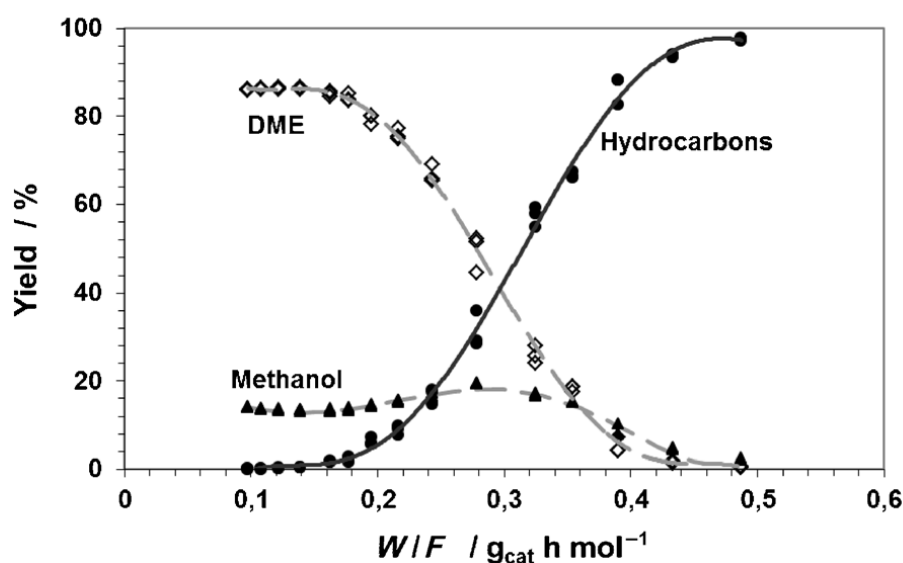
Figure 1-8: Hydrocarbon and dimethyl ether (DME) yield as a function of methanol space time [55].

Dessau et al. [63] attributed the autocatalytic process to the reaction between methanol and olefins, which is much faster than the formation of the first olefins. In 1983, Mole and co-workers [64] reported that deliberately introduced toluene acts as a co-catalyst for the production of olefins. This effect was called the aromatic co-catalysis and lead to the proposal of the hydrocarbon pool mechanism.

1.3.3 Dual cycle hydrocarbon pool mechanism

A widely accepted reaction mechanism for the production of hydrocarbons from methanol is the so-called hydrocarbon pool mechanism [65-67]. This mechanism can explain the first carbon-carbon bond and the autocatalysis [68]. Kolboe et al. [69] proposed a hydrocarbon pool of unspecified structure $(CH_2)_n$ which undergoes methylation and subsequent olefin elimination. These species can be seen as extra catalytic sites for specific production of lower olefins. Haw and coworkers [70] identified methylbenzenes as being the actual active sites for the hydrocarbon pool mechanism. More specifically, methylbenzenes with four to six methyl groups are responsible for the production of propene whereas methylbenzenes with two to three methyl groups produce ethene. Other olefins are formed via alkylation on acidic sites [71, 72]. Hence, it is clear that the hydrocarbon pool model is a necessity to explain the formation of ethene.

Figure 1-9 represents the most complete reaction mechanism for the MTO process up to date. This is called the dual-cycle concept because the formation of lower olefins (ethene and propene) can occur via the hydrocarbon pool, i.e., an aromatic assisted mechanism, and an olefin based mechanism involving methylation, alkylation and cracking of C_{3+} alkenes. It should be noted that ethene is considered not to be formed from the cracking of higher olefins due to a highly energetic primary carbenium ion being formed.
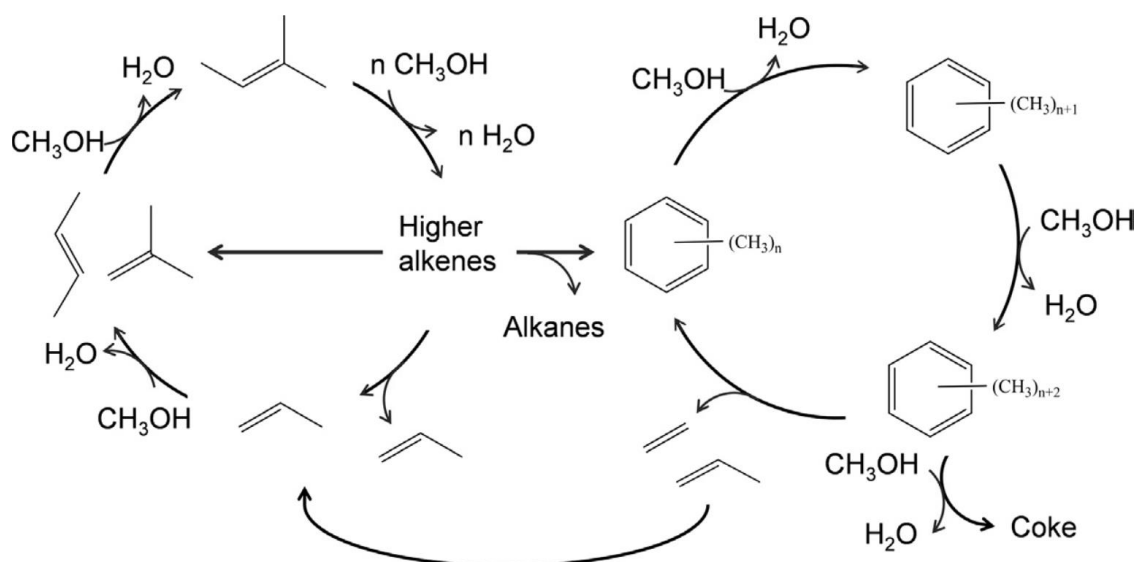
Figure 1-9: The dual-cycle concept of the hydrocarbon pool mechanism for the methanol-to-olefins process [55]: left) methylation and cracking, right) aromatic-assisted cycle.

By choosing a catalyst which suppresses the aromatic-assisted cycle, methanol can be converted solely according to the alkene methylation and cracking cycle (left of Figure 1-9), hence reducing the importance of the aromatic-assisted cycle (right of Figure 1-9) and thus reducing the amount of ethene formed [73]. It was observed that on H-ZSM-5 methylbenzenes up to hexamethylbenzenes are present in the pores, and hence a completely independent operation of one of the two cycles is impossible for H-ZSM-5. The H-BETA zeolite produces mainly propene, since the larger pores allow formation of higher methyl benzenes. H-ZSM-22, consisting of unidirectional 10-ring channels, severely inhibits the aromatics cycle and therefore also the formation of ethene [55]. H-SAPO-34, the most important industrial catalyst for MTO, appears to produce solely ethene and propene. The narrow pores result in strong product shape selectivity, hindering the diffusion of large hydrocarbons and thus favouring ethene formation [74].

An important issue which remains unsolved is the production of the initial hydrocarbon pool species solely from methanol. It has been suggested [67, 75] that impurities in the feed can cause the initial formation of an active hydrocarbon pool species, but this is still a matter of debate. Experiments in which the flow through the reactor was gradually decreased and increased with time, have shown that almost the same sigmoidal curve typical for an autocatalytic reaction is obtained in each cycle [55]. This indicates that the species responsible for the autocatalysis have only a limited life time inside the catalyst pores. Schultz et al. [76]

have shown that on H-ZSM-5 at 573 K the formation of hydrocarbon pool species is slower than at 623 K, and hence, introducing an induction period.

1.4   Scope of the thesis

The objective of the present work is to perform a thorough multiscale study on the conversion of (bio)ethanol to hydrocarbons on zeolite catalysts. As described in this introduction, the reaction mechanism is still a matter of debate and is not yet intensively investigated. The focus will be on elucidating the role of the dehydration and to unravel the mechanisms dominating the production of higher hydrocarbons from ethanol. This will not be addressed by using only a single technique but by combination of several. Also the results of reported ab initio calculations will be employed to gain further insights in the reaction network.

A detailed experimental investigation will be performed and will focus on acquisition of a kinetic data set for both the dehydration and the consecutive production of higher hydrocarbons. Microkinetic modelling will then be utilized to describe the obtained intrinsic kinetic data. A plethora of products can be produced starting from ethanol on an acid catalyst. There is an ever ongoing search for the effective tuning of the product selectivity towards a single product class, e.g. light olefins, ethene or aromatics. Several post-synthesis techniques have been proposed of which metal introduction is one of the most popular. A methodology is presented for properly assessing the catalyst selectivity and the effect of Ni, Ga and Fe introduction is assessed for the conversion of ethanol to higher hydrocarbons.

Finally, a multiscale reactor model is developed to simulate an adiabatic industrial ethanol dehydration reactor. The role of water on key operating parameters such as temperature drop, activity and selectivity can be assessed *in silico.* The developed model can be used to design new/improve the efficiency of ethanol dehydration units.

1.5 Outline of the thesis

This works contains 8 chapters: this introduction, a materials and methods chapter, five result chapters and a chapter with general conclusions and an outlook.

Chapter 2 starts with an description of the information extraction methodology based on intrinsic kinetics developed in this work followed by a detailed description of the two associated high-throughput setups.

Chapter 3 concerns the detailed study of the reaction mechanism of ethanol conversion to hydrocarbons on H-ZSM-5 and employs continuous flow and transient experiments combined with detailed catalyst characterization and the results of ab initio simulations to elucidate the reaction mechanism.

Chapter 4 focusses on the dehydration of ethanol at low temperature and where only ethene and diethyl ether are observed. Ethanol dehydration on H-ZSM-5 will be the prime focus but also other industrially relevant zeolites will be investigated.

Chapter 5 consists of the detailed experimental study of the conversion of higher hydrocarbons from ethanol and ethene and microkinetic modelling of the reaction. Due to the complexity of the production of higher hydrocarbons, a Single-Event MicroKinetic (SEMK) model is constructed which allows the limit the amount of parameters. This model comprises two types of parameters obtained via regression to the experimental data, i.e., kinetic and catalyst descriptors. The kinetic descriptors comprise the single-event pre-exponential factors and activation energies. Protonation enthalpies and concentration of acid sites are then considered to be catalyst descriptors.

Chapter 6 discusses the introduction of metals into H-ZSM-5 as a post-synthesis modification technique to enhance the activity or alter the selectivity towards a specific product class.

Chapter 7 presents an industrial fixed bed reactor model for ethanol dehydration based on an ab initio elucidated reaction network that accounts for the transport limitations typically occurring at the industrial scale. Detailed axial profiles for the temperature, conversion and yield of the products are obtained and discussed.

Chapter 8 summarizes and unifies the conclusions obtained in the different chapters. In additional, an outlook and several suggestions for further research are given.

1.6 References

[1] Nasdaq Stock Exchange, (http://www.nasdaq.com/), accessed on 14/4/2016

[2] Y. Lin, S. Tanaka, Ethanol fermentation from biomass resources: current state and prospects, Applied microbiology and biotechnology, 69 (2006) 627-642.

[3] B.W. McCalley, Model T Ford : the car that changed the world, Krause Publications, Iola, WI, 1994.

[4] V. Tret'yakov, Y.I. Makarfi, K. Tret'yakov, N. Frantsuzova, R. Talyshinskii, The catalytic conversion of bioethanol to hydrocarbon fuel: A review and study, Catalysis in Industry, 2 (2010) 402-420.

[5] R.K. Niven, Ethanol in gasoline: environmental impacts and sustainability review article, Renewable and Sustainable Energy Reviews, 9 (2005) 535-555.

[6] A. Demirbas, Bioethanol from Cellulosic Materials: A Renewable Motor Fuel from Biomass, Energy Sources, 27 (2005) 327-337.

[7] J. Sun, Y. Wang, Recent Advances in Catalytic Conversion of Ethanol to Chemicals, ACS Catalysis, 4 (2014) 1078-1090.

[8] J.A. Posada, A.D. Patel, A. Roes, K. Blok, A.P. Faaij, M.K. Patel, Potential of bioethanol as a chemical building block for biorefineries: preliminary sustainability assessment of 12 bioethanol-based products, Bioresource technology, 135 (2013) 490-499.

[9] J.C. Duarte, M. Sàágua, L. Baeta-Hall, A. Correia, B. Ribeiro, V. Lourenço, J. Pereira, S.M. Paixão, Bioethanol production from agricultural wastes, (2009).

[10] S. Kim, B.E. Dale, Global potential bioethanol production from wasted crops and crop residues, Biomass and bioenergy, 26 (2004) 361-375.

[11] F. Rosillo-Calle, L.A. Cortez, Towards ProAlcool II—a review of the Brazilian bioethanol programme, Biomass and Bioenergy, 14 (1998) 115-124.

[12] H.V. Amorim, M.L. Lopes, J.V. de Castro Oliveira, M.S. Buckeridge, G.H. Goldman, Scientific challenges of bioethanol production in Brazil, Applied microbiology and biotechnology, 91 (2011) 1267-1275.

[13] B. Hahn-Hägerdal, M. Galbe, M.F. Gorwa-Grauslund, G. Lidén, G. Zacchi, Bio-ethanol – the fuel of tomorrow from the residues of today, Trends in Biotechnology, 24 (2006) 549-556.

[14] W. Gerhartz, F. Ullmann, Ullmann's encyclopedia of industrial chemistry, VCH, 1987.

[15] R.A. Britton, Direct hydration of ethylene to ethanol, in, US 3686334 A, 1972.

[16] G.W. Roberts, M.A. Márquez, M.S. McCutchen, Alcohol synthesis in a high-temperature slurry reactor, Catalysis Today, 36 (1997) 255-263.

[17] J.J. Spivey, A. Egbebi, Heterogeneous catalytic synthesis of ethanol from biomass-derived syngas, Chemical Society Reviews, 36 (2007) 1514-1528.

[18] AlcoBioFuel, (http://www.alcobiofuel.com/), accessed on 23/5/2016

[19] W.B. Ellis, Books: Ullmann's Encyclopedia of Industrial Chemistry, Journal of Industrial Ecology, 3 (1999) 192-195.

[20] P. Alvira, E. Tomás-Pejó, M. Ballesteros, M. Negro, Pretreatment technologies for an efficient bioethanol production process based on enzymatic hydrolysis: a review, Bioresource technology, 101 (2010) 4851-4861.

[21] Y. Sun, J. Cheng, Hydrolysis of lignocellulosic materials for ethanol production: a review, Bioresource technology, 83 (2002) 1-11.

[22] G. Sivakumar, D.R. Vail, J. Xu, D.M. Burner, J.O. Lay, X. Ge, P.J. Weathers, Bioethanol and biodiesel: Alternative liquid fuels for future generations, Engineering in Life Sciences, 10 (2010) 8-18.

[23] J.S. Tolan, Iogen's process for producing ethanol from cellulosic biomass, Clean Technologies and Environmental Policy, 3 (2002) 339-345.

[24] J. Szczodrak, J. Fiedurek, Technology for conversion of lignocellulosic biomass to ethanol, Biomass and Bioenergy, 10 (1996) 367-375.

[25] M.J. Taherzadeh, K. Karimi, Acid-based hydrolysis processes for ethanol from lignocellulosic materials: a review, BioResources, 2 (2007) 472-499.

[26] W.O.S. Doherty, P. Mousavioun, C.M. Fellows, Value-adding to cellulosic ethanol: Lignin polymers, Industrial Crops and Products, 33 (2011) 259-276.

[27] N. Sarkar, S.K. Ghosh, S. Bannerjee, K. Aikat, Bioethanol production from agricultural wastes: An overview, Renewable Energy, 37 (2012) 19-27.

[28] J.H. Clark, F.E.I. Deswarte, Introduction to chemicals from biomass, Second edition. ed., John Wiley & Sons, Inc., Chichester, West Sussex, 2015.

[29] P. Haro, P. Ollero, F. Trippe, Technoeconomic assessment of potential processes for bio-ethylene production, Fuel Processing Technology, 114 (2013) 35-48.

[30] R.A. Alvarenga, J. Dewulf, Plastic vs. fuel: Which use of the Brazilian ethanol can bring more environmental gains?, Renewable Energy, 59 (2013) 49-52.

[31] F.F. Roca, L. De Mourgues, Y. Trambouze, Catalytic dehydration of ethanol over silica-alumina, Journal of Catalysis, 14 (1969) 107-113.

[32] H. Pines, J. Manassen, The mechanism of dehydration of alcohols over alumina catalysts, Advances in Catalysis, 16 (1966) 49-93.

[33] A. Morschbacker, Bio-Ethanol Based Ethylene, Polymer Reviews, 49 (2009) 79-84.

[34] Braskem starts up ethanol-to-ethylene plant, (http://www.ethanolproducer.com/articles/7022/braskem-starts-up-ethanol-to-ethylene-plant), accessed on 05 January 2015

[35] J. Weitkamp, Zeolites and catalysis, Solid State Ionics, 131 (2000) 175-188.

[36] International Zeolite Association, (http://www.iza-structure.org/), accessed on 16 April 2016

[37] H.A.W. Mark M. Green, Organic Chemistry, Principles and Industrial Practice, Wiley-VCH, Weinheim, 2003.

[38] H.v. Bekkum, Introduction to zeolite science and practice, 2nd completely rev. and expanded ed., Elsevier, Amsterdam ; New York, 2001.

[39] D. Fan, D.J. Dai, H.S. Wu, Ethylene Formation by Catalytic Dehydration of Ethanol with Industrial Considerations, Materials, 6 (2013) 101-115.

[40] E.G. Derouane, J.B. Nagy, P. Dejaifve, J.H. van Hooff, B.P. Spekman, J.C. Védrine, C. Naccache, Elucidation of the mechanism of conversion of methanol and ethanol to hydrocarbons on a new type of synthetic zeolite, Journal of Catalysis, 53 (1978) 40-55.

[41] S. Chaudhuri, C. Halik, J. Lercher, Reactions of ethanol over HZSM-5, Journal of molecular catalysis, 62 (1990) 289-295.

[42] R. Levanmao, T.M. Nguyen, J. Yao, Conversion of Ethanol in Aqueous-Solution over Zsm-5 Zeolites - Influence of Reaction Parameters and Catalyst Acidic Properties as Studied by Ammonia TPD Technique, Applied Catalysis, 61 (1990) 161-173.

[43] R. Le Van Mao, T.M. Nguyen, G.P. McLaughlin, The bioethanol-to-ethylene (BETE) process, Applied catalysis, 48 (1989) 265-277.

[44] A.G. Gayubo, A.T. Aguayo, A.L. Morán, M. Olazar, J. Bilbao, Role of water in the kinetic modeling of catalyst deactivation in the MTG process, AIChE Journal, 48 (2002) 1561-1571.

[45] X. Li, A. Kant, Y. He, H.V. Thakkar, M.A. Atanga, F. Rezaei, D.K. Ludlow, A.A. Rownaghi, Light olefins from renewable resources: Selective catalytic dehydration of bioethanol to propylene over zeolite and transition metal oxide catalysts, Catalysis Today, (2016).

[46] A. Galadima, O. Muraza, Zeolite catalysts in upgrading of bioethanol to fuels range hydrocarbons: A review, Journal of Industrial and Engineering Chemistry, 31 (2015) 1-14.

[47] J. Oudejans, P. Van Den Oosterkamp, H. Van Bekkum, Conversion of ethanol over zeolite H-ZSM-5 in the presence of water, Applied Catalysis, 3 (1982) 109-115.

[48] A.T. Aguayo, A.G. Gayubo, A.M. Tarrío, A. Atutxa, J. Bilbao, Study of operating variables in the transformation of aqueous ethanol into hydrocarbons on an HZSM-5 zeolite, Journal of chemical technology and biotechnology, 77 (2002) 211-216.

[49] T. Nguyen, R. Le Van Mao, Conversion of ethanol in aqueous solution over ZSM-5 zeolites: study of the reaction network, Applied catalysis, 58 (1990) 119-129.

[50] B. Valle, A. Alonso, A. Atutxa, A.G. Gayubo, J. Bilbao, Effect of nickel incorporation on the acidity and stability of HZSM-5 zeolite in the MTO process, Catalysis Today, 106 (2005) 118-122.

[51] A.K. Talukdar, K.G. Bhattacharyya, S. Sivasanker, HZSM-5 catalysed conversion of aqueous ethanol to hydrocarbons, Applied Catalysis A: General, 148 (1997) 357-371.

[52] J. Schulz, F. Bandermann, Conversion of ethanol over zeolite H-ZSM-5, Chemical engineering & technology, 17 (1994) 179-186.

[53] F.J. Keil, Methanol-to-hydrocarbons: process technology, Microporous and Mesoporous Materials, 29 (1999) 49-66.

[54] S. Wilson, P. Barger, The characteristics of SAPO-34 which influence the conversion of methanol to light olefins, Microporous and Mesoporous Materials, 29 (1999) 117-126.

[55] U. Olsbye, S. Svelle, M. Bjorgen, P. Beato, T.V.W. Janssens, F. Joensen, S. Bordiga, K.P. Lillerud, Conversion of Methanol to Hydrocarbons: How Zeolite Cavity and Pore Size Controls Product Selectivity, Angewandte Chemie-International Edition, 51 (2012) 5810-5831.

[56] D. Lesthaeghe, V. Van Speybroeck, G.B. Marin, M. Waroquier, Understanding the failure of direct C-C coupling in the zeolite-catalyzed methanol-to-olefin process, Angewandte Chemie-International Edition, 45 (2006) 1714-1719.

[57] G.J. Hutchings, R. Hunter, Hydrocarbon formation from methanol and dimethyl ether: a review of the experimental observations concerning the mechanism of formation of the primary products, Catalysis today, 6 (1990) 279-306.

[58] Y. Ono, T. Mori, Mechanism of methanol conversion into hydrocarbons over ZSM-5 zeolite, Journal of the Chemical Society, Faraday Transactions 1: Physical Chemistry in Condensed Phases, 77 (1981) 2209-2221.

[59] C.D. Chang, A.J. Silvestri, The conversion of methanol and other O-compounds to hydrocarbons over zeolite catalysts, Journal of Catalysis, 47 (1977) 249-259.

[60] J.K. Clarke, R. Darcy, B.F. Hegarty, E. O'Donoghue, V. Amir-Ebrahimi, J.J. Rooney, Free radicals in dimethyl ether on H-ZSM-5 zeolite. A novel dimension of heterogeneous catalysis, Journal of the Chemical Society, Chemical Communications, (1986) 425-426.

[61] D. Lesthaeghe, A. Horré, M. Waroquier, G.B. Marin, V. Van Speybroeck, Theoretical Insights on Methylbenzene Side-Chain Growth in ZSM-5 Zeolites for Methanol-to-Olefin Conversion, Chemistry-A European Journal, 15 (2009) 10803-10808.

[62] X. Sun, S. Mueller, H. Shi, G.L. Haller, M. Sanchez-Sanchez, A.C. van Veen, J.A. Lercher, On the impact of co-feeding aromatics and olefins for the methanol-to-olefins reaction on HZSM-5, Journal of Catalysis, 314 (2014) 21-31.

[63] R. Dessau, On the H-ZSM-5 catalyzed formation of ethylene from methanol or higher olefins, Journal of Catalysis, 99 (1986) 111-116.

[64] T. Mole, J.A. Whiteside, D. Seddon, Aromatic co-catalysis of methanol conversion over zeolite catalysts, Journal of Catalysis, 82 (1983) 261-266.

[65] M. Seiler, W. Wang, A. Buchholz, M. Hunger, Direct evidence for a catalytically active role of the hydrocarbon pool formed on zeolite H-ZSM-5 during the methanol-to-olefin conversion, Catalysis letters, 88 (2003) 187-191.

[66] U. Olsbye, M. Bjørgen, S. Svelle, K.-P. Lillerud, S. Kolboe, Mechanistic insight into the methanol-to-hydrocarbons reaction, Catalysis Today, 106 (2005) 108-111.

[67] J.F. Haw, W. Song, D.M. Marcus, J.B. Nicholas, The mechanism of methanol to hydrocarbon catalysis, Accounts of chemical research, 36 (2003) 317-326.

[68] B.E. Langner, Reactions of methanol on zeolites with different pore structures, Applied Catalysis, 2 (1982) 289-302.

[69] I.M. Dahl, S. Kolboe, On the reaction mechanism for hydrocarbon formation from methanol over SAPO-34: I. Isotopic labeling studies of the co-reaction of ethene and methanol, Journal of Catalysis, 149 (1994) 458-464.

[70] W. Song, J.F. Haw, J.B. Nicholas, C.S. Heneghan, Methylbenzenes are the organic reaction centers for methanol-to-olefin catalysis on HSAPO-34, Journal of the American Chemical Society, 122 (2000) 10726-10727.

[71] T.-Y. Park, G.F. Froment, Kinetic modeling of the methanol to olefins process. 1. Model formulation, Industrial & engineering chemistry research, 40 (2001) 4172-4186.

[72] T.-Y. Park, G.F. Froment, Kinetic modeling of the methanol to olefins process. 2. Experimental results, model discrimination, and parameter estimation, Industrial & engineering chemistry research, 40 (2001) 4187-4196.

[73] S. Svelle, F. Joensen, J. Nerlov, U. Olsbye, K.-P. Lillerud, S. Kolboe, M. Bjørgen, Conversion of Methanol into Hydrocarbons over Zeolite H-ZSM-5: Ethene Formation Is Mechanistically Separated from the Formation of Higher Alkenes, Journal of the American Chemical Society, 128 (2006) 14770-14771.

[74] B.P. Hereijgers, F. Bleken, M.H. Nilsen, S. Svelle, K.-P. Lillerud, M. Bjørgen, B.M. Weckhuysen, U. Olsbye, Product shape selectivity dominates the Methanol-to-Olefins (MTO) reaction over H-SAPO-34 catalysts, Journal of catalysis, 264 (2009) 77-87.

[75] W. Song, D.M. Marcus, H. Fu, J.O. Ehresmann, J.F. Haw, An oft-studied reaction that may never have been: Direct catalytic conversion of methanol or dimethyl ether to hydrocarbons on the solid acids HZSM-5 or HSAPO-34, Journal of the American Chemical Society, 124 (2002) 3844-3845.

[76] H. Schulz, Z. Siwei, H. Kusterer, Autocatalysis, Retardation, Reanimation and Deactivation during Methanol Conversion on Zeolite HZSM5, Studies in Surface Science and Catalysis, 60 (1991) 281-290.

Chapter 2

Procedures

This chapter gives an overview of the most important procedures applied in this work. It focusses on the methodology developed in this work consisting of detailed mechanistic investigation and catalyst screening based on intrinsic kinetics employing high throughput kinetic set-ups. These set-ups are located at the Laboratory for Chemical Technology and are discussed in more detail.

2.1 Catalyst Design Methodologies

Several strategies for catalyst design can be found in literature [1] and can be classified into two categories, i.e., so-called statistics- and performance-driven catalyst design, see Figure 2-1 a and b. The alternative methodology proposed in this work is presented in Figure 2-1 c. The differences between these methodologies are more elaborately discussed in the paragraphs below.

2.1.1   Statistics-driven Catalyst Design

Having defined the catalyst characteristics to be optimized, the boundaries of the domain in which they will be varied need to be determined. An experimental design can be subsequently followed to actually determine the 'best' catalyst as shown in Figure 2-1 a. The optimization can occur according to the 'one-variable-at-a-time' principle [2, 3], however more advanced, statistical designs can also be implemented.

A full factorial design may be applied to cover a broad range of experimental conditions. The drawback from such a design is the gargantuan number of experiments that needs to be performed, e.g., for only a 2-level, 7 factor design, a total of 128 experiments needs to be performed. The use of fractional factorial designs conveniently reduces the number of experiments. Several classical symmetrical designs can applied for this, such as circumscribed, inscribed and face centered central composite designs or Box-Behnken designs [4].

The relation established between catalyst characteristics (factors, x_i) and performance (y) is typically of a linear nature in the parameters (b_i) while quadratic and interaction terms for the factors are generally also considered. Such empirical linear relations lack the fundamental detail governing the catalyst performance. It is evident that the use of such relationships is, at most, suited for interpolation purposes and will not lead to reliable extrapolations, not to mention their irrelevance for simulating catalyst behavior at different operating conditions or with alternative feeds.

2.1.2 Performance-driven Catalyst Design

The most experimentally intensive methodology, i.e., the so-called *performance-driven catalyst design,* is depicted in Figure 2-1 b. In contrast to the single-stage development of the *statistics-driven catalyst design*, *performance-driven catalyst design* typically distinguishes between two development stages, i.e., a catalyst screening and a catalyst optimization stage [5-7]. During the catalyst screening stage, a wide variety of catalyst formulations are prepared, kinetically investigated and ranked based on activity, selectivity and stability performance at a single set of operating conditions. An extensive catalyst screening study is required before going into an advanced catalyst development stage. In the optimization stage, the potentially interesting catalysts from the first stage are tested on a more quantitative basis and subject to more prolonged testing. The bottleneck for this methodology is situated in the synthesis and testing of large numbers of catalysts as well as in the relevance of the acquired data for scale-up purposes.
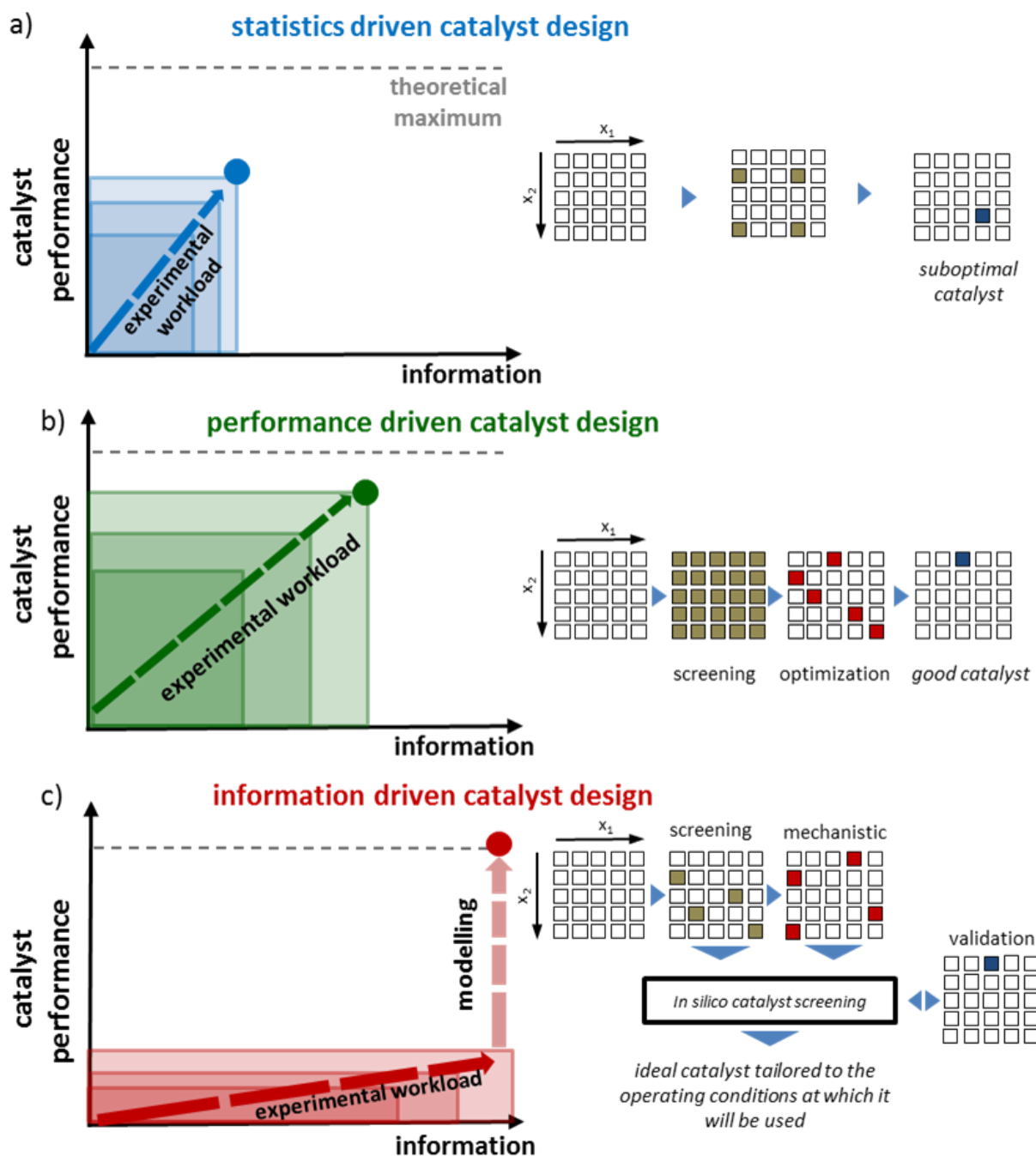
Figure 2-1: Different methodologies in catalyst design: a) *statistics-driven catalyst design***, b)** *performance-driven catalyst design* **and c)** *information-driven catalyst design.* **Catalyst performance is plotted on the y-axis and mechanistic information on the x-axis. The grid below the graphs conceptualizes a corresponding 2-dimensional optimization study where x_1 and x_2 are two factors influencing catalyst performance. Color code: khaki: screening; red: in-depth study; blue: final selection and validation. [8]**

2.1.3 Information-driven Catalyst Design

Information-driven catalyst design, as shown in Figure 2-1 c, overcomes the drawbacks of the previously described methods. Initial catalyst screening is performed to determine which catalysts will allow retrieving a maximum amount of information. The corresponding catalyst selection is based on a preliminary assessment of catalyst property effects on their activity. The selected catalysts will not necessarily be the most active or selective ones, however as mentioned previously, they should be the ones which will allow acquiring the most detailed mechanistic information.

This information is acquired in the second stage of the *information-driven catalyst design* methodology. Aiming at a better understanding of the underlying reaction mechanism, information on the possible intermediates and by-products is obtained as well as on the effect of temperature and pressure on the catalyst performance. The information obtained in both the catalyst screening and kinetic testing, can be combined as input for microkinetic model development. The combination of an in-depth study on a well-selected catalyst and a more explorative study of the catalyst descriptors on a limited selection of catalysts, complemented by the initial screening results yields the desired kinetic and catalyst descriptors for the microkinetic model. Whereas the former capture the reactive properties, such as activity and selectivity, most often in terms of activation energies and pre-exponential factors, the latter specifically account for the effect of the catalyst properties on their performance. The catalyst descriptors constitute its fingerprint, i.e., a unique identifier which can be translated into a specific performance thanks to the microkinetic model [9].

The constructed microkinetic model is used in an *in silico* screening of alternative catalyst formulations. It also eliminates the need for traditional catalyst comparison methods such as the light-off temperature, i.e., temperature at 50% conversion or an apparent activation energy and pre-exponential factor [10]. Due to the fundamental character of the microkinetic model, the virtual screening allows reliable extrapolations beyond the operating conditions and catalyst properties contained in the dataset [11, 12]. Finally, the performance of the novel catalyst formulation is compared to the virtual screening results in the validation step.

By implementation of these models in an adequate reactor model accounting for transport phenomena [13, 14], specific reactor configurations such as a riser reactor [15] or a slurry-bubble column [16] and catalyst deactivation [17], reliable, industrially relevant simulations can be made with these models. This also comprises the extension from model compound behavior, as typically measured at the laboratory scale, to realistic feeds [9, 18]. This methodology may not only lead to successful process scale-up but can also result in adequate reactor down scaling for the development of microreactors [19]. As the observed effects are incorporated on a fundamental level, this methodology allows to limit the number of experiments while still being able to extrapolate towards other operating conditions.

Both experimental stages, i.e., screening and mechanistic investigation, each require a dedicated, experimental high-throughput kinetics set-up. The *high-throughput kinetics screening* (HTK-S) set-up comprises a comparatively large number of parallel reactors with a limited reactor volume operating at identical conditions. Low catalyst masses are required in this set-up since this enables the evaluation of advanced, difficult-to-synthesize catalytic materials. The *high-throughput kinetics mechanistic investigation* (HTK-MI) set-up contains a more limited number of reactors in which operating conditions can be more independently varied such that a systematic exploration of the intrinsic kinetics in a whole range of operating conditions is possible within a limited time frame. The required amount of catalyst in this stage is about one order of magnitude higher such that the scale-up of the catalyst synthesis method can also be validated. The larger scale of the HTK-MI set-up also provides an opportunity for temperature measurement inside the reactor, helping to experimentally ensure the intrinsic kinetics character of the acquired data.

The main prerequisite for extrapolating towards other operating conditions and proper assessment of catalyst properties is the measurement of intrinsic kinetics. Generally, the most frequently encountered lab scale reactor for kinetic measurement is a fixed bed reactor which can either be operated in a differential or an integral regime since it is simple, inexpensive, applicable for both gas, liquid as well as three phase operation and deactivation can be observed immediately when pursuing steady-state conditions [5]. Additionally, in order not to complicate

the construction of the microkinetic models, an ideal flow pattern in the reactor is strived for, i.e., ideal plug flow in the fixed bed reactor.

It is vital to improve the data acquisition efficiency with increasing number of reactors. Depending on the experimental stage, i.e., screening or mechanistic investigation, this can either be achieved by respectively analysis equipment diversification or duplication. Diversification leads to a more flexible analysis section, e.g. multiple gas chromatographs in which complementary columns and/or detectors are present. This is often used for catalyst screening due to large variety of catalysts tested which potentially leads to a diverse product spectrum. Duplicating the analysis equipment is quite straightforward and allows timely data acquisition from a well-selected catalyst tested at a broad range of reaction conditions, i.e., during the mechanistic investigation.

The analysis equipment type typically depends on the reaction investigated. In case only a limited number of products is involved in the reaction, a spectroscopic method may be preferred due to its fast analysis, i.e., millisecond time range. Even mass spectrometry can be applied but has limited quantitative capabilities. When the individual determination of all products is important, chromatographic techniques are typically used.

2.2 Intrinsic kinetics determination

When no heat or transport limitations are present, the reaction can be considered as pseudo-homogeneous. However, if transport phenomena can no longer be neglected, a series of multiple sequential steps have to be taken into account: mass transfer of the reactant from the bulk phase to the catalyst, mass transfer of the reactant inside the pellet, adsorption of the reactant on the active sites, reaction on these active sites, desorption of the products, mass transfer of the products out of the pellet and towards the bulk phase. Experimentally only bulk properties can be measured. The difference between a pseudo-homogeneous and a heterogeneous reaction is illustrated in Figure 2-2.
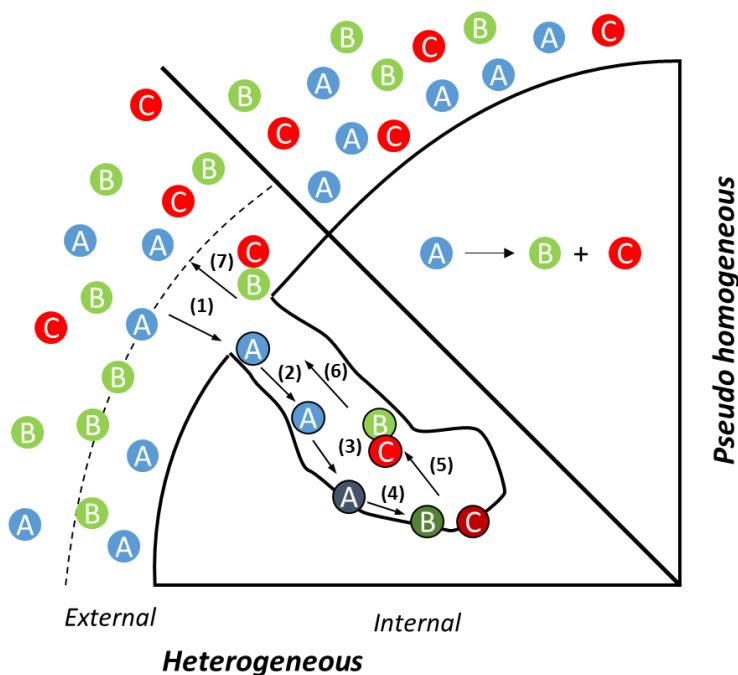
Figure 2-2: Illustration of a pseudo-homogeneous and a heterogeneous reaction: (1) diffusion through the boundary layer, (2) diffusion of reactants inside the pores, (3) adsorption at the active center, (4) reaction at the surface, (5) desorption of products, (6) diffusion of products inside the pores, (7) diffusion of the products through the boundary layer

To develop consistent kinetic models based on these experimental data, measuring intrinsic kinetics is required. Intrinsic kinetics describe the chemical behavior, unaffected by heat or mass transfer limitations [20]. Generally speaking, the observation of intrinsic kinetics means that the observed reaction rate, i.e., R_i^{obs}, does not differ more than 5% from the intrinsic reaction rate, i.e., R_i^{intr}:

$$\frac{R_i^{obs} - R_i^{intr}}{R_i^{intr}} < 0.05 \tag{2-1}$$

Deviations occur when mass or heat transfer from the bulk phase towards the catalyst active sites occurs on a similar timescale as the rate of reaction. Heat and mass transfer limitations can occur at two levels: externally in the film around the catalyst pellet and internally inside the pores of the pellet. Several criteria exist for assessing the intrinsic character of an experiment as shown below. This not only includes the absence of transport limitations on the pellet scale but also the validation of plug flow. It has been verified for all experiments shown in this work that these criteria are met.

2.2.1 Mass transfer limitations

The severity of external mass transfer limitations is expressed by the Carberry number (Ca) [21], as defined in (2-2). This dimensionless group expresses the fractional concentration difference between the concentration of component i in the bulk phase, C_i^b and the concentration of component A at the external surface, C_i^s:

$$Ca = \frac{C_i^b - C_i^s}{C_i^b} = \frac{R_{EtOH}^{obs}}{k_{fi} \, a_s \, C_i^b} < \frac{0.05}{n} \tag{2-2}$$

where R_{EtOH}^{obs} is the observed reaction rate per unit of catalyst mass, k_{fi} the external mass transfer coefficient of component i which can be calculated via correlations, a_s the specific external surface area of the catalyst, i.e., $6/d_p$ for spherical particles, C_i^b an C_i^s refer to the bulk and surface concentration of component i, respectively and n is the apparent reaction order. Here, it is assumed that other transfer limitations are absent. When this criterion is fulfilled, the measured production rate can be considered to be equal to the intrinsic rate. The absence of external mass transfer limitations can also be verified experimentally by performing experiments at fixed space time with different catalyst masses.

The Weisz-Prater criterion [22] as defined in (2-3), can be used to verify the absence of internal diffusion limitations inside the pallet. The Weisz modulus, Φ, expresses the ratio of the observed reaction rate and the diffusion rate:

$$\Phi = \eta\phi^2 = \frac{(n+1)}{2} \frac{d^2 \rho_p R_{EtOH}^{obs}}{6 D_{e,i} C_i^s} < 0.08 \tag{2-3}$$

where n is the apparent order of reaction, d is the diameter of either the catalyst crystallite or the catalyst pellet, ρ_p the density, $D_{e,i}$ the effective diffusion coefficient of component i and C_i^s the concentration of component i at the surface. The deviation caused by internal diffusion limitations is less than 5 %, if Φ is lower than 0.08. The absence of internal mass transport limitations can be determined experimentally by varying the pellet size.

2.2.2 Heat transfer limitations

Mears [23] proposes criteria to assess internal and external heat transfer limitations similar to that of external mass transfer limitations stating that the observed reaction rate should not deviate more than 5% from the rate under isothermal conditions:

$$\frac{R_{EtOH}^{obs} \, \rho_p \, d_p \, |-\Delta H_r|}{6 \, \alpha \, T_b} \frac{E_a}{R \, T_b} < 0.05 \tag{2-4}$$

$$\frac{R_{EtOH}^{obs} \, \rho_p \, d_p^2 \, |-\Delta_r H|}{60 \, \lambda_p \, T_b} \frac{E_a}{R \, T_b} < 0.05 \tag{2-5}$$

where $|-\Delta H_r|$ corresponds to the reaction enthalpy, α the heat transfer coefficient inside the film, λ_p the catalyst pellet thermal conductivity, T_b the bulk temperature and E_a the apparent activation energy of the reaction.

2.2.3 Plug flow, maximal bed dilution and pressure drop

The criterion for negligence of radial gradients (eq. (2-6)) expresses that the particle diameter d_p should be at least 8 times smaller than the tube diameter d_t. The criterion for axial dispersion (eq. (2-7)) expresses that the length of the bed L_B should be at least 50 times higher than the diameter of the pellet d_p.

$$\frac{d_t}{d_p} > 8 \tag{2-6}$$

$$\frac{L_B}{d_p} > 50 \tag{2-7}$$

with d_p the pellet diameter, d_t the tube diameter and L_B the bed length. Increasing the bed length and decreasing the particle diameter has a beneficial effect for passing these criteria. However, also criteria for the maximal pressure drop and the maximal bed dilution exist.

A maximum bed dilution is specified via the correlation (eq. (2-8)), which is an upper bound for the size of the catalyst bed:

$$b_{max} = \frac{0.004\ L_B\ \epsilon\ d_p}{1 + 0.004 L_B\ \epsilon\ d_p}$$

(2-8)

A maximal pressure drop is specified via (2-9) and (2-10) which represent the lower limit for the pellet diameter.

$$\Delta p < 0.2 \frac{p_t}{n}$$

(2-9)

$$\frac{\Delta p}{h_{bed}} = \frac{f_m \rho_G u_s^2}{d_p}$$

(2-10)

with p_t the total pressure, f_m the modified friction factor from the Ergun equation, ρ_f the fluid density, u_s the superficial gas velocity and h_{bed} the bed height.

2.3 High-throughput kinetics information acquisition

Two complementary high-throughput kinetics (HTK) set-ups are available at the Laboratory for Chemical Technology at Ghent University, i.e., a *high-throughput kinetics screening* set-up (HTK-S) and *high-throughput kinetics mechanistic investigation* set-up (HTK-MI). They are specifically designed to achieve the goals put forward in the information driven catalyst design methodology, i.e., catalyst screening and mechanistic investigation while providing reliable intrinsic kinetic data for model construction. Table 2-1 compiles the most relevant features of these set-ups.

Table 2-1: Features of the set-ups used at the Laboratory for Chemical Technology for Information Driven Catalyst Design

		High-Throughput Kinetics Screening (HTK-S)	**High-Throughput Kinetics Mechanistic Investigation (HTK-MI)**
	number of reactors	16	8
	number of heating blocks	4	4
	reactor type	tubular	tubular
reactor dimensions	d_{id} (10^{-3} m)	2.1	11.0
	L (m)	0.8	0.9
reaction conditions	**Feed flow rate control**	per reactor block	per reactor
	T_{min}, T_{max} [K]	323 - 773 (SS) 323 - 1273 (Quartz)	293 - 923
	p_{min}, p_{max} [bar]	1 - 100 (SS) 1- 3 (Quartz)	1 – 200
	W [10^{-3} kg]	0.05 – 0.2	0.5 - 10

2.3.1 Catalyst screening set-up (HTK-S)

The main goal of the HTK-S set-up is the fast parallel testing of a large variety and, hence, number of catalysts. Both simple and complex reaction networks can be dealt with. This set-up corresponds to the screening step as shown in Figure 2-1c. During its design and construction by Integrated Lab Solutions [24], maximum flexibility was ensured with respect to different reaction types and catalysts. This set-up contains 16 parallel tubular reactors (i.d. = 2.1 mm) which are grouped per 4 in a heating block. The user can choose between stainless steel and quartz reactor tubes, depending on the target reaction. An overview and more detailed pictures of the HTK-S set-up are given in Figure 2-3 while the flowsheet focusing on a single reactor is given in Figure 2-4

Figure 2-3: HTK-S set-up pictures: a) front view, b) gas (top) and liquid (bottom) feed section, c) reactor heating blocks, d) heated gas and liquid sampling section and e) analysis section
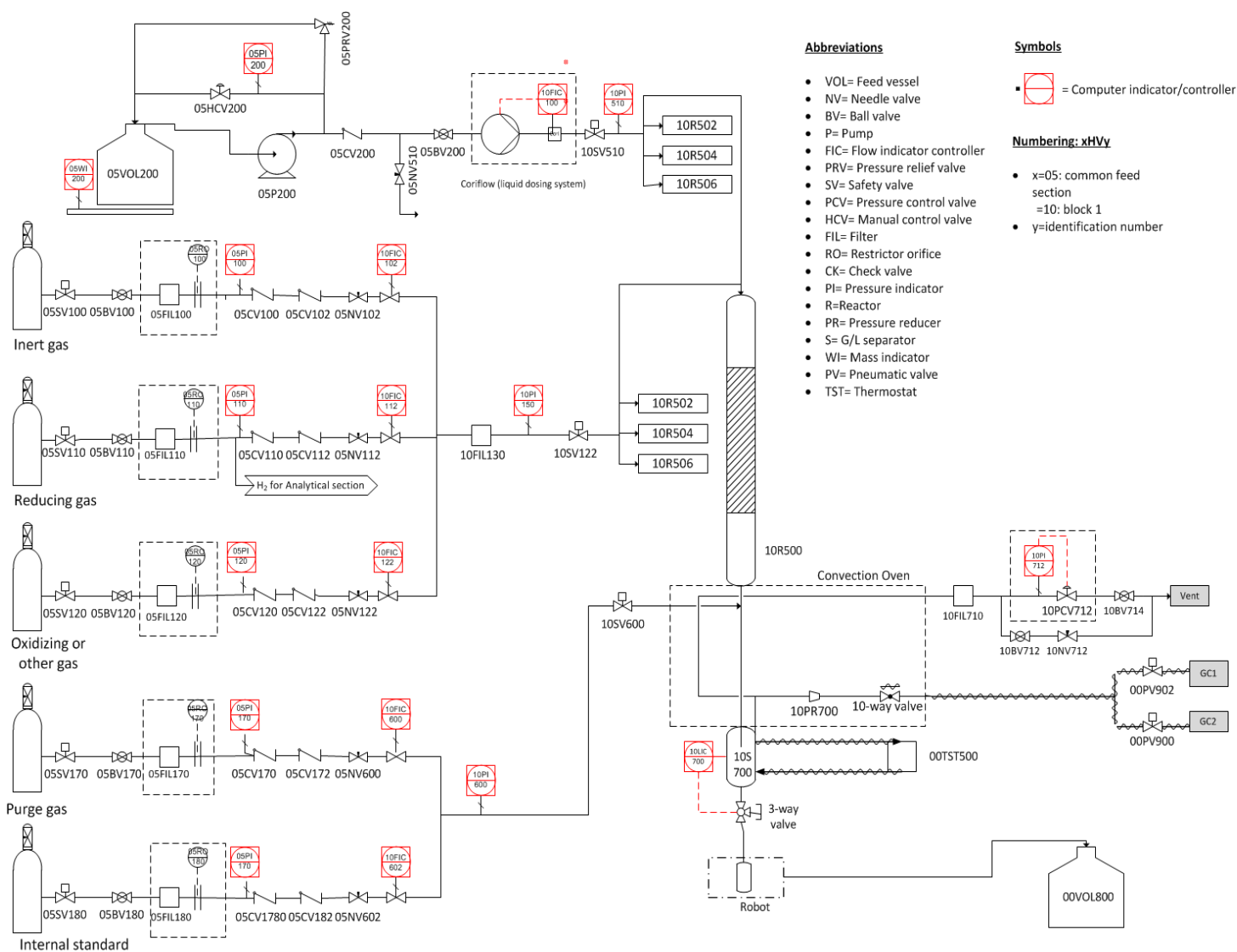
Figure 2-4: Flowsheet of HTK-S located at the Laboratory for Chemical Technology, Ghent University.

(a) Feed section

Three different gases are connected to the set-up for experiments with one Bronkhorst El-Flow thermal mass flow controller for each gas per reactor block, see Figure 2-3 b: an inert gas (10FIC102), e.g. He (flow rate range: $1 - 50$ Nl h^{-1}), a reducing gas (10FIC112), e.g. H$_2$ (flow rate range: $1 - 50$ Nl h^{-1}) and an oxidizing gas (10FIC122), e.g. O$_2$, (flow rate range:1 - 25 Nl h^{-1}). Vary-P controllers are implemented ensuring a flow rate independent of the feed bottle pressure. The liquid is pressurized by using a Lab Alliance 12-6 dual piston pump (05P200), see also Figure 2-3 b. The liquid flow rate per reactor is controlled using a Coriolis Mass Flow Controller (10FIC100), ensuring a flow rate independent of the liquid feed type ($1 - 50$ g h^{-1}).

(b) Reaction section

The reaction section consists of 4 reactor blocks, of which 2 are shown in Figure 2-3 c. The four reactors (10R500; 10R502; 10R504 and 10R506) contained in a reactor block share a single feed line. The feed flow through this line is equally distributed over all 4 reactors in the block making use of capillaries upfront of each of the reactors. These capillaries ensure a pressure drop sufficiently exceeding that over the catalyst bed such that the flow rate is distributed evenly. It is evident that the dimensioning of this capillary distribution system has to be very precise. Its dimensions for gas and liquid were as follows: $L_{cap,g}$= 1.00 m; $d_{cap,g.}$ = 75 µm and $L_{cap,l}$ = 0.75 m; $d_{cap,l.}$ = 75 µm.

Each reactor block is heated by an electrical oven, see Figure 2-3c, which is constructed of Silicon Carbide (SiC) because of its high thermal conductivity. The electrical heating elements are at the outside of the SiC block in which holes were drilled for the reactors. In each block, two thermocouples are present: one located near the heating element measuring the oven temperature T_O, and one in the reactor block center measuring the reactor temperature, i.e., T_M, see Figure 2-3 a and b. The reactor pressure is regulated by using an El-press pressure controller (10PI712; Bronkhorst).
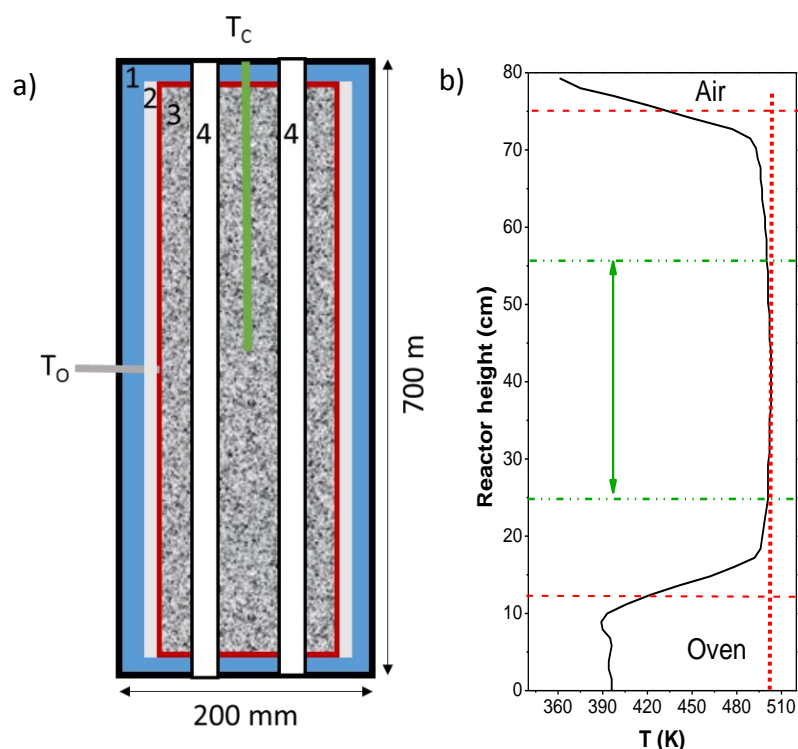
Figure 2-5: Schematic representation of a reactor block of the HTK-S set-up. a) side view (1. insulation, 2. Electrical heating, 3. SiC, 4. reactor well, T_C: central thermocouple; T_O: thermocouple located near the heating elements), b) axial temperature profile measured in the absence of reaction (setpoint: 203 K); isothermal zone indicated in green ($\Delta T < 1$ K).

In principle, the best practice would be to measure the catalyst bed temperature directly to verify the actual reaction temperature. Due to the small reactor diameter, i.e., 2.1 mm, it is impossible to insert an internal thermocouple to measure this local temperature. Therefore, the internal reactor temperature was verified via separate, non-reactive measurements. The temperature in the reactor was measured in the absence of reaction, feed flow rates and a catalyst bed. A thermocouple was placed in the reactor from the top and a temperature was set for the oven. By gradually sliding the thermocouple through the reactor, a temperature profile could be obtained, see Figure 2-5 b. An isothermal zone ($\Delta T < 1$ K) of 0.30 m was determined as indicated in the figure. Via the use of adequate correlations [25], it was determined that even in the presence of highly exo- and endothermic reactions ($|\Delta H_r| > 1000$ kJ mol^{-1}) and at reaction rates sufficiently low to eliminate transport limitations at the scale of the catalyst pellet and at reaction rates sufficiently low to eliminate transport limitations at the scale of the catalyst pellet, no significant temperature profiles will develop in this reactor configuration.

Easy reactor handling is ensured by the utilization of a double O-ring sealing which is able to maintain pressures up to 100 bar. By virtue of these sealings, the time required to remove or load the reactors is significantly reduced compared to using conventional, metal connections. Particular attention needs to be paid to the loading of the catalyst bed, including inert material, to avoid segregation in these small diameter reactors. The generally accepted procedure [26] to pack beds of shaped catalysts diluted with fine powders with intermediate tapping or vibrating, does not work for fine powder beds. As suggested by van Herk et al. [27], premixing the catalyst particles using a tumbler-type mixing to ensure free flow of fluidized swirling power before loading into the reactor is required for a small diameter reactor. A steep angle funnel made of a smooth material, e.g. stainless steel, is used to load the catalyst-inert mixture in small batches to reduce the possibility of segregation. A densification procedure with intense vibration and/or tapping has to be performed before introducing the reactor in the reactor oven. The catalyst-inert mixture can easily be removed from the reactor and can be facilitated by tapping. The reactor is subsequently cleaned with ethanol or another solvent. If coking on the reactor wall occurs, the reactor needs to be treated at elevated temperature under an oxygen rich atmosphere to burn any residuals.

(c) Analysis section

Keeping the whole product spectrum in the gas phase is advantageous since it allows a fast and easy analysis. The presence of a liquid phase would require liquid collection time, additional sampling and more complex data treatment. Therefore, all tubing downstream of the reactor is mounted inside a hot air convection oven (Convection Oven on Figure 2-4) , see Figure 2-3 d. The maximum oven temperature is 473 K, such that heavy product condensation is minimized. The possible introduction of a nitrogen flow (10FIC600) at the reactor outlet allows to decrease the heavy product partial pressures. The gas phase effluent of each reactor can be sampled by using one of the 2 ten-port selection valves, each of them being connected to eight reactors and a calibration or dilution gas. In order to quantify the effluent flow rate and to verify the mass and elemental balances, an internal standard (10FIC602) is introduced downstream of the reactor before sampling.

Since renewable feedstocks are receiving more and more attention, only gas phase analytical equipment was considered not to be sufficient. For example, the decomposition temperature of sucrose is much lower than its vaporization temperature, even at decreased pressures. Therefore, gas-liquid separators (10S700) are installed that can be operated in a temperature range from 293 to 473 K. The gas-liquid separators are mounted near the convection oven and are insulated to prevent cold spots. A 3-way valve is present which is directly connected to the reactor effluent and fills up a dead end-liquid collection tube. When sufficiently filled, the valve is switched and the expulsed liquid is collected in a glass vial. These glass vials are located on a holder plate fixed to a autosampler.

The analysis section comprises 3 gas chromatographs, i.e., 2 Detailed Hydrocarbon Analyzers (DHA, Thermo Fisher Scientific), each analyzing the effluent of 2 reactor blocks, and 1 Refinery Gas Analyzer (RGA, Thermo Fisher Scientific) which is common for all 4 reactor blocks. These GC's are shown in Figure 2-3 e. The RGA comprises a Hayesep N column for separation of $CO_2, C_2H_4, C_2H_6, C_2H_2,$ molesieve 5A for O_2, N_2, CH_4, CO and a Carbosphere for H_2. The analysis of these gases is performed on 2 thermal conductivity detectors (TCD). Hydrocarbon separation up to C_4 hydrocarbon isomers is performed by using an Al_2O_3/KCl column and a flame ionization detector (FID).

While the RGA can only sample on-line, both on and off-line injections can be performed on the DHA. Both DHA GC are equipped with a PONA column (Paraffins, Olefins, Naphthenes and Aromatics) and an additional, more dedicated column, e.g. to separate oxygenates or amines. The presence of both a flame-ionization detector (FID) and nitrogen phosphorous detector (NPD) allows for a versatile and simultaneous effluent stream analysis. The DHA analysis time for a PONA analysis typically requires 1 hour, depending on the product spectrum that needs to be analyzed. The RGA analysis time is limited to 17 minutes and is able to detect a product spectrum from permanent gasses up to C_5 hydrocarbons, allowing for a semi-continuous screening of the catalyst activity.

2.3.2 Mechanistic investigation set-up (HTK-MI)

After the screening stage, a benchmark catalyst is selected on which an extensive experimental study is performed complemented by a few additional catalysts for the catalyst descriptor determination. This is depicted as the *mechanistic investigation* step as shown Figure 2-1c. This mechanistic investigation is performed in the HTK-MI set-up. Its design by Zeton [28] contains 8 parallel tubular reactors (i.d. = 11 mm) which are grouped per pairs in ovens. The temperature can range up to 923 K and the pressure can be elevated up to 200 bar. Due to the larger dimensions of the reactors compared to the HTK-S set-up reactors, no specific caution should be taken with respect to catalyst bed mixing. An overview and more detailed pictures of the HTK-MI set-up are given in Figure 2-6.
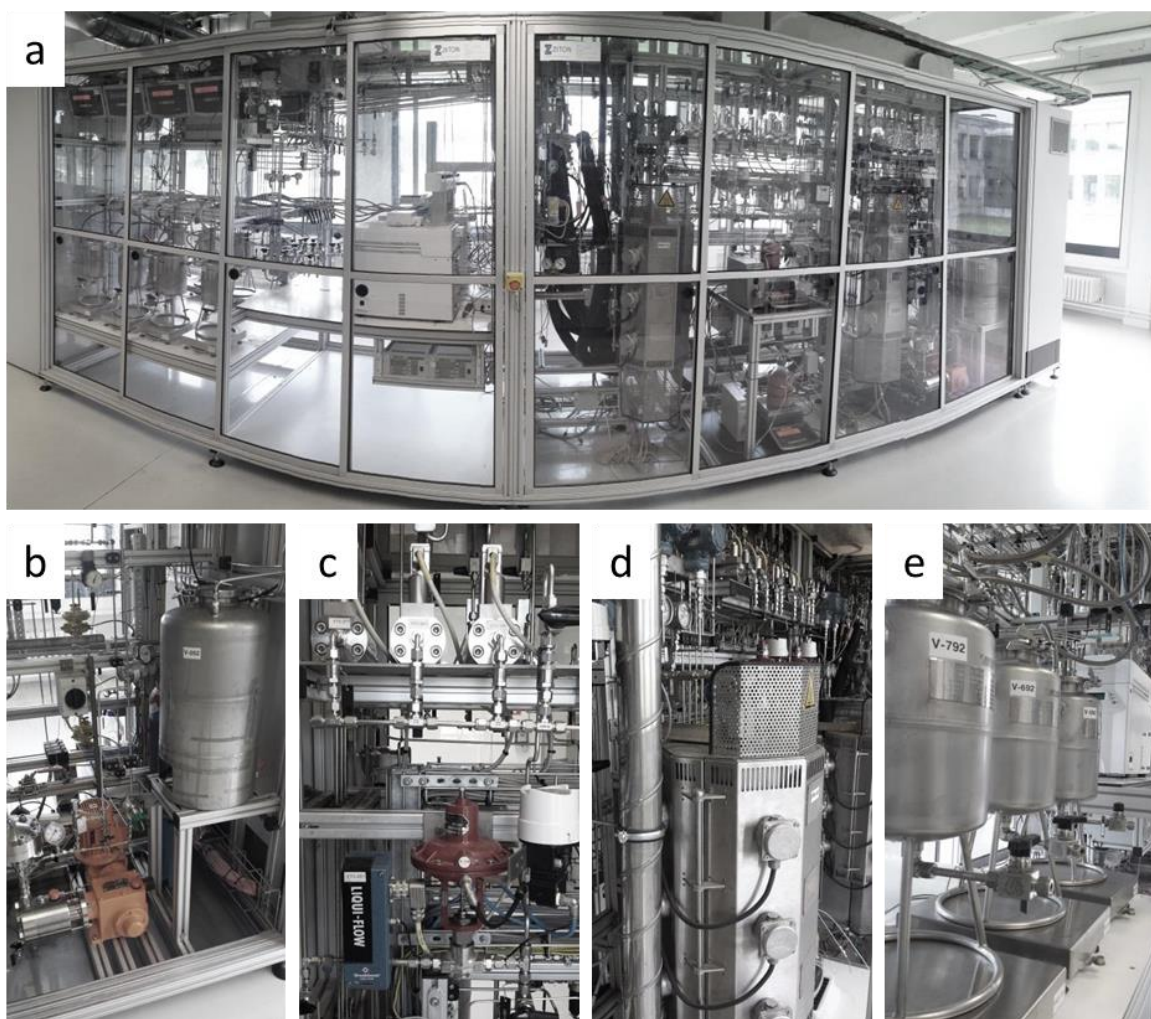
Figure 2-6: HTK-MI set-up pictures: a) front view, b) liquid pump section, c) gas (top) and liquid (bottom) feed section, d) reactor blocks, e) liquid waste collection
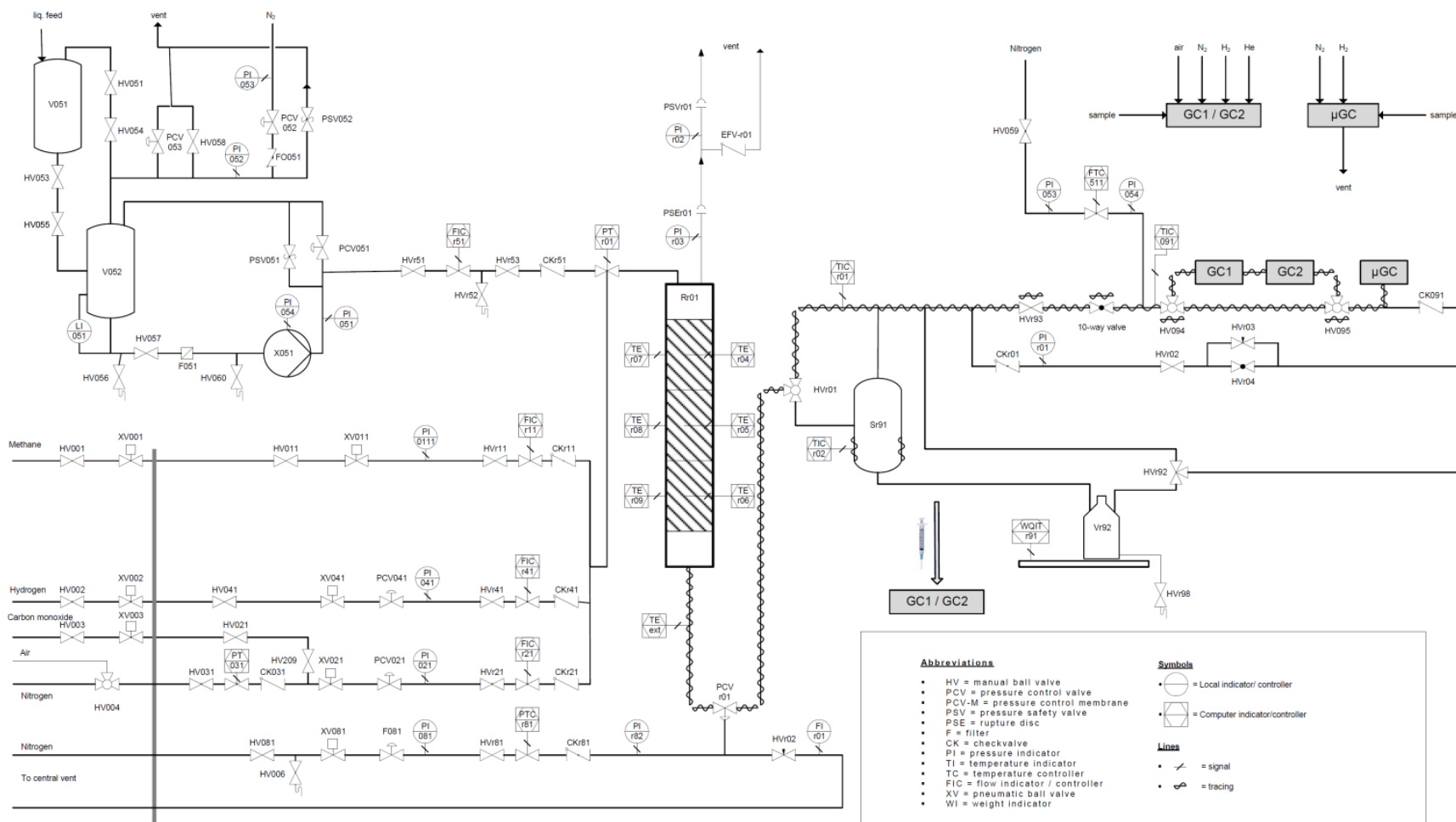
Figure 2-7: Flowsheet of HTK-MI set-up located at the laboratory for Chemical Technology, Ghent University.

(a) Feed section

The set-up has one plunger-diaphragm dosing pump (X051), see Figure 2-6b, which pressurizes and feeds a liquid reactant to all the liquid mass flow controllers (FICr51, Liquid-Flow, Bronkhorst), Figure 2-6c (bottom). A pulsation damper helps to ensure a constant flow rate from the pump. The same feed type is sent to all 8 reactors. The feed flow rate, however, is set individually per reactor. Bronkhorst El-Flow gas mass flow controllers, with a flow rate ranging up to either 10 Nl h^{-1} (FICr11), 100 Nl h^{-1} (FICr41) or 1000 Nl h^{-1} (FICr21) are installed, see Figure 2-6c (top). One of the three gas feed flows is used as internal standard in order to quantify of the effluent flow rate and to verify the mass and elemental balances.

(b) Reaction section

Each reactor is paired with a second one in a reactor block, see Figure 2-6d, and is made of stainless steel (AISI 316 cold worked steel) with a length of 0.9 m and an internal diameter of 11 mm. An internal 3 point thermocouple of 3 mm diameter (TEr04, TEr05 and TEr06) allows to measure and control the actual temperature of the catalyst bed. An additional thermocouple is placed at the outer reactor wall (TEr07, TEr08 and TEr09). The temperature can be controlled either via the inner or outer thermocouple. Temperature control using the external thermocouple is recommended since it leads to a lower dead time. The 3 point character of the used thermocouple allows ensuring a uniform temperature profile throughout the reactor axial direction. The reactor pressure is maintained via back-pressure control (PCVr01)

.

(c) Analysis section

The reactor effluent is initially maintained at sufficiently high temperature via IR-heating (TEext) at the reactor outlet and consequently via heat tracing up to the backpressure regulator. This avoids heavy product condensation when working at gas phase conditions in the reactor. Downstream of the back pressure regulator, the effluent enters a flash drum (Sr91) operated at ambient temperature. The flash drum is used to separate the gas from liquid at ambient temperature in the effluent, if any. The gases continue to the gas analysis section which is also heat traced to avoid condensation of heavy components in the gas effluent. A multiport selection valve (one inlet for each reactor, one for calibration purposes and one outlet to the analysis

equipment; 10-way valve) allows selecting the effluent to be sampled. Downstream of the 10-way valve, the gas stream is sent directly to a micro-GC (μGC). The μGC is a compact device which contains 4 parallel columns (molesieve column: separation of permanent gases and methane, PLOTU column: separation of C_2 and C_3 hydrocarbon, Alumina column: C_3 and C_4 hydrocarbons and OV-1 column: isomer separation of C_4 to C_6 hydrocarbons) with each a thermal conductivity detector (TCD). This is allows a very fast analysis, i.e., less than 5 minutes, and the detection of a product range from permanent gasses to light hydrocarbons up to C_6.

The liquid continues through the set-up by gravity and passes through a sampling device where a GC PAL robotic arm can take a liquid sample to be injected in one of the online GC's. Two GC's (Agilent Technologies 6850 series II network GC system, i.e., GC1 and GC2) are available in the set-up for the analysis of the liquid phase reactor effluent and are equipped with a flame ionization detector (FID) to perform a PONA analysis. If required, the gas effluent can also be analyzed on these GC's. The liquids subsequently continue to the liquid waste storage tanks (Vr92), see Figure 2-6e. These tanks are placed on an electronic weighing scale (WQITr91) with an accuracy of 0.5 g which allow mass balance verification.

2.4 Data processing

The data processing of the GC data is common for both set-ups and is performed according to Toch and Marin [29].

2.4.1 GC data analysis

The relative peak area of a flame ionization detector (FID) relates to the mass fraction of component in the effluent, provided that all the compounds can be detected in the GC. However, components with unsaturated bonds or oxygen molecules will produce a different intensity than expected. To correct this, Dietz [30] reports correction factors for peak areas of most common products.

The general formula for the mass fraction x_i of component i in the effluent is:

$$x_i = \frac{A_i/CF_i}{\sum_{j=1}^{ncomp} A_j/CF_j}$$

(2-11)

with x_i the mass fraction of component *i*, A_i the absolute area of component *i* and CF_i the correction factor as determined by Dietz. Ethanol, for example, contains an oxygen molecule and thus has less carbon-hydrogen bonds to combust. This will produce a smaller peak area than based on the actual mass fraction in the mixture. Dietz reports a factor of 0.46 to correct for this.

This mass fraction can then be converted to molar fractions using the molar mass of the components. The mass fraction of water is determined via stoichiometry. The components constituting the C_2, C_3, C_4 and C_5 hydrocarbon fractions are individually identified in the chromatogram and are treated independently. For the C_{6+} fractions, separate identification of each isomer is no longer possible. An overview of the identified products is given in Appendix A.

An internal standard is added to verify the closure of the mass and carbon balance. A good internal standard is a component which is not getting produced or consumed and is separated well from other peaks. In this work, methane was selected as internal standard. It was verified that methane was not formed nor consumed during the reaction. Since the outlet mass flow of methane equals its mass inflow, the total outlet flow rate can be calculated from the mass fraction of methane in the product mixture via equation (2-12).

$$G_t = \frac{G_{CH4}^0}{x_{CH4}}$$

(2-12)

with G_t the total mass flow rate out of the reactor, G_{CH4}^0 mass flow rate of methane, x_{CH4} the mass fraction of methane.

This total outlet mass flow rate is compared to the inlet mass flow rate and the deviation from the mass balance φ_m is calculated via equation (2-13).

$$\varphi_m = \frac{G_t}{G_{t,0}} \cdot 100\ \%$$

(2-13)

where $G_{t,0}$ and G_t are the total inlet and outlet mass flow rate.

The carbon balance φ_C was determined by

$$\varphi_C = \frac{\sum_{i=1}^{ncomp} CN_i\, F_i}{\sum_{i=1}^{ncomp} CN_i\, F_{i,0}} \cdot 100\ \%$$

(2-14)

where $F_{j,0}$ and F_j is the molar inlet and outlet mass flow rate of component i and CN_j the number of carbon atoms in component i For all experiments shown in this work, the mass and carbon balance is closed within 5%.

2.4.2 Conversion and selectivity

The definitions of conversion and selectivity used in this work are summarized in Table 2-2. These definitions depend on the type of feed being used, i.e, ethanol, methanol, ethene and propene. For ethanol, an ethanol and C_2 conversion is defined.

Table 2-2: Definitions of conversion and carbon-based selectivity for the ethanol, ethene, methanol and propene to higher hydrocarbons.

	Conversion	Selectivity
Ethanol	$X_{EtOH} = \dfrac{F^0_{EtOH} - F_{EtOH}}{F^0_{EtOH}}$	$S_i = \dfrac{CN_i\, F_i}{2 \cdot (F^0_{EtOH} - F_{EtOH})}$
	$X_{C2} = \dfrac{F^0_{EtOH} - (F_{EtOH} + F_{C2H4} + 2F_{DEE})}{F^0_{EtOH}}$	$S_i = \dfrac{CN_i\, F_i}{2 \cdot (F^0_{EtOH} - (F_{EtOH} + F_{C2H4} + 2F_{DEE}))}$
Methanol	$X_{MeOH} = \dfrac{F^0_{MeOH} - (F_{MeOH} + 2F_{DME})}{F^0_{MeOH}}$	$S_i = \dfrac{CN_i\, F_i}{F^0_{MeOH} - (F_{MeOH} + 2F_{DME})}$
Ethene	$X_{C2H4} = \dfrac{F^0_{C2H4} - F_{C2H4}}{F^0_{C2H4}}$	$S_i = \dfrac{CN_i\, F_i}{2 \cdot (F^0_{C2H4} - F_{C2H4})}$
Propene	$X_{C3H6} = \dfrac{F^0_{C3H6} - F_{C3H6}}{F^0_{C3H6}}$	$S_i = \dfrac{CN_i\, F_i}{3 \cdot (F^0_{C3H6} - F_{C3H6})}$

2.5 References

[1] A. Hagemeyer, Strasser, P., Volpe A., High-Throughput Screening in chemical catalysis: Technologies, Strategies and Applications, 2006.

[2] K.D. Shimizu, M.L. Snapper, A.H. Hoveyda, High-throughput strategies for the discovery of catalysts, Chemistry-a European Journal, 4 (1998) 1885-1889.

[3] J.N. Cawse, Experimental Strategies for Combinatorial and High-Throughput Materials Development, Accounts of Chemical Research, 34 (2001) 213-221.

[4] D.L. Massart, Handbook of chemometrics and qualimetrics, Elsevier, Amsterdam ; New York, 1997.

[5] J. Perez-Ramirez, R.J. Berger, G. Mul, F. Kapteijn, J.A. Moulijn, The six-flow reactor technology - A review on fast catalyst screening and kinetic studies, Catalysis Today, 60 (2000) 93-109.

[6] W.F. Maier, K. Stowe, S. Sieg, Combinatorial and high-throughput materials science, Angewandte Chemie-International Edition, 46 (2007) 6016-6067.

[7] R.J. Hendershot, C.M. Snively, J. Lauterbach, High-Throughput Heterogeneous Catalytic Science, Chemistry – A European Journal, 11 (2005) 806-814.

[8] K. Van der Borght, K. Toch, V.V. Galvita, J.W. Thybaut, G.B. Marin, Information-Driven Catalyst Design Based on High-Throughput Intrinsic Kinetics, Catalysts, 5 (2015) 1948-1968.

[9] J.W. Thybaut, G.B. Marin, Single-Event MicroKinetics: Catalyst design for complex reaction networks, Journal of Catalysis, 308 (2013) 352-362.

[10] D. Farrusseng, High-throughput heterogeneous catalysis, Surface Science Reports, 63 (2008) 487-513.

[11] J.W. Thybaut, I.R. Choudhury, J.F. Denayer, G.V. Baron, P.A. Jacobs, J.A. Martens, G.B. Marin, Design of Optimum Zeolite Pore System for Central Hydrocracking of Long-Chain n-Alkanes based on a Single-Event Microkinetic Model, Topics in Catalysis, 52 (2009) 1251-1260.

[12] V.I. Alexiadis, J.W. Thybaut, P.N. Kechagiopoulos, M. Chaar, A.C. Van Veen, M. Muhler, G.B. Marin, Oxidative coupling of methane: catalytic behaviour assessment via comprehensive microkinetic modelling, Applied Catalysis B-Environmental, 150 (2014) 496-505.

[13] B.D. Vandegehuchte, J.W. Thybaut, G.B. Marin, Unraveling Diffusion and Other Shape Selectivity Effects in ZSM5 Using n-Hexane Hydroconversion Single-Event Microkinetics, Industrial & Engineering Chemistry Research, 53 (2014) 15333-15347.

[14] B.D. Vandegehuchte, I.R. Choudhury, J.W. Thybaut, J.A. Martens, G.B. Marin, Integrated Stefan-Maxwell, Mean Field, and Single-Event Microkinetic Methodology for Simultaneous Diffusion and Reaction inside Microporous Materials, Journal of Physical Chemistry C, 118 (2014) 22053-22068.

[15] N.V. Dewachtere, F. Santaella, G.F. Froment, Application of a single-event kinetic model in the simulation of an industrial riser reactor for the catalytic cracking of vacuum gas oil, Chemical Engineering Science, 54 (1999) 3653-3660.

[16] G. Lozano-Blanco, J.W. Thybaut, K. Surla, P. Galtier, G.B. Marin, Simulation of a Slurry-Bubble Column Reactor for Fischer-Tropsch Synthesis Using Single-Event Microkinetics, AIChE Journal, 55 (2009) 2159-2170.

[17] G.F. Froment, Modeling of catalyst deactivation, Applied Catalysis a-General, 212 (2001) 117-128.

[18] B.D. Vandegehuchte, J.W. Thybaut, J.A. Martens, G.B. Marin, Maximizing n-alkane hydroisomerization: the interplay of phase, feed complexity and zeolite catalyst mixing, Catalysis Science & Technology, 5 (2015) 2053-2058.

[19] D. van Herk, M.T. Kreutzer, M. Makkee, J.A. Moulijn, Scaling down trickle bed reactors, Catalysis Today, 106 (2005) 227-232.

[20] G. Marin, G.S. Yablonsky, Kinetics of chemical reactions, John Wiley & Sons, 2011.

[21] P.B. Weisz, J.S. Hicks, The behaviour of porous catalyst particles in view of internal mass and heat diffusion effects, Chemical Engineering Science, 17 (1962) 265-275.

[22] P.B. Weisz, C.D. Prater, Interpretation of Measurements in Experimental Catalysis, in: V.I.K. W.G. Frankenburg, E.K. Rideal (Eds.) Advances in Catalysis, Academic Press, 1954, pp. 143-196.

[23] D.E. Mears, Diagnostic Criteria for Heat Transport Limitations in Fixed Bed Reactors, Journal of Catalysis, 20 (1971) 127-132.

[24] Integrated Lab Solutions, (http://www.integratedlabsolutions.com/), accessed on 23/9/2015 2015

[25] R.J. Berger, E.H. Stitt, G.B. Marin, F. Kapteijn, J.A. Moulijn, Eurokin - Chemical reaction kinetics in practice, Cattech, 5 (2001) 30-60.

[26] M.H. Al-Dahhan, Y. Wu, M.P. Dudukovic, Reproducible Technique for Packing Laboratory-Scale Trickle-Bed Reactors with a Mixture of Catalyst and Fines, Industrial & Engineering Chemistry Research, 34 (1995) 741-747.

[27] D. van Herk, P. Castaño, M. Quaglia, M.T. Kreutzer, M. Makkee, J.A. Moulijn, Avoiding segregation during the loading of a catalyst–inert powder mixture in a packed micro-bed, Applied Catalysis A: General, 365 (2009) 110-121.

[28] Zeton, (http://www.zeton.com/site/home.html), accessed on 23/9/2015

[29] K. Toch, G.B. Marin, Calculation of outlet composition, flow rates, conversions and selectivities in continuous flow (multiphase) reactors, Ghent University,2011

[30] W. Dietz, Response factors for gas chromatographic analyses, Journal of Chromatographic Science, 5 (1967) 68-71.

Chapter 3

Insights into the reaction mechanism of ethanol conversion to hydrocarbons on H-ZSM-5

The acid catalyzed conversion of ethanol on H-ZSM-5 potentially holds the key for sustainable production of light olefins such as ethene and propene. A detailed understanding of the reaction mechanism should facilitate its industrial implementation and help in developing new and improved catalysts. The mechanistic investigation is a key step in the *information-driven catalyst design* which was presented in Chapter 2. Several techniques, such as continuous flow experiments, transient experiments, UV/VIS characterization and ab initio calculations, are combined to elucidate the reaction mechanism of ethanol conversion to higher hydrocarbons. Key aspects that will be addressed are the role of dehydration, the effect of water content and the importance of the aromatic-assisted mechanism, i.e., the hydrocarbon pool.

3.1   Introduction

Most research on ethanol conversion to higher hydrocarbons on zeolites focuses on catalyst improvement via post-synthesis treatments [1], phosphorus addition [2] and metal modification [3, 4], but only few mechanistic studies are available [5-7]. Viswanadham et al. found that zeolites with stronger acidic sites yield a higher fraction of aromatic products [8], which will deactivate the catalyst, whereas attenuating the acidic sites will yield a higher fraction of olefins [9-12]. Several mechanisms have been proposed in literature for the conversion of ethanol to C_{3+} hydrocarbons on H-ZSM-5 in literature. First of all, a simplified acid catalyzed reaction mechanism with ethene as primary product of the fast dehydration reaction and the subsequent production of higher hydrocarbons requiring the direct coupling of ethene as crucial reaction step was proposed by Gayubo et al. [13].

Maderia et al. [14] investigated different zeolites for the conversion of ethanol to C_{3+} hydrocarbons and observed a loss in Brønsted acidity and microporosity of the catalyst with time-on-stream, without the loss of catalytic performance. Simultaneously, an increase in retained coke molecules is observed. Hence it was concluded that these molecules have a catalytic effect and can be regarded as an extra catalytic site. Investigation with IR spectroscopy and GC-MS shows that these coke molecules are highly alkyl-substituted aromatics which are identified by the authors as radical cation species using electron paramagnetic resonance [15]. A change with time-on-stream of the nature of these species corresponds with the formation of large polyaromatic molecules which block access to the active sites and ultimately cause deactivation of the catalyst, leading to a decrease in the C_{3+} hydrocarbon formation while ethanol conversion remains complete. The dehydration was found to be unaffected by coke deposition [16] from Schulz and Bandermann concluded that the dehydration of ethanol occurs on the external surface of the catalyst. These radical species are regarded as an active aromatic pool for the conversion to C_{3+} hydrocarbons and is a second type of reaction mechanism encountered in literature.

A dual cycle mechanism [17] was proposed by Johansson et al. for the conversion of ethanol on H-ZSM-5. The authors observed a similar product distribution in ethanol conversion as in methanol-to-olefins. Interestingly, the authors observed a higher amount of retained ethyl substituted aromatics inside the catalysts. This mechanism is analogous to the one proposed for the methanol-to-olefins (MTO) process [18]. It comprised also an aromatic-assisted mechanism for the production of ethene and propene, and a methylation/cracking cycle for the production of higher olefins. For MTO, this was confirmed from both experimental [19-21] and theoretical studies [22, 23]. Recently, the methylation/cracking cycle has gained interest as the dominant mechanism in the conversion of methanol on H-ZSM-5 [24, 25].

A detailed mechanistic investigation of the conversion of ethanol to higher hydrocarbons is presented in this work. This resulted in a unifying mechanism which is supported by experimental evidence from continuous flow and transient experiments combined with quantum chemical calculations on the dehydration of ethanol and the consecutive oligomerization of ethene. The nature of the surface species was derived from isotopic labelled transient experiments and UV-VIS spectroscopy of spent catalyst.

3.2   Procedures

3.2.1   Catalyst performance testing

The zeolite used in this work is the commercially available NH_4-ZSM-5 (Zeolyst, CBV8024) with a Si/Al = 40**.** The acid form was obtained by calcining at 823 K for 3 h with a temperature ramp of 1 K min^{-1}. The continuous flow experiments were performed in the HTK-MI reactor set-up as described in Chapter 2.

The transient studies were performed in a state-of-the-art system Temporal Analysis of Products (TAP-3E) reactor (Mithra Technologies, St. Louis, USA). The system comprises a manifold, a micro-reactor and a quadruple mass spectrometer. High speed pulse valves in the manifold assembly are used for injecting pulses of reactants into the micro-reactor. A micro-reactor made of quartz tube with dimensions of 58 mm length and 4 mm internal diameter is used for this reaction.

Reactor and mass spectrometer are housed in a high vacuum chamber of approx. 4.10^{-7} Torr. A turbo molecular pump (Turbo-V 301-AG) and diffusion pump (VHS-400 from Agilent technologies) were used to generate a high vacuum inside the system. Gas phase products from the micro-reactor were monitored by Extrel 150QC quadruple mass spectrometer with millisecond time resolution.

Single-pulse experiments of ethene were performed at 673 K temperature in transient mode. A pulse of ethene containing 10^{17} molecules is injected into the micro-reactor by a pulse valve. 11 mg of catalysts is placed between layers of inert quartz particles in thin-zone TAP reactor (TZTR) configuration. Collection time for each pulse is 2 seconds with a delay of 0.1 s for the subsequent pulse. The amount of molecules interacting with the active sites of the catalyst is of one order smaller in magnitude. Products resulting from a state of fresh catalyst to a state-altered mode were screened by the mass spectrometer in this transformation process. Products quantification is performed by use of helium (m/e = 4) as inert gas standard. Fragments associated with paraffins were not observed in these conditions. Lower olefinic products such as propene (m/e = 42), butene (m/e = 56), pentene(m/e = 70) and hexene (m/e = 84) were observed. Benzene (m/e = 78) and ethylbenzene (m/e = 91) were also detected. Mass fragments resulting from higher olefins are subtracted to correct for their presence in the signal associated with lower olefins in the products. Calibration factors were determined to obtain the outlet composition in mol. More details related to the experimental set-up and the type of experiments are described by Gleaves et al. elsewhere [26].

3.2.2 Computational methodology

H-ZSM-5 is a 3-dimensional medium pore zeolite consisting of 10-membered ring straight and zigzag channels [27]. $Al_{12}O_{24}H$, located at the intersection of these channels, is chosen as the acid site because of its accessibility for bulky reactants. This location for the acid site has also been proposed by Sauer and co-workers [28]. The optimized unit cell parameters are a = 2047.2 pm, b = 2010.9 pm, c = 1357.6 pm, α = 89.97°, β = 89.88°, and γ = 89.99° [29].

Dispersion corrected periodic DFT calculations were performed with the Vienna Ab Initio Simulation Package (VASP) using plane wave basis sets [30-33]. The electron-ion interactions were described using the projector–augmented wave (PAW) method [34, 35] with a plane-wave energy cut-off value of 600 eV. The exchange-correlation energies were calculated on the basis of the generalized gradient approximation (GGA) according to Perdew, Burke and Ernzerhof (PBE) [36]. Brillouin zone sampling was restricted to the Γ-point. A maximum force convergence criterion of 0.02 eV Å−1 was used and each self-consistency loop was iterated until a convergence level of 10−8 eV was achieved. Dispersive corrections for the van der Waals interactions were included by adding a pairwise interaction term to the Kohn–Sham energy using the DFT-D2 approach proposed by Grimme [37] and extended by Kerber et al. [38] for periodic calculations. The electronic charge on atoms and fragments was calculated using Bader analysis [39] as implemented by Henkelman et al. [40]. The dimer method [41] was used to locate transition states on the potential energy surface.

Normal mode analysis was performed using a Partial Hessian Vibrational Analysis (PHVA), considering the T5 cluster (HAl(SiO$_4$)$_4$) of the zeolite framework and the adsorbate molecule to be free for the numerical Hessian calculation. Previous studies for physisorption and chemisorption in zeolites have shown that the partial hessian approach leads to a marginal difference in the result as compared to a Full Hessian Vibration Analysis (FVHA) [42]. Since the low-lying frequencies (< 50 cm^{-1}) associated with the frustrated motions of the surface bound species (such as translation or rotation of the molecule within the zeolite pore structure) can lead to significant errors in the entropy calculations [43], these low frequencies were replaced by normal modes of 50 cm^{-1}.

Standard enthalpies, entropies, and Gibbs free energies for reactants, products, and transition states were calculated using statistical thermodynamics [44]. The partition functions for the gas-phase species included vibrational, rotational and translational degrees of freedom, while only the vibrational contributions were taken into account for the surface species. The standard

pressure used for all gas phase species was taken to be 100 kPa. Equilibrium coefficients for each elementary reaction were obtained using the following formula:

$$K = \exp\left(-\frac{\Delta H^0 - T\Delta S^0}{RT}\right) = \exp\left(-\frac{\Delta G}{RT}\right) \tag{3-1}$$

where R is the gas constant, T is the temperature, ΔH^0 is the, ΔS^0 is the standard entropy of reaction, and ΔG^0 is the standard Gibbs free energy of reaction. Rate coefficients for each elementary reaction were calculated on the basis of transition state theory:

$$k = \frac{k_B T}{h} \exp\left(-\frac{\Delta S^{0,\ddagger}}{R}\right) \exp\left(-\frac{\Delta H^{0,\ddagger}}{RT}\right) = \frac{k_B T}{h} \exp\left(-\frac{\Delta H G^{0,\ddagger}}{RT}\right) \tag{3-2}$$

where k_B is the Boltzmann constant, h is the Planck constant, $\Delta H^{0,\ddagger}$ is the standard enthalpy of activation, $\Delta S^{0,\ddagger}$ is the standard entropy of activation, and $\Delta G^{0,\ddagger}$ is the standard Gibbs free energy of activation. Arrhenius pre-exponential factors (A) and activation energies (E_a) for the activated elementary steps were obtained by regression of equation (3-2) in the temperature range of 300 – 800 K. For non-activated reactions, like adsorption/desorption and rearrangement steps, the rate coefficient in the exothermic direction (e.g. adsorption) was calculated from equation (3-2) assuming $\Delta G^{0,\ddagger} = 0$, while the rate coefficient in the endothermic direction (e.g. desorption) was calculated from thermodynamic consistency.

An isothermal plug flow reactor model was used for the reactor simulations:

$$\frac{dF_i}{dW} = R_i \tag{3-3}$$

in which F_i is the molar flow rate of gas phase component I, W the catalyst mass, R_i the net rate of formation of gas phase component i.

The following continuity equations were applied for the gas-phase components i and surface species k along with a site balance:

$$R_i = C_t \sum_j v_{ji} r_j \tag{3-4}$$

$$R_k = C_t \sum_j v_{jk} r_j = 0 \tag{3-5}$$

$$\theta_{H^+} + \sum_k \theta_k = 1 \qquad\qquad (3\text{-}6)$$

where r_j is the turnover frequency of elementary step j, v_{ji} the stoichiometric coefficient of component i in the elementary step j, θ_k the fractional coverage of surface species k, θ^* the fractional coverage of free acid sites, C_t the acid site concentration, F_i the molar flow rate of gas-phase component i, W the mass of the catalyst and R_i the net production rate of gas-phase species i. This set of equations was solved numerically using DDASPK .

3.3 Reaction mechanism elucidation

The product distribution was monitored as function of temperature (433 – 633 K) in order to find suitable reaction conditions for investigation of the reaction mechanism within the experimental limitations of the HTK-MI set-up, i.e., mass flow rates of ethanol and inert. It should be noted that both temperature and conversion are varied simultaneously. As can be seen from Figure 3-1, at 440 K ethanol is selectively converted to diethyl ether:

$$2\ C_2H_5OH\ \rightarrow C_2H_5OC_2H_5 +\ H_2O \qquad\qquad (3\text{-}7)$$
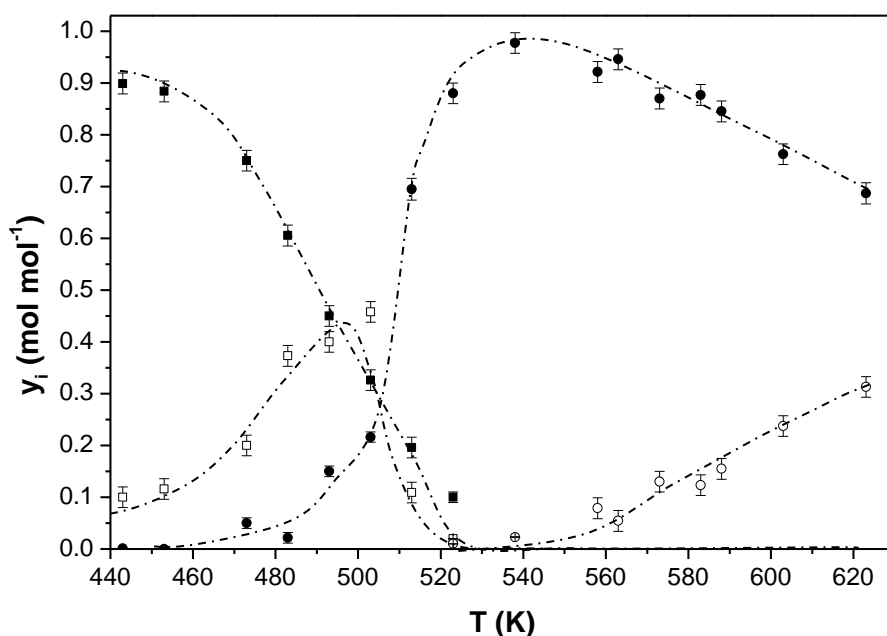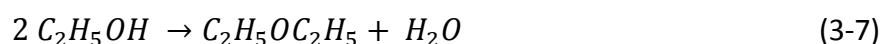
Figure 3-1: Mole fractions as function of temperature on H-ZSM-5 (■ : ethanol; □ : diethyl ether; ● : ethene; ○ : C$_{3+}$ hydrocarbons) (W $F_{EtOH,0}^{-1}$ = 8 kg$_{cat}$ s mol^{-1}; p$_{EtOH,0}$ = 10 kPa). Lines are to guide the eye.

As temperature increases to 500 K, a mixed outlet flow of ethene and diethyl ether is produced where ethene can either be formed via the direct dehydration of ethanol (eq. 3-8) or via diethyl ether [45] (eq. 3-9):

$$C_2H_5OH \rightarrow C_2H_4 + H_2O \qquad (3\text{-}8)$$

$$C_2H_5OC_2H_5 \rightarrow C_2H_4 + C_2H_5OH \qquad (3\text{-}9)$$

Increasing the temperature to 523 K results in ethene as the sole product and almost no residual diethyl ether is detected. No other hydrocarbons than ethene are detected below 523 K. The dehydration of ethanol is discussed in more detail in Chapter 4.

Above 523 K, ethene concentration begins to decrease and higher hydrocarbons begin to form. Formation of other oxygenates were not observed in the entire temperature range. The most abundant products are the light olefins containing two to five carbon atoms and in minor quantities light paraffins (C_2 – C_4), aromatics and fraction in the gasoline range i.e. C_{5+} hydrocarbons. 573 K was chosen as reaction temperature to perform the mechanistic investigation study as it as an intermediate temperature between the region where only ethanol dehydration is observed and the temperature region where higher hydrocarbons are observed.

3.3.1 Continuous flow experiments

The importance of the dehydration in the production of the higher hydrocarbons, i.e., hydrocarbons containing more than two carbon atoms, was investigated by continuous flow experiments in which the site time was varied. It can be observed from Figure 3-2 a that under steady state conditions at 573 K and below 1.0 mol_{H+} s mol^{-1}, ethanol dehydration is incomplete and both diethyl ether (DEE) and ethene are produced, indicating that the dehydration is not spontaneous at higher temperature as proposed in literature [46]. Higher hydrocarbon formation, which is quantified by the C_2 conversion, is only observed at site times exceeding 1.5 mol_{H+} s mol^{-1}.
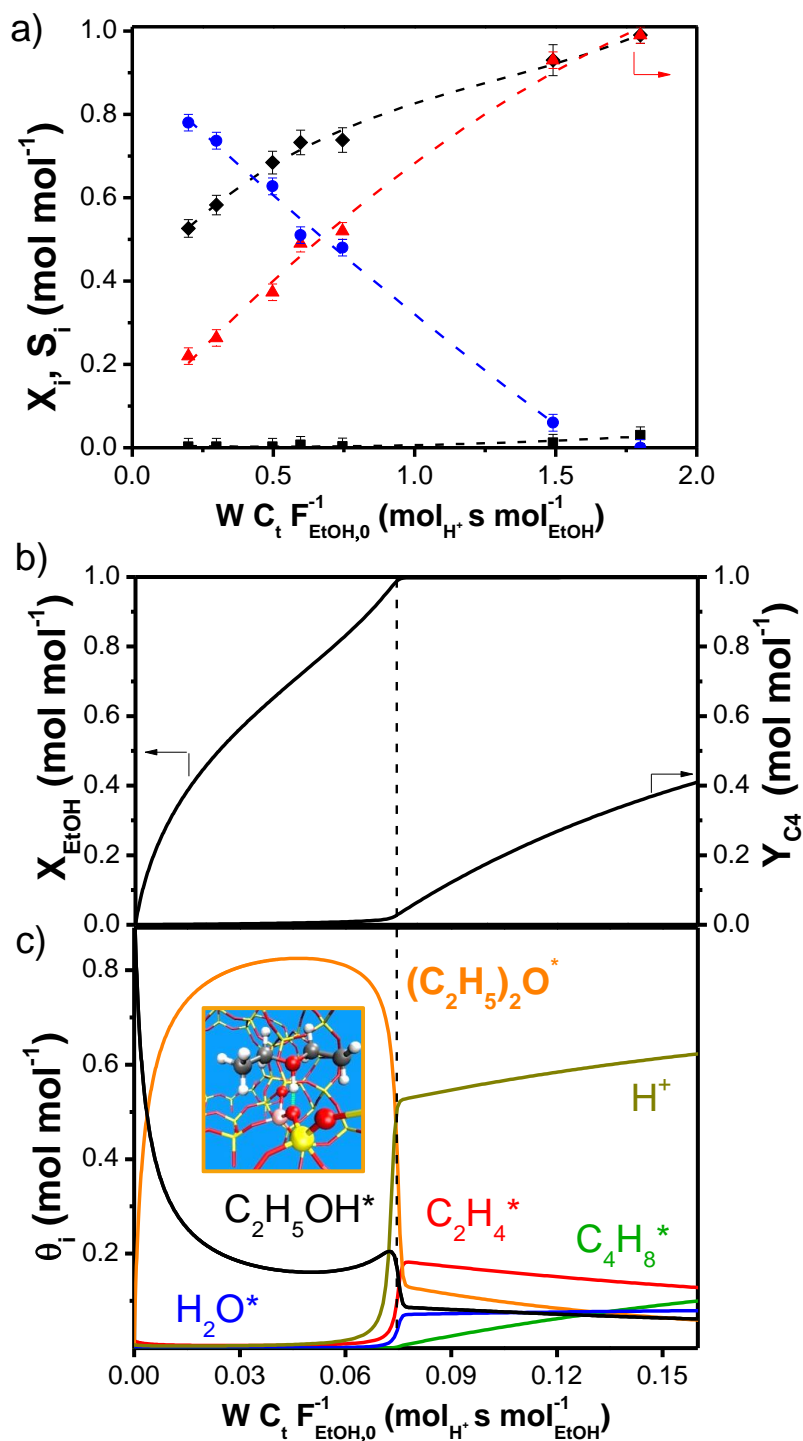
Figure 3-2: a) Ethanol conversion (♦, black), C₂ conversion, as defined in paragraph 2.4.2 (■, black) and selectivity to ethene (○, red) and diethyl ether (▼, blue) as function of ethanol site time. Lines are to guide the eye. b) Simulated ethanol (X_{EtOH}) and C₄ yield (Y_{C4}) as function of ethanol site time using ab initio calculated rate and equilibrium coefficients and integration of equation (3-3) and simultaneously solving eqs. (3-4) and (3-5), c) Corresponding simulated fractional surface coverages as function of site time with black: adsorbed ethanol ($C_2H_5OH^*$), red: adsorbed ethene ($C_2H_4^*$), orange: adsorbed diethyl ether ($(C_2H_5)_2O^*$), blue: adsorbed water (H_2O^*), green: adsorbed 1-butene ($C_4H_8^*$) and khaki : free acid sites (H⁺). (T = 573 K, $p_{EtOH,0}$ = 30 kPa).

This separation between ethanol dehydration and higher hydrocarbon formation can be explained using Density Functional Theory (DFT) based microkinetic modeling of ethanol dehydration [45] and dimerization of ethene to 1-butene which is the critical step in the formation of higher hydrocarbons. As shown in Figure 3-2 b, the production of the higher hydrocarbons, here represented by 1-butene, only starts when ethanol conversion is almost complete as observed experimentally. The surface coverages plotted in Figure 3-2 c, show that the surface is initially covered with protonated ethanol ($C_2H_5OH^*$) which is rapidly replaced by protonated diethyl ether ($(C_2H_5)_2O^*$). The surface remains fully covered during dehydration. Free sites (H^+) for the adsorption of ethene ($C_2H_4^*$) and the production of higher hydrocarbons become available only when ethanol conversion is almost complete ($X_{EtOH} > 0.9$). The calculated dependency of the surface concentrations on the site time is due to the pronounced differences of the equilibrium coefficients for adsorption as can be seen in Figure 3-3. It can be seen that diethyl ether adsorbs the most strong followed by ethanol, ethene, water and finally 1-butene which has an adsorption equilibrium coefficient which is 10^5 times lower.
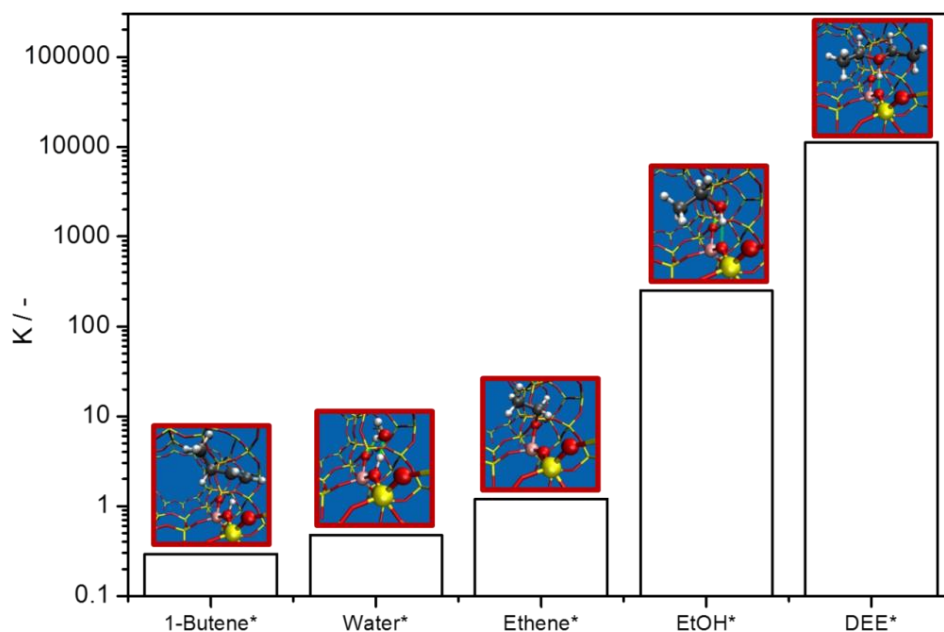
Figure 3-3: Equilibrium coefficients for 1-butene, water, ethene, ethanol and diethyl ether at 573 K

The conversion of ethanol to C_{3+} hydrocarbons, represented by the C_2 conversion, i.e., X_{C2}, as function of site time in continuous flow experiments exhibits an induction period which is typical for an autocatalytic mechanism as can be seen in Figure 3-4. This was already reported for methanol conversion [47, 48] but not yet for ethanol conversion. The same experiment but with an ethene feed results in a shift of the site time – conversion curve to lower site times but the same onset to a sigmoidal curve remains visible which was also not yet identified in olefin conversion. From Figure 3-4, the production rate of C_{3+} hydrocarbons from ethanol and ethene, taken as the slope in the conversion – site time curve beyond the induction period, can be calculated to be, respectively, $(9.1 \pm 1.1) \ 10^{-2}$ mol s^{-1} mol$_{H+}^{-1}$ and $(10.5 \pm 0.6) \ 10^{-2}$ mol s^{-1} mol$_{H+}^{-1}$, i.e., not significantly different at the 95 % confidence level.
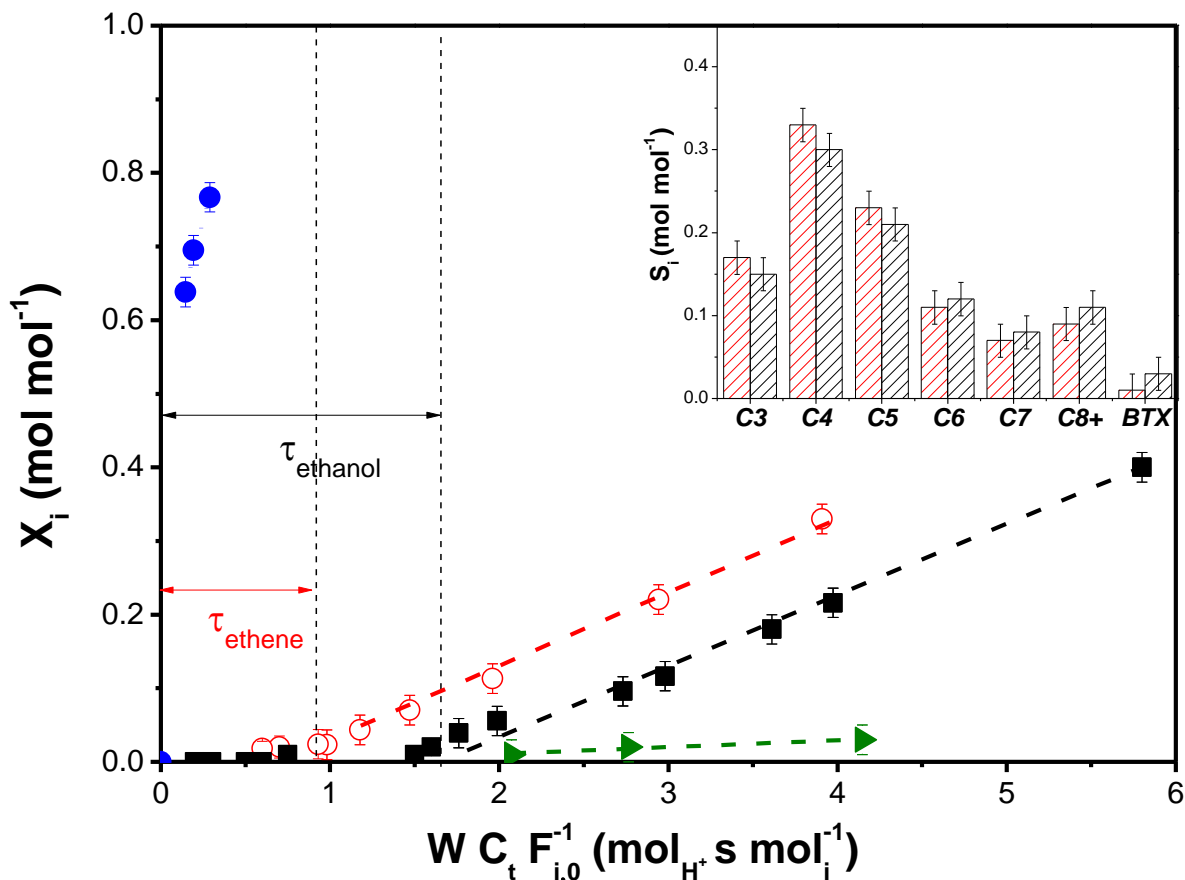
Figure 3-4: Conversion of different feeds: ethanol (C_2-conversion as defined in paragraph 2.4.2, ■, black), ethene (○, red), propene (●, blue) and methanol (▶, green) as a function of site time. Inset: selectivity towards higher hydrocarbons (C_3 to C_{8+}) and aromatics (Benzene-Toluene-Xylenes) at X_{C2} = 0.2 for an ethene feed (red) and an ethanol feed (black) (T = 573 K, $p_{EtOH,MeOH,0}$= 30 kPa, $p_{ethene,propene,0}$ = 27 kPa). Lines are to guide the eye.

The induction period observed in ethene conversion corresponds to the time scale on which the species responsible for the autocatalysis are formed. The induction period observed in ethanol conversion then consists of the sum of both time scales time i.e., the time required for dehydration of ethanol and the time for formation of the autocatalytic species. The site time-conversion behavior was also found to be reversible, i.e., when working at high site time, followed by a switch to a lower site time by altering the flow rate and subsequently going back to the original site time results in the same conversion.

The product distribution observed at 20% C_2 conversion in the continuous flow experiments is shown as an inset in Figure 3-4 and consists primarily of olefins with carbon numbers up to 10 while the selectivity towards aromatics is around 1 %. Similar selectivity towards the different product classes are observed at same C_2 conversion for ethanol and ethene feeds illustrating that the selectivity is unaffected when comparing ethanol and ethene feeds. Propene and butenes are identified as primary C_{3+} hydrocarbon products for both ethanol and ethene feeds using a delplot analysis [49] as can be seen from Figure 3-5.
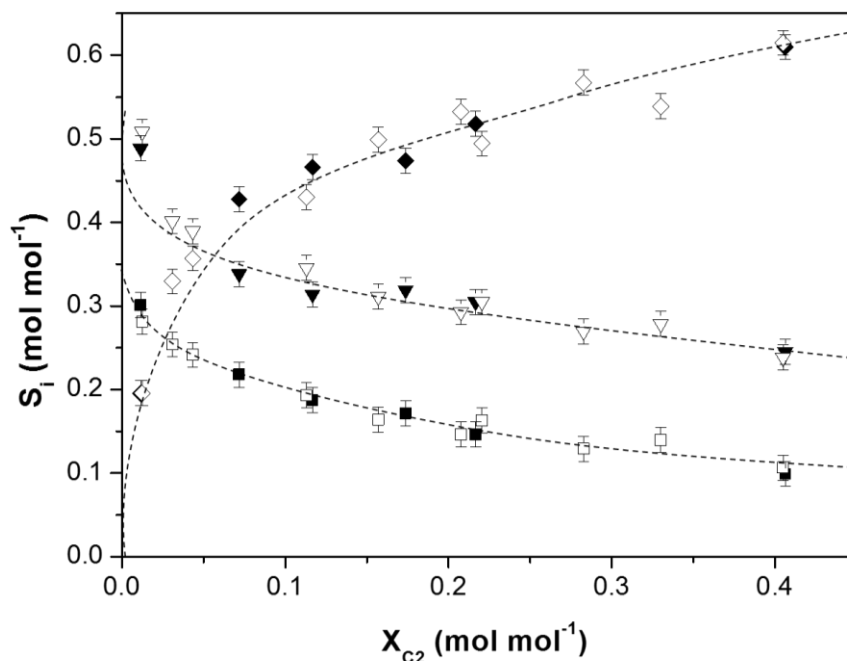
Figure 3-5: Selectivity as function of C_2 conversion, as defined in paragraph 2.4.2, for C_4 olefins (▼,▽), propylene (■,□) and C_{5+} hydrocarbons (♦,◊) using ethanol (full symbols) and ethene (hollow symbols) as feed (T = 573 K). Dashed lines are guides to the eye.

It can also be seen from Figure 3-4 that propene exhibits a much higher reactivity compared to ethanol and ethene which can be attributed to the involvement of a secondary surface intermediate in the initiation step while the conversion of ethanol and ethene depends on the dimerization of ethene which involves the formation of a less stable primary reaction intermediate. Methanol conversion to hydrocarbons remains fairly low at these reaction conditions which is in accordance with Qian et al., who found a higher activation energy for the formation of the aromatics which can assist in the hydrocarbon pool mechanism when starting from methanol compared to ethanol on SAPO-34 [50].

3.3.2 Transient experiments

As it is challenging to discriminate between the different routes for the production of light olefins solely based on continuous flow experiments, a transient technique, i.e., Temporal Analysis of Products reactor (TAP-3E), was employed and is illustrated in Figure 3-6. Here, a pulse containing $\sim10^{17}$ reactant molecules (A) is sent through a catalyst bed and product formation (P) is followed using mass spectrometry. The number of molecules in each pulse is at least one order of magnitude smaller than the amount of acid sites. Two types of experiments were performed: state-defining, in which only a limited amount of reactant pulses are sent over the catalyst bed and state-altering, where changes of the catalyst state, e.g. carbon deposition, occur by multi-pulsing.

No significant C_{3+} production was observed when pulsing ethanol over H-ZSM-5. This can again be explained by incomplete ethanol conversion which inhibits the production of C_{3+} hydrocarbons as explained above. In contrast, when pulsing ethene all olefinic products ($C_2 - C_6$) are already observed from the first pulse onwards as shown in Figure 3-6 a and b. This indicates that the rate of dimerization is slower compared to production of olefins via acid catalyzed steps.
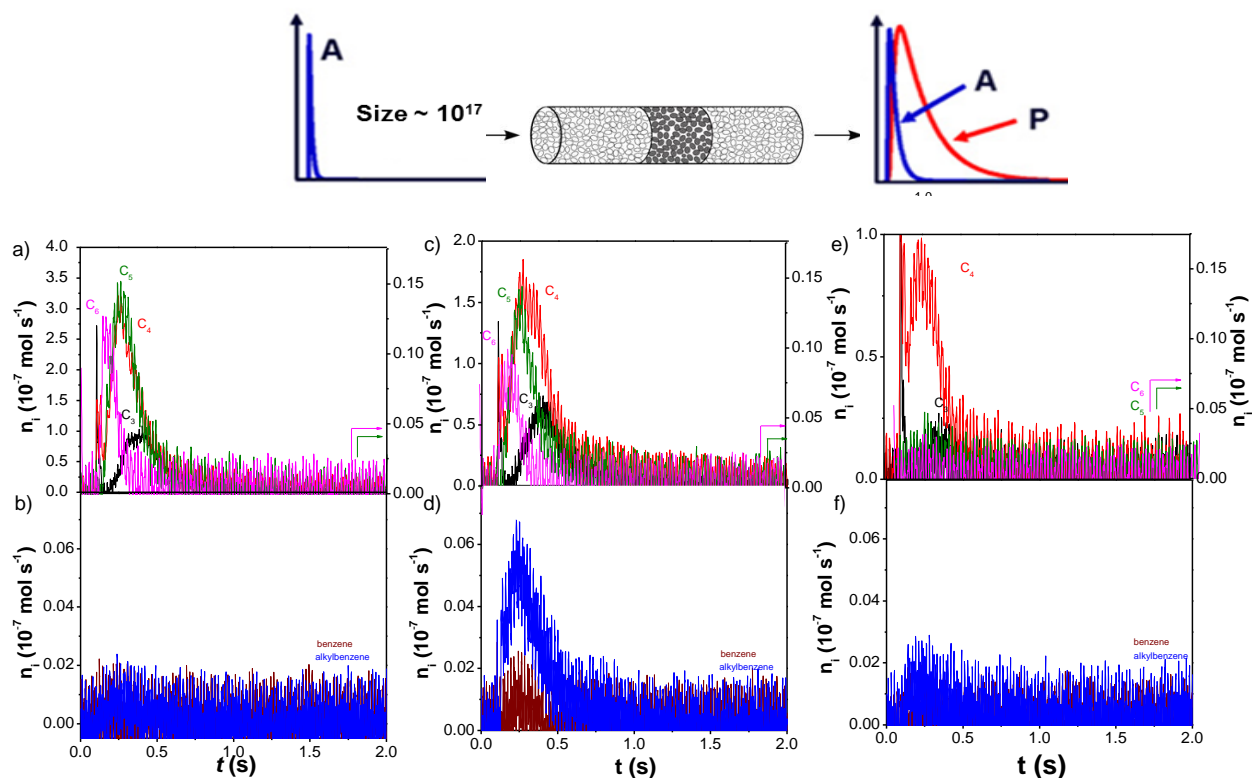
Figure 3-6: a) & b) response to 1st ethene pulse, c) & d) response to 25th ethene pulse, e) & f) response to 400th ethene pulse. Product evolution monitored for each a.m.u. separately over fresh catalyst bed in TAP-3E (color code: butenes (C$_4$; m/e = 56, red), propene (C$_3$; m/e = 42, black), pentenes (C$_5$; m/e = 70, green), hexenes (C$_6$; m/e = 84, magenta), benzene (m/e = 78, wine) and VI) alkylaromatics (m/e = 91, blue)) (n$_{ethene}$ = 10^{17} molecules/pulse; W = 11 mg, T= 648 K)

No aromatics are observed in the gas phase during the first pulse which is due to the insufficient occupancy of species on the surface required for the production of aromatics. The same olefinic products are still being formed after 25 pulses (Figure 3-6 c and d) but now gas phase aromatics are also observed. After 400 pulses as shown in Figure 3-6 e and f, aromatics are no longer observed. Olefins are thus the primary products in ethene conversion and the formation of propene and butene in the catalyst state of apparent steady state behavior is preceded by the simultaneous formation of higher olefins and aromatics.

During 400 pulses of ethene, the ethene conversion per pulse was found to decrease to a constant value of 5 - 10 %, as shown in Figure 3-7a, which can be related to the formation of surface species which block the active sites and/or to the formation of coke. The activity after 400 pulses of ethene could be restored by treatment with oxygen at 773 K. However, the activity can also

restored by simply increasing temperature to 773 K in the absence of oxygen. This temperature programmed desorption was followed by mass spectrometer and only fragments of m/e = 78 (Figure 3-7b) and 91 were observed and no fragments associated with olefins. These fragments are representative for aromatic species.
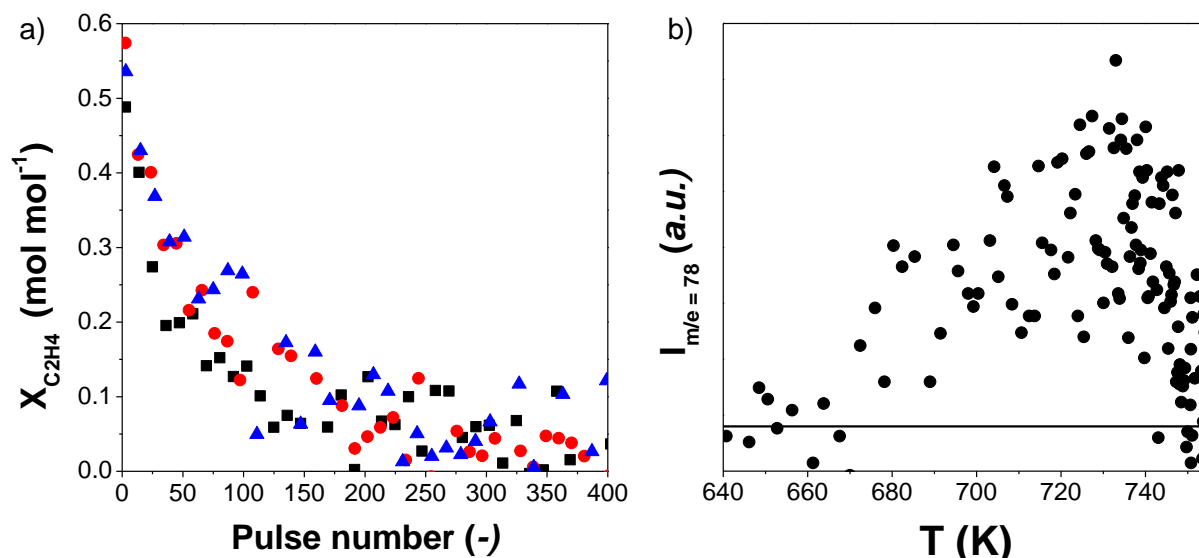
Figure 3-7: Ethene conversion (X_{C2H4}) as function of pulse number over fresh H-ZSM-5 (■ , black), H-ZSM-5 after reaction and one temperature programmed desorption (▲, blue), H-ZSM-5 after two times of reaction and temperature programmed desorption (●, red), b) Intensity of m/e = 78 (representative for aromatics) during temperature programmed desorption after treatment of catalyst with 400 pulses of ethene. (n_{ethene} = 10^{17} molecules/pulse; W = 27 mg, T= 648 K)

The role of the long-lived intermediates such as aromatics, in propene and butene formation was investigated via transient experiments using ^{13}C labeling. After 400 pulses of ^{13}C ethene, the catalyst was kept under vacuum during 30 s at 648 K to remove the short-lived surface species before switching the feed to ^{12}C ethene. The evolution of the mass fragments of labelled and unlabelled propene after the ^{13}C/^{12}C ethene feed switch is shown in Figure 3-8.
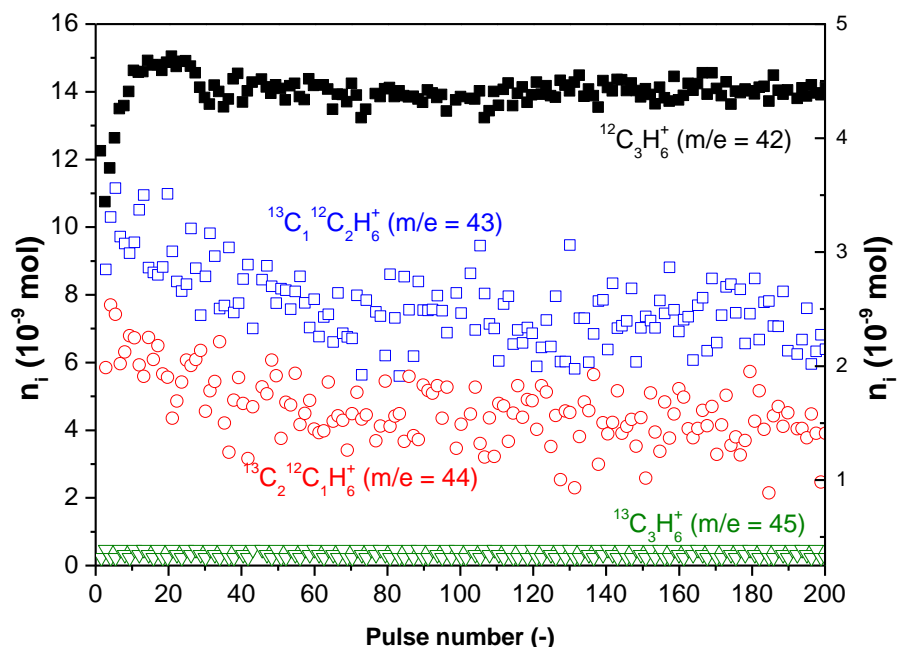
Figure 3-8: Evolution of propene formation (unlabelled and labelled) as function of number of $^{12}C_2H_4$ pulses after treatment of the catalyst with 400 pulses of isotopic labelled ethene ($^{13}C_2H_4$) with black: unlabelled propene (m/e = 42), blue & red: scrambled propene (m/e = 43 and m/e = 44) and green: fully labelled propene (m/e = 45) (n_{ethene} = 10^{17} molecules/pulse; W = 27 mg, T= 648 K)

It can be seen that no fully labelled propene is presented indicating that propene does not form from decomposition of surface species. An evolution is observed in the ratio between unlabelled propene and propene with 1 or 2 ^{13}C atoms. This is evidence for the involvement of surface species in the reaction mechanism of ethene to higher hydrocarbons.

3.3.3   UV-VIS spectroscopy

The evolution of the colour of the catalyst bed was studied in a dedicated set-up equipped with quartz reactors and is shown in Figure 3-9. The first four pictures of catalyst bed are taken at 573 K where the first corresponds to the catalyst bed under inert atmosphere in the absence of reaction and the next three to C_2 conversion of 0.1, 0.3 and 0.5 which are obtained by site time variation.
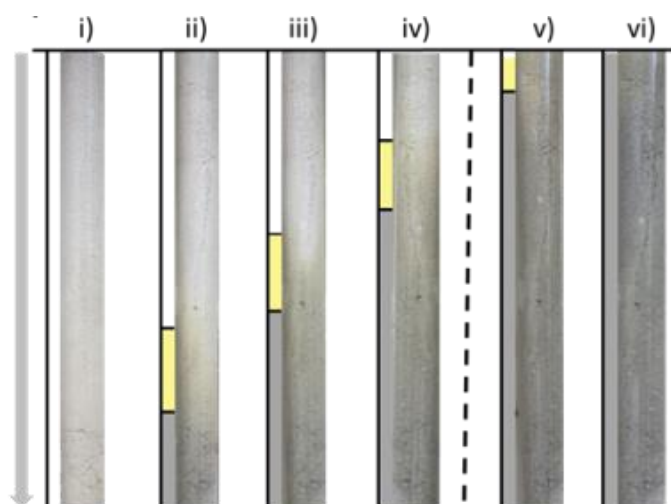
Figure 3-9: Picture of the catalyst bed during ethanol conversion: i) 573 K, $X_{C2} = 0$, ii) 573 K, $X_{C2} = 0.1$, iii) 573 K, X_{C2} = 0.2 iv) 573 K, $X_{C2} = 0.3$, v) 593 K $X_{C2} > 0.8$, vi) 623 K, $X_{C2} > 0.8$. Arrow indicates the direction of the feed flow.

The first part of the catalyst bed is white which can be attributed to the dehydration of ethanol to ethene and diethyl ether. This is followed by a yellow region which gradually turns into a greyish zone. As the site time increases and C_{3+} production increases, the white zone diminishes in favour of the grey zone. As we increase temperature (Figure 3-9 v) and vi)), the white zone completely disappears and the entire bed becomes grey since the C_2 conversion was also above 0.8. Regarding the interpretation of the colour formation, it is important to mention that the colour change is fast, that the colour change did not disappear when the ethanol flow is stopped and that the C_2 and ethanol conversion remained constant. A UV/VIS probe was used to scan the catalyst bed after the reaction. The catalyst bed was allowed to cool down during 1 h under nitrogen atmosphere.

The nature of the surface species was investigated using UV-VIS spectroscopy of the used catalyst in the continuous flow experiments. This catalyst bed clearly shows three distinct regions along the reactor axis (x) as illustrated in Figure 3-10. The different colors in the catalyst bed have also been observed for MTO catalysts such as SAPO-34 and are associated with different types of aromatic compounds [51, 52]. The first zone of the catalyst bed (x = 0 − 2 cm) shows no absorbance at the investigated wavelengths. It can be associated with ethanol dehydration and shows that no aromatic species are retained in the catalyst at this stage and is accompanied by a

steep increase in ethene yield. At reactor lengths above 2 cm, absorption starts at wavelengths below 400 nm, reported to be characteristic of monoalkylaromatics [53]. These species correspond to the long-lived surface species, C_{aro}*. A redshift from 400 nm towards 420 nm is observed when continuing along the reactor coordinate and is associated with the formation of diaromatics. This redshift is simultaneously occurring with an increased absorbance at 470 nm which is related to diaromatics, anthracenic and phenantrenic species. At the end of this zone, ethene is the major observed gas phase product. In the grey zone of the catalyst bed which shows a reduction in ethene yield due to consecutive conversion to higher hydrocarbons (x > 6 cm), an increased absorbance around 600 nm can be seen, which can be attributed to anthracenic, phenantrenic and tetracenic species. These species can finally lead to the formation of polynuclear aromatics on the external surface which is situated around 700 nm. The aromatic species can reside inside the catalyst pores for prolonged times due to confinement effects.

x (cm)
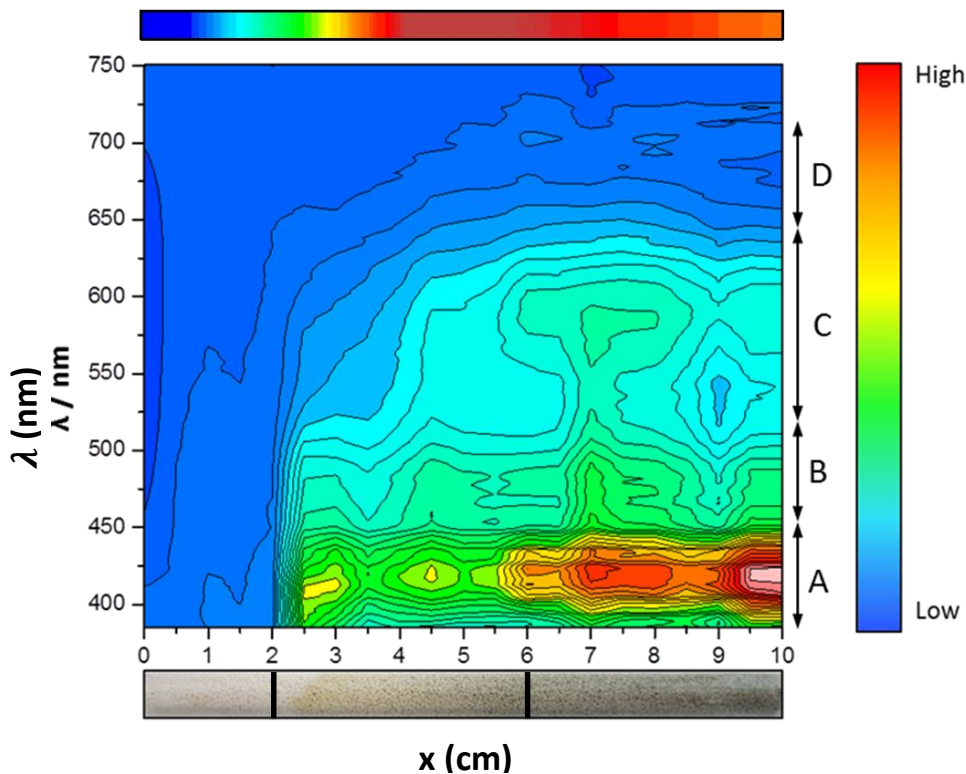
Figure 3-10: UV-VIS signal as function of wavelength λ (y-axis) and axial reactor coordinate x (x-axis) during continuous feeding of ethanol. Scale right: color scale ranging low amount (blue) to high amount (red). Top scale: ethene yield. Bottom picture: catalyst bed with three different zones, i.e., between x = 0 -2, x = 2 − 6 and x = 6 - 10 cm. Wavelength ranges are labelled according to Hemelsoet et al. [53] and Mores et al. [54] with A) monoalkylaromatics & diaromatics B) diaromatics, antracenic and phenantracenic structures C) antracenic, phenantracenic and tetracenic structures, D) polynuculear aromatics (number of aromatics ring > 4) (conditions: TOS =4 h, T = 573 K, W C_t $F^{-1}_{EtOH,0}$ = 4 mol$_{H+}$ s mol^{-1}, p$_{EtOH,0}$ =30 kPa).

3.4 Discussion

Based on the experimental observations presented above, the following reaction mechanism can be proposed for the conversion of ethanol to hydrocarbons and is given in Figure 3-11.
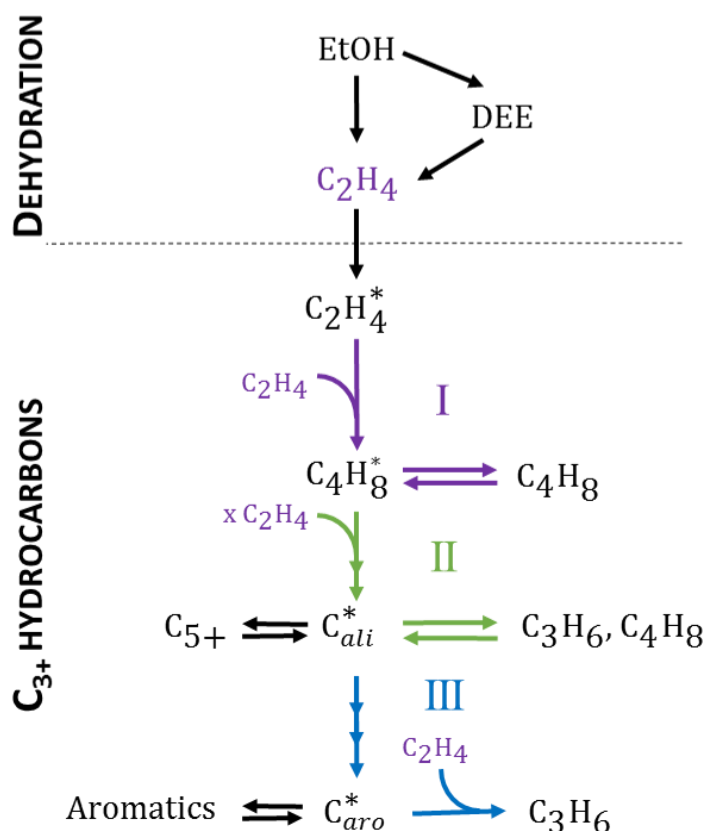
Figure 3-11: Reaction mechanism for the conversion of ethanol to hydrocarbons with: EtOH: ethanol, DEE: diethyl ether, C_2H_4: ethene, C_3H_6: propene, C_4H_8: butene, C_{5+}: olefinic hydrocarbons containing more than 5 carbon atoms, aromatics: hydrocarbons containing one or more aromatic rings, $C_2H_4^*$: ethene surface species; $C_4H_8^*$: butene surface species; C_{ali}^*: aliphatic surface species, C_{aro}^*: aromatic surface species. Route I (violet): the dimerization of ethene to butene, Route II (green): formation of propene and butene via aliphatic surface intermediates, Route III (blue): formation of propene via aromatic surface intermediates.

This mechanism consists of two consecutive stages. The first stage involves fast dehydration of ethanol to ethene which can take place either via a monomolecular or bimolecular pathway with diethyl ether as intermediate product. In the second stage, three routes for the production of light olefins can be distinguished which are mediated by different types of surface intermediates: butene formation via alkylation of adsorbed ethene ($C_2H_4^*$) with gas phase ethene (Route I), propene and butene formation via different types of surface species. These surface species can either desorb or be involved in consecutive reactions and are typically called the *hydrocarbon*

pool in the methanol-to-olefins process. It was found that the surface species do not only consist of aromatics, i.e., C^*_{aro}, which allow enhanced production of light olefins (route III) via paring and side-chain reaction mechanisms but also of shorter lived aliphatic species, i.e., C^*_{ali}, which can undergo classical acid catalyzed reaction steps such as β-scission, isomerization and alkylation (Route II).

The induction period observed in the continuous flow experiments and the observation of all olefinic products from the first pulse onwards indicate that the rate of the dimerization of ethene is much slower than the formation of C_{3+} via alkylation and β-scission. This is supported by quantum chemical calculations comparing the dimerization to ethene and several other reactions involving ethene which are shown in Figure 3-12.
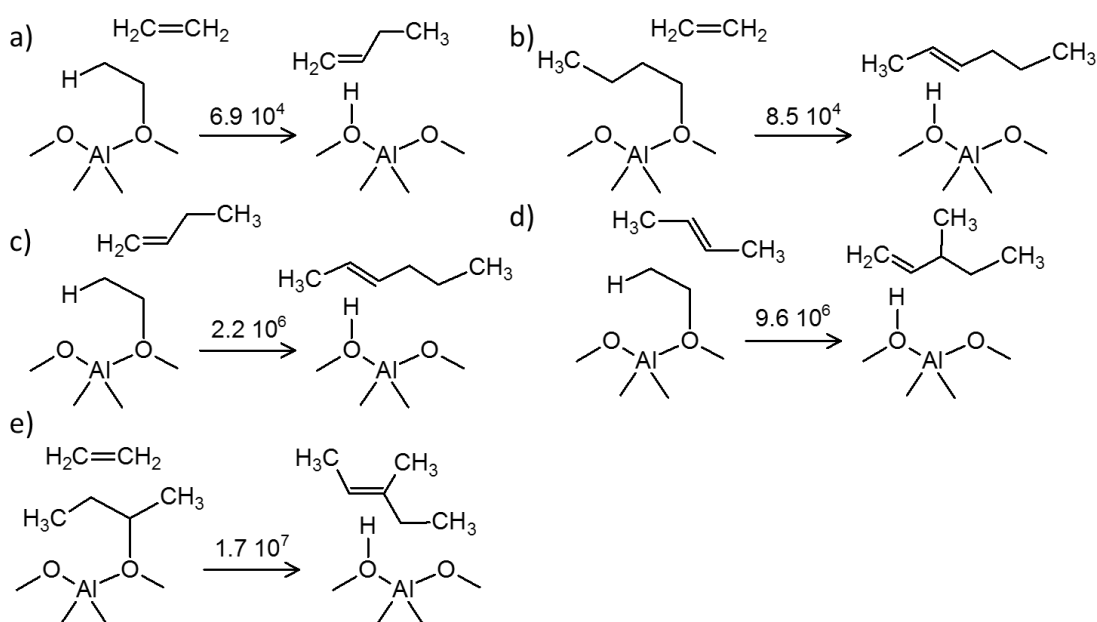
Figure 3-12: Selection of oligomerization reactions involved in Route II of Figure 3-11: a) reaction of ethoxy species with gas phase ethene, b) reaction of primary butoxy species with gas phase ethene, c) reaction of ethoxy species with gas phase 1-butene, d) reaction of ethoxy species with gas phase 2-butene, e) reaction of secondary butoxy species with gas phase ethene. The corresponding rate coefficients (s^{-1}) at 573 K are shown above the reaction arrows.

Besides the dimerization of ethene, the oligomerization of ethene with different surface intermediates, i.e., ethoxy, primary and secondary butoxy species is considered. Also the reaction of an ethoxy species and gas phase 1- or 2-butene was considered. The reaction of ethene with an ethoxy species (reaction a) and the reaction of ethene with a primary butoxy species (reaction

b) have similar rate coefficients as indicated above the reaction arrows. This illustrates that reactions involving primary carbenium ions and gas phase ethene have quite similar rate coefficients and are not effected by chain length effects of the surface species.

When sufficient ethene has dimerized to butenes, reactions of surface ethoxy species with gas phase 1- or 2-butene can also occur (reaction c and d). The rate coefficients are around 100 times higher than the reactions involving gas phase ethene and primary surface species. Reaction of a secondary butoxy species with gas phase ethene (reaction e) is also 100 times faster than the reaction of gas phase ethene with a primary butoxy species but has a similar rate coefficient as the reaction of 2-butene with surface ethoxy species. This nicely illustrate that the dimerization of ethene to 1-butene can easily be bypassed once sufficient surface species other than the primary $C_2H_4^*$ are formed.

A competition exists between the routes mediated by these two types of intermediates to propene and/or butenes. The predominant route depends on the reaction conditions, i.e., temperature and pressure. The evolution of the total 12C content in gas phase propene and butene after the 13C/12C ethene feed switch is shown in Figure 3-13.
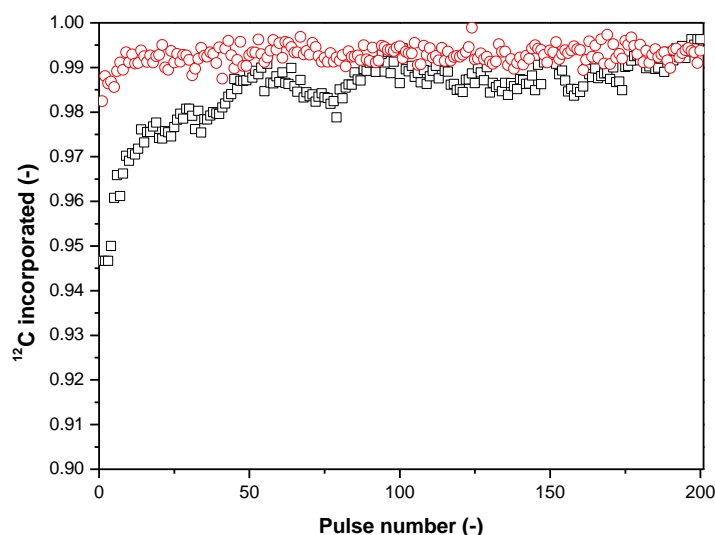
Figure 3-13: Evolution of the ^{12}C content in propene (□, black) and butene (○, red) as function of pulse number after switch from ^{13}C labelled ethene feed to ^{12}C labelled ethene. (n_{ethene} = 10^{17} molecules/pulse; m_{cat} = 27 mg, T= 648 K)

Strikingly, butene shows no ^{13}C incorporation while for propene the ^{13}C uptake amounts to some 5% and gradually disappears after 50 pulses when complete isotope exchange is approached. These observations suggest that, under the investigated reaction conditions, butene formation does not proceed via a route involving long-lived aromatic surface intermediates (C_{aro}^*) but instead mainly occurs through dimerization of ethene and further transformation of adsorbed butene ($C_4H_8^*$) involving fast produced short-lived aliphatic surface intermediates (C_{ali}^*). Shape selective effects and steric constraints are apparently prohibiting the formation of specific aromatic intermediates required for the formation of butene via Route III. From the pulse evolution of the ^{12}C incorporation in propene, it can be concluded that, in contrast to butene formation, propene formation partly occurs via a mechanism that involves long-lived aromatic surface species. The exact role of the aromatic species is still not fully elucidated. As could be seen from the UV-VIS measurements, the amount increases with conversion however, no distinct changes in activity or selectivity are observed. It is possible that only a few select aromatic hydrocarbon pool species are active in the aromatic-assisted route and that the rest can be considered as spectator molecules.

3.5 Conclusions

A systematic investigation of the conversion of ethanol to hydrocarbons on H-ZSM-5 is presented in this chapter. It was found that ethanol dehydration to ethene is mechanistically decoupled from the production of higher hydrocarbons due to complete surface coverage by adsorbed ethanol and diethyl ether. This fully covered surface prevents C_{3+} hydrocarbon formation before ethanol conversion is complete.

The unique combination of comparing continuous flow and transient experiments allow to gain detailed insight in the reaction mechanism of ethanol and ethene conversion. Evidence for an autocatalytic mechanism is given via the identification of an induction period in both ethanol and ethene conversion. Three routes for the production of hydrocarbons from ethene are identified: the dimerization of ethene to butene and two routes involving two different types of surface

species labeled as aliphatic and aromatic surface species. It was confirmed via quantum chemical calculations that the dimerization is much slower compared to other oligomerization reaction.

Isotopic labelling during the transient experiments showed that around 5 % of the propene is formed via long-lived surface species, i.e. aromatic species. The majority of the propene thus finds its origin in the route via short-lived intermediates, i.e., aliphatic surface species.

3.6 References

[1] H. Xin, X. Li, Y. Fang, X. Yi, W. Hu, Y. Chu, F. Zhang, A. Zheng, H. Zhang, X. Li, Catalytic dehydration of ethanol over post-treated ZSM-5 zeolites, Journal of Catalysis, 312 (2014) 204-215.

[2] Z.X. Song, A. Takahashi, I. Nakamura, T. Fujitani, Phosphorus-modified ZSM-5 for conversion of ethanol to propylene, Applied Catalysis A: General, 384 (2010) 201-205.

[3] K. Van der Borght, V.V. Galvita, G.B. Marin, Ethanol to higher hydrocarbons over Ni, Ga, Fe-modified ZSM-5: Effect of metal content, Applied Catalysis A: General, 492 (2015) 117-126.

[4] N.R.C.F. Machado, V. Calsavara, N.G.C. Astrath, C.K. Matsuda, A. Paesano Junior, M.L. Baesso, Obtaining hydrocarbons from ethanol over iron-modified ZSM-5 zeolites, Fuel, 84 (2005) 2064-2070.

[5] F.F. Madeira, N.S. Gnep, P. Magnoux, H. Vezin, S. Maury, N. Cadran, Mechanistic insights on the ethanol transformation into hydrocarbons over HZSM-5 zeolite, Chemical Engineering Journal, 161 (2010) 403-408.

[6] A.T. Aguayo, A.G. Gayubo, A. Atutxa, M. Olazar, J. Bilbao, Catalyst deactivation by coke in the transformation of aqueous ethanol into hydrocarbons. Kinetic modeling and acidity deterioration of the catalyst, Industrial & Engineering Chemistry Research, 41 (2002) 4216-4224.

[7] A.T. Aguayo, A.G. Gayubo, A.M. Tarrio, A. Atutxa, J. Bilbao, Study of operating variables in the transformation of aqueous ethanol into hydrocarbons on an HZSM-5 zeolite, Journal of Chemical Technology and Biotechnology, 77 (2002) 211-216.

[8] N. Viswanadham, S.K. Saxena, J. Kumar, P. Sreenivasulu, D. Nandan, Catalytic performance of nano crystalline H-ZSM-5 in ethanol to gasoline (ETG) reaction, Fuel, 95 (2012) 298-304.

[9] A.G. Gayubo, A. Alonso, B. Valle, A.T. Aguayo, J. Bilbao, Deactivation kinetics of a HZSM‐5 zeolite catalyst treated with alkali for the transformation of bio‐ethanol into hydrocarbons, AIChE Journal, 58 (2012) 526-537.

[10] Y. Furumoto, Y. Harada, N. Tsunoji, A. Takahashi, T. Fujitani, Y. Ide, M. Sadakane, T. Sano, Effect of acidity of ZSM-5 zeolite on conversion of ethanol to propylene, Applied Catalysis A: General, 399 (2011) 262-267.

[11] A.G. Gayubo, A. Alonso, B. Valle, A.T. Aguayo, J. Bilbao, Selective production of olefins from bioethanol on HZSM-5 zeolite catalysts treated with NaOH, Applied Catalysis B: Environmental, 97 (2010) 299-306.

[12] Z. Song, A. Takahashi, I. Nakamura, T. Fujitani, Phosphorus-modified ZSM-5 for conversion of ethanol to propylene, Applied Catalysis A: General, 384 (2010) 201-205.

[13] A.G. Gayubo, A.M. Tarrío, A.T. Aguayo, M. Olazar, J. Bilbao, Kinetic Modelling of the Transformation of Aqueous Ethanol into Hydrocarbons on a HZSM-5 Zeolite, Industrial & Engineering Chemistry Research, 40 (2001) 3467-3474.

[14] F.F. Madeira, K.B. Tayeb, L. Pinard, H. Vezin, S. Maury, N. Cadran, Ethanol transformation into hydrocarbons on ZSM-5 zeolites: Influence of Si/Al ratio on catalytic performances and deactivation rate. Study of the radical species role, Applied Catalysis A: General, 443 (2012) 171-180.

[15] F.F. Madeira, H. Vezin, N. Gnep, P. Magnoux, S. Maury, N. Cadran, Radical Species Detection and Their Nature Evolution with Catalyst Deactivation in the Ethanol-to-Hydrocarbon Reaction over HZSM-5 Zeolite, ACS Catalysis, 1 (2011) 417-424.

[16] J. Schulz, F. Bandermann, Conversion of ethanol over zeolite H‐ZSM‐5, Chemical engineering & technology, 17 (1994) 179-186.

[17] R. Johansson, S.L. Hruby, J. Rass-Hansen, C.H. Christensen, The Hydrocarbon Pool in Ethanol-to-Gasoline over HZSM-5 Catalysts, Catalysis Letters, 127 (2009) 1-6.

[18] U. Olsbye, S. Svelle, M. Bjorgen, P. Beato, T.V.W. Janssens, F. Joensen, S. Bordiga, K.P. Lillerud, Conversion of Methanol to Hydrocarbons: How Zeolite Cavity and Pore Size Controls Product Selectivity, Angewandte Chemie-International Edition, 51 (2012) 5810-5831.

[19] R.M. Dessau, On the H-Zsm-5 Catalyzed Formation of Ethylene from Methanol or Higher Olefins, Journal of Catalysis, 99 (1986) 111-116.

[20] I.M. Dahl, S. Kolboe, On the Reaction Mechanism for Hydrocarbon Formation from Methanol over SAPO-34: I. Isotopic Labeling Studies of the Co-Reaction of Ethene and Methanol, Journal of Catalysis, 149 (1994) 458-464.

[21] M. Bjørgen, S. Svelle, F. Joensen, J. Nerlov, S. Kolboe, F. Bonino, L. Palumbo, S. Bordiga, U. Olsbye, Conversion of methanol to hydrocarbons over zeolite H-ZSM-5: On the origin of the olefinic species, Journal of Catalysis, 249 (2007) 195-207.

[22] D. Lesthaeghe, V. Van Speybroeck, G.B. Marin, M. Waroquier, Understanding the failure of direct C-C coupling in the zeolite-catalyzed methanol-to-olefin process, Angewandte Chemie-International Edition, 45 (2006) 1714-1719.

[23] D. Lesthaeghe, B. De Sterck, V. Van Speybroeck, G.B. Marin, M. Waroquier, Zeolite shape-selectivity in the gem-methylation of aromatic hydrocarbons, Angewandte Chemie-International Edition, 46 (2007) 1311-1314.

[24] C.-M. Wang, Y.-D. Wang, Y.-J. Du, G. Yang, Z.-K. Xie, Computational insights into the reaction mechanism of methanol-to-olefins conversion in H-ZSM-5: nature of hydrocarbon pool, Catalysis Science & Technology, (2016).

[25] X. Sun, S. Mueller, Y. Liu, H. Shi, G.L. Haller, M. Sanchez-Sanchez, A.C. van Veen, J.A. Lercher, On reaction pathways in the conversion of methanol to hydrocarbons on HZSM-5, Journal of Catalysis, 317 (2014) 185-197.

[26] J.T. Gleaves, G. Yablonsky, X. Zheng, R. Fushimi, P.L. Mills, Temporal analysis of products (TAP)—Recent advances in technology for kinetic analysis of multi-component catalysts, Journal of Molecular Catalysis A: Chemical, 315 (2010) 108-134.

[27] International Zeolite Association: Structural Databases, (http://www.iza-structure.org/databases), accessed on July 7 2015

[28] M. Brandle, J. Sauer, Acidity differences between inorganic solids induced by their framework structure. A combined quantum mechanics molecular mechanics ab initio study on zeolites, Journal of the American Chemical Society, 120 (1998) 1556-1570.

[29] C.M. Nguyen, M.F. Reyniers, G.B. Marin, Theoretical study of the adsorption of C1-C4 primary alcohols in H-ZSM-5, Physical Chemistry Chemical Physics, 12 (2010) 9481-9493.

[30] G. Kresse, J. Hafner, Ab-Initio Molecular-Dynamics for Open-Shell Transition-Metals, Physical Review B, 48 (1993) 13115-13118.

[31] G. Kresse, J. Hafner, Ab-Initio Molecular-Dynamics Simulation of the Liquid-Metal Amorphous-Semiconductor Transition in Germanium, Physical Review B, 49 (1994) 14251-14269.

[32] G. Kresse, J. Furthmuller, Efficiency of ab-initio total energy calculations for metals and semiconductors using a plane-wave basis set, Computational Materials Science, 6 (1996) 15-50.

[33] G. Kresse, J. Furthmuller, Efficient iterative schemes for ab initio total-energy calculations using a plane-wave basis set, Physical Review B, 54 (1996) 11169-11186.

[34] P.E. Blochl, Projector Augmented-Wave Method, Physical Review B, 50 (1994) 17953-17979.

[35] G. Kresse, D. Joubert, From ultrasoft pseudopotentials to the projector augmented-wave method, Physical Review B, 59 (1999) 1758-1775.

[36] J.P. Perdew, K. Burke, M. Ernzerhof, Generalized gradient approximation made simple, Physical Review Letters, 77 (1996) 3865-3868.

[37] S. Grimme, Semiempirical GGA-type density functional constructed with a long-range dispersion correction, Journal of Computational Chemistry, 27 (2006) 1787-1799.

[38] T. Kerber, M. Sierka, J. Sauer, Application of semiempirical long-range dispersion corrections to periodic systems in density functional theory, Journal of Computational Chemistry, 29 (2008) 2088-2097.

[39] R.F.W. Bader, Atoms in Molecules - A Quantum Theory, Oxford University Press 1990.

[40] G. Henkelman, A. Arnaldsson, H. Jonsson, A fast and robust algorithm for Bader decomposition of charge density, Computational Materials Science, 36 (2006) 354-360.

[41] G. Henkelman, H. Jonsson, A dimer method for finding saddle points on high dimensional potential surfaces using only first derivatives, Journal of Chemical Physics, 111 (1999) 7010-7022.

[42] B.A. De Moor, A. Ghysels, M.F. Reyniers, V. Van Speybroeck, M. Waroquier, G.B. Marin, Normal Mode Analysis in Zeolites: Toward an Efficient Calculation of Adsorption Entropies, Journal of Chemical Theory and Computation, 7 (2011) 1090-1101.

[43] B.A. De Moor, M.F. Reyniers, G.B. Marin, Physisorption and chemisorption of alkanes and alkenes in H-FAU: a combined ab initio-statistical thermodynamics study, Physical Chemistry Chemical Physics, 11 (2009) 2939-2958.

[44] C.J. Cramer, Essentials of Computational Chemistry: Theories and Models, 2nd ed, Wiley, 2005.

[45] M.-F. Reyniers, G.B. Marin, Experimental and Theoretical Methods in Kinetic Studies of Heterogeneously Catalyzed Reactions, Annual Review of Chemical and Biomolecular Engineering, 5 (2014) 563-594.

[46] A.G. Gayubo, A. Alonso, B. Valle, A.s.T. Aguayo, J. Bilbao, Kinetic Model for the Transformation of Bioethanol into Olefins over a HZSM-5 Zeolite Treated with Alkali, Industrial & Engineering Chemistry Research, 49 (2010) 10836–10844.

[47] T.V.W. Janssens, S. Svelle, U. Olsbye, Kinetic modeling of deactivation profiles in the methanol-to-hydrocarbons (MTH) reaction: A combined autocatalytic–hydrocarbon pool approach, Journal of Catalysis, 308 (2013) 122-130.

[48] N.Y. Chen, W.J. Reagan, Evidence of autocatalysis in methanol to hydrocarbon reactions over zeolite catalysts, Journal of Catalysis, 59 (1979) 123-129.

[49] N.A. Bhore, M.T. Klein, K.B. Bischoff, Species rank in reaction pathways: Application of Delplot analysis, Chemical Engineering Science, 45 (1990) 2109-2116.

[50] Q. Qian, J. Ruiz-Martínez, M. Mokhtar, A.M. Asiri, S.A. Al-Thabaiti, S.N. Basahel, H.E. van der Bij, J. Kornatowski, B.M. Weckhuysen, Single-Particle Spectroscopy on Large SAPO-34 Crystals at Work: Methanol-to-Olefin versus Ethanol-to-Olefin Processes, Chemistry – A European Journal, 19 (2013) 11204-11215.

[51] D. Mores, E. Stavitski, M.H.F. Kox, J. Kornatowski, U. Olsbye, B.M. Weckhuysen, Space- and Time-Resolved In-situ Spectroscopy on the Coke Formation in Molecular Sieves: Methanol-to-Olefin Conversion over H-ZSM-5 and H-SAPO-34, Chemistry – A European Journal, 14 (2008) 11320-11327.

[52] D.S. Wragg, M.G. O'Brien, F.L. Bleken, M. Di Michiel, U. Olsbye, H. Fjellvåg, Watching the Methanol-to-Olefin Process with Time- and Space-Resolved High-Energy Operando X-ray Diffraction, Angewandte Chemie-International Edition, 51 (2012) 7956-7959.

[53] K. Hemelsoet, Q. Qian, T. De Meyer, K. De Wispelaere, B. De Sterck , B.M. Weckhuysen, M. Waroquier, V. Van Speybroeck, Identification of Intermediates in Zeolite-Catalyzed Reactions by In Situ UV/Vis Microspectroscopy and a Complementary Set of Molecular Simulations, Chemistry – A European Journal, 19 (2013) 16595-16606.

[54] D. Mores, J. Kornatowski, U. Olsbye, B.M. Weckhuysen, Coke Formation during the Methanol-to-Olefin Conversion: In Situ Microspectroscopy on Individual H-ZSM-5 Crystals with Different Bronsted Acidity, Chemistry-a European Journal, 17 (2011) 2874-2884.

Chapter 4

Ethanol dehydration on H-ZSM-5 and other industrially relevant zeolites: effect on activity and selectivity

The consecutive nature of the dehydration of ethanol and the production of C_{3+} hydrocarbons was observed in Chapter 3. Therefore, it is opted for in the present chapter to investigate the dehydration at lower temperature in order to eliminate side reactions, such as the formation of aromatics and other olefins, as much as possible. The influence of key operating parameters such as temperature, conversion and water content on the product selectivity will be discussed in this chapter. The experimental results will be compared to the results of microkinetic simulations based on periodic density functional theory calculations. The activity and selectivity on several industrially relevant zeolites will be assessed and correlated to an experimentally determined catalyst characteristic, i.e., the NH_3 desorption energy.

4.1 Introduction

Ethanol dehydration has been studied over a variety of heterogeneous catalysts including alumina, transition state metal oxides, heteropolyacids and zeolites [1-6]. The ones most selective towards ethene are alumina, silica-alumina and zeolites. Alumina and silica-alumina require higher reaction temperatures (T > 600 K) to have sufficient activity. Zeolites on the other hand are already active below 473 K but suffer from secondary reactions which form long chain hydrocarbons that can cause deactivation by coke formation. In addition to the renewable character of the ethanol dehydration process, it can also serve as a kinetic characterization reaction, which allows to assess the effect of zeolite topology and acidity. Ethanol dehydration is proposed to proceed via two competitive reaction paths at low temperature [7]. This includes the monomolecular dehydration of ethanol to ethene and water and the bimolecular dehydration of ethanol to water and diethyl ether which is the major by-product at low temperatures. A consecutive path in which diethyl ether is further converted to ethene and ethanol is also observed [8]. Therefore, a parallel-consecutive scheme is typically presented for ethanol dehydration as shown in Figure 4-1.
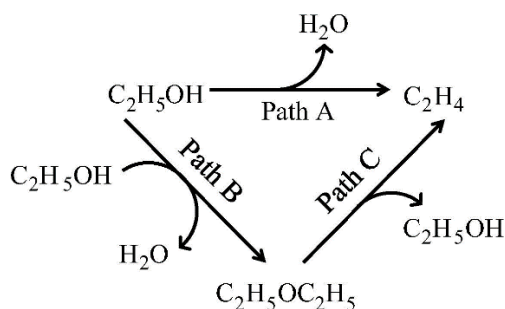
Figure 4-1: Parallel-consecutive reaction scheme for ethanol dehydration. Path A: direct ethanol dehydration to ethene, Path B: ethanol dehydration to diethyl ether, Path C: decomposition of diethyl ether to ethene and ethanol [9].

This study will focus on five industrially relevant zeolites: FAU, MFI, FER, BEA and MOR [10] which are shown in Table 4-1. H-ZSM-5 is the most intensively studied zeolite although most research focused on catalyst modification [11-13]. H-ZSM-5 is the aluminosilicate form of MFI and is composed of pentasil units. It consists of elliptical straight channels and near circular sinusoidal channels that intersect perpendicularly [14]. The framework of faujasite type zeolites (FAU) is built by lining sodalite cages through double six-membered rings. This creates a large cavity in
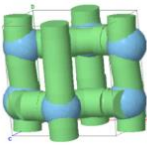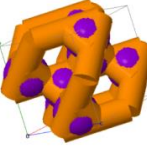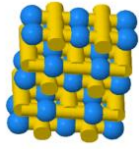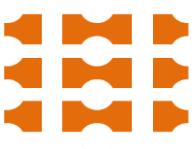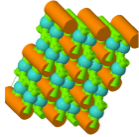
faujasites typically referred to as a supercage. Zeolite beta (BEA) consists of an intergrowth of three distinct structures termed Polymorphs A, B and C. The polymorphs grow as two-dimensional sheets and alternate randomly. The polymorphs have a three dimensional network of 12-ring pores. The intergrowth of the polymorphs does not significantly affect the pores in two of the dimensions, but in the direction of the faulting, the pore becomes tortuous, but not blocked. Ferrierite (FER) is a two-dimensional zeolite with 8- and 10- membered ring pores that cross perpendicularly. Mordenite (MOR) is a one-dimensional zeolite defined by a 12 membered ring pore system with side pockets constituted of 8 membered rings.

Only few comparative studies of different zeolites in ethanol dehydration have been performed. Chiang and Bhan found that ethene formation only occurs on H-MOR because the small 8-membered ring side pockets protect ethanol monomers from forming bulky ethanol dimers [7]. Phung et al. reported the highest activity for H-MOR but observed a higher turnover frequency for H-MFI [4].

In this chapter, the effect of key operating conditions such as conversion, temperature and water content will be investigated for ethanol dehydration on H-ZSM-5. The experimental results will be compared to the results of microkinetic simulations of which the parameters were obtained from quantum chemical calculations. An assessment of different types of zeolites will be performed in terms of activity and selectivity. A structure-activity relationship between the catalyst performance results and an experimentally measurable catalyst characteristic, i.e., the NH_3 desorption energy as determined by NH_3-TPD, will also be presented.

Table 4-1: Zeolites studied in this work

	Structure	Representation	Industrial applications [15]
MFI			Catalytic cracking, oligomerization, aromatization
FAU			Catalytic cracking, hydrocracking
BEA			Alkylation
FER			Isomerization
MOR			Alkylation, hydroisomerization

4.2 Procedures

The zeolites used in this work (Zeolyst) are summarized in Table 4-3. Prior to the catalytic performance testing, the zeolites were calcined at 823 K using a heating ramp of 1 K min^{-1} and maintaining this maximum temperature for 3 hours. N_2 adsorption at 77 K was performed to determine the BET surface area and pore volume using a Micromeritics Tristar II. Acidity measurements were performed by temperature programmed desorption with ammonia (NH_3-TPD) in a Micromeritics AutoChem 2920. First, a pretreatment step was executed to remove adsorbed water and CO_2 from the catalyst by heating the catalyst in helium with a temperature ramp of 10 K min^{-1} to 823 K. The temperature was lowered to 373 K while being in helium atmosphere. Adsorption of NH_3 was then performed by flowing a NH_3/He mixture (Air Liquide, 3.996 v% NH_3) during 2 h over the catalyst. The catalyst was subsequently purged with helium to remove all non-adsorbed ammonia

until a stable baseline was obtained, which was followed by heating to 950 K with variable heating rates. The NH_3-TPD spectrum was deconvoluted into the number of observable peaks. The total concentration of acid sites, i.e., C_t, is directly proportional to the area under the deconvoluted peak in the range of 573 - 773 K under the assumption that one NH_3 molecule reacts with one H^+ at the zeolite surface. The thermal conductivity detector (TCD) was calibrated with known volumes of NH_3. A similar procedure has been reported in literature [16, 17]. Based on replicate experiments, the error on the total concentration of accessible acid sites was calculated to be 9%. The NH_3 desorption energy, E_d, can be derived from the NH_3-TPD profiles with different heating ramps and the maximum desorption temperature, i.e., T_M, via [18]:

$$2 \ln T_M - \ln \beta = \ln \frac{E_d}{R A_d} + \frac{E_d}{R} \frac{1}{T_M} \tag{4-1}$$

The range of operating conditions at which the mechanistic investigation on H-ZSM-5 is performed can be found in Table 4-2.

Table 4-2: Operating conditions used for the mechanistic investigation on H-ZSM-5

Operating condition	Value
T (K)	453 – 523
$p_{EtOH,0}$ (kPa)	10 - 60
$W\,F_{EtOH,0}^{-1}$ (kg s^{-1} mol^{-1})	2 - 29

A description of the experimental set-ups can be found in Chapter 2, while the details related to the microkinetic model can be found in Chapter 3.

Table 4-3: Properties of zeolites used in this work with A_{BET} the BET surface area, A_{ext} the external crystallite surface as determined by t-plot method, V_{tot} is the total pore volume, V_{pore} is the micropore volume, V_{meso} is the mesopore volume and C_t is the concentration of acid sites. Error indicates the 0.95 confidence interval.

Catalyst	Code[a]	Si/Al	Topology	A_{BET} [10^{-3} m^2 kg^{-1}]	A_{ext} [10^{-3} m^2 kg^{-1}]	V_{tot} [10^{-5} m^3 kg^{-1}]	V_{pore} [10^{-5} m^3 kg^{-1}]	V_{meso} [10^{-5} m^3 kg^{-1}]	C_t [10^{-2} mol kg^{-1}]
H-Y(3)	CBV500	3	FAU	640 ± 13	70 ± 2	35 ± 2	27 ± 1	9 ± 1	122 ± 11
H-Y(15)	CBV720	15	FAU	723 ± 12	199 ± 4	51 ± 3	24 ± 1	27 ± 1	52 ± 6
H-Y(30)	CBV760	30	FAU	740 ± 15	226 ± 4	53 ± 3	24 ± 1	29 ± 1	30 ± 4
H-MOR	CBV21A	10	MOR	458 ± 9	50 ± 2	26 ± 1	19 ± 1	7 ± 1	99 ± 9
H-BEA	CP814E	13	BEA	446 ± 10	193 ± 4	75 ± 4	12 ± 1	63 ± 3	125 ± 10
H-FER	CP914C	10	FER	323 ± 7	41 ± 2	22 ± 1	13 ± 1	9 ± 1	95 ± 9
H-ZSM-5(15)	CBV3024	15	MFI	369 ± 9	123 ± 3	27 ± 1	11 ± 1	16 ± 1	75 ± 7
H-ZSM-5(40)	CBV8014	40	MFI	370 ± 8	111 ± 2	20 ± 1	12 ± 1	8 ± 1	42 ± 5

[a] Zeolyst [19]

4.3 Characterization results

4.3.1 Textural properties

The N_2 adsorption isotherms for all zeolites investigated in this chapter are shown in Figure 4-2 and the corresponding surface area and pore volumes are given in Table 4-3. No significant difference in BET surface area is observed between the H-ZSM-5 zeolites with different Si/Al ratios. All FAU zeolites, i.e., H-Y(3), H-Y(15) and H-Y(30), have been subjected to a steaming procedure which results in the formation of mesopores. H-Y(15) and H-Y(30) are derived from H-Y(3) via a second dealumination procedure: the mesopore volumes triples compared to the parent zeolite, i.e., H-Y(3). The generation of mesopores is also reflected in a larger crystallite external surface area, associated with the presence of these mesopores. A small increase in BET surface area can be observed for the dealuminated samples. A remarkably high mesopore volume and external surface area is observed for H-BEA. The textural properties of H-FER and H-MOR are quite similar to the H-ZSM-5 samples.
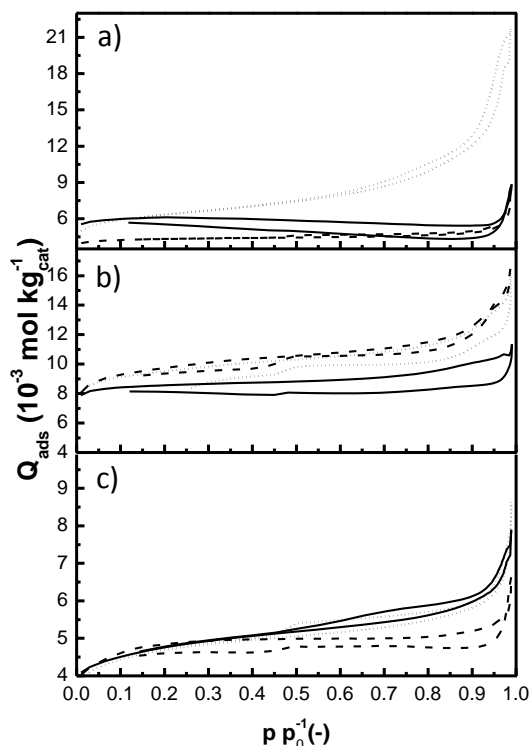
Figure 4-2: N_2 adsorption isotherms for a) H-MOR (full line), H-BEA (dotted line) and H-FER (dashed line), b) H-Y(3) (full line), H-Y(15) (dotted) and H-Y(30) (dashed line) and c) H-ZSM-5 (15) (full line), H-ZSM-5(25) (dotted line) and H-ZSM-5(40) (dashed line)

4.3.2 Acid properties

In general, two peaks are observed in the NH_3-TPD profile as can be seen from Figure 4-3: the *h*-peak (T_M = 573 - 873 K) which is attributed to decomposition of NH_4^+ formed on Bronsted sites while the *l*-peak (T_M = 373 - 473 K) is attributed to weakly adsorbed ammonia on NH_4^+ cations or on silanol groups. NH_3-TPD has been shown to be an adequate technique to describe the acid properties of zeolites [20]. The temperature of NH_3 desorption has been limited to 950 K since at higher temperatures, dehydroxylation has been observed [21], which will result in loss of acid sites and in the most severe conditions to destruction of the zeolite frame work. Quite distinct *l*- and *h*-peaks are observed for all investigated zeolites except for H-BEA where there is an extensive overlap between both peaks.
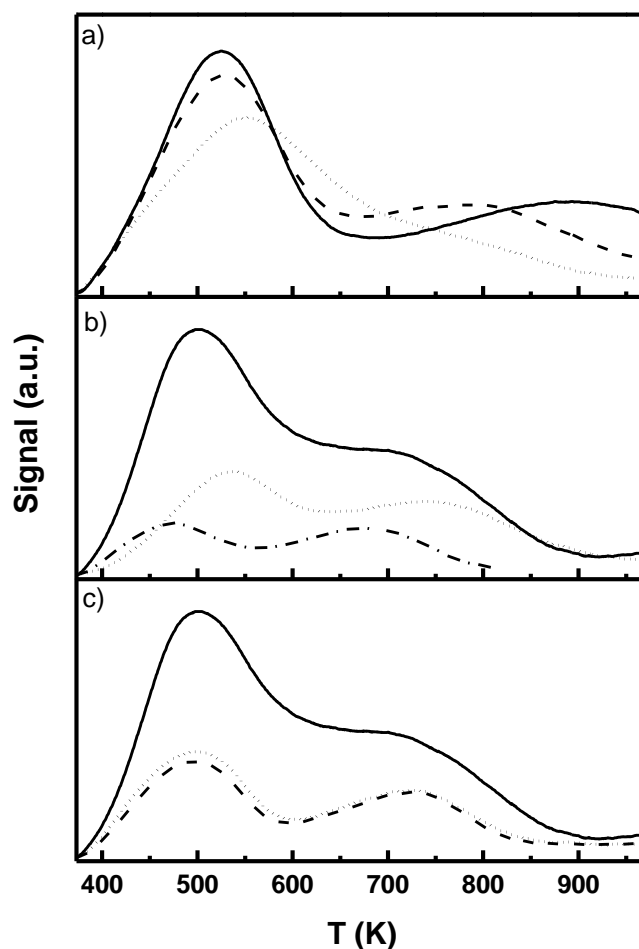
Figure 4-3: NH_3-TPD profiles of a) H-MOR (full line), H-BEA (dotted line) and H-FER (dashed line), b) H-Y(3) (full line), H-Y(15) (dotted) and H-Y(30) (dashed line) and c) H-ZSM-5 (15) (full line), H-ZSM-5 (25) (dotted line) and H-ZSM-5 (40) (dashed line). (β = 10 K min^{-1}).

Via the deconvolution procedure explained in section 4.2, the concentration of acid sites, i.e., C_t, can be determined for each catalyst (see Table 4-3). As correct determination of the concentration is crucial for correct interpretation of the catalytic results, a comparison with literature data has been made in Figure 4-4. Good agreement is found between literature values for the concentration of acid sites [16, 22-24], the theoretical concentration of acid sites determined from the Si/Al ratio and the values for the concentration of acid sites determined in this work which can be found in Table 4-2.
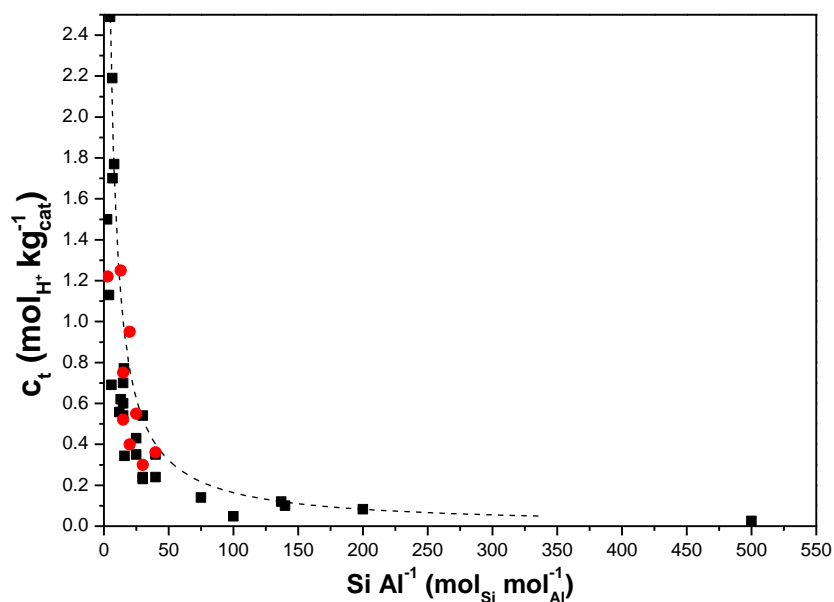
Figure 4-4: Concentration of acid sites as function of Si/Al ratio: concentration of acid sites for various zeolites reported in literature [16, 22-24] (■, black), concentration of acid sites determined for the zeolites studied in this work and given in Table 4-3 (●, red) and theoretical concentration of acid sites as determined from the Si/Al ratio of a zeolite determined via the Si/Al ratio (dashed line).

The acidity of a zeolite is characterized by the concentration of acid sites on the one hand and the strength of the acid sites on the other hand. The concentration of acid sites, i.e., C_t, will be taken into account by working with site time rather than space time and thus offers a correction for the amount of acid sites present in each zeolite. Accounting for the acid strength of the zeolite is much more complicated as a zeolite is characterized by an acid strength distribution [20]. Therefore, a catalyst property, the NH_3 desorption energy, i.e., $E_{d,NH3}$, which can be determined experimentally by NH_3-TPD, will be used as parameter for correlation with activity and selectivity. Figure 4-5 a) shows the left hand side of eq. (4-1) as function of the reciprocal of the maximum desorption temperature of the high temperature peak, i.e., the peak associated with the Bronsted

acid sites, observed during NH_3-TPD and allows to derive the NH_3 desorption energy according to the procedure explained in paragraph 4.2. For all zeolites considered in this work, linear trends are obtained.

It can be seen from Figure 4-5 b) that the desorption energy for the different H-Y zeolites remains fairly constant while the desorption energy of the MFI zeolites shows a slight decreasing strength with increasing Si/Al ratio. H-ZSM-5(25), which has a Si/Al of 25, is added to the graph for illustrative purposes. It can be generalized that a higher desorption energy is found for the H-ZSM-5 zeolites than for the faujasites (120 kJ mol^{-1} compared to 80 kJ mol^{-1}). H-BEA(30) has a low desorption energy of around 60 kJ mol^{-1}. H-MOR and H-FER have the highest desorption energy.
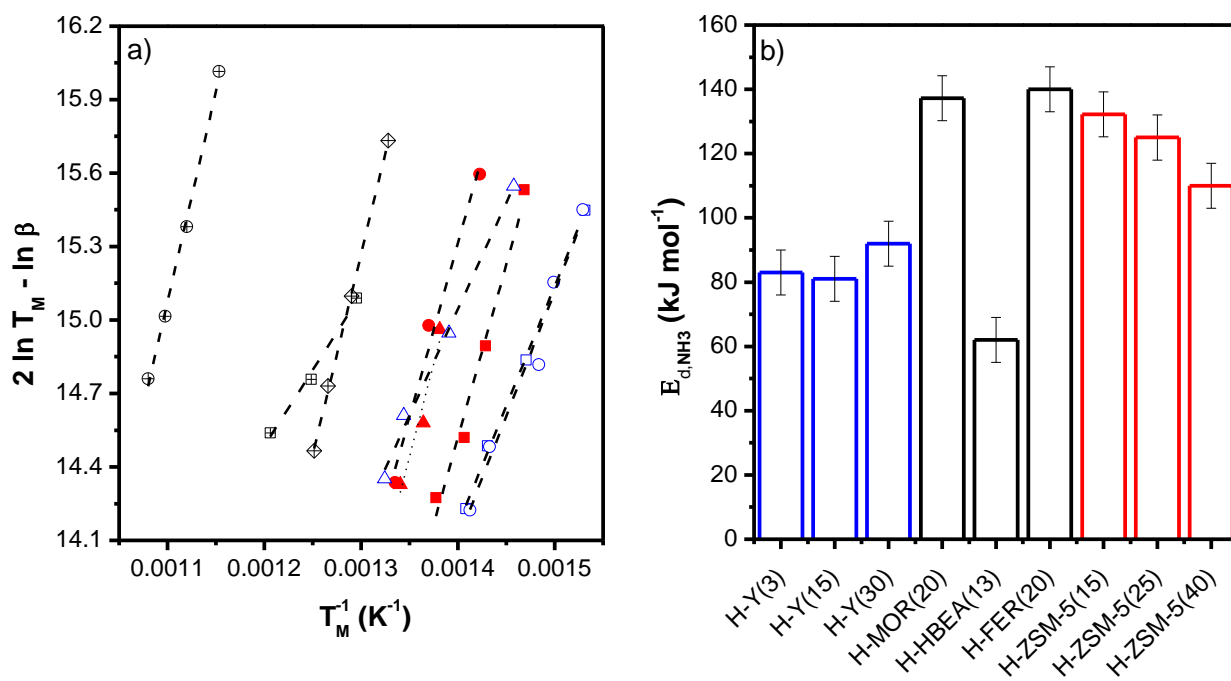
Figure 4-5: a) Left hand side of eq. (4-1) as function of the reciprocal of the desorption temperature at which a maximum has been observed during NH$_3$-TPD, i.e., the *h*-peak associated with the Bronsted acid sites (blue: FAU, red: MFI, black: other zeolites) and b) NH$_3$ desorption energy for the different zeolites studied in this chapter. Error bars indicate the 95% confidence interval.

The ranking of the zeolites based on the ammonia desorption energy is as followed: FER > MOR > MFI > FAU > BEA. It should be noted that this ranking is quite similar as found in literature, i.e., MOR > FER > MFI > BEA > FAU [25, 26].

4.4 Mechanistic study on H-ZSM-5

4.4.1 Experimental results

No deactivation is observed during the ethanol dehydration experiments on H-ZSM-5 at the conditions considered in this work (Table 4-2). The only dehydration products are ethene and diethyl ether and no other olefins or oxygenates are detected. The effect of conversion on product yields is studied by systematically increasing the site time at constant temperature and pressure, thus increasing the conversion of ethanol. The ethene yield is found to increase steadily with increasing site time, while the diethyl ether yield passes through a maximum as function of site time as can be seen in Figure 4-6 a. The decrease in diethyl ether yield at higher site times can be attributed to the decomposition of diethyl ether to ethene and ethanol (Path C in Figure 4-1). From the delplot analysis [27] shown in Figure 4-6 b, it can be seen that diethyl ether is the major primary product. This indicates that ethene is predominantly produced via the decomposition of diethyl ether. It can be concluded that the formation of diethyl ether (path B in Figure 4-1) is dominant at low ethanol conversion, while the decomposition of diethyl ether (path C in Figure 4-1) gains importance with increasing conversion.

The effect of Si/Al on the ethanol dehydration reaction is shown in Figure 4-6 by comparing H-ZSM-5(15) and H-ZSM-5(40). No difference is observed between the ethanol dehydration results obtained experimentally using H-ZSM-5 with Si/Al ratio of 15 or 40. According to Rodriguez-Gonzalez et al. [16], low Si/Al H-ZSM-5 can contain significant amounts of extra-framework aluminium (EFAL), which can amount up to 10% for H-ZSM-5 with Si/Al = 15. Higher Si/Al almost show no extra framework aluminium. The catalytic tests show however that no effect of the possible extra Lewis acidity coming from EFAL is observed. This is confirmed by Moser et al. who report a constant reaction rate for ethanol dehydration in the Si/Al region of 35 to 126 [28].
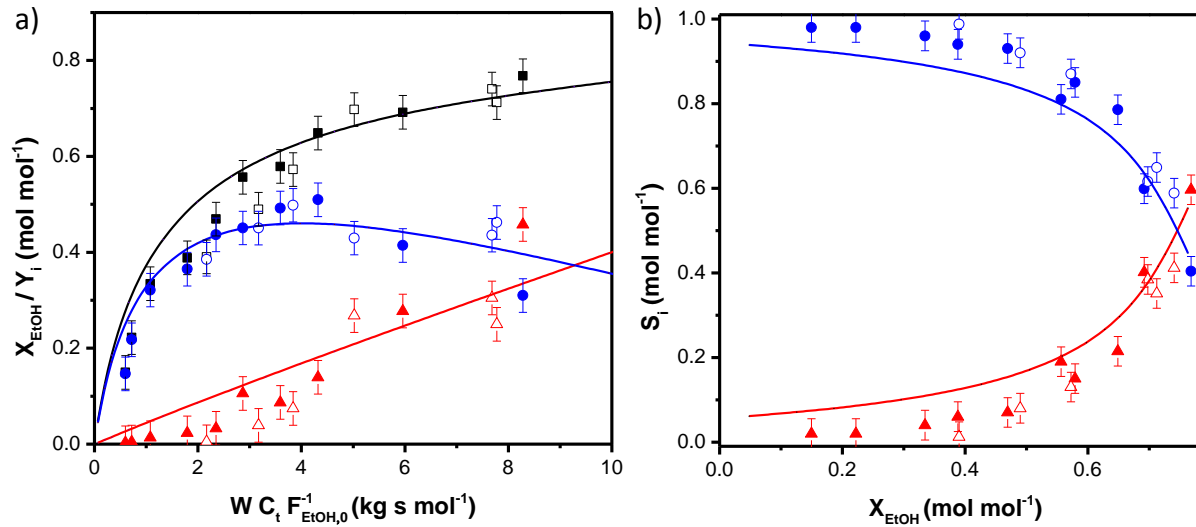
Figure 4-6: a) Ethanol conversion (X_{EtOH}, ■, black) and product yield of diethyl ether (Y_{DEE}, ●, blue) and ethene (Y_{C2H4}, ▲, red) as function of site time and b) effect of ethanol conversion on ethene (S_{C2H4}, ●, red) and diethyl ether selectivity (S_{DEE}, ●, blue) for H-ZSM-5(15) (full symbols) and H-ZSM-5(40) (hollow symbols). The plug-flow reactor simulations, using ab initio calculated rate and equilibrium coefficients given in Table 4-4 and integration of equation (3-3) and simultaneously solving eqs. (3-4) and (3-5), are shown as full lines, while the experimental data points are indicated with their 95 % confidence interval. (T = 503 K, $p_{EtOH,0}$ = 20 kPa)

The effect of temperature on activity and selectivity is shown in Figure 4-7. An increase in the reaction temperature is associated with an increase in ethanol conversion which also has a significant impact on the product distribution. The changes in product distribution can thus be attributed to a conversion effect or to a kinetic effect, i.e., effect of temperature on the rate coefficient. Therefore, when comparing product selectivity at different temperatures, the conversion needs to be fixed in order to decouple this kinetic effect from possible conversion effects.
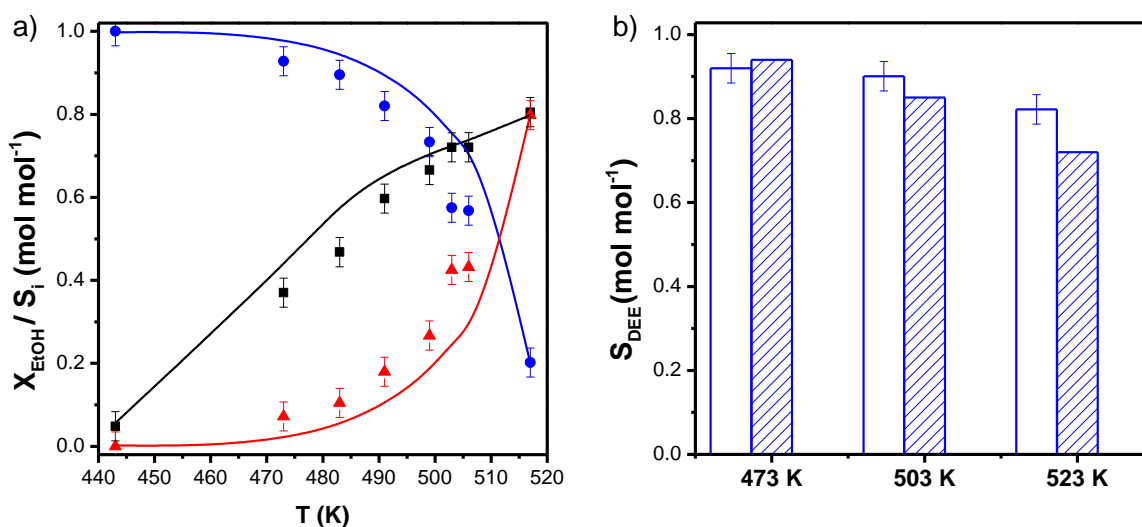
Figure 4-7: a) Ethanol conversion (X_{EtOH}, ■, black), diethyl ether selectivity (S_{DEE}, ●, blue) and ethene selectivity (S_{C2H4}, ▲, red) as function of temperature. b) diethyl ether selectivity at conversion of 0.5 at three different temperatures (full = experimental point, shaded = model simulation). The plug-flow reactor simulations, using ab initio calculated rate and equilibrium coefficients given in Table 4-4 and integration of equation (3-3) and simultaneously solving eqs. (3-4) and (3-5), are shown as full lines in a) and shaded in b), while the experimental data points are indicated with their 95 % confidence interval. (H-ZSM-5(40), $W\,C_t\,F_{EtOH,0}^{-1}$ = 4.6 mol$_{H+}$ s mol^{-1}, $p_{EtOH,0}$ = 24 kPa)

Figure 4-7 b shows the effect of temperature on diethyl ether selectivity at a constant inlet pressure of ethanol and a fixed conversion level of 50%. It can be seen that diethyl ether is the principal product at low temperatures, while the product selectivity gradually shifts towards ethene at higher temperature. This indicates that the majority of the ethene formed at low temperature originates from the bimolecular dehydration route involving diethyl ether as an intermediate, while at higher temperature the monomolecular dehydration route becomes more important.

The effect of the partial pressure of water on the ethanol dehydration reaction is of prime interest for the production of ethene from bio-ethanol. Therefore, a kinetic inhibition effect of water was investigated by evaluating the effect of water pressure at a constant inlet partial pressure of ethanol and a reaction temperature of 503 K. As can be seen from Figure 4-8, the presence of water in the feed mixture does not have significant impact on the activity nor on the selectivity, even at feed compositions exceeding the azeotropic composition. This indicates a zero order dependence of the partial pressure of water on the kinetics. The results are in agreement with other literature reporting no kinetic inhibition effect of water on the dehydration of ethanol on H-ZSM-5 [29-31].
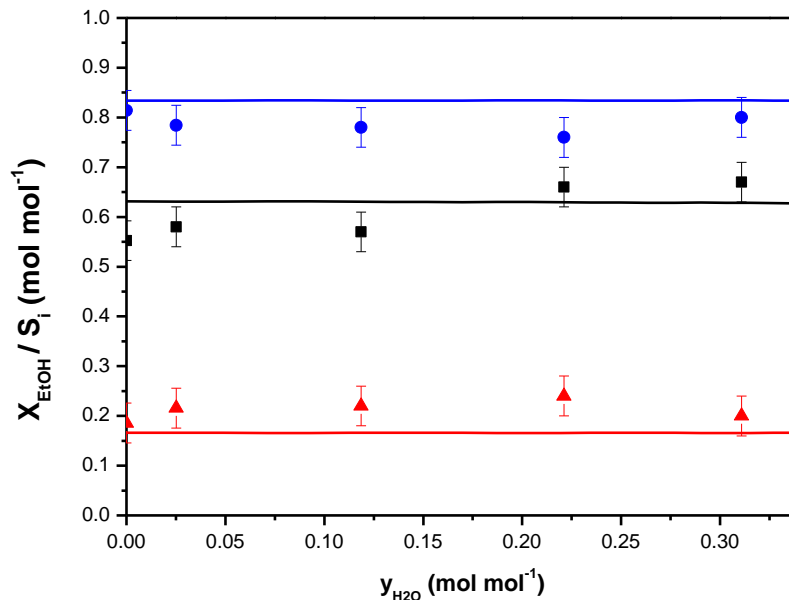
Figure 4-8: Ethanol conversion (X_{EtOH}, ■, black), ethene (S_{C2H4}, ▲, red) and diethyl ether selectivity (S_{DEE}, ●, blue) as function of water content. The plug-flow reactor simulations using ab initio calculated rate and equilibrium coefficients given in Table 4-4 and integration of equation (3-3) and simultaneously solving eqs. (3-4) and (3-5), are shown as full lines, while the experimental data are indicated with their 95 % confidence interval. (H-ZSM-5(40), T = 503 K, $p_{EtOH,0}$ = 30 kPa, $W\,C_t\,F_{EtOH,0}^{-1}$= 4.2 kg s mol^{-1})

4.4.2   Comparison between experimental observations and microkinetic simulations

The simplified reaction network shown in Figure 4-1, was fully elucidated in terms of elementary steps as shown in Figure 4-9 [9]. The experimental observations can then be compared to the microkinetic model (equations given in section 3.2.2) using only quantum chemically determined parameters.
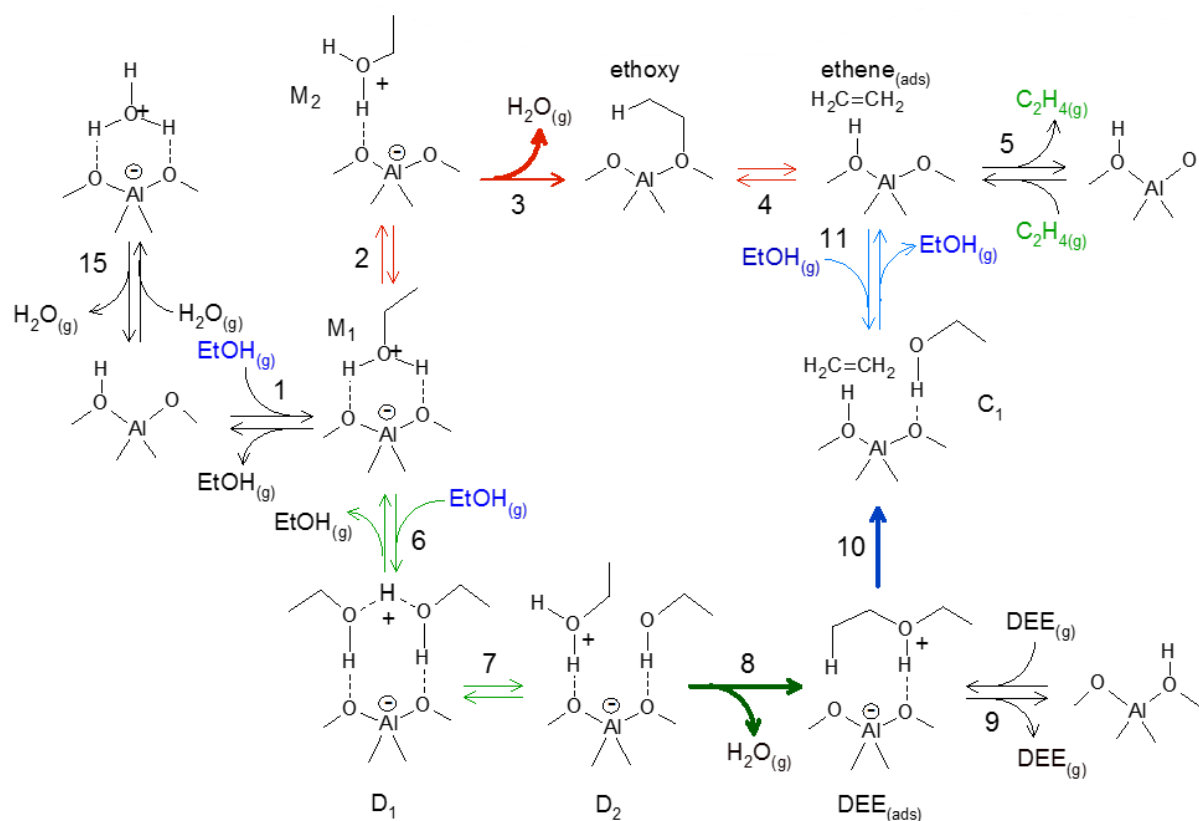
Figure 4-9: Reaction mechanism for ethanol dehydration (red: monomolecular dehydration, green: bimolecular dehydration, blue: diethyl ether decomposition). Modified from [32].

In this network, the monomolecular dehydration to ethene, i.e., path A in Figure 4-1, proceeds via a ethoxide-mediated mechanism: after ethanol adsorption and protonation, the protonated ethanol monomer (M1) rearranges to M2 which undergoes a nucleophilic substitution reaction to form a surface-bound ethoxide. Here, the primary carbon of the protonated ethanol breaks its bond with the leaving water group and forms a new bond with the basic oxygen of the zeolite surface. Subsequently, the surface-bound ethoxide is deprotonated to form physisorbed ethene which can desorb to regenerate the active site. The occurrence of this ethoxide was also observed experimentally [33].

The formation of diethyl ether (path B in Figure 4-1) occurs via a so-called dimer-mediated mechanism: monomolecular and bimolecular adsorption of ethanol is followed by rearrangement of the protonated ethanol dimer. The protonated ethanol then breaks its bond with the leaving water group and concurrently forms a new bond with the oxygen of the physisorbed ethanol. The protonated ether can then deprotonate and desorb to form gas phase diethyl ether. The decomposition of diethyl ether to ethene and ethanol (Path C in Figure 4-1) occurs via adsorption and protonation of diethyl ether. The protonated ether undergoes a heterolytic cleavage of a C-O bond and a concurrent abstraction of a β-hydrogen by the basic oxygen of the zeolite surface. Arrhenius pre-exponential factors (A) and activation energies (E_a) for the activated elementary steps in this reaction network can be found in Table 4-4.

Table 4-4: Standard reaction enthalpy (ΔH_r^0 in kJ mol^{-1}), standard reaction entropy (ΔS_r^0 in J mol^{-1} K^{-1}), activation energy ($E_{a(f)}$ in kJ mol^{-1}) and pre-exponential factor (A_f in s^{-1} or 10^{-2} kPa^{-1} s^{-1}) of the forward reaction for the elementary steps, numbered as indicated in Figure 4-9. The activated steps are indicated in bold.

	Elementary steps	ΔH_r^0	ΔS_r^0	$E_{a(f)}$	A_f
1	$EtOH_{(g)}$ + * $\leftrightarrow$ M_1	-122	-167	-	-
2	M_1 $\leftrightarrow$ M_2	14	7	-	-
3	**M_2 $\leftrightarrow$ Ethoxy + H2O(g)**	**77**	**146**	**118**	**4.0 10^{13}**
4	**Ethoxy $\leftrightarrow$ Ethene$_{(ads)}$**	**44**	**60**	**106**	**9.4 10^{12}**
5	Ethene$_{(ads)}$ $\leftrightarrow$ $C_2H_{4(g)}$ + *	48	99	-	-
6	M_1 + $EtOH_{(g)}$ $\leftrightarrow$ D_1	-99	-162	-	-
7	D_1 $\leftrightarrow$ D_2	44	24	-	-
8	**D_2 $\leftrightarrow$ DEE$_{(ads)}$ + $H_2O_{(g)}$**	**16**	**125**	**92**	**3.5 10^{12}**
9	$DEE_{(ads)}$ $\leftrightarrow$ $DEE_{(g)}$	139	165	-	-
10	**DEE$_{(ads)}$ $\leftrightarrow$ C_1**	**114**	**51**	**145**	**4.6 10^{13}**
11	C_1 $\leftrightarrow$ Ethene* + $EtOH_{(g)}$	59	175	-	-
12	Ethoxy + Ethene $\leftrightarrow$ C_2	-33	-113	-	-

As can be seen from Figure 4-10, a good agreement between model simulations and experiments is observed. This is quite remarkable given the fact that the reaction network and the pre-exponential factors and activation energies are obtained solely from quantum chemical calculations. Also, the performance of the model in describing the effect of conversion, temperature and water content as shown in Figures 4-6 to 4-8, can also be considered as reasonable.
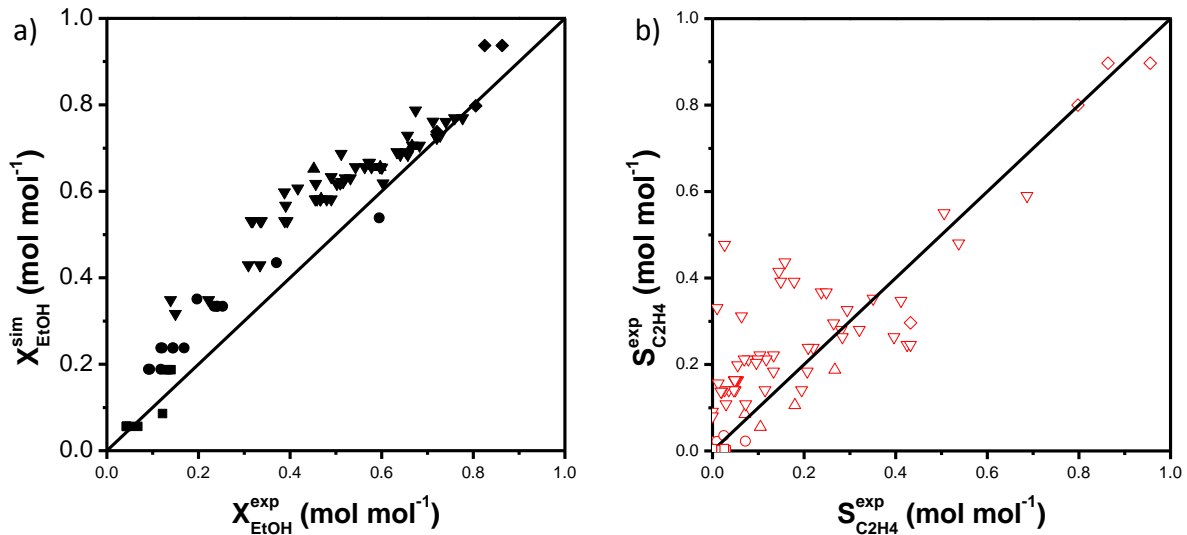
Figure 4-10: a) parity diagram of experimental vs calculated ethanol conversion (X_{EtOH}), b) parity diagram of experimental vs calculated ethene selectivity (S_{C2H4}) at 453 K (■) , 473 K (●), 483 K (▲), 503 K (▼), 523 K (♦).The plug-flow reactor simulations using ab initio calculated rate and equilibrium coefficients and integration of equation (3-3) and simultaneously solving eqs. (3-4) and (3-5) for the operating conditions given in Table 4-2. (catalyst: H-ZSM-5(15) and H-ZSM-5(40))

4.5 Catalytic performance of other zeolites

The results of the catalytic performance of several other industrially relevant zeolites at 523 K are shown in Figure 4-11. Rather than focusing on a single condition as typically shown in comparison studies, a range of site times was investigated to assess the effect on activity and selectivity. The use of site time allows to account for the effect of concentration of acid sites on the conversion, as it is logical that more acid sites will result in a higher activity.

H-Y(15) and H-Y(30) show a lower activity than H-Y(3). H-Y(3) is prepared by steaming of a Na-Y zeolite, while the H-Y(15) and H-Y(30) were steamed a second time at higher temperatures and subsequently leached with a mineral acid. The lower activity of the latter two samples compared to the parent sample, i.e. H-Y(3), are consistent with catalytic activity tests on n-heptane hydroisomerization. Remy et al. [23] explained this drop in activity by the removal of the extra-framework aluminium species during the acid treatment. H-ZSM-5, H-MOR and H-BEA all exhibit similar activity. The highest activity is observed for H-MOR, which is consistent with the experiments by Phung at al. [4].
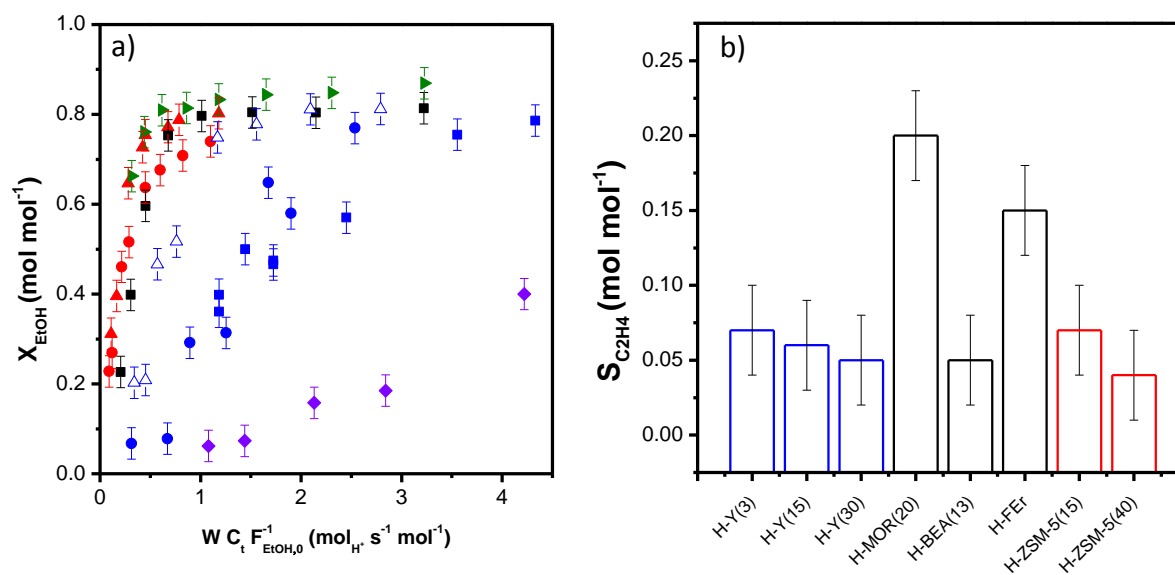
Figure 4-11: a) Ethanol conversion as function of site time for H-FER (♦, purple), H-Y(3) (Δ, blue), H-Y (15) (■, blue), H-Y(30) (●, blue), H-BEA (■, black), H-MOR (▶, green), H-ZSM-5(15) (▲, red), H-ZSM-5(40) (●,red) (T = 523 K, $p_{EtOH,0}$ = 113 kPa); b) ethene selectivity at 70% conversion for the different topologies (additional points for H-FER at higher site times have been measured but are not shown on Figure 4-11 a) for reasons of clarity) (T = 523 K, $p_{EtOH,0}$ = 113 kPa)

When comparing the selectivity for the different zeolites at 70% conversion, it can be seen that H-MOR and H-FER have the highest selectivity towards ethene. The other zeolites all show similar selectivity towards ethene. This indicates that the monomolecular dehydration is favoured on H-MOR and H-FER at the investigated conditions. It should be noted that for all zeolites, high levels of ethanol conversion are required ($X_{EtOH} > 0.70$) to form significant amounts of ethene. It is evident that on all zeolites the formation of diethyl ether is favoured.

The higher ethene selectivity obtained on H-MOR can be explained by the existence of the side pockets [7], which are typical for mordenite zeolites. In these side pockets, it is likely that only one molecule of ethanol can enter. This obviously favours the conversion of ethanol to ethene as the production of diethyl ether obviously needs the vicinity of another ethanol molecule. Thus, sites located in these side pockets can well likely be the most active and most selective for the monomolecular dehydration. On larger cavities or open channels and at low ethanol conversion, this reaction is in competition with the bimolecular reaction production of diethyl ether.
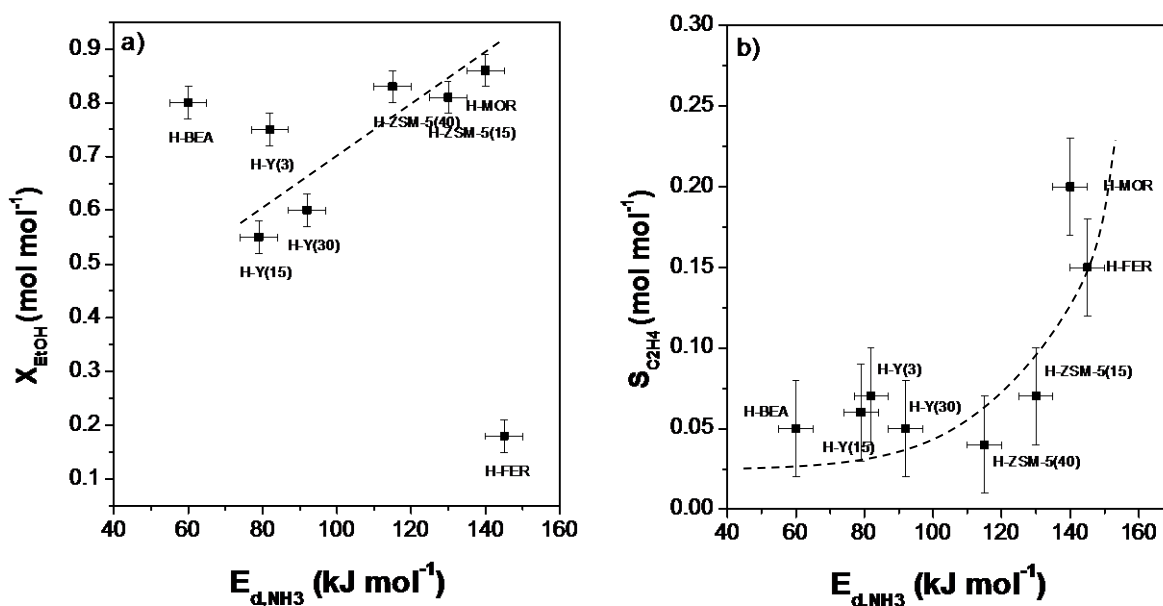
Figure 4-12: a) Ethanol conversion at W C_t F^{-1} = 2 mol_{H+} s mol^{-1} and b) ethene selectivity at 70 % conversion as function of NH_3 desorption energy (T = 523 K, $p_{EtOH,0}$ = 113 kPa). Dashed lines are guides to the eye.

The relationship between activity and ethene selectivity and an experimentally determined parameter, i.e., the NH_3 desorption energy, is shown in Figure 4-12 and a reasonable correlation is found with only two outliers: H-BEA and H-FER. Here, structural and/or confinement effects could play a role. From Figure 4-12 b, it is clear that a unique relationship exists between the NH_3 desorption energy and the ethene selectivity: the highest NH_3 desorption energy results in the highest ethene selectivity.

After reaction, the catalyst colour has changed for some catalysts as can be seen in Figure 4-13. H-ZSM-5 (40) maintains its white colour after reaction while H-FER and H-BEA exhibits a change in colour towards brown. As seen in Chapter 3, the formation of aromatic species was the cause of the colour change on H-ZSM-5. These aromatic species can block active sites and thus bias the observed activity of the catalyst.
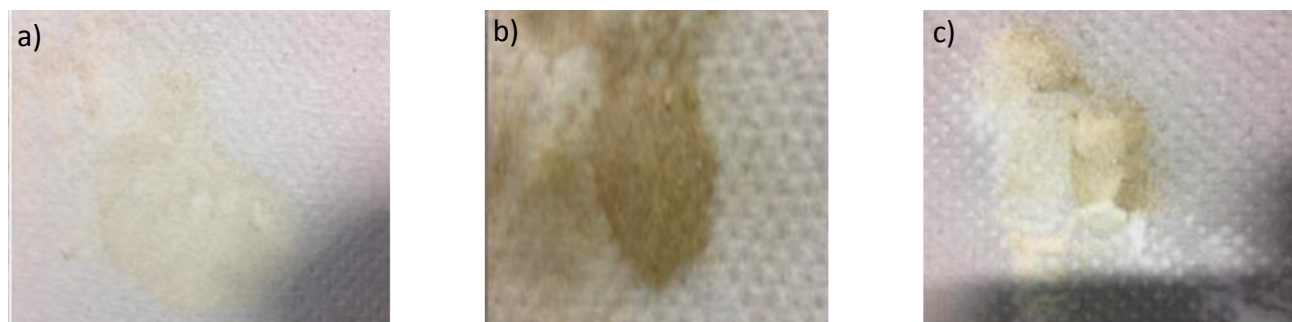
Figure 4-13: Catalyst colour after 35 hours on stream for a) H-ZSM-5 (40), b) H-FER and c) H-BEA (T=523 K, $p_{EtOH,0}$ = 113 kPa)

The NH_3 desorption energy is only an average parameter and a more in-depth study is required to fully understand this effect. Typical phenomena such as shape selectivity and confinement need to be addressed. However, it is very difficult to discriminate between shape selectivity and confinement effects solely based on experimental data. Shape selectivity is a key phenomenon which restricts reactions involving transition states, intermediates, reactants and/or products for which the size exceeds that of the catalyst cavities. Additional stabilization of the reactants and/or transition state via confinement effects can result in enhanced or decreased activity.

4.6 Conclusions

The present chapter provides a description of the behaviour of ethanol dehydration at low temperatures on H-ZSM-5 and several other industrially relevant zeolites. Higher reaction temperatures and higher site times favour a high ethene yield on H-ZSM-5. No effect of water is observed on the reaction kinetics. The absence of a water inhibition effect makes the dehydration of aqueous bio-ethanol an attractive option for the production of bio-ethene, which can serve as a feedstock for the chemical industry. The good agreement between the simulated and the experimental conversion and selectivity demonstrates the potential of DFT-based microkinetic models for increased insight in catalytic reaction mechanisms. Such models allow to retrieve information on key surface species and the most dominant pathway without prior knowledge or experimental observations.

A comparison of several industrially relevant zeolites shows large differences in activity with H-Y and H-FER exhibiting a low activity. The highest ethene selectivity is observed on H-MOR and H-FER but this is still limited to 20 %. A relationship between activity and selectivity and the NH_3 desorption energy, as determined by NH_3-TPD, is observed. A more in-depth experimental study is required in this respect. Also the colour change of certain catalysts after reaction should be examined in more detail.

4.7 References

[1] G. Chen, S. Li, F. Jiao, Q. Yuan, Catalytic dehydration of bioethanol to ethylene over TiO2/[gamma]-Al2O3 catalysts in microchannel reactors, Catalysis Today, 125 (2007) 111-119.

[2] Y. Chen, Y.L. Wu, L. Tao, B. Dai, M.D. Yang, Z. Chen, X.Y. Zhu, Dehydration reaction of bio-ethanol to ethylene over modified SAPO catalysts, Journal of Industrial and Engineering Chemistry, 16 (2010) 717-722.

[3] Y.J. Guan, Y. Li, R.A. van Santen, E.J.M. Hensen, C. Li, Controlling reaction pathways for alcohol dehydration and dehydrogenation over FeSBA-15 catalysts, Catalysis Letters, 117 (2007) 18-24.

[4] T.K. Phung, L.P. Hernandez, A. Lagazzo, G. Busca, Dehydration of ethanol over zeolites, silica alumina and alumina: Lewis acidity, Bronsted acidity and confinement effects, Applied Catalysis A: General, 493 (2015) 77-89.

[5] T. Zaki, Catalytic dehydration of ethanol using transition metal oxide catalysts, Journal of Colloid and Interface Science, 284 (2005) 606-613.

[6] W. Alharbi, E. Brown, E.F. Kozhevnikova, I.V. Kozhevnikov, Dehydration of ethanol over heteropoly acid catalysts in the gas phase, Journal of Catalysis, 319 (2014) 174-181.

[7] H. Chiang, A. Bhan, Catalytic consequences of hydroxyl group location on the rate and mechanism of parallel dehydration reactions of ethanol over acidic zeolites, Journal of Catalysis, 271 (2010) 251-261.

[8] T.K. Phung, G. Busca, Diethyl ether cracking and ethanol dehydration: Acid catalysis and reaction paths, Chemical Engineering Journal, 272 (2015) 92-101.

[9] K. Alexopoulos, M. John, K. Van der Borght, V. Galvita, M.-F. Reyniers, G.B. Marin, DFT-based microkinetic modeling of ethanol dehydration in H-ZSM-5, Journal of Catalysis, 339 (2016) 173-185.

[10] S. Kulprathipanja, Zeolites in Industrial Separation and Catalysis, WILEY-VCH Verlag GmbH & Co. KGaA, Weinheim, 2010.

[11] K. Ramesh, L.M. Hui, Y.F. Han, A. Borgna, Structure and reactivity of phosphorous modified H-ZSM-5 catalysts for ethanol dehydration, Catalysis Communications, 10 (2009) 567-571.

[12] D.S. Zhang, R. Wang, X.X. Yang, Effect of P content on the catalytic performance of P-modified HZSM-5 catalysts in dehydration of ethanol to ethylene, Catalysis Letters, 124 (2008) 384-391.

[13] H. Xin, X. Li, Y. Fang, X. Yi, W. Hu, Y. Chu, F. Zhang, A. Zheng, H. Zhang, X. Li, Catalytic dehydration of ethanol over post-treated ZSM-5 zeolites, Journal of Catalysis, 312 (2014) 204-215.

[14] G.T. Kokotailo, S.L. Lawton, D.H. Olson, D.H. Olson, W.M. Meier, Structure of Synthetic Zeolite ZSM-5, Nature, 272 (1978) 437-438.

[15] M. Guisnet, J.-P. Gilson, Zeolites for cleaner technologies, Imperial College Press, London, 2002.

[16] L. Rodriguez-Gonzalez, F. Hermes, M. Bertmer, E. Rodriguez-Castellon, A. Jimenez-Lopez, U. Simon, The acid properties of H-ZSM-5 as studied by NH3-TPD and Al-27-MAS-NMR spectroscopy, Applied Catalysis A: General, 328 (2007) 174-182.

[17] A.S. Al-Dughaither, H. de Lasa, HZSM-5 Zeolites with Different SiO2/Al2O3 Ratios. Characterization and NH3 Desorption Kinetics, Industrial & Engineering Chemistry Research, 53 (2014) 15303-15316.

[18] G. Ertl, H. Knözinger, J. Weitkamp, Handbook of heterogeneous catalysis, VCH, Weinheim, 1997.

[19] Zeolyst, (www.zeolyst.com), accessed on 27/5/2016

[20] B. Hunger, M. Heuchel, L.A. Clark, R.Q. Snurr, Characterization of acidic OH groups in zeolites of different types: An interpretation of NH3-TPD results in the light of confinement effects, The Journal of Physical Chemistry B, 106 (2002) 3882-3889.

[21] A.M. Camiloti, S.L. Jahn, N.D. Velasco, L.F. Moura, D. Cardoso, Acidity of Beta zeolite determined by TPD of ammonia and ethylbenzene disproportionation, Applied Catalysis A: General, 182 (1999) 107-113.

[22] R. Van Borm, M.F. Reyniers, J.A. Martens, G.B. Marin, Catalytic Cracking of Methylcyclohexane on FAU, MFI, and Bimodal Porous Materials: Influence of Acid Properties and Pore Topology, Industrial & Engineering Chemistry Research, 49 (2010) 10486-10495.

[23] M.J. Remy, D. Stanica, G. Poncelet, E.J.P. Feijen, P.J. Grobet, J.A. Martens, P.A. Jacobs, Dealuminated H-Y zeolites: Relation between physicochemical properties and catalytic activity in heptane and decane isomerization, Journal of Physical Chemistry, 100 (1996) 12440-12447.

[24] F. Lónyi, J. Valyon, On the interpretation of the NH3-TPD patterns of H-ZSM-5 and H-mordenite, Microporous and Mesoporous Materials, 47 (2001) 293-301.

[25] K. Suzuki, T. Noda, N. Katada, M. Niwa, IRMS-TPD of ammonia: Direct and individual measurement of Bronsted acidity in zeolites and its relationship with the catalytic cracking activity, Journal of Catalysis, 250 (2007) 151-160.

[26] N. Katada, K. Nouno, J.K. Lee, J. Shin, S.B. Hong, M. Niwa, Acidic Properties of Cage-Based, Small-Pore Zeolites with Different Framework Topologies and Their Silicoaluminophosphate Analogues, Journal of Physical Chemistry C, 115 (2011) 22505-22513.

[27] N.A. Bhore, M.T. Klein, K.B. Bischoff, Species rank in reaction pathways: Application of Delplot analysis, Chemical Engineering Science, 45 (1990) 2109-2116.

[28] W.R. Moser, R.W. Thompson, C.C. Chiang, H. Tong, Silicon-Rich H-Zsm-5 Catalyzed Conversion of Aqueous Ethanol to Ethylene, Journal of Catalysis, 117 (1989) 19-32.

[29] C.B. Phillips, R. Datta, Production of ethylene from hydrous ethanol on H-ZSM-5 under mild conditions, Industrial & Engineering Chemistry Research, 36 (1997) 4466-4475.

[30] T.M. Nguyen, R. Levanmao, Conversion of Ethanol in Aqueous-Solution over Zsm-5 Zeolites - Study of the Reaction Network, Applied Catalysis, 58 (1990) 119-129.

[31] W.R. Moser, R.W. Thompson, C.-C. Chiang, H. Tong, Silicon-rich H-ZSM-5 catalyzed conversion of aqueous ethanol to ethylene, Journal of Catalysis, 117 (1989) 19-32.

[32] M.-F. Reyniers, G.B. Marin, Experimental and Theoretical Methods in Kinetic Studies of Heterogeneously Catalyzed Reactions, Annual Review of Chemical and Biomolecular Engineering, 5 (2014) 563-594.

[33] J.N. Kondo, D. Nishioka, H. Yamazaki, J. Kubota, K. Domen, T. Tatsumi, Activation energies for the reaction of ethoxy species to ethene over zeolites, The Journal of Physical Chemistry C, 114 (2010) 20107-20113.

Chapter 5

Production of higher hydrocarbons on H-ZSM-5: experimental and model-based investigation

In this chapter, a more in-depth investigation on the production of higher hydrocarbons from ethanol over H-ZSM-5 is presented. This will consist of an experimental study on the one hand and detailed microkinetic modelling on the other hand. The elucidated reaction mechanism obtained in Chapter 3 presented a global overview, but no detailed information on the effect of process conditions nor on the important reaction families was acquired. Here, the effect of temperature, ethanol partial pressure and water content will be discussed. Also, similarities with ethene conversion will be examined in more detail. Subsequently, a single-event microkinetic model will be developed for the production of higher hydrocarbons starting from ethene. The focus of this modelling will be on gaining more insight in the autocatalytic behaviour of the reaction.

5.1 Introduction

Literature results on the effect of process conditions on the conversion of ethanol to hydrocarbons mainly focused on global trends such as the effect of temperature and pressure on the product yields [1, 2]. Aguayo et al. for instance primarily focused on temperatures above 673 K which favour the formation of aromatics [1]. An attenuating effect of water on the activity was found, which was attributed to a weakening of the Brönsted acid sites, which were hydrated to form, among others, H_3O^+, $H_5O_2^+$, $H_7O_3^+$ with a hydration degree that increased by increasing the water concentration in the reaction medium. Deactivation during C_{3+} hydrocarbon formation was also observed. A distinction was made between coke formation and dealumination due to high water content of the feed as causes of deactivation.

Detailed understanding of a chemical process requires a multiscale approach in which kinetics are situated between the fundamental phenomena occurring at the active site and the phenomena occurring at the reactor scale. Kinetic modelling is an excellent tool to bridge the gap between the experimentally observed variables and the events occurring on the catalyst surface. As the reaction mechanism of ethanol conversion is still a matter of debate in literature, as discussed in Chapter 3, kinetic modelling can serve as a tool to gain additional insights into the reaction mechanism. Depending on the level of detail required, a different type of kinetic model will be proposed.

Chang et al. [3] proposed a lumped kinetic model for ethanol conversion to explain the overall production pathways of ethanol to olefins, aromatics and paraffins. In total, eight reactions were considered between seven products lumps, i.e., ethanol, di-ethyl ether, ethene, ethane, C_3-C_6 olefins, C_3-C_6 paraffins and C_{6+} aliphatic hydrocarbons and aromatics. Overall, this yielded a simplified kinetic model which resulted in a nice description of the experimental data, particularly at lower temperatures. Gayubo et al. developed a lumped kinetic model to describe the effect of process conditions and water content [4]. This model was expanded to also describe catalyst deactivation [5] and the effect of catalyst modifications such as desilication [6] and nickel introduction [7]. In case of ethanol conversion, catalyst deactivation can be an important topic,

when working at temperatures above 723 K. Several models for deactivation by coke were compared and the significant model appeared to be the parallel deactivation depending directly on ethene. The kinetic model seemed to fit the experimental observations rather well. However, no physical significance could be attributed to the estimated parameters. Physical significance can only be achieved if each elementary step is individually accounted for. This would however result in an enormous amount of parameters. The latter opens up perspectives for parameter reduction techniques such as the single-event methodology.

The single-event concept was first introduced to heterogeneous catalysed processes by Baltanas and Froment [8] and has already been successfully applied to pure acid catalysed [9, 10], metal catalysed [11, 12] and bifunctional processes [13]. Rather than lumping species into pseudo-components, which has been the only procedure for ethanol conversion until now, a limited number of elementary reaction families is defined to reduce the number of model parameters. Per reaction family only one rate coefficient, i.e., the single-event rate coefficient, is required. The single-event rate coefficient is multiplied with the number of single-events to account for the indistinguishable manners in which an elementary step can occur and results in the actual rate coefficient of the elementary step.

A distinction is typically made between kinetic and catalyst descriptors. A kinetic descriptor describes the intrinsic properties of an elementary reaction, e.g. pre-exponential factor and activation energy, and are assumed to be independent from the catalyst type. Catalyst descriptors, on the other hand are used to describe the effect of the catalyst properties on the observed kinetics such as acid site strength through the protonation enthalpy in acid catalysis. This distinction facilitates catalyst design, since it allows to screen catalysts *in silico* and determine the catalyst descriptors corresponding to the most optimal catalyst [14].

First, a detailed investigation of the kinetic dataset will be performed and the effect of temperature, partial pressure and water content will be discussed. The experimental results will also be compared to ethene conversion to higher hydrocarbons. Subsequently, a fundamental single-event microkinetic (SEMK) model for the production of C_{3+} hydrocarbons will be developed to gain more insight in the conversion of ethanol to hydrocarbons on H-ZSM-5. The parameters in this model will be regressed to intrinsic kinetic data, that is, in the absence of transport limitations, acquired over a broad range of process conditions.

5.2   Procedures

5.2.1   Catalytic performance testing

The catalyst used in this work is NH_4-ZSM-5 (Zeolyst, CBV8014) with a Si/Al of 40. In order to obtain the acid form, i.e. H-ZSM-5(40), a calcination procedure was applied to remove the NH_3 by heating to 823 K in air with a ramp of 1 K min^{-1} and maintaining the material at 823 K for 3 hours. The total acid site concentration was determined by NH_3-TPD and was found to be 0.36 mol kg^{-1}. Prior to loading the catalyst into the reactor, the catalyst powder was pressed into flakes and crushed into pellets with a diameter of 200 – 400 μm to avoid mass transport limitations at the pellet scale. The experiments were performed in a continuous isothermal tubular bench scale reactor (HTK-MI) specifically designed for measurement of intrinsic kinetics as discussed in Chapter 2. The experimental conditions are listed in Table 5-1.

Table 5-1: Experimental conditions, i.e., temperature, space time and partial pressure used for the conversion of ethanol and ethene to hydrocarbons

	Ethanol	Ethene
T (K)	573 - 623	573 - 623
W $F_{i,0}^{-1}$ (kg s mol^{-1})	2 – 17	1 - 9
$p_{i,0}$ (kPa)	20 – 60	20 – 60

5.2.2 Regression analysis

The weighted sum of squares, i.e., $S(\beta)$, between the observed and the calculated outlet flow rates of the various product responses is minimized by adjusting the model parameter vector b, which is expected to approach the real parameter vector β at the minimum of the objective function.

$$S(\beta) = \sum_{j=1}^{n_{exp}} \sum_{i=1}^{n_{resp}} w_i (F_{i,j} - \hat{F}_{i,j})^2 \longrightarrow Min \tag{5-1}$$

with n_{exp} being the number of experiments, n_{resp} the number of responses and w_i the weighing factor for response *i*. The latter are calculated from the covariance matrix of the experimental errors:

$$w_i = \frac{1}{\sigma_{ii}^2} = \left[\frac{\sum_{j=1}^{n_{exp}} w_i (F_{i,j} - \hat{F}_{i,j})^2}{n_{exp} n_{resp} - n_{par}} \right]^{-1} \tag{5-2}$$

A combination of a Rosenbrock and a Levenberg-Marquardt algorithm is used to minimize the objective function. An in-house developed code for the Rosenbrock algorithm [15] was used to find an adequate direction to the global optimum, since it is quite robust against divergence. The more accurate Levenberg-Marquardt algorithm [16] subsequently allows to reach the global minimum. For the Levenberg-Marquardt algorithm, ODRPACK 2.01 from Netlib is used [17]. Some additional code was added to ODRPACK to retrieve statistical information. Seven responses have been experimentally determined, that is, the molar outlet flow rate of the feed molecule, i.e., F_{C2H4}, propene, i.e., F_{C3H6}, the lump containing butene isomers, i.e., F_{C4H8}, the lump containing pentene isomers, i.e., F_{C5H10}, a lump containing hexene isomers, i.e., F_{C6H12}, a lump containing heptene isomers, i.e., F_{C7H14} and a lump containing all C_{8+} olefins, i.e., F_{C8+}. It should be noted that each species contained in the lump was identified separately until five carbon atoms. Beyond this, the amount of isomers becomes too large.

Several statistical tests are performed to evaluate the regression on a statistical basis in addition to the physical significance of the parameters. The global significance of the regression is expressed by the F_{regres} value obtained as the ratio of the regression and the residual sum of squares divided by their respective degrees of freedom.

$$F_{regres} = \frac{\dfrac{\sum_{i=1}^{n_{exp}} \sum_{j=1}^{n_{resp}} \hat{F}_{i,j}^2}{n_{par}}}{\dfrac{\sum_{i=1}^{n_{exp}} \sum_{j=1}^{n_{resp}} (F_{i,j} - \hat{F}_{i,j})^2}{n_{exp}\, n_{resp} - n_{par}}} \tag{5-3}$$

A F_{regres} value higher than the tabulated F value at the 95 % probability level with the corresponding degrees of freedom, corresponds to rejection of the null hypothesis that all parameters will simultaneously equal zero and, hence, to a globally significant regression. In practice, the aforementioned null hypothesis is easily rejected, and, hence, for having a reliable assessment of the global significance of the model, the calculated F values should be at least several times higher than the tabulated value.

The *t* value for parameter β_i is calculated as the ratio between the difference of estimate b_i and the postulated value b_i^*, i.e. zero in most cases, and the corresponding standard deviation, i.e., $s(b_i)$:

$$t = \frac{b_i - 0}{s(b_i)} \tag{5-5}$$

This test will assess the individual significance of a parameter. A parameter is estimated significantly different from zero when its individual t value exceeds the corresponding tabulated t-value at 95 % probability level. An individual confidence interval for each parameter can be determined via this *t* value. This gives the range in which the true value of the parameter can be found with a certain confidence level, e.g. 95%:

$$b_i - t_{n_{exp}\, n_{resp} - n_{par}}(95\%)\, s(b_i) \leq \beta_i \leq b_i + t_{n_{exp}\, n_{resp} - n_{par}}(95\%)\, s(b_i) \tag{5-6}$$

The binary correlation coefficient between two parameters, i.e., $\rho_{i,j}$, is calculated via the (co)variances of the two parameters.

$$\rho_{i,j} = \frac{V(b)_{i,j}}{\sqrt{V(b)_{i,i} V(b)_{j,j}}}$$

(5-7)

When $\rho_{i,j}$ approaches 1, a strong correlation exists between the parameters.

A pseudohomogeneous, one-dimensional ideal plug flow reactor model is used to simulate the experimental data in which no transport limitation or transient behavior, e.g. deactivation, is observed. The continuity equation for a gas phase component i can be written as:

$$\frac{dF_i}{dW} = R_i \qquad F_j(W = 0) = F_j^0$$

(5-9)

in which W is the catalyst mass, F_i the flow rate of component i and R_i the net rate of formation of component i.

5.3   Experimental observations in ethanol/ethene conversion

5.3.1 Stability of the catalyst

Deactivation of H-ZSM-5 during ethanol conversion has been reported to be significant [1], especially when working at elevated temperature, i.e., above 723 K. However, as shown in Figure 5-1, at 623 K, i.e., the highest temperature studied in this work, no deactivation is observed during 12 h time-on-stream. This is confirmed for both an ethanol (Figure 5-1 a) and an ethene feed (Figure 5-1 b). Reliable intrinisic steady state data can thus be acquired.
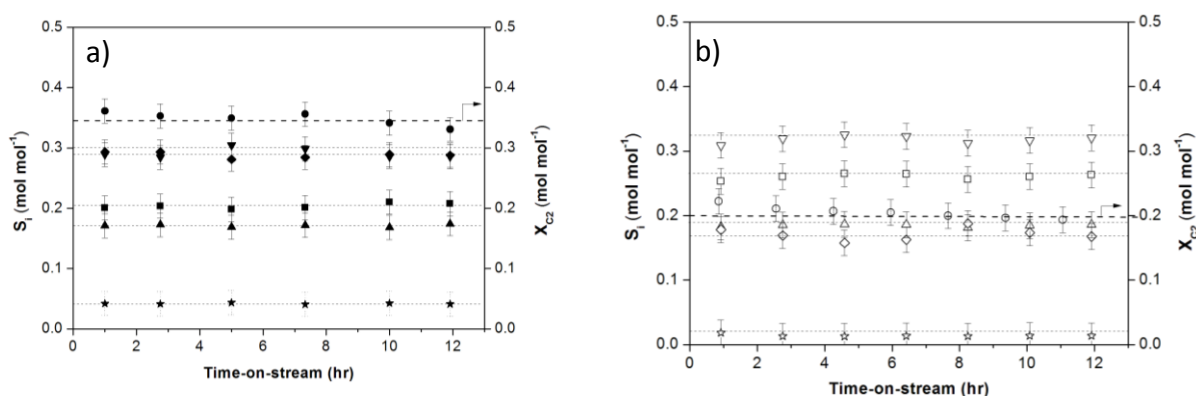
Figure 5-1: Conversion and selectivity as function of time-on-stream for a) an ethanol feed and b) an ethene feed. C_2 conversion as defined in Chapter 2 (●) and selectivity to C_3 (■), C_4 isomers (▼), C_5 isomers (▲), C_{6+} isomers (♦) and aromatics (★) (T = 623 K, $p_{EtOH,0}$ = 30 kPa, $p_{C2H4,0}$ = 27 kPa, W C_t $F_{i,0}^{-1}$ = 3 mol s^{-1} mol^{-1}). Lines are a guide to the eye.

A typical product distribution for the conversion of ethanol to C_{3+} hydrocarbons is shown in Figure 5-2. Hydrocarbons ranging from 2 to 10 carbon atoms are observed at the conditions given in Table 5-1. Since the number of olefins rises exponentially from six carbon atoms on, only the products up to pentene isomers can be identified individually. Products with carbon numbers higher than 7 are lumped together in the C_{8+} lump. The aromatic species benzene, toluene, xylene and ethyl-benzene can be identified separately and are reported accordingly. Almost no saturated hydrocarbons have been observed. The selectivity towards aromatics typically remains quite low, i.e., less than 0.02. An important observation is the high amount of odd-carbon numbered hydrocarbons.
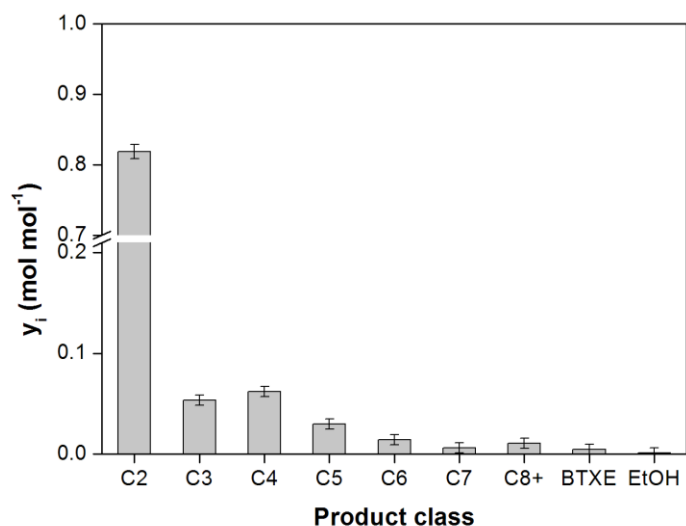
Figure 5-2: Typical product distribution for the reaction of ethanol over H-ZSM-5 (Si/Al = 40). (T = 623 K, $p_{EtOH,0}$ = 30 kPa, $W\,F_{EtOH,0}^{-1}$ = 8 kg s mol^{-1}, X_{C2} = 0.18). The chromatogram corresponding to this experiment can be found in Appendix A.

It was found that olefins with the same carbon number are in thermodynamic equilibrium. This means that the composition of the olefinic lump containing all double bond and structural isomers is the same as the composition at thermodynamic equilibrium. It was verified that thermodynamic equilibrium was not obtained between the different olefinic lumps. This is in agreement with literature findings on olefin oligomerization [18] and methanol-to-olefins [10].

5.3.2 Effect of temperature, partial pressure and water content

Figure 5-3 shows a plot of C_2 conversion at three different temperatures as a function of ethanol site time. The slope of the curves in this representation is directly proportional to the production rate of C_{3+} hydrocarbons. The reaction rate increases with increasing temperature as is expected from the Arrhenius law. At all three temperatures, an induction period is present although this induction period reduces with increasing temperature.
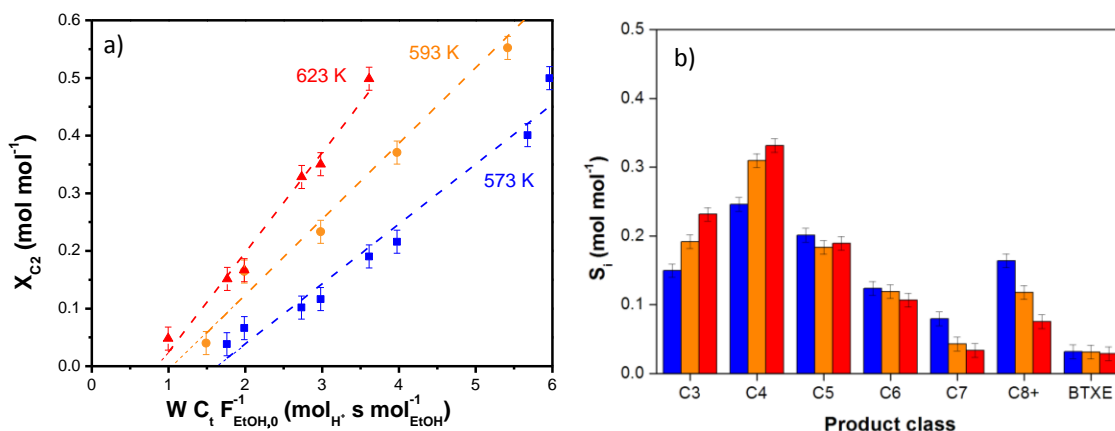
Figure 5-3: a) C_2 conversion as a function of ethanol site time at three different temperature 573 K (■, blue), 593 K (●, orange) and 623 K (▲, red) and b) Effect of temperature on product selectivity at isoconversion (X_{C2} = 0.2). (623 K, (blue); 593 K, (orange); 573 K, (red), $p_{EtOH,0}$ = 30 kPa). Lines are to guide the eye.

The effect of temperature on the selectivity towards the different product lumps at a C_2 conversion of 0.2 is shown in Figure 5-3 b. An increase in selectivity for propene and butene isomers is observed with increasing temperature. This indicates that β-scission reactions of higher olefins become more important at higher temperatures, which is indeed verified by the decreasing selectivity to C_7 and C_{8+} olefins. The C_5 and C_6 olefins seem to be unaffected by any temperature change, which is most likely due to their intermediate nature between alkylation reactions of lower olefins and β-scission reactions of higher olefins. The selectivity towards aromatics remains fairly constant in the investigated temperature range.

The effect of ethanol inlet partial pressure at 573 K on the C_2 conversion is shown in Figure 5-4 a. Increasing the ethanol inlet partial pressure results in a higher reaction rate and again the induction period decreases. When increasing the partial pressure of ethanol, more higher hydrocarbons are produced as shown by the comparison at isoconversion (X_{C2} = 0.2) in Figure 5-4 b. This is as expected, as bimolecular reactions, such as alkylation, are favoured by higher partial pressures.
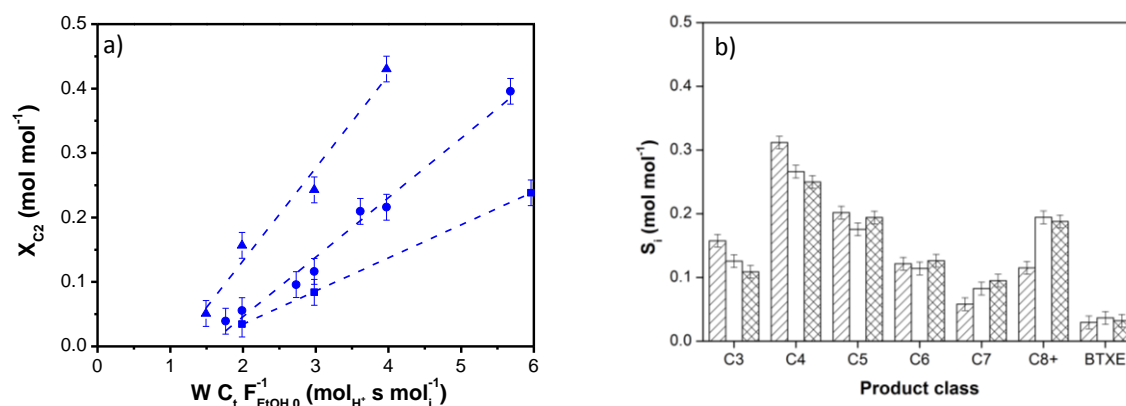
Figure 5-4: a) C_2 conversion as a function of ethanol site time at three different ethanol inlet partial pressures: 20 kPa (■), 30 kPa (●) and 60 kPa (▲) (T = 573 K), b) Effect of ethanol inlet partial pressure on product selectivity (single shaded: 20 kPa, empty: 30 kPa and double shaded: 60 kPa). (T = 573 K, X_{C2} = 0.2). Lines are to guide the eye.

A considerable amount of water remains in the mixture when ethanol is produced from fermentation of biomass. Removal of water from this mixture is energy intensive and hence it can be beneficial to use an ethanol feed with residual water directly as a reactor inlet. A feed with 20 v% water in ethanol is therefore studied and the conditions are adjusted to maintain a constant ethanol inlet partial pressure.

115
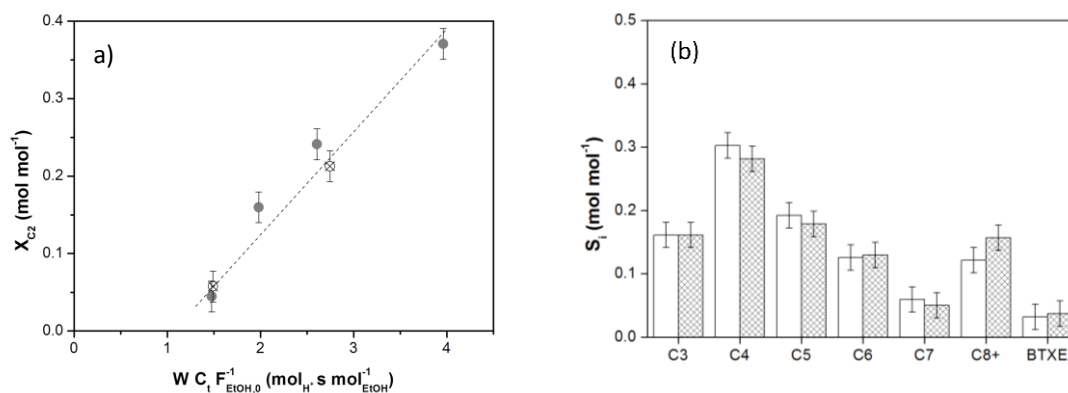
Figure 5-5: a) C₂-conversion as a function of ethanol site time for 0 mol% water(●) and 20 mol% water (⊜) and b) product selectivity at X_{C2} = 0.2; ethanol (empty); ethanol + water (pattern). (T = 573 K, $p_{EtOH,0}$ = 30 kPa). Line is to guide the eye.

Figure 5-5 clearly illustrates that water has no effect on conversion when comparing similar ethanol partial pressure and ethanol site time. This is valid for the conversion as well as for the selectivity towards the different products. In literature, a decrease in activity is reported [19-21] but this can be attributed to the diluting effect of water, i.e., lower ethanol inlet partial pressure or different process conditions

5.3.3 Discussion on the experimental study

As can be seen from the site time – conversion plots (Figures 5-4 to 5-6), an induction period is observed which is typical for an autocatalytic reaction and which has been thoroughly examined in Chapter 3. In Figure 5-6, this induction period is compared to ethene conversion to hydrocarbons on H-ZSM-5 at different temperatures, i.e., 573 K and 623 K. It can be seen that the induction period for ethanol conversion decreases as the temperature is increased, the induction period for ethene conversion remains fairly constant. The decrease in the induction period for ethanol conversion is related to the rapid increase in the ethanol dehydration reaction rate.
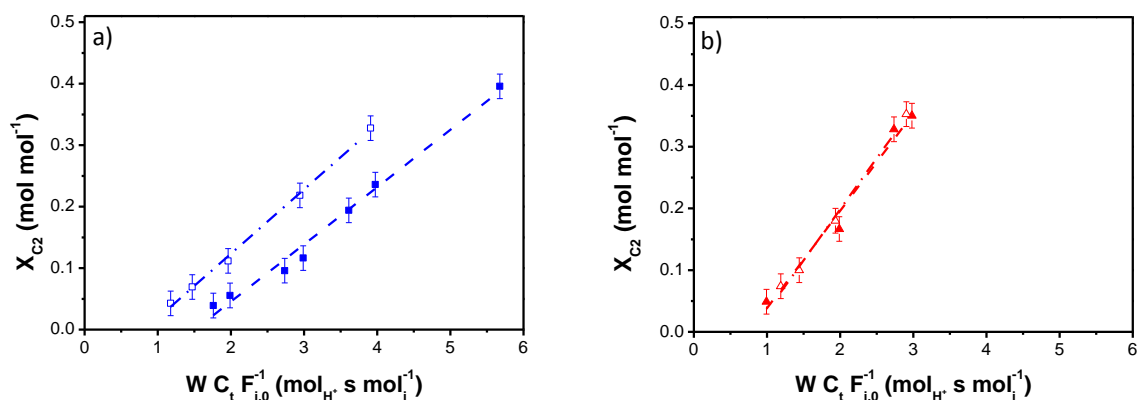
Figure 5-6: C$_2$ conversion as a function of site time at a) 573 K for ethanol (■) and ethene (□), and b) 623 K for ethanol (▲) and ethene (Δ), (p$_{EtOH,0}$ = 30 kPa, p$_{C2H4,0}$ = 27 kPa).

From the site time – conversion plots, a net production rate of C$_{3+}$ hydrocarbons can be calculated from the slope of the curve. Figure 5-7a shows the corresponding Arrhenius plot for both an ethanol and ethene feed in which a first order in ethanol partial pressure has been assumed. It can be seen that the curves are quite alike and also the activation energies (37 ± 13 kJ mol^{-1} for ethanol and 29 ± 11 kJ mol^{-1} for ethene) derived from this plot are quite similar. No difference is observed for the production of higher hydrocarbons when starting from ethanol or ethene at the investigated temperature range.
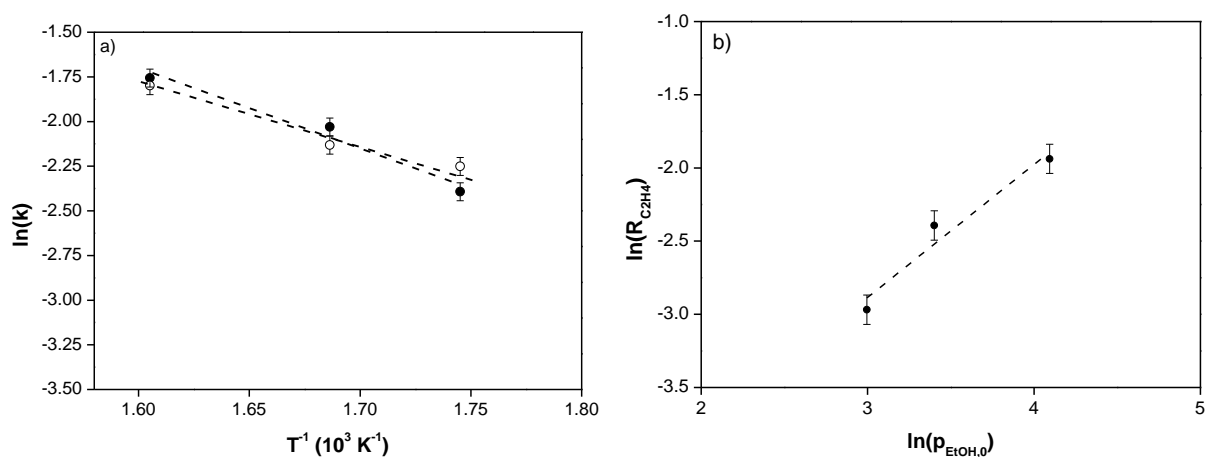
Figure 5-7: a) Arrhenius plot for the reaction of ethanol (●) and ethylene (○), (T = 573, 593 and 623 K, p$_{EtOH,0}$ = 30 kPa, p$_{C2H4,0}$ = 27 kPa) b) ln(R$_{C2H4}$) as a function of ln(p$_{EtOH}$) (T = 573 K). Error bars indicate the 95% confidence interval. Lines are to guide the eye.

The observed reaction order (α) of ethanol can be derived from:

$$R_i = k \, p_i^\alpha \iff \ln(R_i) = \ln k + \alpha \ln(p_i)$$

(5-10)

Using the reaction rate at different partial pressures and the linearization of eq. (5-10) as shown in Figure 5-7 b, a slope of 0.91 is obtained, indicating that the reaction is nearly first order in the partial pressure of ethanol.

Figure 5-8 shows the reaction mechanism for C_{3+} hydrocarbon formation from ethene in terms of elementary reactions, obtained by combining the detailed mechanistic investigation from Chapter 3 and the investigation of the experimental data in this chapter. Ethanol dehydration was found not to play a role in the production of C_{3+} hydrocarbons and, hence, is no longer included in the reaction mechanism.
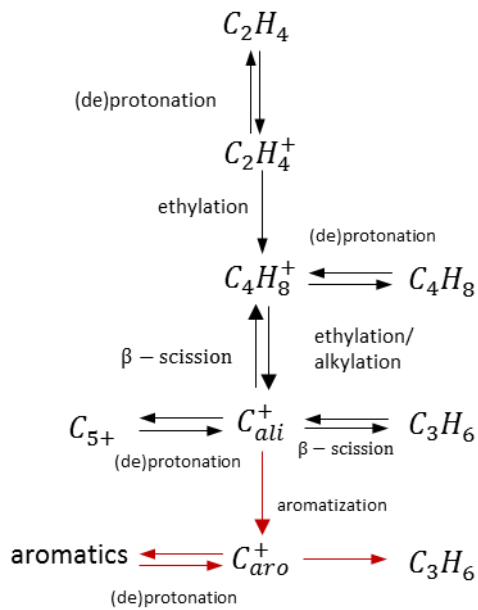
Figure 5-8: Reaction mechanism for C$_{3+}$ hydrocarbon production from ethene in terms of elementary steps. (black steps are included in the microkinetic model)

Ethene first protonates to form an activated ethyl species which can then alkylate a second ethene to form a surface butene species. This species can either deprotonate to form a gas phase butene isomer or alkylate with another gas phase olefin. This results in the formation of aliphatic surface species which can either deprotonate to form a C_{5+} olefin or undergo a β-scission to form lighter molecules. It was found in Chapter 3 that these aliphatic surface species can aromatize to

form aromatic compounds. These can then intervene in an aromatic-assisted mechanism for the production of propene. It was however indicated in Chapter 3 that the major contribution to light olefin formation corresponded to the transformation of the aliphatic surface species into light olefins. The relative importance of each elementary reaction and the origin of the induction period was however not fully explained. This can now be tackled by using single-event microkinetic modelling.

5.4 SEMK model construction

5.4.1 Reaction network

The elementary steps involved in the conversion of ethene to hydrocarbons are generated using an in-house developed network generation program, called ReNGeP [22], and are depicted in Figure 5-9.
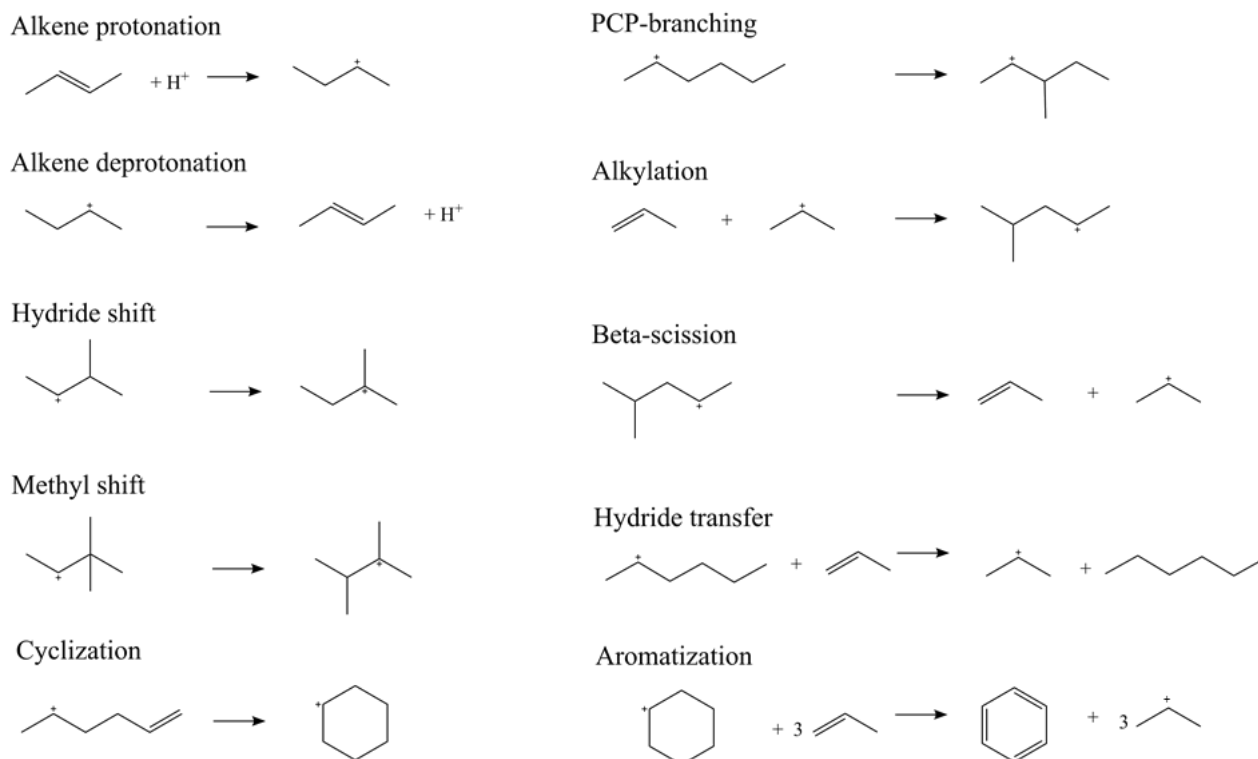
Figure 5-9: A selection of the most important elementary steps on solid acid catalysts for olefin alkylation, cracking, isomerization, cyclization and aromatization [23].

An olefin is first activated by protonation on an acid site to form a carbenium ion. This carbenium ion can either be subjected to structural rearrangement reactions such as hydride shift, methyl shift and PCP branching or to reactions which change the carbon number such as alkylation and β-scission. Hydride transfer reaction can transfer the proton from a carbenium ion to an olefin. Once an olefinic carbenium ion is formed, cyclization reactions can occur, which yield the starting molecule to form aromatic compounds via aromatization reactions. It should be noted that hydride transfer and aromatization also result in the formation of paraffins.

Typically, only secondary and tertiary carbenium ions are considered [24]. However, in MTO [10, 25], primary carbenium ions are allowed in some cases. Primary carbenium ions are far less stable than other types of carbenium ions and quantum mechanics studies and experimental observations suggest that an ethoxy species is formed on the surface [26-28]. The formation of a primary carbenium ion from the reaction of an ethyl surface species with an olefin has only been taken into account when the produced primary carbenium ion is more stable than the reactant carbenium ion. For example, the reaction of an ethyl carbenium ion with a gas phase ethene molecule yielding a primary butyl carbenium ion is considered in the reaction mechanism since no alternative reaction pathway is available:
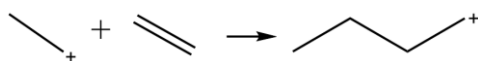
All other reactions producing a primary carbenium ion are omitted from the model. For example the reaction of an ethyl carbenium ion with propene yields 2-pentyl rather than the 2-methyl-1-butyl carbenium ion:
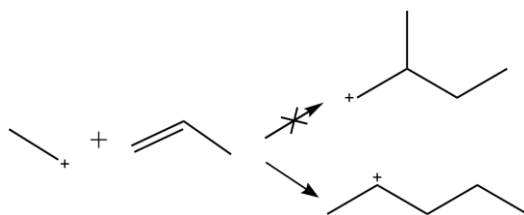
The reaction network is the result of a compromise between accounting for sufficient detail and limiting the extent of the network to what is relevant for the description of the observed data. Considering the discussions in the previous paragraphs, the following assumptions are made:

a. Double bound and branched isomers were found to be in thermodynamic equilibrium. Hence, hydride transfer, alkylshifts and PCP branching are considered as such.

b. Only hydrocarbons up to carbon number 10 have been observed and hence, the network will be generated for a maximum of 10 carbon atoms.

c. Aromatic formation was found to be negligible for all experiments considered in this work. Cyclization and aromatization are thus not considered. This also implies negligence of hydride transfer reactions which result in paraffin formation.

d. The consecutive nature of ethanol dehydration and C_{3+} hydrocarbons allows for the use of ethene as starting molecule for the production of hydrocarbons.

e. Cracking reaction with formation of ethene is not allowed.

In total, 452 olefins and 352 carbenium ions are considered formed by 682 (de)protonations, 94 ethylations, 148 alkylations and 148 β-scissions.

5.4.2 Single-event concept

The number of rate coefficients required for this reaction network corresponds to the number of elementary steps and, hence, is very large. The single-event methodology defines a unique rate coefficient for each reaction family and thus reduces the number of adjustable parameters in this model [29]. According to transition state theory, every reaction occurs via an activated complex. The standard entropy and enthalpy difference between the reactant and transition state species determines this rate coefficient as seen in the Eyring equation [30]:

$$k = \frac{k_B T}{h} \exp\left(\frac{\Delta S^{0,\ddagger}}{R}\right) \exp\left(-\frac{\Delta H^{0,\ddagger}}{RT}\right)$$

(5-11)

with k_B the Boltzmann constant, T the temperature, h Planck constant, R the universal gas constant, $\Delta S^{0,\ddagger}$ and $\Delta H^{0,\ddagger}$ the standard entropy and enthalpy of the activated complex, respectively.

The number of parameters can be reduced by introduction of the number of single events, i.e., n_e:

$$k = n_e\tilde{k} = \frac{k_B T}{h} n_e \exp\left(\frac{\Delta\tilde{S}^{0,\ddagger}}{R}\right)\exp\left(-\frac{\Delta H^{0,\ddagger}}{RT}\right) = \tilde{A}\, n_e\, \exp\left(-\frac{\Delta H^{0,\ddagger}}{RT}\right) \qquad (5\text{-}12)$$

A single-event frequency factor $\tilde{A}$ remains, which does not depend on the symmetry of the reactant and activated complex. The rate coefficient of an elementary step is thus the product of a single-event rate coefficient and the number of single-events.

The number of single events n_e is calculated using the symmetry numbers of the reactant and the transition state and provides information about the number of symmetrically equivalent pathways between the reactant and the transition state of the corresponding elementary step in the reaction family.

$$n_e = \frac{\sigma_{glob,r}}{\sigma_{glob,\ddagger}} \qquad (5\text{-}13)$$

The global symmetry number σ_{glob} is calculated as follows:

$$\sigma_{glob} = \frac{\sigma_{int}\sigma_{ext}}{2^n} \qquad (5\text{-}14)$$

with σ_{int} and σ_{ext} being, respectively, the internal and external symmetry number and n the number of chiral atoms.

In Figure 5-10, an example is given to illustrate the calculation of the number of single-events. Both the forward and reverse reaction are methyl shifts of a secondary carbenium ion to a secondary carbenium ion [31]. Identical rate coefficients would be assigned for both steps based on energetic considerations. However, it is evident from the figure that in the forward direction, no distinction can be made between the branch and the end of the chain. Hence two possible methyl groups can shift. In the reverse direction, there is only one methyl which can shift. This clearly shows that the number of single-events for the forward reaction will be double of that for the reverse reaction.
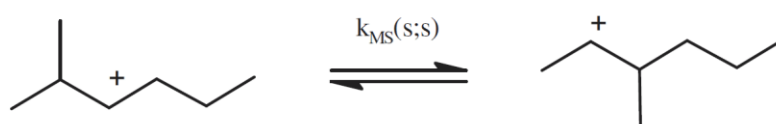
Figure 5-10: Isomerization between the 2 methyl hept-3-yl and the 3 methyl hept-2-yl ion via a secondary–secondary methyl-shift reaction [31].

5.4.3 Rate equations

As illustrated in paragraph 5.3.1, the olefin isomers were found to be in thermodynamic equilibrium and thus hydride shift, methyl shift and PCP branching do not require corresponding rate coefficients in the model. The thermodynamic equilibrium established between olefins with the same carbon number is accounted for in the kinetic model by redistribution of the net rate of formation of the alkenes according to the thermodynamic equilibrium at the reaction conditions considered. These equilibrium coefficients are calculated using the Bensons group contribution method [32]. The elementary steps thus considered for the production of C_{3+} hydrocarbons on acid sites are ethylation, alkylation and β-scission.

The rates of the elementary steps are calculated from the law of mass action. For ethylation, three single-event rate coefficients are considered depending on the type of product carbenium ion (n), that is, primary, i.e., the dimerization of ethene to 1-butene, secondary or tertiary:

$$r_{\text{eth(p,n)}} = n_e \tilde{k}_{\text{eth(p,n)}} C^+_{C2H4} \, p_j \qquad (5\text{-}15)$$

The rate coefficients for alkylation reactions depend on the nature of the carbenium ions that participate as reactant (m) and product (n), that is, secondary-secondary, secondary-tertiary, tertiary-secondary and tertiary-tertiary but not on the olefin that is being consumed:

$$r_{alk(m,n)} = n_e \tilde{k}_{alk(m,n)} C_i^+ p_j \qquad (5\text{-}16)$$

Similar considerations are taken into account for β-scission and also result in four different kinds of rate coefficients, equally depending on the type of carbenium ions involved:

$$r_{bs(m,n)} = n_e \tilde{k}_{bs(m,n)} C_i \qquad (5\text{-}17)$$

The number of parameters to be estimated is reduced by considering alkylation as the reverse from cracking and corresponding activation energies are calculated by applying thermodynamic consistency as illustrated in Figure 5-11.
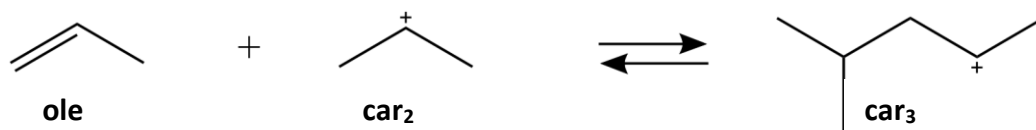
Figure 5-11: Alkylation reaction between propene (ole₁) and a 2-propyl carbenium ion (car₂) forming 4-methyl-2-pentyl carbenium ion (car₃), and the reverse β-scission reaction.

The forward (alkylation) and reverse (β-scission) activation energy can be related to each other via equation (5-18), which indicates thermodynamic consistency as displayed in the equation below:

$$E_{a,alk} = E_{a,bs} - \Delta_r H^0_{alk} \qquad (5\text{-}18)$$

The standard reaction enthalpy for alkylation can be calculated from the standard formation enthalpy of the components involved:

$$\Delta_r H^0_{alk} = \Delta_f H^0_{ole3} - (\Delta_f H^0_{ole1} + \Delta_f H^0_{ole2}) \qquad (5\text{-}19)$$

The standard formation enthalpy of these species involved can be determined with Benson's group contribution method.

The concentrations of the carbenium ions are obtained from the protonation equilibrium and the corresponding olefin which leads to this carbenium ion:

$$C_i^+ = K_{prot,i} \, p_i \, C_{H^+} \qquad (5\text{-}20)$$

Similar to the rate coefficients of the elementary steps, symmetry contributions in the protonation equilibrium coefficients are accounted for via symmetry numbers of the alkene and the carbenium ion involved:

$$K_{prot,i} = \frac{\sigma_{glob,r}}{\sigma_{glob,\ddagger}} \widetilde{K}_{prot,i} \tag{5-21}$$

The number of single-event protonation/deprotonation equilibrium coefficients is reduced by expressing them as a product of the single-event protonation equilibrium coefficient of a well-chosen reference alkene per carbon number and the single event isomerization equilibrium coefficients between the alkene *i* and the reference alkene *j*, $\widetilde{K}_{isom,i,j}$:

$$\widetilde{K}_{prot,i} = \widetilde{K}_{isom,i,j} \widetilde{K}_{prot,r} \tag{5-22}$$

The single-event protonation equilibrium coefficient of this reference alkene comprises both the physical adsorption of alkene and the subsequent protonation on the acid site and is calculated using thermodynamic data generated with Benson's group contribution method. Physisorption is accounted for, according to the experimental observations made by Denayer et al. [33]. It is assumed that the protonation enthalpy, ΔH_{prot}, only depends on the type of carbenium ion formed (e.g. primary, secondary and tertiary).

The concentration of available acid sites can be determined via the acid site balance:

$$C_{H^+} = C_t - \sum_{k=1}^{n_{car}} C_k^+ \tag{5-23}$$

The net rate of formation of an olefin is determined as the sum of the reaction rates, i.e., $r_{i,j}$ as determined via eqs. (5-15) to (5-17), in which the olefin or the corresponding carbenium ion is involved:

$$R_i = \sum_{j=1}^{n_{elem}} \sum_{i=1}^{n_{ole}} \alpha_{i,j} \, r_{i,j} \tag{5-24}$$

5.4.4 Single-event pre-exponential factors calculation

The single-event pre-exponential factor for an elementary step j is given by

$$\widetilde{A}_j = \frac{k_B T}{h} \exp\left(\frac{\Delta \widetilde{S}^{0,\ddagger}}{R}\right)$$

(5-25)

It has been assumed that the entropy change associated to a protonation step is dominated by the loss of translation entropy. The translation entropy of a gas phase molecule has been approximated using the Sackur-Tetrode equation:

$$\Delta S^0_{prot} = \Delta S^0_{trans} = R \ln\left(\frac{R\,T}{p^0 N_A}\left(\frac{2\pi\left(\frac{M_w}{N_A}\right)k_B T}{h^2}\right)^{\frac{3}{2}}\right) + \frac{5}{2}\,R$$

(5-26)

For β-scission, it has been assumed that the entropy change is equal to the one translational degree of freedom of the reference olefin. The single-event pre-exponential factor for alkylation and ethylation is calculated from the forward single-event pre-exponential factor and the single-event reaction entropy, following the principle of microscopic reversibility:

$$\widetilde{A}_{alk} = \frac{\widetilde{A}_{bs}}{\exp\left(\frac{\Delta \widetilde{S}^0_{r,j}}{R}\right)}$$

(5-27)

The single-event entropy change of an elementary reaction j, $\Delta \widetilde{S}^0_{r,j}$, is calculated as:

$$\Delta \widetilde{S}^0_{r,j} = \sum_{i=1}^{n_{prod}} v_i \widetilde{S}^0_i - \sum_{k=1}^{n_{react}} v_k \widetilde{S}^0_k$$

(5-28)

The standard entropies of the associated molecules in the gas phase, $\widetilde{S}^0_{gas,i}$, are calculated using the Benson group contribution method [32].

5.5 Model regression and assessment

According to the model proposed, a total of twenty parameter values needs to be determined i.e., 10 activation energies and 10 pre-exponential factors. The entropy changes are calculated based on the assumptions made in the previous paragraph. The remaining parameters are estimated by model regression to the experimental data. These parameters are three catalyst descriptors, i.e., the protonation enthalpies for primary, secondary and tertiary carbenium ions, and 7 kinetic descriptors, i.e., four activation energies for β-scission which also correspond to the activation energies for alkylation via thermodynamic consistency and three activation energies for ethylation towards primary, secondary and tertiary carbenium ions. Table 5-2 gives an overview of the estimates for the remaining kinetic model parameters together with reported literature values. The F_{regres} value for the model significance amounts to 1106 which largely exceeds the corresponding tabulated F value. It is evident from the parameter estimates and their individual confidence intervals that all of them are statistically significant.

The alkene standard protonation enthalpies to form secondary carbenium ions is estimated significantly as -74.1 ± 8.6 kJ mol^{-1}, while the protonation enthalpy towards tertiary intermediates amounts to -101.6 ± 4.2 kJ mol^{-1}. The difference in stability between secondary and tertiary carbenium ions is 28 kJ mol^{-1}, which is close to the 30 kJ mol^{-1} reported in literature [34]. The standard protonation enthalpy of ethene (-52.9 ± 12.1 kJ mol^{-1}) is considerably higher than estimated by Kumar et al., i.e., - 11 kJ mol^{-1} [10]. This estimated standard protonation enthalpy of ethene is more in line with the value found for the protonation of methanol [10] and the formation of alkoxide species [35].

As can be seen from Table 5-2, the values for the activation energies for β-scission reactions found in literature differ widely. The activation energies estimated in this work fall well within the ranges described in literature. It should be noted that the activation energies for β-scission agree quite well with those reported by Van Borm et al. [9], i.e., $E_{a,bs}$ (s,s) = 126 kJ mol^{-1}, $E_{a,bs}$ (s,t) = 119 kJ mol^{-1}, $E_{a,bs}$ (t,s) = 154 kJ mol^{-1} and $E_{a,bs}$ (t,t) = 140 kJ mol^{-1}.

It can be expected that less stable reactants and more stable products result in lower activation energies when comparing different types of ethylation reactions. From Table 5-2, it is clear that this statement is valid and that a higher activation is required for the reaction of a primary surface species with a gas phase olefin to form a primary carbenium ion, i.e., the dimerization of ethene to 1-butene, than the reaction of a primary surface species to form a tertiary carbenium ion.

Table 5-2: Model parameters as well as statistical performance indicators, all at 95% confidence level, determined by non-linear regression of the model, given by integration of eq. (5-9) in which the net rates of formation are given by eq. (5-24) and the pre-exponential parameters as described in 5.4.4, to the experimental data measured at the operating conditions given in Table 5-1.

	Estimated values (kJ mol^{-1})	Reported values (kJ mol^{-1})	Reference
$\Delta H_p\ (p)$	-52.9 ± 12.1	-11[a]	[10]
$\Delta H_p\ (s)$	-74.1 ± 8.6	-71	[36]
$\Delta H_p\ (t)$	-101.6 ± 4.2	-101	[36]
$E_{a,bs}\ (s,s)$	119.6 ± 5.4	$115\ \text{-}238$	[9, 34, 37-40]
$E_{a,bs}\ (s,t)$	118.3 ± 6.1	$115 - 161$	[9, 34, 37-40]
$E_{a,bs}\ (t,s)$	178.4 ± 7.3	$149\text{-}\ 202$	[9, 34, 37-40]
$E_{a,bs}\ (t,t)$	135.7 ± 7.1	$102 - 243$	[9, 34, 37-40]
$E_{a,et}\ (p,p)$	93.9 ± 14.4	132[b]	[10]
$E_{a,et}\ (p,s)$	60.1 ± 12.1	93[b]	[10]
$E_{a,et}\ (p,t)$	59.5 ± 10.1	55[b]	[10]
significance (tabulated value)		1106 (2.8)	

[a] ethene protonation enthalpy to ethyl carbenium ion

[b] activation energies for methylation reaction
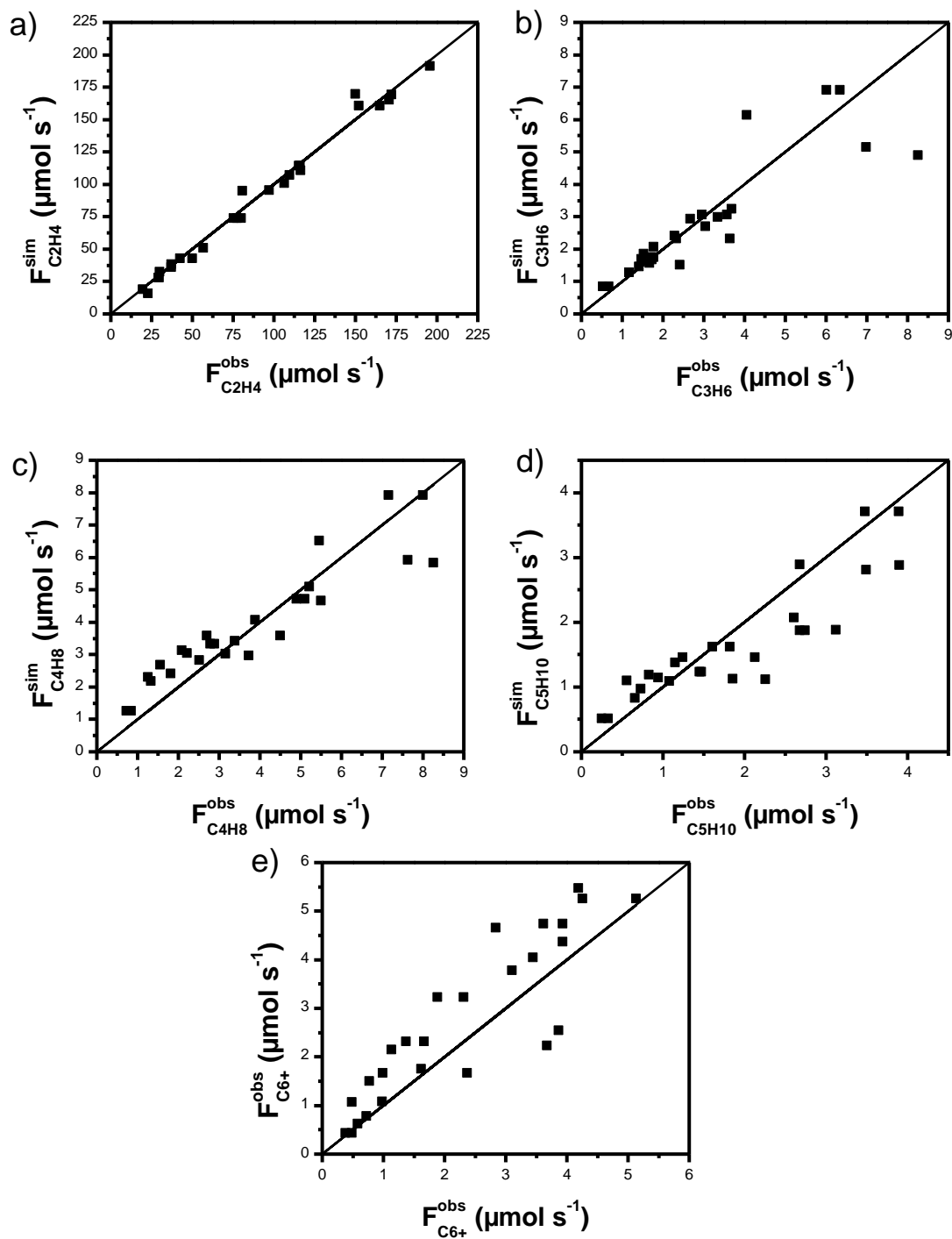
Figure 5-12: Parity diagrams for the molar outlet flow rate of a) ethene, b) propene, c) butene isomers, c) pentene isomers and e) C$_{6+}$ hydrocarbons as determined by non-linear regression of the model, given by integration of eq. (5-9) in which the net rates of formation are given by eq. (5-24) with the parameters given in Table 5-2 and the pre-exponential parameters as described in 5.4.4, to the experimental data measured at the operating conditions given in Table 5-1.

The SEMK model simulates the outlet flow rates rather well as can be seen from the parity diagrams shown in Figure 5-12. A good agreement between model simulations and experiments is claimed taking into account the complex product pattern encountered in ethene conversion.

The binary correlation coefficients between the parameter estimates are given in Table 5-3. The binary correlation coefficient between the standard protonation enthalpy towards primary surface species, i.e. ΔH_p (p), and the ethylation activation energy for the reaction of a primary surface species with a gas phase olefin to form a primary carbenium ion, i.e. $E_{a,et}$ (p,p) which corresponds to the dimerization of ethene, is 0.99 which could be expected as both parameters have a direct effect on the dimerization of ethene. Also the activation energies of (s,s) and (s,t) β-scission appear to be correlated.

Table 5-3: Binary correlation coefficient matrix as determined by non-linear regression of the model given by integration of eq. (5-9) in which the net rates of formation are given by eq. (5-24) with the parameters given in Table 5-2 to the experimental data measured at the operating conditions given in Table 5-1.

	ΔH_p (p)	ΔH_p (s)	ΔH_p (t)	$E_{a,bs}$ (s,s)	$E_{a,bs}$ (s,t)	$E_{a,bs}$ (t,s)	$E_{a,bs}$ (t,t)	$E_{a,et}$ (p,p)	$E_{a,et}$ (p,s)	$E_{a,et}$ (p,t)
ΔH_p (p)	1.00	-0.71	-0.13	0.02	0.06	0.13	0.12	-0.99	-0.99	-0.42
ΔH_p (s)	-0.71	1.00	-0.09	0.12	0.12	0.15	0.17	0.69	0.68	0.47
ΔH_p (t)	-0.13	-0.10	1.00	0.19	0.12	-0.50	-0.60	0.10	0.11	0.28
$E_{a,bs}$ (s,s)	0.02	0.12	0.19	1.00	0.96	0.69	0.53	-0.07	-0.04	0.17
$E_{a,bs}$ (s,t)	0.06	0.12	0.12	0.96	1.00	0.78	0.66	-0.12	-0.08	0.19
$E_{a,bs}$ (t,s)	0.13	0.15	-0.50	0.69	0.78	1.00	0.93	-0.18	-0.14	0.01
$E_{a,bs}$ (t,t)	0.12	0.17	-0.60	0.53	0.66	0.93	1.00	-0.16	-0.12	0.00
$E_{a,et}$ (p,p)	-0.99	0.6	0.10	-0.07	-0.12	-0.18	-0.16	1.00	0.98	0.42
$E_{a,et}$ (p,s)	-0.99	0.68	0.11	-0.04	-0.08	-0.14	-0.12	0.98	1.00	0.31
$E_{a,et}$ (p,t)	-0.42	0.47	0.28	0.17	0.19	0.01	0.00	0.42	0.31	1.00

As can be seen in Figure 5-13, the model is capable to simulate the observed induction period for C$_{3+}$ hydrocarbon formation. The induction period is rather independent of temperature as already mentioned in the experimental observations (see Figure 5-6) and this is also reflected in the model simulation. Also, the effect of temperature on the production of hydrocarbons is simulated adequately.
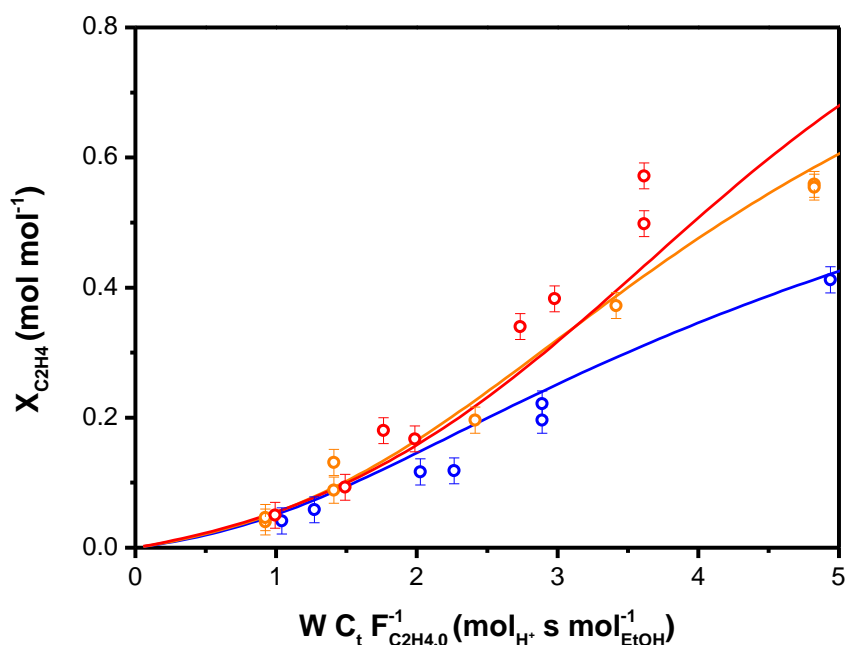
Figure 5-13: C$_2$ conversion, as defined in 2.4.2, as a function of ethene site time at three different temperature 573 K (blue), 593 K (orange) and 623 K (red). ($p_{C2H4,0}$ = 27 kPa). Symbols represent experimental observations, lines represent model simulations. Model simulations are obtained by integration of eq. (5-9) in which the net rates of formation are given by eq. (5-24) and the parameter values reported in Table 5-2.

A more detailed analysis of the individual reaction rates at 573 K is shown in Figure 5-14. It is clear from Figure 5-14 a) that for the given reaction conditions the induction period is indeed present when looking at the conversion as a function of ethene site time. This is reflected in the disappearance rate of ethene, i.e. R_{C2}, which starts around 5 mmol kg^{-1} s^{-1} at a conversion of 0.01 and gradually increases to a maximum production rate of 45 mmol kg^{-1} s^{-1}. After this, the disappearance rate of ethene drops to 30 mmol kg^{-1} s^{-1} at a conversion of 0.45. It should be noted that this rate corresponds nicely to the rate calculated from the experimental points, i.e. 31 mmol kg^{-1} s^{-1}.
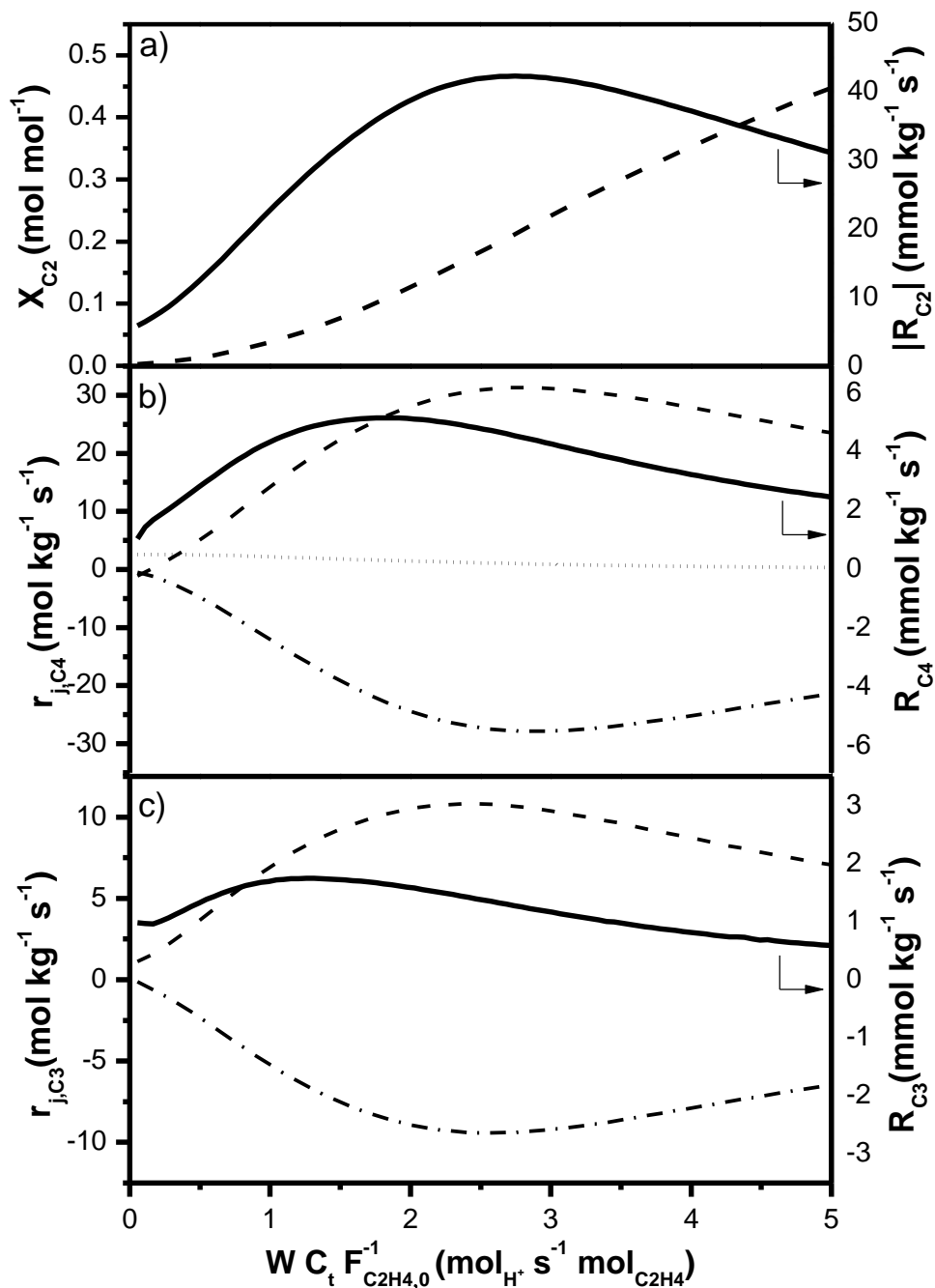
Figure 5-14: a) Simulated ethene conversion, i.e. X_{C2} (dashed line) as defined in 2.4.2, and the corresponding disappearance rate of ethene, i.e. R_{C2}, b) total production rate of butene isomers, i.e. R_{C4}, (full line) and the individual butene isomers production rates, i.e. $r_{j,C4}$, via dimerization (dotted line), ethylation (dashed-dotted line) and alkylation/β-scission (dashed line) and c) total production rate of propene, i.e. R_{C3}, (full line) and the individual propene production rates, i.e. $r_{j,C3}$, via ethylation (dashed-dotted line) and alkylation/β-scission (dashed line) as function of ethene site time. Model simulations obtained by integration of eq. (5-9) in which the net rates of formation are given by eq. (5-24) and the parameter values reported in Table 5-2. (T = 573 K, $p_{C2H4,0}$ = 27 kPa)

A similar maximum is found for the total production rate of butene isomers, i.e. R_{C4}, as shown in shown in Figure 5-14 b. Initially, butene is produced from the dimerization of ethene at low rate, i.e. 3 mmol kg^{-1} s^{-1} at X_{C2} = 0.01. Once sufficient 1-butene is formed, these species will engage in reactions to form C_{5+} hydrocarbons as can be seen by the disappearance rate of butene isomers via the ethylation reactions. In the beginning of the reaction (X_{C2} < 0.02), alkylation is dominant, but it is rapidly overtaken by the β-scission reactions. A decline in total production rate of butene isomers is observed at a conversion of 0.1. The behaviour of propene production is given in Figure 5-14 c and can be considered to be quite identical: a maximum total production rate is observed albeit at a lower ethene site time than the total production rate of butene. Also for propene, the ratio of β-scission reactions and alkylation reaction is in favour of the cracking reactions.

5.6 Conclusions

H-ZSM-5 is found to be a stable catalyst for the production of hydrocarbons from ethanol and ethene. Logical trends for the effect of temperature, partial pressure and water content are observed in the experimental data set. The autocatalytic behaviour is present at all conditions considered in this work. Comparison with the production of higher hydrocarbons from ethene as starting molecule, shows that the same net production rate is observed. This confirms the statement that ethene is the real reactant for higher hydrocarbon production made in Chapter 3.

The kinetics governing the formation of these higher hydrocarbons can be described using the developed microkinetic model. The single-event concept allows to reduce the number of adjustable parameters. The estimated activation energies and protonation enthalpies reflect the trends as expected considering the type of carbenium ions involved. The induction period for the formation of higher hydrocarbons is also described by the model. The rate analysis illustrates the capabilities of a microkinetic model for reaction mechanism investigation and indicated the dimerization of ethene as the elementary step responsible for the autocatalytic behaviour. An accurate microkinetic model offers the advantage that it can be used for rational catalyst design for future purposes as illustrated in the *information-driven catalyst design* as discussed in Chapter 2.

5.7 References

[1] A.T. Aguayo, A.G. Gayubo, A.M. Tarrio, A. Atutxa, J. Bilbao, Study of operating variables in the transformation of aqueous ethanol into hydrocarbons on an HZSM-5 zeolite, Journal of Chemical Technology and Biotechnology, 77 (2002) 211-216.

[2] E. Costa, A. Uguina, J. Aguado, P.J. Hernandez, Ethanol to gasoline process: effect of variables, mechanism, and kinetics, Industrial & Engineering Chemistry Process Design and Development, 24 (1985) 239-244.

[3] C.L. Chang, A.L. DeVera, D.J. Miller, A lumped kinetic model for dehydration of ethanol to hydrocarbons over H-ZSM-5, Chemical Engineering Communications, 95 (1990) 27-39.

[4] A.G. Gayubo, A.M. Tarrío, A.T. Aguayo, M. Olazar, J. Bilbao, Kinetic Modelling of the Transformation of Aqueous Ethanol into Hydrocarbons on a HZSM-5 Zeolite, Industrial & Engineering Chemistry Research, 40 (2001) 3467-3474.

[5] A.T. Aguayo, A.G. Gayubo, A. Atutxa, M. Olazar, J. Bilbao, Catalyst deactivation by coke in the transformation of aqueous ethanol into hydrocarbons. Kinetic modeling and acidity deterioration of the catalyst, Industrial & Engineering Chemistry Research, 41 (2002) 4216-4224.

[6] A.G. Gayubo, A. Alonso, B. Valle, A.s.T. Aguayo, J. Bilbao, Kinetic Model for the Transformation of Bioethanol into Olefins over a HZSM-5 Zeolite Treated with Alkali, Industrial & Engineering Chemistry Research, 49 (2010) 10836–10844.

[7] A.G. Gayubo, A. Alonso, B. Valle, A.T. Aguayo, M. Olazar, J. Bilbao, Kinetic modelling for the transformation of bioethanol into olefins on a hydrothermally stable Ni-HZSM-5 catalyst considering the deactivation by coke, Chemical Engineering Journal, 167 (2011) 262-277.

[8] M.A. Baltanas, G.F. Froment, Computer generation of reaction networks and calculation of product distributions in the hydroisomerization and hydrocracking of paraffins on Pt-containing bifunctional catalysts, Computers & Chemical Engineering, 9 (1985) 71-81.

[9] R. Van Borm, M.F. Reyniers, G.B. Marin, Catalytic cracking of alkanes on FAU: Single-event microkinetic modeling including acidity descriptors, AIChE Journal, 58 (2012) 2202-2215.

[10] P. Kumar, J.W. Thybaut, S. Svelle, U. Olsbye, G.B. Marin, Single-Event Microkinetics for Methanol to Olefins on H-ZSM-5, Industrial & Engineering Chemistry Research, 52 (2012) 1491-1507.

[11] G. Lozano-Blanco, K. Surla, J.W. Thybaut, G.B. Marin, Extension of the Single-Event Methodology to Metal Catalysis: Application to Fischer-Tropsch Synthesis, Oil & Gas Science and Technology-Revue D Ifp Energies Nouvelles, 66 (2011) 423-435.

[12] K. Toch, J.W. Thybaut, G.B. Marin, Ethene oligomerization on Ni-SiO2-Al2O3: Experimental investigation and Single-Event MicroKinetic modeling, Applied Catalysis A: General, 489 (2015) 292-304.

[13] B.D. Vandegehuchte, J.W. Thybaut, A. Martínez, M.A. Arribas, G.B. Marin, n-Hexadecane hydrocracking Single-Event MicroKinetics on Pt/H-beta, Applied Catalysis A: General, 441–442 (2012) 10-20.

[14] K. Van der Borght, K. Toch, V.V. Galvita, J.W. Thybaut, G.B. Marin, Information-Driven Catalyst Design Based on High-Throughput Intrinsic Kinetics, Catalysts, 5 (2015) 1948-1968.

[15] H.H. Rosenbrock, An automatic method for finding the greatest or least value of a function, The Computer Journal, 3 (1960) 175-184.

[16] J.J. Moré, The Levenberg-Marquardt algorithm: implementation and theory, in: Numerical analysis, Springer, 1978, pp. 105-116.

[17] Netlib, (http://www.netlib.org), accessed on 30/5/2016

[18] R.J. Quann, L.A. Green, S.A. Tabak, F.J. Krambeck, Chemistry of Olefin Oligomerization over Zsm-5 Catalyst, Industrial & Engineering Chemistry Research, 27 (1988) 565-570.

[19] J. Oudejans, P. Van Den Oosterkamp, H. Van Bekkum, Conversion of ethanol over zeolite H-ZSM-5 in the presence of water, Applied Catalysis, 3 (1982) 109-115.

[20] T. Nguyen, R. Le Van Mao, Conversion of ethanol in aqueous solution over ZSM-5 zeolites: study of the reaction network, Applied catalysis, 58 (1990) 119-129.

[21] A.K. Talukdar, K.G. Bhattacharyya, S. Sivasanker, HZSM-5 catalysed conversion of aqueous ethanol to hydrocarbons, Applied Catalysis A: General, 148 (1997) 357-371.

[22] G.G. Martens, J.W. Thybaut, G.B. Marin, Single-event rate parameters for the hydrocracking of cycloalkanes on Pt/US-Y zeolites, Industrial & Engineering Chemistry Research, 40 (2001) 1832-1844.

[23] J.A. Martens, P. Jacobs, Chapter 12 Introduction to Acid Catalysis with Zeolites in Hydrocarbon Reactions, in: E.M.F. H. van Bekkum, J.C. Jansen (Eds.) Studies in Surface Science and Catalysis, Elsevier, 1991.

[24] B.D. Vandegehuchte, J.W. Thybaut, A. Martinez, M.A. Arribas, G.B. Marin, n-Hexadecane hydrocracking Single-Event MicroKinetics on Pt/H-beta, Applied Catalysis a-General, 441 (2012) 10-20.

[25] T.-Y. Park, G.F. Froment, Kinetic modeling of the methanol to olefins process. 1. Model formulation, Industrial & engineering chemistry research, 40 (2001) 4172-4186.

[26] J.F. Haw, J.B. Nicholas, T. Xu, L.W. Beck, D.B. Ferguson, Physical organic chemistry of solid acids: Lessons from in situ NMR and theoretical chemistry, Accounts of chemical research, 29 (1996) 259-267.

[27] V. Kazansky, M. Frash, R. Van Santen, Quantumchemical study of the isobutane cracking on zeolites, Applied Catalysis A: General, 146 (1996) 225-247.

[28] J.N. Kondo, K. Ito, E. Yoda, F. Wakabayashi, K. Domen, An ethoxy intermediate in ethanol dehydration on bronsted acid sites in zeolite, Journal of Physical Chemistry B, 109 (2005) 10969-10972.

[29] J.W. Thybaut, G.B. Marin, Single-Event MicroKinetics: Catalyst design for complex reaction networks, Journal of Catalysis, 308 (2013) 352-362.

[30] H. Eyring, The Activated Complex and the Absolute Rate of Chemical Reactions, Chemical Reviews, 17 (1935) 65-77.

[31] J. Thybaut, G. Marin, Single-Event MicroKinetics: Catalyst design for complex reaction networks, Journal of Catalysis, 308 (2013) 352-362.

[32] S.W. Benson, F.R. Cruickshank, D.M. Golden, G.R. Haugen, H.E. O'Neal, A.S. Rodgers, R. Shaw, R. Walsh, Additivity rules for the estimation of thermochemical properties, Chemical Reviews, 69 (1969) 279-324.

[33] J.F. Denayer, W. Souverijns, P.A. Jacobs, J.A. Martens, G.V. Baron, High-temperature low-pressure adsorption of branched C5-C8 alkanes on zeolite beta, ZSM-5, ZSM-22, zeolite Y, and mordenite, The Journal of Physical Chemistry B, 102 (1998) 4588-4597.

[34] J.W. Thybaut, C.S.L. Narasimhan, G.B. Marin, J.F.M. Denayer, G.V. Baron, P.A. Jacobs, J.A. Martens, Alkylcarbenium ion concentrations in zeolite pores during octane hydrocracking on Pt/H-USY zeolite, Catalysis Letters, 94 (2004) 81-88.

[35] C.M. Nguyen, B.A. De Moor, M.F. Reyniers, G.B. Marin, Physisorption and Chemisorption of Linear Alkenes in Zeolites: A Combined QM-Pot(MP2//B3LYP:GULP)-Statistical Thermodynamics Study, Journal of Physical Chemistry C, 115 (2011) 23831-23847.

[36] B.D. Vandegehuchte, J.W. Thybaut, G.B. Marin, Unraveling Diffusion and Other Shape Selectivity Effects in ZSM5 Using n-Hexane Hydroconversion Single-Event Microkinetics, Industrial & Engineering Chemistry Research, 53 (2014) 15333-15347.

[37] M.A. Sanchez-Castillo, N. Agarwal, C. Miller, R.D. Cortright, R.J. Madon, J.A. Dumesic, Reaction kinetics study and analysis of reaction schemes for isobutane conversion over USY zeolite, Journal of Catalysis, 205 (2002) 67-85.

[38] G.G. Martens, G.B. Marin, J.A. Martens, P.A. Jacobs, G.V. Baroni, A fundamental kinetic model for hydrocracking of C-8 to C-12 alkanes on Pt/US-Y zeolites, Journal of Catalysis, 195 (2000) 253-267.

[39] R. Quintana-Solorzano, J.W. Thybaut, G.B. Marin, A single-event microkinetic analysis of the catalytic cracking of (cyclo)alkanes on an equilibrium catalyst in the absence of coke formation, Chemical Engineering Science, 62 (2007) 5033-5038.

[40] G. Yaluris, R.J. Madon, J.A. Dumesic, Catalytic ramifications of steam deactivation of Y zeolites: An analysis using 2-methylhexane cracking, Journal of Catalysis, 186 (1999) 134-146.

Chapter 6

Ethanol to higher hydrocarbons over Ni, Ga, Fe-modified ZSM-5: effect of metal content

In the previous chapters, the reaction mechanism of ethanol dehydration and the subsequent production of higher hydrocarbons is investigated. It could be seen that the majority of the products were olefins with only minor quantities of aromatics. Effectively tuning the product distribution via catalyst modification is the ultimate goal in the search for industrial implementation. This modification can be performed using a variety of techniques of which post-synthesis metal modification is one of the most popular. The effect of metal content on catalyst properties was studied in this chapter by comparing unmodified H-ZSM-5 and 0.5-7 wt.% Ga, Fe and Ni modified H-ZSM-5 in the ethanol conversion to hydrocarbons at 623 K by combining detailed catalyst characterization (XRD, TEM, N_2 adsorption, H_2-TPR and NH_3-TPD) and catalytic testing.

6.1 Introduction

Post-synthesis modifications are often performed to improve catalyst performance. Post synthesis modifications of zeolites that are often encountered in literature are impregnation and ion exchange with metals salts resulting in metal modified zeolites, phosphorus modification, alkali treatment and steaming. These modifications claim to result either in improved hydrothermal stability, reduced deactivation, or increased activity or selectivity towards a specific product class [1]. In this chapter, the focus lies on metal modified zeolites.

The metal function in zeolites depends on the process. In hydrocracking for example, both the metal and the acid function have clear distinct functions: the metal dehydrogenates the alkane and forms an olefin which in turn is protonated on the acid site where the formed carbenium ion is isomerized and cracked and then undergoes the reverse steps [2]. There are however numerous processes where the metal function is not fully understood and explained [3, 4]. Addition of gallium showed good results for light alkene and alkane aromatization and cracking reactions [5, 6] while the effect of nickel was demonstrated in catalytic cracking [7]. Nickel catalyzed reaction pathways have also been described on various supports in the literature [8] where it is often used for olefin oligomerization and, more specifically, ethene oligomerization to linear α-olefin, where the active species are identified as Ni^{2+} ions. The activity enhancing properties of iron modification in catalytic cracking have also been claimed [9].

Addition of metal to H-ZSM-5 in the ethanol conversion to hydrocarbons has already been investigated for nickel [10], iron [11, 12], gallium [13], molybdenum [14] and rare earth metals [15]. Nickel is reported to improve the hydrothermal stability of the catalyst in ethanol conversion to higher hydrocarbons by altering the acid site balance and thus having also an effect on product distribution. Addition of iron to H-ZSM-5 is claimed to reduce the formation of aromatics and paraffins, while gallium has the opposite effect: an increased formation of aromatics is reported. The origins of these effects are explained by either the suppression or the promotion of hydrogen transfer reactions. However, little attention is given to the effect of metal addition on the catalyst properties, reaction mechanism and product selectivity and more specifically ethene selectivity.

Assessing the effects of metal content on catalyst performance based on literature can be complicated due to the different reaction conditions, different amounts of metal, and deactivation. Furthermore, only few comparative studies are available [16, 17].

In this work, metal modification of H-ZSM-5 is performed in attempt to effectively tune product selectivities. A systematic approach is applied where Fe, Ga and Ni loaded ZSM-5 catalysts with different amounts of metal are evaluated to see the influence of metal content on catalyst properties. Catalytic activity tests are performed to assess the effect of metal introduction on the product formation at same conversion and are combined with detailed catalyst characterization to reveal whether metal introduction is the correct way to modify product selectivity.

6.2 Procedures

6.2.1 Catalyst synthesis

The zeolite used in this work is commercially available NH_4-ZSM-5 (Zeolyst, CBV3024) with a Si/Al = 15. The acid form was obtained by calcining at 823 K for 3 h with a temperature ramp of 1 K min^{-1} is taken as the reference (H-ZSM-5). Ni, Ga and Fe loaded ZSM-5 were produced by incipient wetness impregnation. A metal precursor ($Ni(NO_3)_3.6H_2O$, $Ga(NO_3)_3.xH_2O$ or $Fe(NO_3).9H_2O$) containing solution was added to the reference catalyst (H-ZSM-5) under continuous stirring. The solvent was removed by drying for 5 h at 393 K. The catalysts were then calcined at 823 K for 3 h with a temperature ramp of 1 K min^{-1}.

The objective was to obtain samples with a nominal value of 1 wt.%, 2 wt.%, 4 wt.% and 7 wt.% metal onto H-ZSM-5 (Si/Al = 15). The synthesized samples will be named #M/H-ZSM-5 where M indicates the metal deposited and # the nominal value of metal deposition on the pristine H-ZSM-5 (Si/Al = 15). Actual metal amounts varied from 0.6 to 7.1 wt.% as verified by means of inductively coupled plasma emission spectrometry (ICP-AES) (IRIS Advantage system, Thermo Jarell Ash), and are listed in Table 6-1.

Table 6-1: Properties of as-prepared catalysts. M is the amount of metal in the catalyst, A_{BET} is the BET surface area, V_p the pore volume, $T_{d,max}$ is the maximum of the desorption peak in the following temperature ranges: 373 – 473 K, 474 – 573 K and 573 – 773 K and C_t is the total concentration of available acid sites.

Sample Name	M^a	A_{BET}^b	$V_{pore}{}^c$	$T_{M,}$ (K) ^{d}	T_M (K) ^{d}	T_M(K) ^{d}	C_t^d
	(wt.%)	(10^3 m² kg$_{cat}^{-1}$)	(10^{-5} cm² kg$_{cat}^{-1}$)	373 – 473 K	573 – 773 K	473– 573 K	(mol kg$_{cat}^{-1}$)
H-ZSM-5	0.0	336	9.6	463	648	/	0.75 ± 0.05
1Fe/H-ZSM-5	0.6	327	9.2	453	643	/	0.80 ± 0.05
2Fe/H-ZSM-5	1.5	325	9.3	454	638	/	0.59 ± 0.04
4Fe/H-ZSM-5	2.7	305	9.6	454	633	/	0.50 ± 0.04
7Fe/H-ZSM-5	5.9	277	7.2	458	620	503	0.46 ± 0.03
1Ni/H-ZSM-5	0.8	320	9.2	459	633	/	0.81 ± 0.05
2Ni/H-ZSM-5	1.6	295	9.0	455	628	/	0.71 ± 0.05
4Ni/H-ZSM-5	3.9	274	8.1	453	623	500	0.61 ± 0.04
7Ni/H-ZSM-5	7.1	252	7.3	454	614	517	0.51 ± 0.04
1Ga/H-ZSM-5	0.7	320	9.5	459	642	/	0.77 ± 0.05
2Ga/H-ZSM-5	1.4	306	9.6	458	640	/	0.70 ± 0.04
4Ga/H-ZSM-5	3.2	304	8.2	453	632	/	0.55 ± 0.04
7Ga/H-ZSM-5	5.8	271	7.8	457	627	524	0.51 ± 0.04

^{a} determined by ICP/AES ^{b} determined by N$_2$ adsorption - BET equation ^{c} determined by N$_2$ adsorption – *t-plot*
^{d} calculated via deconvolution of the NH$_3$-TPD profiles

6.2.2 Catalyst performance testing

Catalyst testing was performed in a tubular reactor specifically designed for the screening of catalysts (HTK-S as described in Chapter 2). A feed consisting of ethanol mixed with helium as a carrier gas was used. The inlet pressure of ethanol was kept at 10 kPa while the total pressure was 101 kPa. The effect of space time, W/F^0_{EtOH} on the product distribution was evaluated at 623 K between 1 - 27 kg_{cat} s mol^{-1}.

The molar fraction of component *i* in the effluent is expressed as

$$y_i = \frac{CN_i\, F_i}{\sum_{i=1}^{n} CN_i\, F_i}$$

(6-1)

where y_i is the molar fraction of component *i* in the outlet stream, F_i the molar outlet flow rate of component *i*, CN_i the number of carbon atoms in component *i* and *n* the number of components. Definitions of conversion and selectivity are given in Chapter 2.

The space time yield of component or product class *i* can be defined as:

$$\text{Space time yield}_i = \frac{F_i}{W}$$

(6-2)

with F_i the molar outlet flowrate of component or product class *i* and W the catalyst mass.

The site-time yield is used to compare the activity of the catalysts and is defined as:

$$\text{Site time yield} = \frac{(F^0_{C_2H_5OH} + F^0_{C_2H_4})X_{C_2}}{W\, C_t}$$

(6-3)

where C_t is the total concentration of accessible acid sites.

6.2.3 Catalyst characterization

N_2 adsorption at 77 K was applied to determine the BET surface area and total pore volume using a Micrometrics Gemini V. The state of the metals of the as-prepared catalysts was investigated by temperature programmed reduction with hydrogen (H_2-TPR), TEM and X-ray diffraction. H_2-TPR was performed on a Micromeritics AutoChem 2920 by first pretreating the as-prepared catalyst with helium to 823 K to remove adsorbed water and CO_2. The sample was then cooled to

room temperature and subsequently heated to 1173 K in hydrogen atmosphere (Air Liquide, 5% H_2/Ar). The outlet stream was monitored with a thermal conductivity detector (TCD). TEM measurements were performed on a JEOL JEM2200FS-Cs-corrected microscope, operated at 200 kV and equipped with a Schottky-type FEG, EDX JEOL JED-2300D and JEOL in-column omega filter.

Crystallographic analyses of the as-prepared catalysts (XRD) were performed using a Bruker-AXS D8 Discover apparatus with lynx eye detector covering 3° and 192 channels over the range 15-85° with a step of 0.04°. By fitting a Gaussian function to a diffraction peak, a mean crystallite size can be determined via the Scherrer equation:

$$d = \frac{K\lambda}{\beta \cos\theta} \qquad (1)$$

where d is the mean crystallite size, K is a dimensionless shape factor with a value of 0.9, λ the X-ray wavelength, β the full width at half maximum and θ the Bragg angle.

Acidity measurements were performed by temperature programmed desorption with NH_3 (NH_3-TPD) in a Micrometrics AutoChem 2920. First, a pretreatment step was executed to remove adsorbed water and CO_2 from the catalyst by heating the catalyst in helium with a temperature ramp of 10 K/min to 823 K. The temperature was then lowered to 373 K while being in helium atmosphere. Adsorption of NH_3 was then performed by flowing a NH_3/He mixture (Air Liquide, 3.996 v% NH_3) during 2 h over the catalysts. The catalysts were then purged with helium to remove all non-adsorbed ammonia until a stable baseline was obtained, which was then followed by heating to 823 K with a temperature ramp of 5 K/min. A thermal conductivity detector was used to detect the desorbed ammonia. The NH_3-TPD spectrum was deconvoluted into the number of observable peaks by using Gaussian functions. A similar procedure has been reported in literature [18, 19]. The total concentration of accessible acid sites C_t is then directly proportional to the area under the deconvoluted peak in the range of 573 - 773 K. A calibration factor was determined by calibrating the detector with known volumes of NH_3. Based on replicate experiments, the error on the total concentration of accessible acid sites was calculated to be 7%.

6.3 Results

6.3.1 Catalyst performance testing

Catalyst stability was verified at 623 K and it was observed that over the course of several hours, the activity did not vary nor did the selectivity change for the different product classes. The most abundant products are the light olefins containing two to five carbon atoms and in minor quantities light paraffins (C_2 – C_4), aromatics and fraction in the gasoline range i.e. C_{5+} hydrocarbons containing olefins and paraffins. As the formation of C_{3+} hydrocarbons is almost not observed at temperatures below 573 K and the catalyst can be considered stable at 623 K, this temperature is chosen as the reference reaction temperature.

Figure 6-1 shows the outlet composition as function of space time at 623 K on unmodified H-ZSM-5. Full conversion of ethanol was achieved at the investigated conditions. At low space times (below 0.5 $kg_{cat}.s.mol^{-1}$), only ethene is observed as a product. As space time increases, a decrease in ethene selectivity is observed which corresponds to the consecutive conversion of ethene to higher hydrocarbons. This illustrates the separation in time scales between the dehydration reaction and the production of C_{3+} hydrocarbons at 623 K.
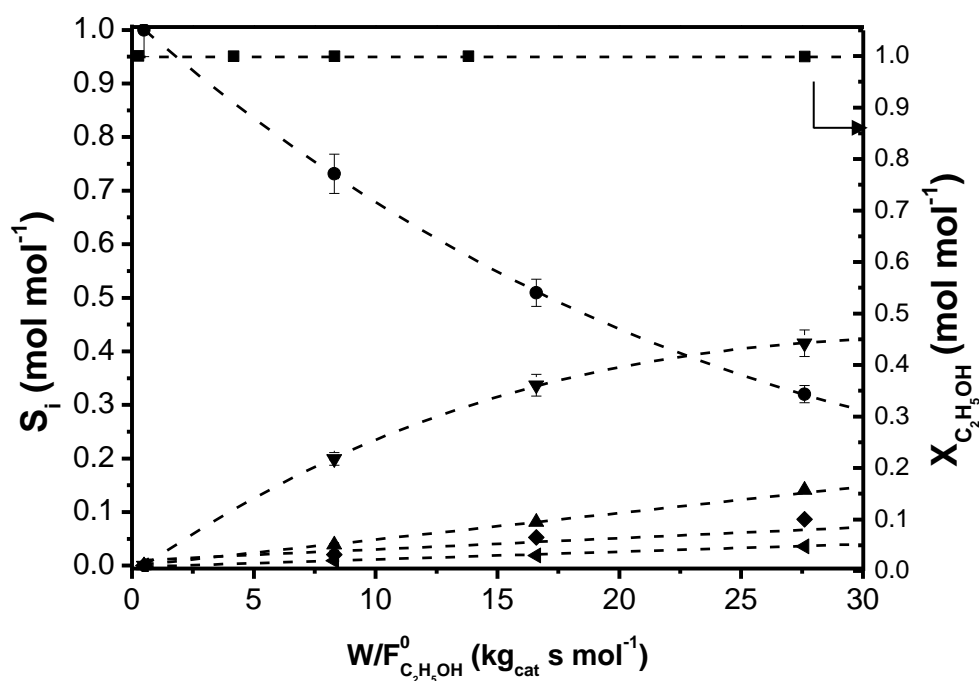
Figure 6-1: Ethanol conversion and product selectivity as function of space time for H-ZSM-5 (■: ethanol conversion; ●: ethene selectivity; ▼: C_3-C_5 olefin selectivity; ▲: C_{5+} hydrocarbons selectivity; ◆: C_2-C_5 paraffin selectivity; ◀: Aromatics; T= 623 K, W $F_{EtOH,0}^{-1}$= 1 - 27 kg s mol^{-1}; $p_{EtOH,0}$ = 10 kPa). Lines are to guide the eye.

Comparison of the metal modified H-ZSM-5 was performed at fixed space time, i.e., W/F_{EtOH}^0= 17 kg$_{cat}$ s mol^{-1}. Deactivation was not observed for all metal containing catalysts. In Figure 4, C_2 conversion (X_{C2}) versus metal content is shown. It can be seen that adding a small amount of metal (1Ga, 1Fe, 1Ni/H-ZSM-5) results in a slightly higher C_2 conversion. However, when metal content was further increased (2M, 4M, 7M/H-ZSM-5 samples with M being the type of metal introduced), the C_2 conversion decreased. In the case of the highest metal content (7Ga, 7Fe and 7Ni/H-ZSM-5), the C_2 conversion was halved compared to H-ZSM-5. It can also be observed that the decrease is similar for all metals investigated in this study.
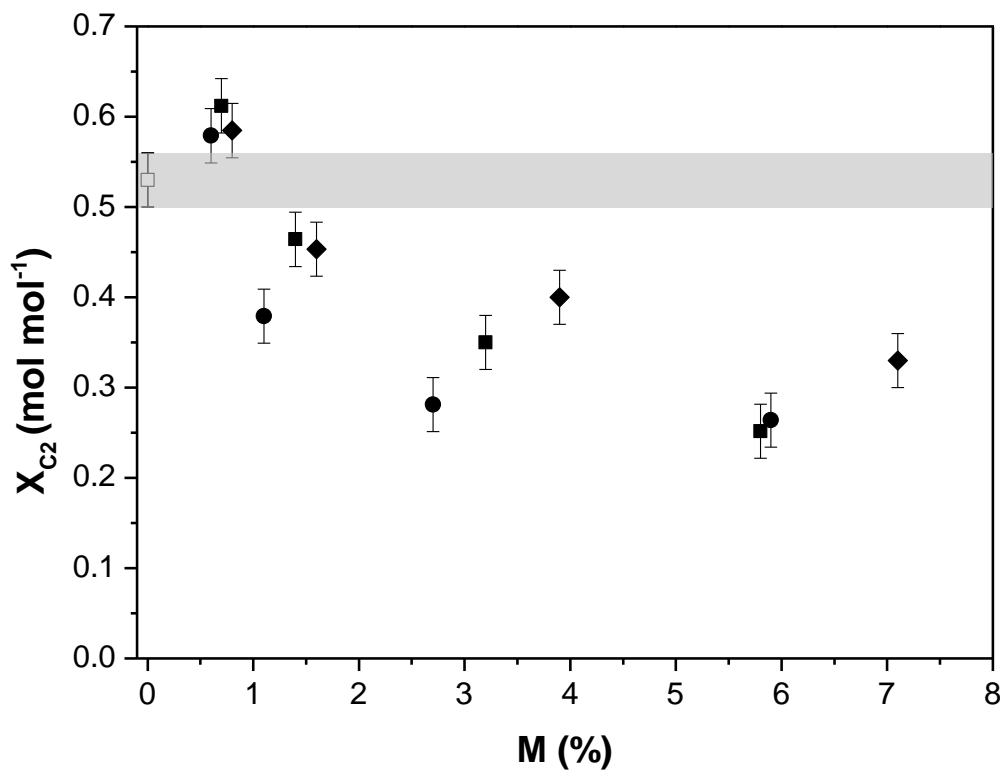
Figure 6-2: C$_2$ conversion as function of metal content. (□: H-ZSM-5, ●: Fe/H-ZSM-5, ■: Ga/H-ZSM-5 and ♦ : Ni/H-ZSM-5, T= 623 K, W F$_{EtOH,0}^{-1}$= 17 kg s mol^{-1}; p$_{EtOH,0}$ =10 kPa;). Gray band represents the 95% confidence interval of H-ZSM-5.

6.3.2   Catalyst characterization

The structural effects of the metal introduction on H-ZSM-5 were investigated by XRD, H$_2$-TPR, TEM and N$_2$ adsorption. The XRD patterns as shown in Figure 6-3 of the as-prepared catalysts show that the introduction of metal in the zeolite does not induce any changes in crystallinity compared with that of the starting material.
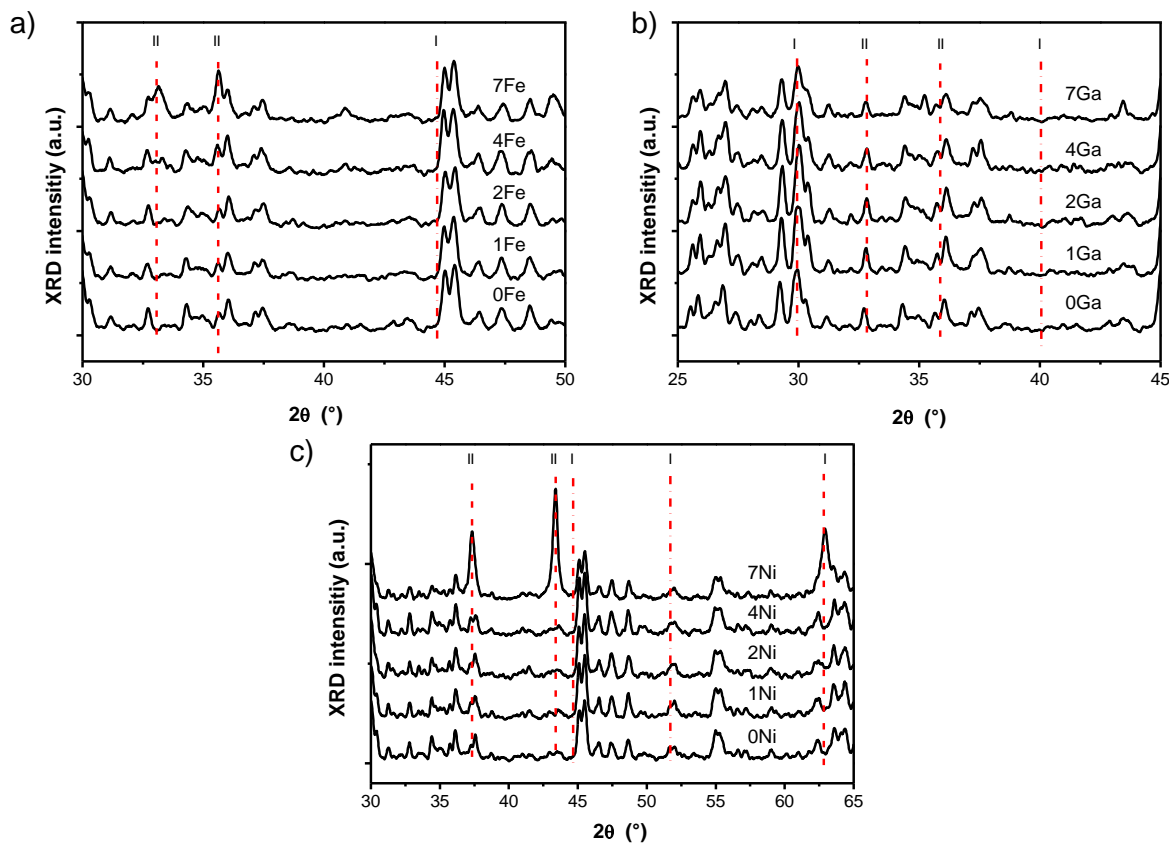
Figure 6-3: XRD measurement of as prepared (a) Fe/H-ZSM-5, (b) Ga/H-ZSM-5 and (c) Ni/H-ZSM-5. Highlighted diffraction angles: I - metal and II - metal oxide.

At metal contents smaller than 4 wt.%, no characteristic peaks of metal oxide or metal appear for all metals. However, the XRD measurements of samples with higher metal content (metal content > 4 wt.%), indicate the presence of a metal oxide phase, in particular Fe_2O_3, NiO and Ga_2O_3. For the iron loaded samples (Figure 6-3 (a)), the diffraction angles of 33° (104) and 36° (311) of Fe_2O_3 are visible at high metal content. The same holds for the nickel loaded samples (NiO: 37° (101), 43° (012) and 63° (104)) and the gallium loaded samples (Ga_2O_3: 33° (104) and 36° (110)) which are shown in Figure 6-3 (b) and (c). None of the samples show the presence of pure metal. A mean crystallite size was calculated via the Scherrer equation and a value of 7 nm and 5 nm is obtained for respectively 7Fe and 7Ni/H-ZSM-5 This is in accordance with other studies [20]. A comparison was also performed between as-prepared and 7Fe/H-ZSM-5 after 8 h of time on stream. No differences in XRD patterns were observed between as-prepared and used catalyst indicating that no changes in metal state have occurred.

H_2-TPR was used to investigate the reducibility of the as-prepared metal modified H-ZSM-5 catalysts. In Figure 6-4, the temperature programmed reduction profiles for all metal loaded catalysts are displayed. H_2-TPR of unmodified H-ZSM-5 did not show hydrogen consumption in the investigated temperature range. Figure 6-4 (a) shows the profiles for iron loaded H-ZSM-5: a metal content smaller than 2 wt.% does not lead to any visible peaks. Increase in iron content results in several peaks in different temperature ranges: (i) region 573 – 673 K: reduction of Fe_2O_3 to Fe_3O_4, (ii) region 673 K – 973 K: reduction of Fe_3O_4 to FeO and Fe. Similar profiles of reduction of iron oxide are reported in literature [21, 22].

Figure 6-4 (b) combines the H_2-TPR profiles for the gallium modified samples. A reduction of the gallium species is observed from 723 K onwards which can be ascribe to the reduction of Ga_2O_3, which is consistent with the findings of Kwak et al. [23]. A shift of these peak with increasing gallium content is observed to lower temperatures, which is indicative for larger Ga_2O_3 particles.

H_2-TPR profiles for the nickel loaded samples shown in Figure 6-4 (c). Low metal content sample (< 2 wt.%) do not show signs of significant hydrogen consumption, while increasing the metal content induces an increase in hydrogen consumption. The TPR profile can be separated into three domains: (i) between 473 – 573 K, (ii) between 573 – 723 K and (iii) above 723 K. The former corresponds to the reduction of NiO to metallic nickel. The two latter peaks can be assigned to the reduction of NiO of different crystal size located on the outer zeolite surface while the latter peak are attributed to nickel clusters present in the zeolite channels [7].
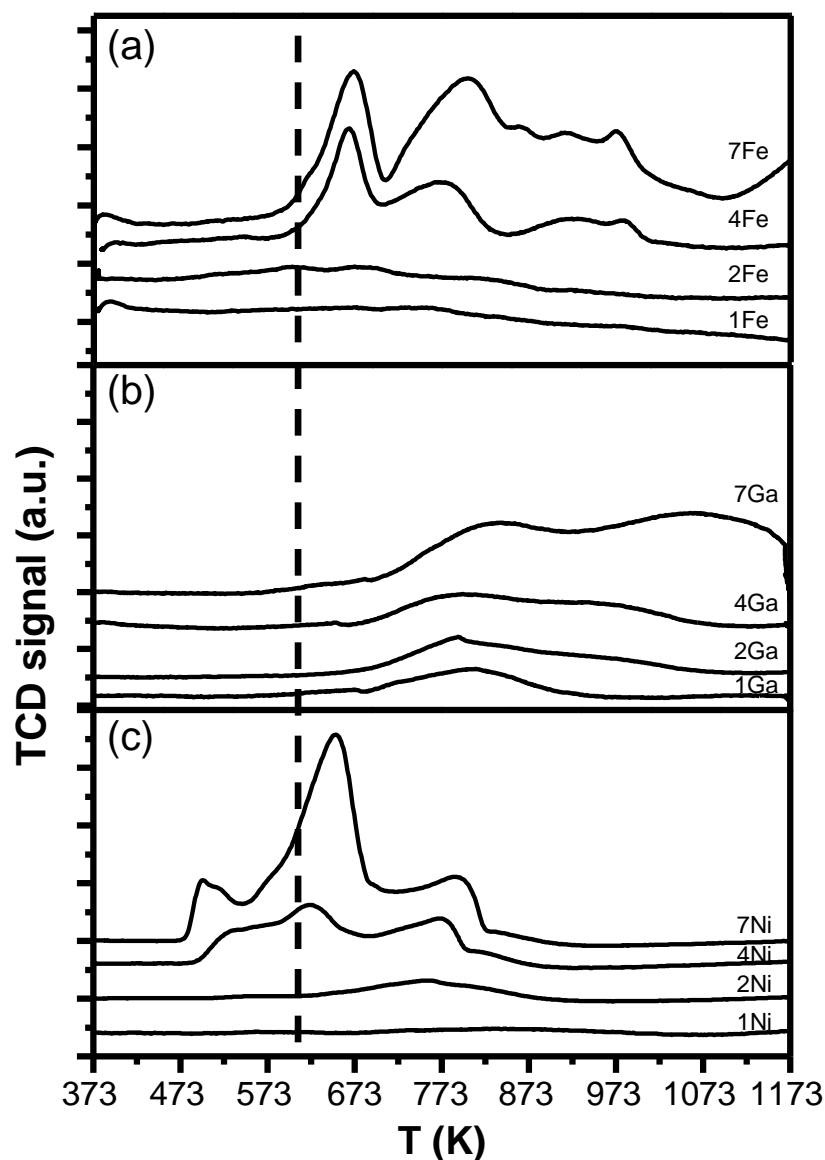
Figure 6-4: H$_2$-TPR profiles of as-prepared a) Fe/H-ZSM-5, b) Ga/H-ZSM-5 and c) Ni/H-ZSM-5 (β = 10 K min^{-1}). Bold dashed line indicates the investigated reaction temperature.

Further investigation of the metal oxide phase in the as-prepared catalysts was performed using transmission electron microscope (TEM). In Figure 6-5 and Figure 6-6 TEM images of 2Ni, 2Fe, 7Ni, 7Ga and 7Fe/H-ZSM-5 are shown. No metal or metal oxide clusters were detected in the case of samples with low amounts of metal (content < 2 wt.%) which is in accordance with the XRD and H$_2$-TPR results. However, the EDX measurements, which are also shown in Figure 6-5, confirm that the metal was indeed present in the samples.
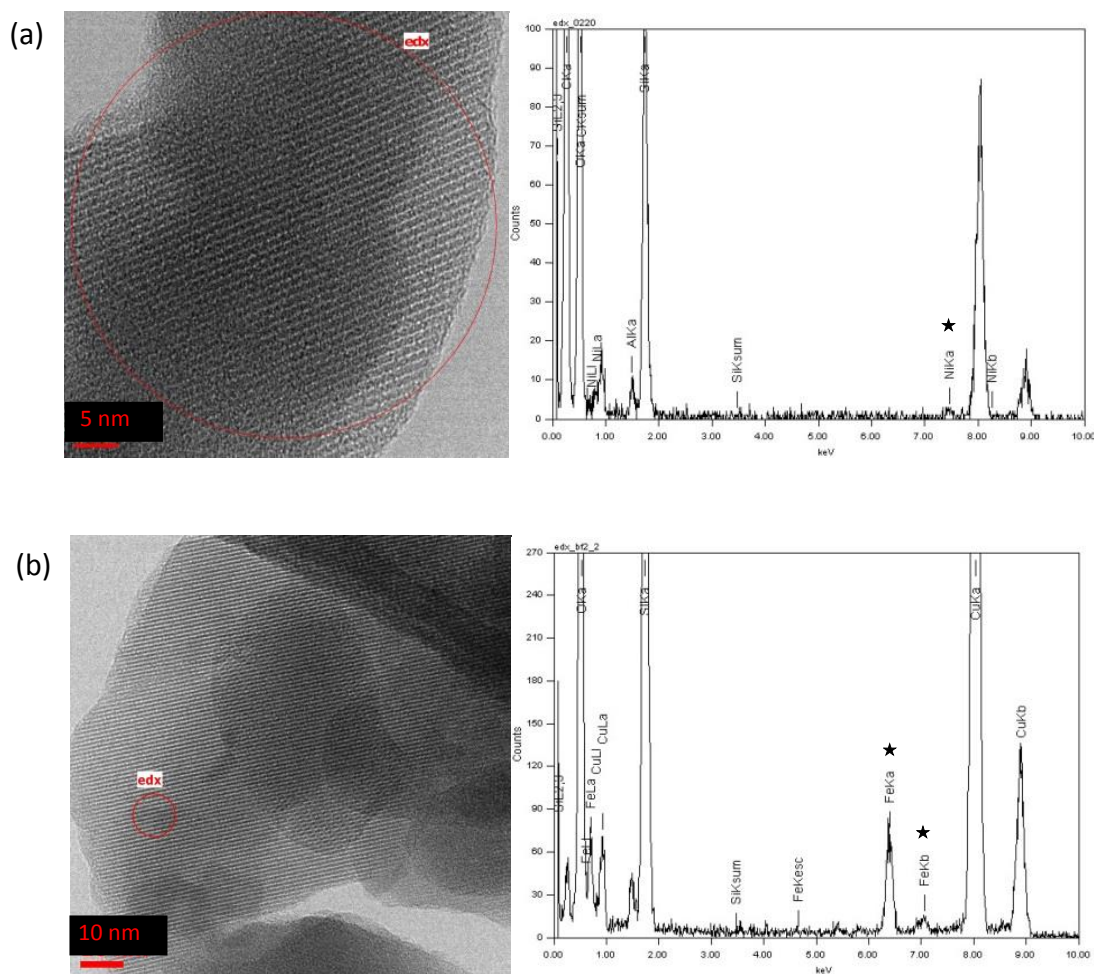
Figure 6-5: Transmission electron microscope image of as-prepared (a) 2Ni/H-ZSM-5 and (b) 2Fe/H-ZSM-5 (left: HRTEM images; right: EDX profile; ★: characteristic X-ray energy)

Figure 6-6 displays the TEM images and the EDX line scan results for the modified H-ZSM-5 with the highest metal content (7Fe, 7Ni and 7Ga/H-ZSM-5). The EDX line scans shown in the picture, confirm the presence of large metal particles and thus show that the metal is not equally distributed over the framework. In 7Ga/H-ZSM-5, a concentration gradient of Ga in the articles is observed ranging from 1.9 – 11.2 atomic%. Based on the TEM images, the metal particles have a size ranging between 5 to 15 nm, which is in line with the values found from XRD for Ni and Fe loaded H-ZSM-5.

(a)

(b)

(c)
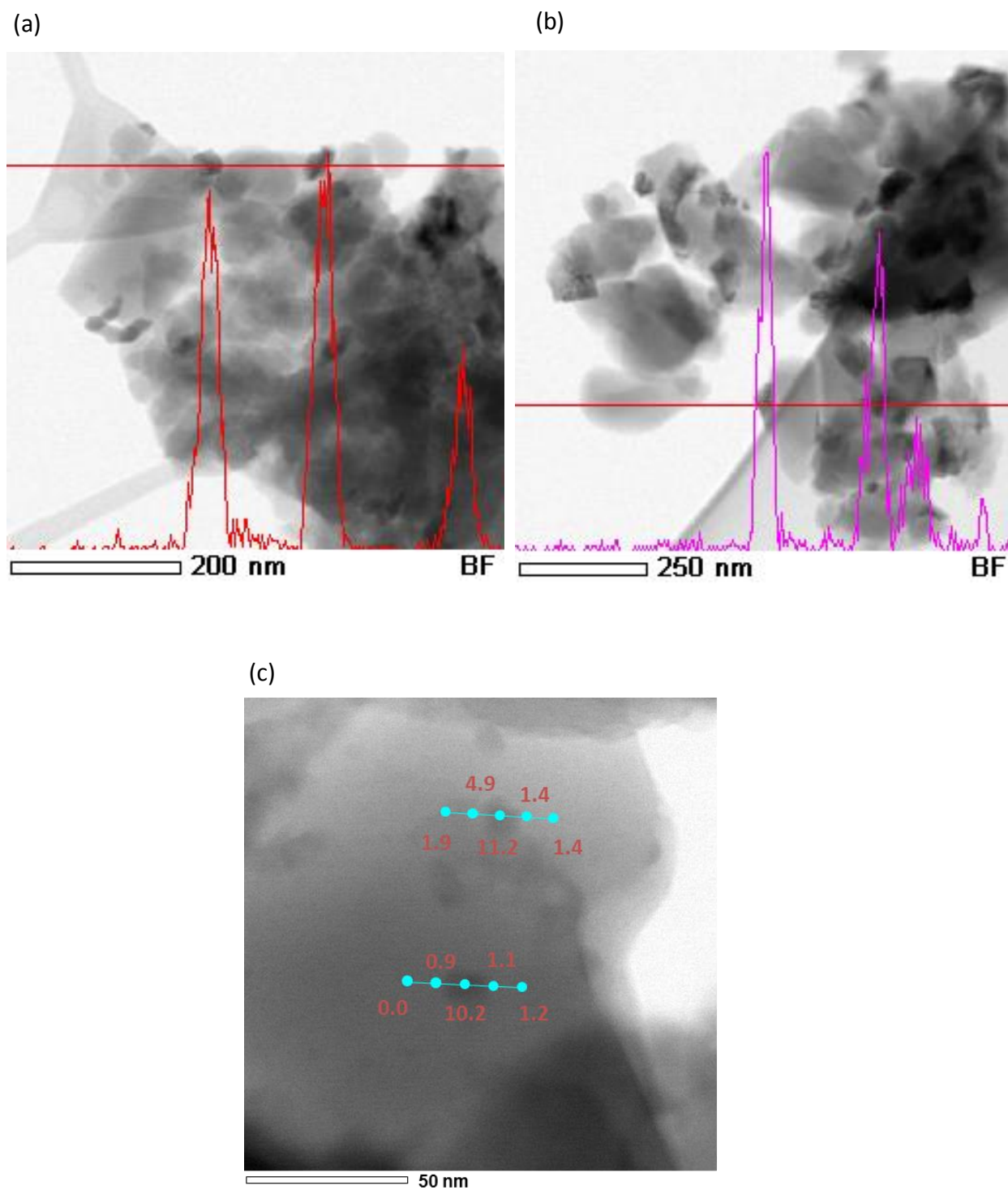
Figure 6-6: EDX line scan through a STEM frame of as-prepared (a) 7Fe/H-ZSM-5, (b) 7Ni/H-ZSM-5 and (c) 7Ga/H-ZSM-5 (numbers indicate the metal content (atomic%)).

NH₃-TPD is performed in order to assess the differences in acidity between the unmodified and metal modified catalysts. Figure 6-7 shows the effect of metal content on the NH₃-TPD profiles for (a) iron, (b) gallium and (c) nickel loaded H-ZSM-5. The NH₃-TPD profile for the unmodified H-ZSM-5 is also shown in each graph. Two distinct maxima can be observed here: a low temperature maximum (373– 473 K) (*l*-peak*)* and a high temperature maximum (573 - 773 K) (*h*-peak). Brønsted acidity is usually attributed to acid sites with a desorption temperature above 573 K, while the desorption of ammonia at lower temperatures (< 473 K) is usually associated with weakly adsorbed NH₃ on the external surface of the zeolite or impurities [24, 25]. For all as-prepared metal modified H-ZSM-5 samples, similar NH₃-TPD profiles were obtained which showed that $T_{d,max}$ of the *l*-peak remains fairly constant while the maximum of the *h*-peaks decreases slightly at high metal content which indicates that the acid strength decreases due to the addition of metal.
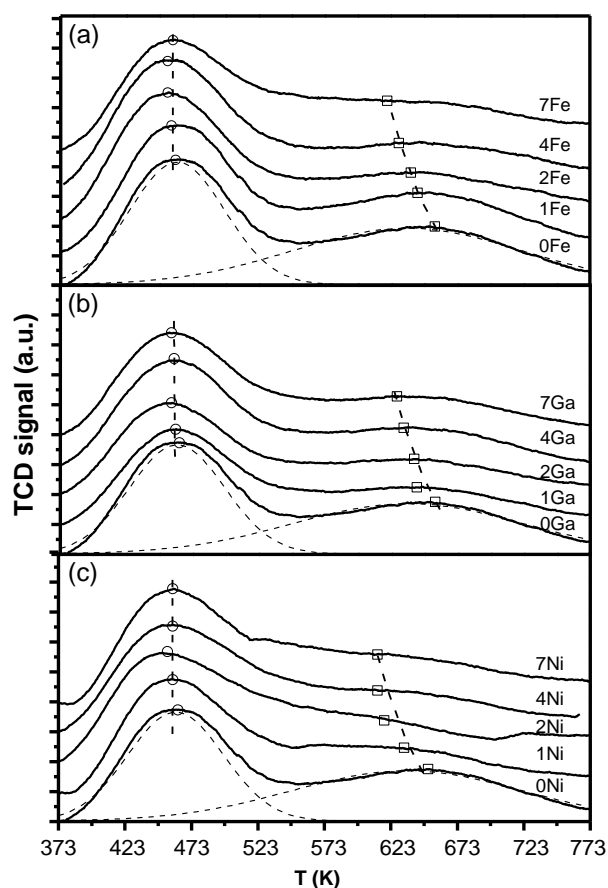
Figure 6-7: NH₃-TPD profiles of as-prepared a) Fe/H-ZSM-5, b) Ga/H-ZSM-5 and c) Ni/H-ZSM-5 (β = 5 K min⁻¹) (○ maxima of the *l*-peak, and □ the *h*-peak as determined by deconvolution).

For the catalysts with the highest metal content, three peaks, are required to perform the deconvolution procedure. These peaks are located between 373 – 473 K, 573 – 773 K and 473–573 K. This can be attributed to the creation of acid sites with a lower acid strength at the expense of Brønsted acid sites. Same observations are also reported in literature by using other modification techniques [26].

The total concentration of accessible acid sites C_t can be derived from the deconvolution procedure by using the area of the peak located between 573 – 773 K. The effect of metal content on the total concentration of accessible acid sites is shown in Figure 6-8 (a). A decrease in the accessible acidity was observed for the metal modified H-ZSM-5 samples with a metal content larger than 1 wt.%: the total concentration of accessible acid sites was decreased by 30% when comparing H-ZSM-5 and 7M/H-ZSM-5 (M = Ni, Ga and Fe).

The effect of metal content on surface area and porosity is shown in Figure 6-8. Low metal content (M < 1 wt.%) does not alter the BET surface area and porosity significantly, while higher metal content results in a linear decrease in surface area and porosity. The results from the N_2 adsorption measurements at 77 K are listed in Table 6-1. It can be observed that the changes in the total concentration of accessible acid sites, BET surface area and pore volume are the same for all metals.
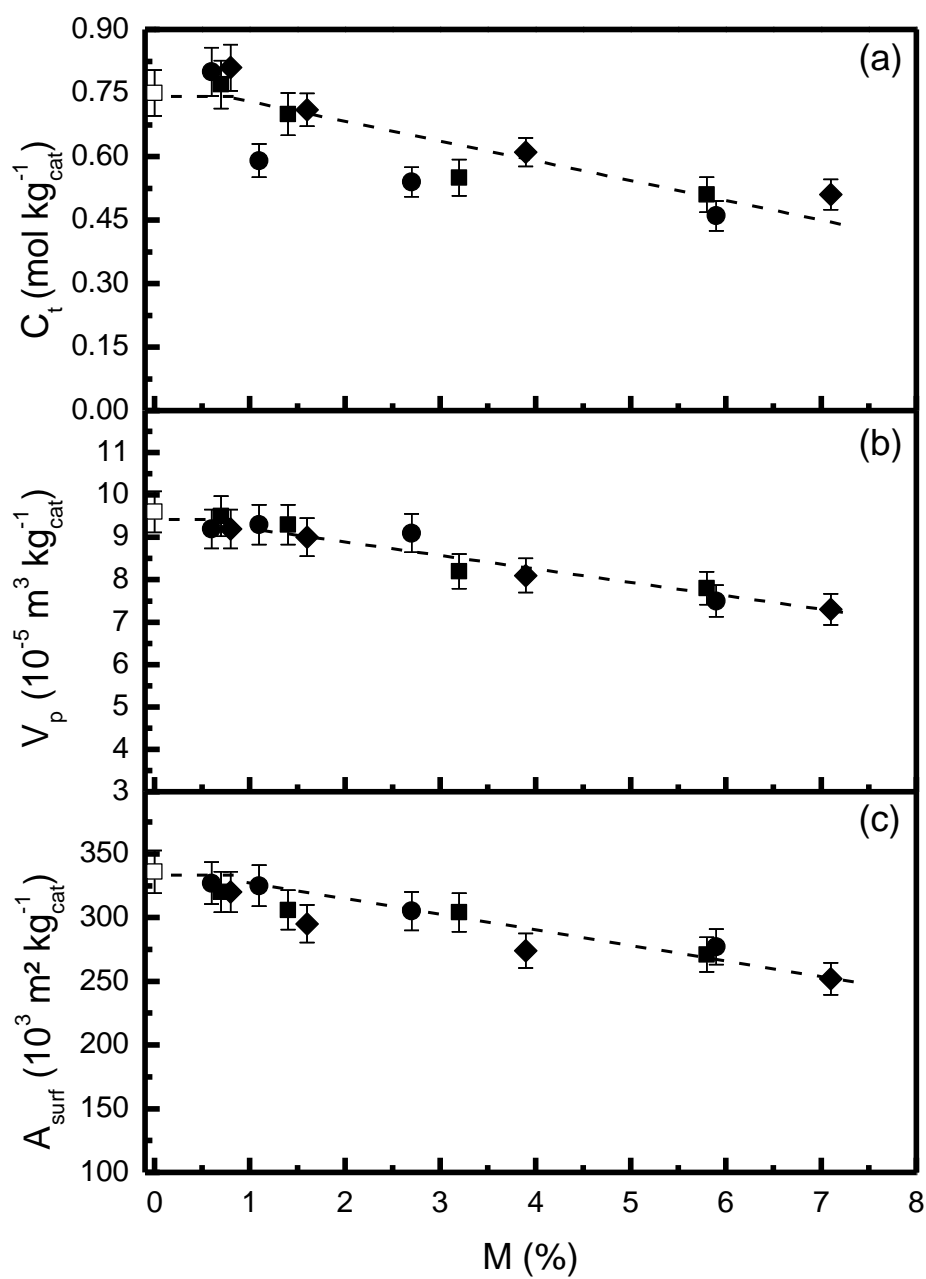
Figure 6-8. (a) total concentration of accessible acid sites, (b) pore volume and (c) BET surface area as function of metal content (□: H-ZSM-5, ●: Fe/H-ZSM-5, ■ : Ga/H-ZSM-5 and ♦ : Ni/H-ZSM-5)

6.4 Discussion

In order to assess whether metal modification introduces new reaction steps and thus also alters the reaction mechanism, a comparison between the catalysts at same C_2 conversion is performed. Figure 6-9 shows the space time yield for various product classes: a) C_3-C_5 olefins and C_2-C_5 paraffins and b) aromatics and a fraction consisting of C_{5+} hydrocarbons as function of C_2 conversion for the metal modified ZSM-5 catalysts. These are compared to H-ZSM-5 where variation in conversion was obtained by space time variation ($W/F_{EtOH}^0 = 1 - 27$ kg s mol^{-1}) at a fixed temperature of 623 K.

The space time yields of the metal modified ZSM-5 are identical to those on unmodified H-ZSM-5 when comparing at same conversion. This holds for all products classes (light olefins, light paraffins, aromatics and C_{5+} hydrocarbons). This shows that no additional functionalities were included in the catalysts nor that extra reaction paths were added to the reaction mechanism. Thus, it can be concluded that only the activity of the catalysts is affected by the metal modification.
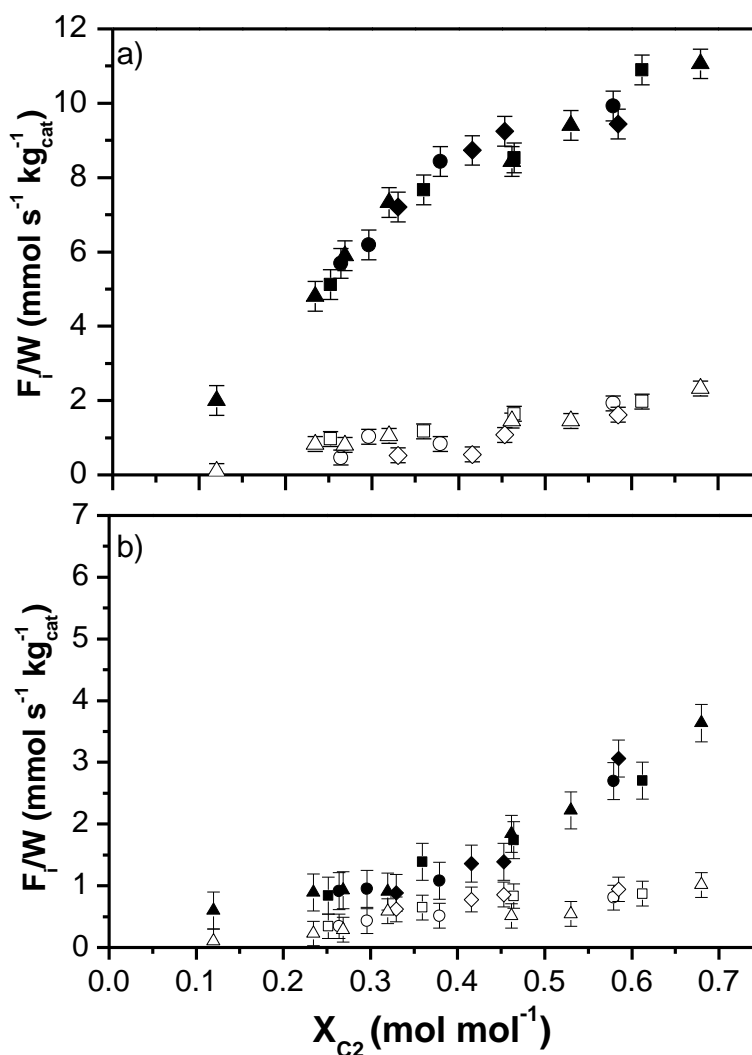
Figure 6-9: Space time yield of a) $C_3 – C_5$ olefins (filled symbols) and $C_2 – C_5$ paraffins (empty symbols) and b) C_{5+} hydrocarbons (filled symbols) and aromatics (empty symbols) as function of C_2 conversion (T= 623 K; $p_{EtOH,0}$ = 10 kPa; ▲ : H-ZSM-5; ●: Fe/H-ZSM-5; ■ : Ga/H-ZSM-5; ♦ : Ni/H-ZSM-5)

Oligomerization on Ni ions to 1-olefins was not observed under the process conditions investigated in this work, which could be related to differences in temperature and pressure range since oligomerization is typically performed at lower temperatures and higher pressures. Introduction of Ga_2O_3 is often used for increasing the yields of aromatics and is especially investigated in catalytic cracking and paraffin activation reactions: an additional functionality is introduced via gallium oxide where dehydrogenation and aromatization takes place and oligomerization, cyclization, dealkylation, transalkylation and isomerization take place on the acid site [27]. This is typically performed at higher temperatures.

A variety of characterization techniques was utilized to understand the effect of the metal content on the catalytic properties and thus also the catalytic performance. Low metal content (< 1 wt.%) does not alter structural properties such as surface area and pore volume. No bulk metal oxide was detected in these samples, as can be seen from H_2-TPR, XRD and the TEM images. This is consistent with reports in the literature where the introduction of small amounts of nickel by impregnation resulted in the occurrence of nickel as a compensating cation in addition to small metal clusters which were not observable via XRD or TEM [7]. Similar conclusions were also found in the literature for gallium and iron [21, 28]. Thus the metal is present as a compensating cation or as very small metal clusters inside the zeolite pores. The introduction of metal results in a small increase in total concentration of accessible acid sites as can be seen in Figure 6-8.

If the metal content is raised (> 2 wt.%), the formation of metal oxides becomes more prominent: large metal amounts are deposited onto H-ZSM-5 and inside the pores and metal clusters begin to appear on XRD and TEM images which results in a decrease in porosity due to pore blockage. As can be seen from Figure 6-8, the same trend can be observed for reduction of acid sites, porosity and surface area for metal modified H-ZSM-5 with a metal content greater than 1 wt.%. This illustrates the correlation between loss in porosity and decrease the concentration of acid sites as shown in Figure 6-8.

Since ethanol and the hydrocarbons that are being formed during reaction, possess the capability of reducing the metal oxide to metal during reaction, a H_2 pretreatment was performed to study this effect. However, it was found that this had no effect on the catalytic results. Furthermore, no differences in XRD pattern between as-prepared and used catalyst were observed. The state of the metal can thus be considered to be metal oxide under reaction conditions. It should also be noticed that water formed via the dehydration of ethanol is able to reoxidize metal back to metal oxide.
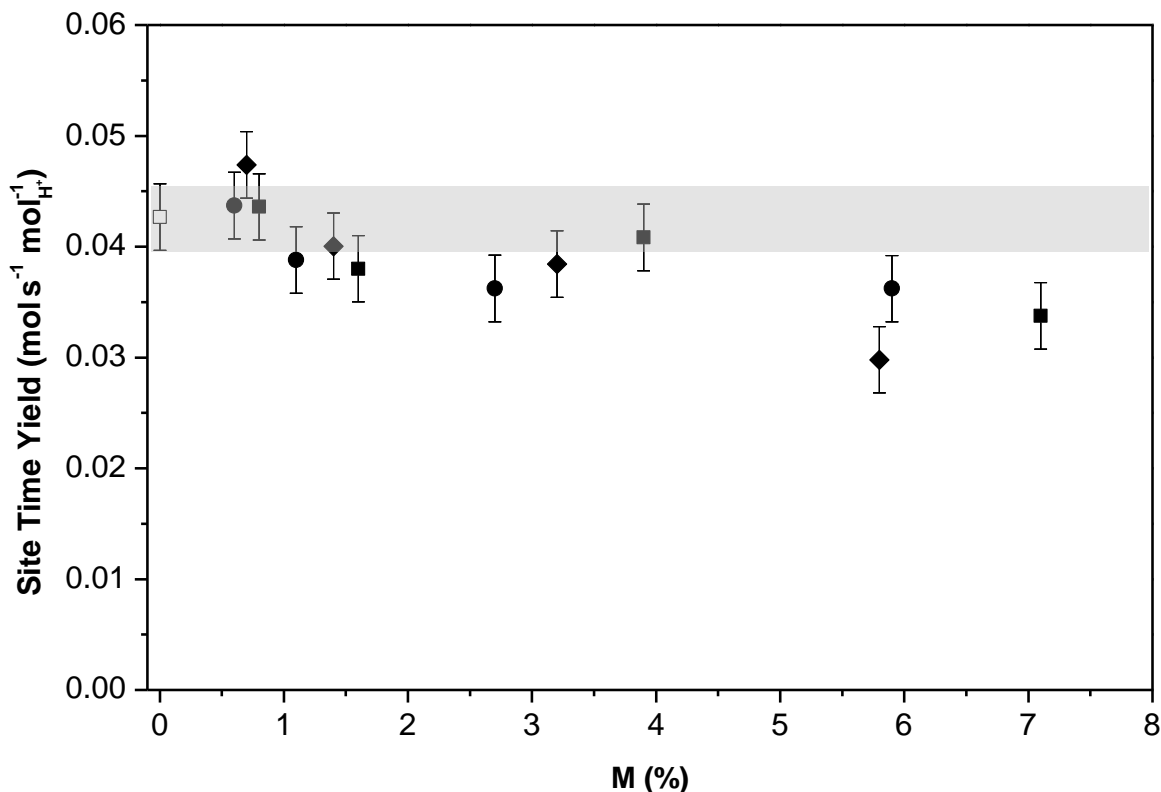
Figure 6-10. Site time yield as defined by Eq. (6-3) of metal modified ZSM-5 as a function of metal content (□: H-ZSM-5, ■: Ga/H-ZSM-5, ●: Fe/H-ZSM-5 and ♦: Ni/H-ZSM-5; T = 623 K, W $F_{EtOH,0}^{-1}$= 17 kg$_{cat}$ s mol^{-1}; p$_{EtOH,0}$ = 10 kPa). Gray band represents the 95% confidence interval of H-ZSM-5 data.

The effect of metal introduction on the acid sites is reported by Lu et al. who illustrate that the introduction of Fe altered the amount of acid sites and had a great effect on catalytic activity [9]. In this work, it was found that introduction alters the concentration of accessible Brønsted acid sites and two regions can be distinguished: a region where the concentration of acid sites of the modified H-ZSM-5 comparable to the concentration of acid sites of pristine H-ZSM-5 and a second region where the total concentration of accessible acid sites decreases with increasing metal content which is attributed to pore blockage.

From the space time yield and the total concentration of accessible acid sites, the site time yield can be calculated for each catalyst according to eq. (6) and is shown in Figure 6-10. The site time yield of 1M/H-ZSM-5 was found to be slightly higher or comparable to the site time yield of unmodified H-ZSM-5. Further increasing the metal loading results in decreasing site time yields

which suggests lower acid strength. These lower acid strengths were also shown in the NH_3-TPD profiles which exhibit decreasing maximum desorption temperatures for the h-peak.

6.5 Conclusions

Conversion of ethanol to higher hydrocarbons was studied on metal modified H-ZSM-5 (Si/Al = 15) and compared with the conversion on unmodified H-ZSM-5. At 623 K, a variety of products were detected, including light olefins, light paraffins, aromatics and a heavy fraction consisting of C_{5+} hydrocarbons which are all formed via the consecutive conversion of ethene.

H-ZSM-5 was modified with several metals (Fe, Ni and Ga) in varying quantities. A combination of catalytic testing and detailed catalyst characterization (XRD, TEM, N_2 adsorption, NH_3-TPD and H_2-TPR) resulted in the identification of two different effects on the activity depending on the amount of metal added to the catalyst. A positive effect on the production of C_{3+} hydrocarbons was found for metal content less than 1 wt.% which is attributed to an increase in the total concentration of accessible acid sites. However, high metal content resulted in a decrease in production of higher hydrocarbons which can be attributed to bulky metal clusters leading to pore blockage and decreased acid strength. Comparison of the investigated catalysts at same C_2 conversion showed that the selectivities between the various product classes were not altered and the same reaction mechanism as for unmodified H-ZSM-5 holds.

6.6 References

[1] N. Rahimi, R. Karimzadeh, Catalytic cracking of hydrocarbons over modified ZSM-5 zeolites to produce light olefins: A review, Applied Catalysis A: General, 398 (2011) 1-17.

[2] J.W. Thybaut, G.B. Marin, Kinetic modeling of the conversion of complex hydrocarbon feedstocks by acid catalysts, Chemical Engineering & Technology, 26 (2003) 509-514.

[3] Z.Y. Zakaria, J. Linnekoski, N.A.S. Amin, Catalyst screening for conversion of glycerol to light olefins, Chemical Engineering Journal, 207 (2012) 803-813.

[4] M. Conte, J.A. Lopez-Sanchez, Q. He, D.J. Morgan, Y. Ryabenkova, J.K. Bartley, A.F. Carley, S.H. Taylor, C.J. Kiely, K. Khalid, G.J. Hutchings, Modified zeolite ZSM-5 for the methanol to aromatics reaction, Catalysis Science & Technology, 2 (2012) 105-112.

[5] A. Hagen, F. Roessner, Ethane to Aromatic Hydrocarbons: Past, Present, Future, Catalysis Reviews: Science and Engineering, 42 (2000) 403-437.

[6] N. Viswanadham, G. Muralidhar, T.S.R.P. Rao, Cracking and aromatization properties of some metal modified ZSM-5 catalysts for light alkane conversions, Journal of Molecular Catalysis A: Chemical, 223 (2004) 269-274.

[7] A.J. Maia, B. Louis, Y.L. Lam, M.M. Pereira, Ni-ZSM-5 catalysts: Detailed characterization of metal sites for proper catalyst design, Journal of Catalysis, 269 (2010) 103-109.

[8] J. Heveling, C.P. Nicolaides, M.S. Scurrell, Catalysts and conditions for the highly efficient, selective and stable heterogeneous oligomerisation of ethylene, Applied Catalysis A: General, 173 (1998) 1-9.

[9] J. Lu, Z. Zhao, C. Xu, P. Zhang, A. Duan, FeHZSM-5 molecular sieves – Highly active catalysts for catalytic cracking of isobutane to produce ethylene and propylene, Catalysis Communications, 7 (2006) 199-203.

[10] A.G. Gayubo, A. Alonso, B. Valle, A.T. Aguayo, M. Olazar, J. Bilbao, Hydrothermal stability of HZSM-5 catalysts modified with Ni for the transformation of bioethanol into hydrocarbons, Fuel, 89 (2010) 3365-3372.

[11] M. Inaba, K. Murata, M. Saito, I. Takahara, Production of olefins from ethanol by Fe-supported zeolite catalysts, Green Chemistry, 9 (2007) 638-646.

[12] N.R.C.F. Machado, V. Calsavara, N.G.C. Astrath, C.K. Matsuda, A. Paesano Junior, M.L. Baesso, Obtaining hydrocarbons from ethanol over iron-modified ZSM-5 zeolites, Fuel, 84 (2005) 2064-2070.

[13] S.K. Saha, S. Sivasanker, Influence of Zn- and Ga-doping on the conversion of ethanol to hydrocarbons over ZSM-5, Catalysis Letters, 15 (1992) 413-418.

[14] F. Solymosi, R. Barthos, A. Szechenyi, Decomposition and aromatization of ethanol on ZSM-based catalysts, Journal of Physical Chemistry B, 110 (2006) 21816-21825.

[15] D. Goto, Y. Harada, Y. Furumoto, A. Takahashi, T. Fujitani, Y. Oumi, M. Sadakane, T. Sano, Conversion of ethanol to propylene over HZSM-5 type zeolites containing alkaline earth metals, Applied Catalysis A: General, 383 (2010) 89-95.

[16] Z. Song, A. Takahashi, N. Mimura, T. Fujitani, Production of Propylene from Ethanol Over ZSM-5 Zeolites, Catalysis Letters, 131 (2009) 364-369.

[17] M. Inaba, K. Murata, M. Saito, I. Takahara, Ethanol conversion to aromatic hydrocarbons over several zeolite catalysts, Reaction Kinetics and Catalysis Letters, 88 (2006) 135-141.

[18] L. Rodriguez-Gonzalez, F. Hermes, M. Bertmer, E. Rodriguez-Castellon, A. Jimenez-Lopez, U. Simon, The acid properties of H-ZSM-5 as studied by NH3-TPD and Al-27-MAS-NMR spectroscopy, Applied Catalysis A: General, 328 (2007) 174-182.

[19] F. Lónyi, J. Valyon, On the interpretation of the NH3-TPD patterns of H-ZSM-5 and H-mordenite, Microporous and Mesoporous Materials, 47 (2001) 293-301.

[20] B. Pawelec, R. Mariscal, R.M. Navarro, J.M. Campos-Martin, J.L.G. Fierro, Simultaneous 1-pentene hydroisomerisation and thiophene hydrodesulphurisation over sulphided Ni/FAU and Ni/ZSM-5 catalysts, Applied Catalysis A: General, 262 (2004) 155-166.

[21] L.J. Lobree, I.-C. Hwang, J.A. Reimer, A.T. Bell, Investigations of the State of Fe in H–ZSM-5, Journal of Catalysis, 186 (1999) 242-253.

[22] V. Galvita, K. Sundmacher, Redox behavior and reduction mechanism of Fe2O3–CeZrO2 as oxygen storage material, Journal of Materials Science, 42 (2007) 9300-9307.

[23] B.S. Kwak, W.M.H. Sachtler, Effect of Ga/Proton Balance in Ga/HZSM-5 Catalysts on C3 Conversion to Aromatics, Journal of Catalysis, 145 (1994) 456-463.

[24] M. Niwa, N. Katada, K. Okumura, Solid Acidity of Zeolites, in: Characterization and Design of Zeolite Catalysts, Springer Berlin Heidelberg, 2010, pp. 9-27.

[25] N.Y. Topsoe, K. Pedersen, E.G. Derouane, Infrared and Temperature-Programmed Desorption Study of the Acidic Properties of ZSM-5-Type Zeolites, Journal of Catalysis, 70 (1981) 41-52.

[26] X.L. Zhu, L.L. Lobban, R.G. Mallinson, D.E. Resasco, Tailoring the mesopore structure of HZSM-5 to control product distribution in the conversion of propanal, Journal of Catalysis, 271 (2010) 88-98.

[27] M. Guisnet, N.S. Gnep, Aromatization of propane over GaHMFI catalysts. Reaction scheme, nature of the dehydrogenating species and mode of coke formation, Catalysis Today, 31 (1996) 275-292.

[28] K.M. Dooley, G.L. Price, K. VI, H. VI, Gallium-loaded zeolites for light paraffin aromatization: Evidence for exchanged gallium cation active centers, Catalysis Today, 31 (1996) 305-315.

Chapter 7

First-principles based simulation of a fixed bed reactor for ethanol dehydration

The step towards new, economically viable chemical processes often lies in translating the observed lab scale phenomena into an industrial scale reactor. In this work, a proof-of-concept reactor is presented for an industrial ethanol dehydration unit simulated using ab initio obtained rate and equilibrium coefficients. Heat and mass transfer limitations for the industrial design case have been assessed via literature correlations. This resulted in a multiscale reactor model covering nanoscale over microscale to macroscale. Good agreement between the simulations and a patent plant case was obtained. The industrial reactor model can be used as a tool to improve the performance of existing and to design new process units, e.g. by varying the water content as exemplified in this work.

7.1 Introduction

Since its initial discovery in the late 1970's, the oxygenates conversion processes are rapidly gaining importance as an alternative route for the production of fuels and chemicals [1]. Most industrial focus has been given to the conversion of methanol to hydrocarbons with products ranging from light olefins to gasoline. Both fixed bed and fluidized beds are encountered in

industry: a fluidized bed is often proposed with SAPO-34 catalysts which offers the advantage of better coping with rapid catalyst deactivation and high exothermicity of the MTO reaction. However, it performs poorly due to its notable catalyst attrition and low single-pass methanol conversion in addition to its high investment cost. A fixed bed is simple in construction and can easily be operated, certainly in adiabatic operation.

The first records on ethanol dehydration remounts to the 18th century and several plants have been in operation in the course of the 20th century. In contrast to methanol-to-olefins, ethanol dehydration is an endothermal process. These were principally multitubular, isothermal reactors operating at temperatures above 623 K via circulation of a heating fluid externally to the tubes. Such a configuration, which employs indirect heating via a heating fluid, has some disadvantages both in its technical and economic aspects [2]. This resulted in a shift towards adiabatic fixed bed reactors. Initially, the catalyst employed was alumina or silica-alumina but zeolites have also drawn attention for this process recently [3].

A schematic overview of an ethanol dehydration plant is shown in Figure 7-1. When starting from a fermentation broth, a distillation column (1) can be installed to remove water from this ethanol-water mixture to the desired water content. The ethanol feedstock can then be mixed with unreacted ethanol from the purification zone. Next, a heat exchanger (2) allows heat recovery from the reactor effluent, i.e., the latent heat of the effluent is used to vaporize the ethanol 51ethanol feedstock is superheated. A furnace (5) is installed to bring the feed to the temperature of the first ethanol dehydration reactor (6). The effluent from the first reactor is sent, via an additional furnace (7) to the next ethanol dehydration reactor (8). The number of reactors in series depend on the reaction conditions and the aimed conversion. The effluent of the second reactor undergoes a series of heat exchanges as described above to achieve maximal heat recovery.

Downstream of the reactor, the effluent is separated in a gas/liquid separation column (9) into a top stream comprising ethene and a bottom stream consisting of water, side products and unreacted ethanol. The latter is sent to a second separation column (10) and results in three streams: side products (C_{3+} olefins and oxygenates), water and unconverted ethanol which can be recycled.
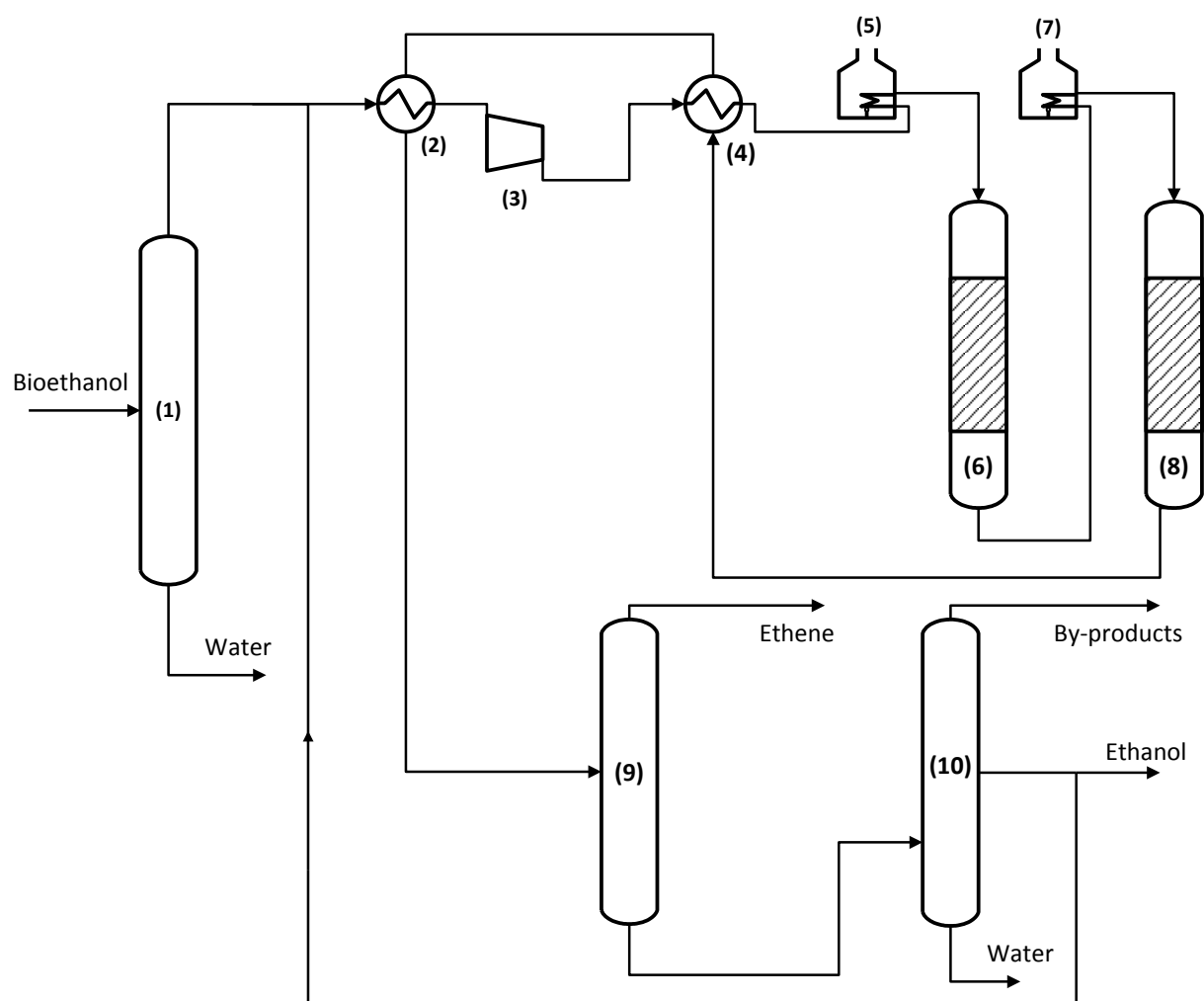
Figure 7-1: Flow sheet of an ethanol dehydration plant consisting of (1) a pretreatment distillation column, (2) and (4): heat exchangers, (3) a compressor, (5) and (7): heating furnace, (6) and (8): ethanol dehydration reactor and (9) and (10) gas/liquid separation columns.

The capability of accurately simulating the behavior of a chemical reaction over a broad range of process conditions opens up perspectives for the design and optimization of industrial chemical reactors. Current reactor models described in literature typically use simplified kinetic models [4]. Efforts have already been undertaken to extend this towards more complex reaction networks

based on elementary steps [5, 6] which can potentially require the use of parameter estimation techniques such as the single-event methodology [7]. However, using a model consisting of parameters obtained via regression to experimental results, does not guarantee that the reaction network accurately describes all the kinetically relevant underlying chemistry and allows extrapolation to other reaction conditions. Ab initio developed models incorporate information on the level of the active site and represent truly the intrinsic kinetics of the investigated reactions.

The chemical reaction rates are described via a kinetic model that is combined with a suitable reactor model which includes all relevant physical transport phenomena. Ab initio based reactor modelling has already been successfully applied for thermal processes [8] but due to the complexity of catalytic reaction, only few examples of simulations of catalytic processes solely based on ab initio obtained rate and equilibrium coefficients are reported such as NH_3 synthesis [9] and benzene hydrogenation [10]. For zeolite catalysis, a successful simulation of an industrial reactor can provide proof-of-principle that reliable ab initio modeling of catalytic reactions is possible from molecular to industrial scale.

A reactor model can provide guidelines for the design, optimization and operation in industrial reactors. Alwahabi and Froment [11] developed a conceptual reactor design for a SAPO-34 catalyst and compared three different types of configurations: a multi-tubular quasi-isothermal reactor, a multi-bed adiabatic reactor with intermediate heat exchangers and a bubbling fluidized bed reactor with internal heat exchanger. The advantages of a fundamental kinetic model were already demonstrated by Park and Froment [12] who explored the use of a multi-bed adiabatic reactor for maximum propylene yield on H-ZSM-5. CFD based models for a fixed bed [13] and a fluidized bed [14] using lumped kinetics have also been proposed. However, no industrial reactor simulation model has been developed for the dehydration of ethanol.

In the present work, a multi-bed adiabatic reactor model was developed for the dehydration of ethanol on H-ZSM-5. The model also accounts for intermediate heat exchange between the beds. The kinetics implemented in the reactor model are solely based on quantum chemically obtained rate and equilibrium coefficients. A comparison of the ab initio-based reactor simulation results with data found in patent literature provides the ultimate test of the validity of the models and methodology presented in this work. The benefits of an accurate reaction and reactor model is illustrated by exploration of the water content effect .

7.2 Assessment of internal and external mass and heat transfer limitations

A key factor in the development of an accurate reactor model is the assessment of resistance to mass and heat transfer inside the catalyst particle, i.e., the *internal heat and mass transport limitations*, and the difference in conditions in the bulk of the fluid and on the catalyst surface, i.e., the *external heat and mass transport limitations.* The evaluation of the relative importance of these limitations is performed via correlations and is discussed in paragraph 2.2.

The most extensively studied catalyst for ethanol dehydration is H-ZSM-5, which is composed of pentasil units. It consists of elliptical straight channels (0.53 nm × 0.56 nm) and near circular sinusoidal channels (0.51 nm × 0.55 nm) that perpendicularly intersect [15]. The pore network is located in small crystallites with a size (d_c) ranging between 10^{-7} and 10^{-5} m. For an industrial pellet these crystallites area typically imbedded in a binder to increase the mechanical strength and allow the formation of larger pellets ($d_p = 10^{-3}$ -10^{-2} m) in order to limit the pressure drop over the catalyst bed. Therefore two different length scale for internal mass transport limitations exists. An assessment of the relative importance of these limitations can be performed using the Weisz-Prater criterion [16]:

$$\frac{(n+1)}{2}\frac{d^2\rho_p R_i^{obs}}{6D_{e,i}C_i^s} < 0.08 \qquad (7\text{-}1)$$

in which n is the apparent order of reaction, d is the diameter of either the catalyst crystallite (d_c) or the catalyst pellet (d_p), ρ_p the density, $D_{e,i}$ the effective diffusion coefficient of component *i* (m² s^{-1}) and C_i^s the concentration of component *i* at the surface.

Table 7-1 shows the results of the transport limitations assessment in an industrial reactor using H-ZSM-5. It can be seen that the catalyst particle is practically isothermal which is consistent with Froment et al. [17]. Also external transport limitations can be neglected.

Table 7-1: External and internal heat and mass transport limitations in an industrial ethanol dehydration reactor.

	Heat transport limitations			
External	eq. (2-4)	$\left\|\Delta T_{film}\right\|$	0.012	< 2.35
Internal	eq. (2-5)	$\left\|\Delta T_{pellet}\right\|$	0.736	< 2.35
	Mass transport limitations			
External	eq. (2-2)	Ca	0.00764	< 0.05

The result of the Weisz-Prater criterion is shown in Figure 7-2 for a wide range of pellet and crystallite diameters and effective diffusion coefficients. The area below the black line, which indicates the limit of 0.08, is the region where internal diffusion limitations will occur. Above that line, no internal diffusion limitations will occur. It can be seen that internal mass transfer limitations will only occur at the pellet scale under the conditions and catalyst studied in this work.
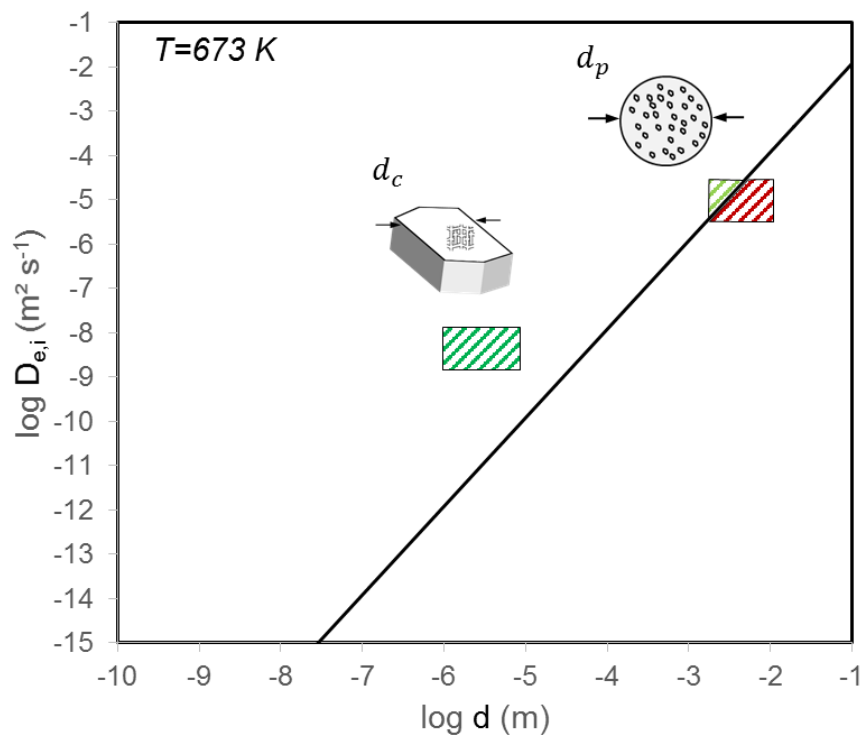
Figure 7-2: Internal mass transfer limitations assessed by the Weisz-Prater criterion (eq. (7-4)) in an industrial ethanol dehydration reactor as function of the particle diameter d which can either correspond to the crystallite diameter, i.e., d_c, or the pellet diameter, i.e., d_p, and the effective diffusion coefficient $D_{e,i}$. The black line indicates the limit of 0.08. Boxes indicate the typical ranges of diffusion coefficient and diameter for either the crystallite or pellet. (Green: no internal mass transport limitations; red: internal mass transport limitations).

7.3 Industrial reactor model for ethanol dehydration

A graphical representation of the reactor model and the phenomena that are taken into consideration is given in Figure 7-3. The reactor model consists of a tubular reactor with a specified length and diameter, i.e., L_r and d_r. The molar inlet flow rate of ethanol and water, inlet temperature and pressure are specified. The reactor is operated in adiabatic mode. The pressure drop along the axial reactor coordinate is also taken into account. The reactor model also explicitly includes intraparticle mass transfer limitations which results in a concentration profile as shown below the catalyst pellet.
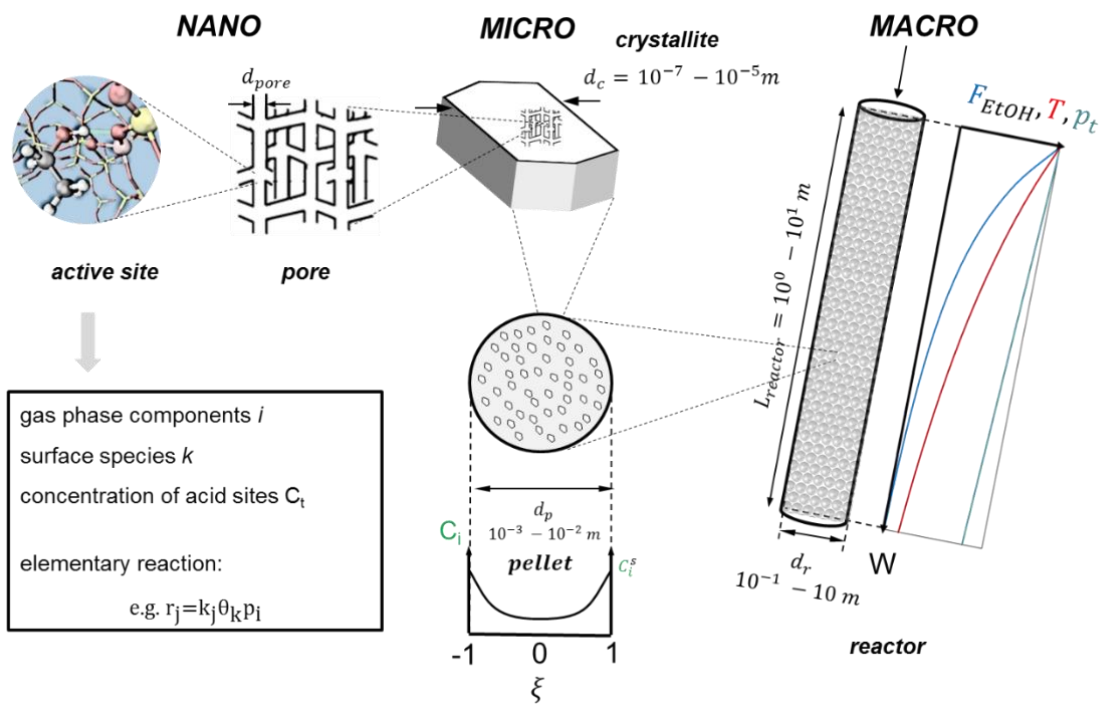
Figure 7-3: Graphical representation of the fixed bed reactor model for ethanol dehydration

7.3.1 Macroscale: the reactor

The reactor is described by three continuity equations, i.e., conservation of mass, energy and momentum. The reactor is considered to be in steady state and hence, accumulation is neglected. A one-dimensional heterogeneous reactor model with plug flow was considered. The continuity equation for component i in the gas phase, i.e., ethanol, is given by:

$$\frac{dF_i}{dW} = \bar{R}_i \qquad (7\text{-}2)$$

in which F_i is the molar flow rate of gas phase component i (mol s^{-1}), W the catalyst mass (kg), $\bar{R}_i$ the net rate of formation of gas phase component i (mol s^{-1} kg^{-1}) and C_t the concentration of acid sites (mol kg^{-1}).

As the reactor is operated adiabatically, no heat exchange with the wall is occurring and thus, the energy equation for the gas phase is given by:

$$\frac{dT}{dW} = \frac{1}{Gc_p} \sum_{i=1}^{ncomp} \Delta H_{f,i}\, \bar{R}_i \qquad (7\text{-}3)$$

T is the temperature (K), $\Delta H_{f,i}$ is the standard formation enthalpy of component i (J mol^{-1}), G is the total mass flow rate (kg s^{-1}), c_p is the heat capacity of the gas (J kg^{-1} K^{-1}) and is determined via the method of Chung et al.[18]. The standard formation enthalpy can be determined via a group additivity method such as Benson or taken from literature [18].

Momentum can be lost throughout the reactor because of friction of the gas with the packed bed and is represented by:

$$\frac{dp_t}{dW} = -f \frac{G^2}{\rho_b \rho_f A_r^3 d_p} \qquad (7\text{-}4)$$

Where p_t is the total pressure in the reactor (Pa), ρ_f the density of the fluid (kg m^{-3}), ρ_b the bed density of the reactor (kg m^{-3}), A_r the cross-sectional surface area of the reactor tube (m²) and d_p the diameter of the catalyst pellet (m).

The friction factor f is determined by a correlation proposed by Hicks [19]:

$$f = 6.8 \frac{(1 - \varepsilon_B)^{1.2}}{\varepsilon_B^3} Re_p^{-0.2} \tag{7-5}$$

with ε_B the bed porosity and Re_p the pellet Reynolds number which is given by:

$$Re_p = \frac{\rho_b u_s d_p}{\mu(1 - \varepsilon_B)} \tag{7-6}$$

with u_s the superficial velocity (m s^{-1}) and μ the dynamic viscosity of the gas phase mixture (Pa s) which was determined according to the method of Chung et al. [18] (see Appendix C).

The bed porosity ε_B can be found via the correlation of Haughey and Beveridge [20]:

$$\varepsilon_B = 0.38 + 0.073 \left(1 + \frac{\left(\frac{d_t}{d_p} - 2 \right)^2}{\left(\frac{d_t}{d_p} \right)^2} \right) \tag{7-7}$$

with d_t the diameter of the reactor (m).

The initial conditions for this set of differential equation (equations $6 - 8$) are given by:

$$\left. \begin{array}{l} F_i = F_i^0 \\ T = T^0 \\ p_t = p_t^0 \end{array} \right\} \quad at \ W = 0 \tag{7-8}$$

7.3.2 Microscale: the catalyst pellet

A one-dimensional mass balance for each gas phase component i over an infinitesimal volume of the catalyst pellet is considered:

$$\frac{\partial C_i}{\partial t} = R_i \rho_s - \frac{4}{d_p^2} \left(\frac{s}{\xi} D_{e,i} \frac{\partial C_i}{\partial \xi} + \frac{\partial D_{e,i}}{\partial \xi} \frac{\partial C_i}{\partial \xi} + D_{e,i} \frac{\partial^2 C_i}{\partial \xi^2} \right) \tag{7-9}$$

Here ρ_s is the solid density of the catalyst (kg m^{-3}), C_i the concentration of gas phase component i inside the catalyst pellet (mol m^{-3}), ξ the position coordinate within the pellet, s is the pellet shape factor, i.e., 0, 1 or 2 for resp. a slab, cylinder or sphere, R_i is the net rate of formation at location ξ inside the catalyst pellet (mol s^{-1} kg^{-1}) and $D_{e,i}$ is the effective diffusion coefficient for gas phase component i (m² s^{-1}).

For this set of differential equations the following initial conditions were considered:

$$C_i = C_i^s \quad \xi = 1$$
$$\frac{dC_i}{d\xi} = 0 \quad \xi = 0 \tag{7-10}$$

In contrast to a homogeneous medium, the porous pellets consist of interconnected non-uniform pores in which the fluid may flow. This internal void fraction of the porous material and the tortuous nature of the pores is taken into account by using, the effective diffusivity for component i, i.e., $D_{e,i}$:

$$D_{e,i} = \frac{\varepsilon_p}{\tau_p} D_i \tag{7-11}$$

where ε_p is the porosity, i.e., the fraction of the volume occupied by the pores and τ_p the tortuosity.

The diffusion coefficient, D_i, is given as the sum of two resistances by the so-called Bosanquet equation [21] which is composed of the diffusion coefficient corresponding to intermolecular collisions, i.e., $D_{i,m}$, and the Knudsen diffusion coefficient, i.e., $D_{i,K}$, corresponding to the collisions of the molecules with the pore wall:

$$\frac{1}{D_i} = \frac{1}{D_{i,m}} + \frac{1}{D_{i,K}} \tag{7-12}$$

The molecular diffusion coefficient $D_{i,m}$ is preferably calculated using the rigorous Stefan-Maxwell model [22, 23] but this can be computationally demanding. The bulk diffusivity of gas phase component i in a gas mixture, $D_{m,i}$, can also be calculated from the individual binary diffusion coefficients using the Wilke equation [24]:

$$D_{i,m} = \left(\sum_{\substack{j=1 \\ j \neq i}} \frac{y_j}{D_{ij}} \right)^{-1} \tag{7-13}$$

The Wilke equation assumes diffusion in a stagnant mixture and is valid when using dilute systems. Solsvik and Jakobsen [25, 26] compared the rigorous Stefan-Maxwell to the simpler Wilke model and concluded that it is appropriate to use in the simulation of a fixed backed-bed methanol synthesis reactor. Good results from the use of the Wilke-Bosanquet combination for

determination of the diffusivity in multicomponent gas mixtures at low pressures have been obtained in combination with complex reactions such as Methanol-To-Olefins [27] and hydrodesulphurization [6].

The molecular binary diffusion coefficient of component i in component j, $D_{i,j}$, is calculated using the Füller-Schettler-Giddings relation [28] which is recommended by Reid et al. [29]:

$$D_{i,j} = 1 \times 10^{-7} \frac{T^{1.75}}{p_t \left(\frac{1}{M_i} + \frac{1}{M_j}\right)^{-1/2} \left((\Sigma_v)_i^{1/3} + (\Sigma_v)_j^{1/3}\right)^2} \qquad (7\text{-}14)$$

with T the temperature (K), p_t the total pressure, M_i the molecular mass of component i (mol kg^{-1}) and $(\Sigma_v)_i$ the atomic diffusion volume for component i which were found to be 51.77 for ethanol, 41.04 for ethene, 92.81 for diethyl ether and 13.1 for water.

The Knudsen diffusion coefficient of component i, $D_{i,K}$, is given by:

$$D_{i,K} = \frac{2}{3} \frac{d_{pore}}{2} \sqrt{\frac{8RT}{\pi M_i}} \qquad (7\text{-}15)$$

This differential equations originating from equation (12) was solved transiently rather than as a steady state mass balance, because in the case of second order differential equations, solving the latter balances is not guaranteed to lead to a solution. A finite difference method was used for solving second order differential equations: the pellet diameter was discretized over a user-defined number of mesh points, n_{mesh}. Every partial differential equation is rewritten as a set of n_{mesh} ordinary differential equations.

The net production rate of component i in case of diffusion limitations, i.e., $\bar{R}_i$, can be determined via:

$$\bar{R}_i = \int_0^V R_i dV \qquad (7\text{-}16)$$

This was practically obtained by averaging the pointwise net rate of formation of component i at position ξ of the catalyst pellet. A number of equidistant grid points was defined and a trapezoidal discretization produce was followed for integration:

$$\bar{R}_i = \int_0^V R_i dV = \frac{s+1}{2n_{grid}} \sum_{j=1}^{n_{grid}} \left[R_i(r_{p,j}) r_{p,j}^s + R_i(r_{p,j+1}) r_{p,j+1}^s \right] \qquad (7\text{-}17)$$

where n_{grid} is the number of grid points, $R_i(r_{p,j})$ is the net production rate of component i at location $r_{p,i}$ inside the pellet and V the pellet volume.

The catalyst effectiveness factor is calculated as the ratio of the reaction rate with pore diffusion resistance and the reaction rate in the absence of diffusion limitation, i.e., at gas bulk concentrations:

$$\eta = \frac{\bar{R}_i}{R_i^s} = \frac{\int_0^V R_i dV}{R_i^s} \qquad (7\text{-}18)$$

The catalyst effectiveness factor as function of number of mesh points was nearly constant after 25 mesh points. In this work, 35 mesh points were used in the simulations.

7.3.3 Nanoscale: the active site

A fully ab initio derived reaction network [30, 31] consisting of 15 elementary steps was used for describing the intrinsic kinetics of ethanol dehydration and is shown in Figure 7-4. Three different reaction pathways can be identified and are given below along with the corresponding reaction enthalpies:

$$C_2H_5OH \rightarrow C_2H_4 + H_2O \qquad \Delta H_r = 46 \text{ kJ mol}_{EtOH}^{-1} \qquad (7\text{-}19)$$

$$2\, C_2H_5OH \rightarrow (C_2H_5)_2O + H_2O \qquad \Delta H_r = -12 \text{ kJ mol}_{EtOH}^{-1} \qquad (7\text{-}20)$$

$$(C_2H_5)_2O \rightarrow C_2H_4 + C_2H_5OH \qquad \Delta H_r = 70 \text{ kJ mol}_{EtOH}^{-1} \qquad (7\text{-}21)$$
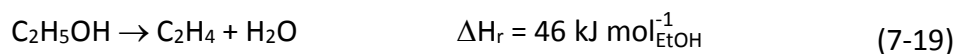
The monomolecular pathway (eq. 7-22) describes the direct dehydration of ethanol to ethene which is endothermic. The alternative route towards ethene consists of the bimolecular dehydration of ethanol to diethyl ether (eq. 7-23) and the subsequent decomposition of diethyl ether to ethanol and ethene (eq. 7-24). The former is slightly exothermic while the latter is endothermic. The mechanism for the production of hydrocarbons from ethanol is still a matter of debate [32-34]. Therefore it was opted to include the dimerization of ethene to 1-butene which serves as a crucial step in the formation of higher hydrocarbons:

$$2\, C_2H_4 \rightarrow C_4H_8 \qquad \Delta H_r = -53 \text{ kJ mol}_{C2H4}^{-1} \qquad (7\text{-}22)$$
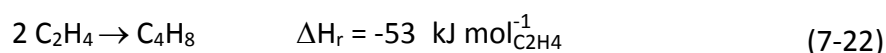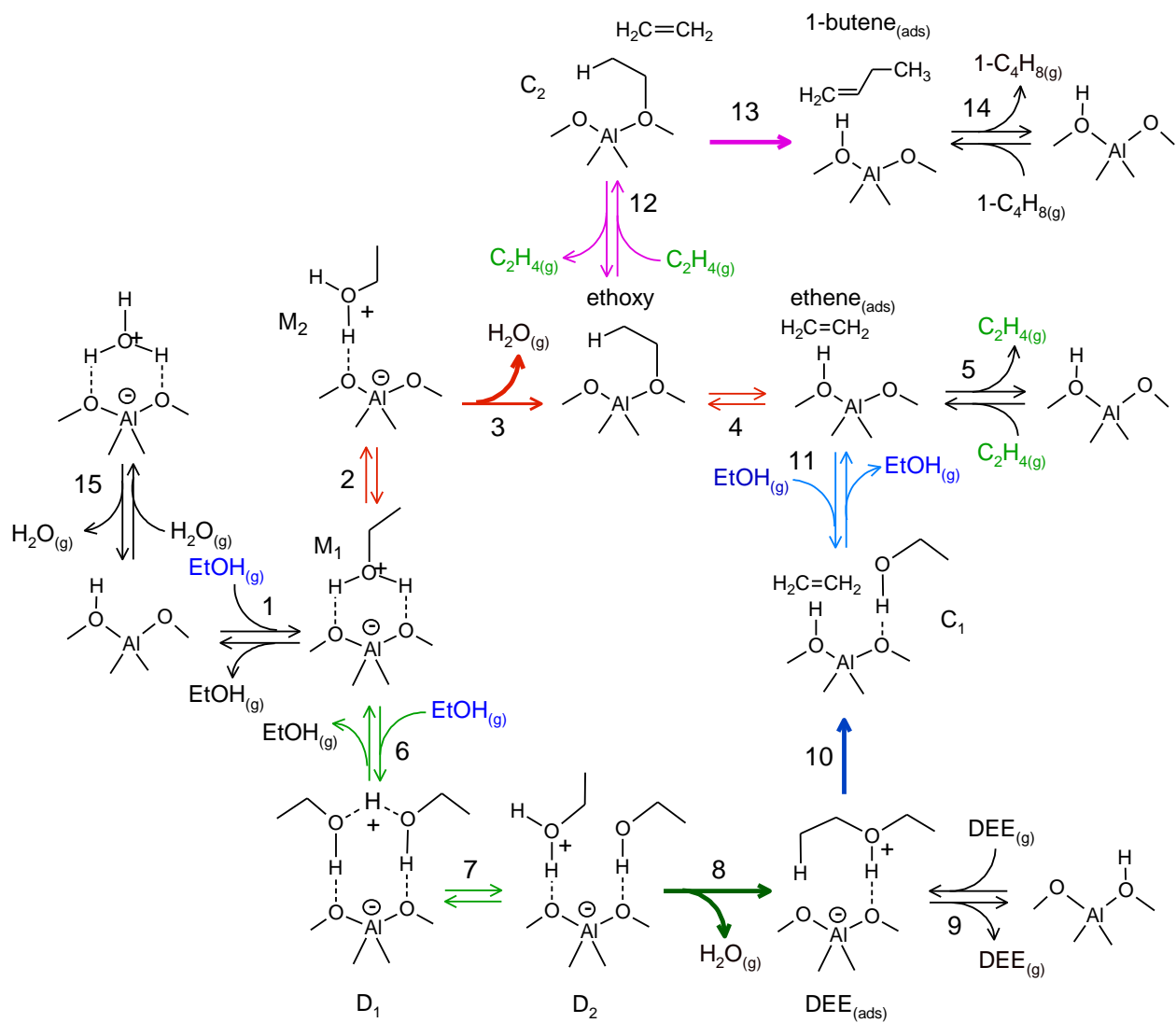
Figure 7-4: Reaction mechanism used for the simulation of the industrial reactor (red: monomolecular dehydration, green: bimolecular dehydration, blue: diethyl ether decomposition, magenta: ethene dimerization). Modified from [30].

The following continuity equations were applied for the gas phase components i and surface species k complemented with a site balance:

$$R_k = C_t \sum_j v_{jk} r_j = 0 \tag{7-23}$$

$$R_i = C_t \sum_j v_{ji} r_j \tag{7-24}$$

$$\theta_{H^+} + \sum_k \theta_k = 1 \tag{7-25}$$

where r_j is the turnover frequency of elementary step j, v_{ji} and v_{jk} the stoichiometric coefficient of gas phase component i or surface species k in the elementary step j. The forward reaction rate of a typical elementary step j can be written as:

$$r_j = k_j \theta_k^n p_i^m \tag{7-26}$$

where θ_k is the fractional occupancy of surface species k and p_i the partial pressure of gas phase component i.

Equilibrium coefficients for each elementary reaction were obtained using the following formula:

$$K_j = \exp\left(-\frac{\Delta H^0 - T\Delta S^0}{RT}\right) = \exp\left(-\frac{\Delta G^{0,\#}}{RT}\right) \tag{7-27}$$

where R is the universal gas constant, T is the temperature, ΔH^0 is the, ΔS^0 is the standard entropy of reaction, and ΔG^0 is the standard Gibbs free energy of reaction. Rate coefficients for each elementary reaction were calculated on the basis of transition state theory:

$$k_j = \frac{k_B T}{h} \exp\left(\frac{\Delta S^{0,\ddagger}}{R}\right) \exp\left(\frac{\Delta H^{0,\ddagger}}{RT}\right) = \frac{k_B T}{h} \exp\left(-\frac{\Delta G^{0,\ddagger\#}}{RT}\right) \tag{7-28}$$

where k_B is the Boltzmann constant, h is the Planck constant, $\Delta H^{0,\ddagger}$ is the standard enthalpy of activation, $\Delta S^{0,\ddagger}$ is the standard entropy of activation, and $\Delta G^{0,\ddagger}$ is the standard Gibbs free energy of activation. Arrhenius pre-exponential factors (A) and activation energies (E_a) for the activated elementary steps were obtained by regression of equation (7-28) in the temperature range of 300 − 800 K and can be found in Table 7-2. More details related to the computational work can be found in Chapter 3.

Table 7-2: Standard reaction enthalpy (ΔH_r^0 in kJ mol^{-1}), standard reaction entropy (ΔS_r^0 in J mol^{-1} K^{-1}), activation energy ($E_{a(f)}$ in kJ mol^{-1}) and pre-exponential factor (A_f in s^{-1} or 10^{-2} kPa^{-1} s^{-1}) of forward reaction for the elementary steps, numbered as indicated in Figure 7-4. The activated steps are indicated in bold.

	Elementary steps	ΔH_r^0	ΔS_r^0	$E_{a(f)}$	A_f
1	EtOH$_{(g)}$ + * $\leftrightarrow$ M$_1$	-122	-167	-	-
2	M$_1$ $\leftrightarrow$ M$_2$	14	7	-	-
3	**M$_2$ $\leftrightarrow$ Ethoxy + H2O(g)**	**77**	**146**	**118**	**4.0 10^{13}**
4	**Ethoxy $\leftrightarrow$ Ethene$_{(ads)}$**	**44**	**60**	**106**	**9.4 10^{12}**
5	Ethene$_{(ads)}$ $\leftrightarrow$ C$_2$H$_{4(g)}$ + *	48	99	-	-
6	M$_1$ + EtOH$_{(g)}$ $\leftrightarrow$ D$_1$	-99	-162	-	-
7	D$_1$ $\leftrightarrow$ D$_2$	44	24	-	-
8	**D$_2$ $\leftrightarrow$ DEE$_{(ads)}$ + H$_2$O$_{(g)}$**	**16**	**125**	**92**	**3.5 10^{12}**
9	DEE$_{(ads)}$ $\leftrightarrow$ DEE$_{(g)}$	139	165	-	-
10	**DEE$_{(ads)}$ $\leftrightarrow$ C$_1$**	**114**	**51**	**145**	**4.6 10^{13}**
11	C$_1$ $\leftrightarrow$ Ethene* + EtOH$_{(g)}$	59	175	-	-
12	Ethoxy + Ethene $\leftrightarrow$ C$_2$	-33	-113	-	-
13	**C$_2$ $\leftrightarrow$ 1-butene$_{(ads)}$**	**-82**	**-25**	**81**	**1.7 10^{12}**
14	1-butene$_{(ads)}$ $\leftrightarrow$ 1-butene + *	90	159	-	-
15	W $\leftrightarrow$ H$_2$O$_{(g)}$ + *	83	151	-	-

7.4 Simulation results

No detailed information on the industrial operation of an ethanol dehydration reactor is available in literature. Therefore, patent US 2013/0090510 [35] will be used for assessing the correctness of the model developed in this work. The process conditions and catalyst properties for this design case are given in Table 7-3. The reactor configuration consists of two adiabatic reactors in series with intermediate heating having a total catalyst mass of 6 ton. The inlet temperature and pressure for the first adiabatic reactor is 673 K and 590 kPa while 679 K and 530 kPa is set for the second adiabatic reactor. The feedstock used is an aqueous ethanol mixture containing 26 wt.%

ethanol with a considerably higher ethanol content compared to the fermentation broth (10 wt.% ethanol). The inlet flow rate of ethanol is 360 kton per year.

Table 7-3: Experimental operating conditions: catalyst mass (W_t), inlet temperature (T_0) and pressure ($p_{t,0}$) for each adiabatic reactor and the annual ethene production capacity (G_{C2H4}) and inlet water content to the first reactor ($x_{EtOH,0}$) .

Operating condition	Reactor 1	Reactor 2
W (ton)	3	3
T_0 (K)	673	679
$p_{t,0}$ (kPa)	590	530
$G_{C2H5OH,0}$ (kton y^{-1})	360	
$x_{EtOH,0}$	0.26	
Catalyst property		
d_p (m)	4 10^{-3}	
ε_p (-)	0.6	
τ (-)	5	
ρ_p (kg m^{-3})	700	
C_t (mol kg^{-1})	0.003	

The results for a case study found in patent literature for the configuration consisting of two adiabatic reactors are given in Table 7-4. Herein, ethanol conversion (X_{EtOH}) and yield of gas phase component i (Y_i) is defined as:

$$X_{EtOH} = \frac{F_{EtOH}^0 - F_{EtOH}}{F_{EtOH}^0}$$ (7-29)

$$Y_i = \frac{F_i}{F_{EtOH}^0}$$ (7-30)

in which F_{EtOH}^0 and F_{EtOH} is the molar inlet and outlet flow rate of ethanol and F_i the molar outlet flow rate of gas phase component i.

In the first reactor, an ethanol conversion of 0.71 is observed and a corresponding ethene yield of 0.69. The by-product described in Coupard et al. [35] in the outlet of the reactor is said to be oxygenates, represented in the kinetic model by diethyl ether. A temperature drop of more than 80 K is observed. At the end of the second reactor almost complete conversion of ethanol is achieved together with a high yield of ethene (0.97). It can be seen from Table 7-4 that the by-product in this case are higher olefins, represented in the kinetic model employed in this work by 1-butene. A limited temperature drop of 26 K is observed over the second catalyst bed.

Table 7-4: Experimental results, i.e., conversion (X_{EtOH}), ethene, oxygenates and C_{3+} olefin yield (resp., Y_{C2H4}, Y_{oxy}, Y_{ole}), temperature (T) and pressure (p_t), as described in Coupard et al. [35].

	X_{EtOH} (-)	Y_{C2H4} (-)	Y_{oxy} (-)	Y_{ole}(-)	T (K)	p_t (kPa)
Reactor 1	0.71	0.69	0.02	0.00	591	560
Reactor 2	0.99	0.97	0.00	0.01	653	500

Figure 7-5 shows the conversion and yield profiles along the axial reactor position. It can be seen that ethene is the most abundant product throughout the reactor. At the end of the first catalyst bed, around 2 % oxygenates product, represented in the reaction network by diethyl ether, is observed which is nicely described by the kinetic model. At the end of the second bed, diethyl ether is not present due to the decomposition of diethyl ether to ethene and ethanol, while formation of higher hydrocarbons by-products, here represented by 1-butene is observed. The reactor model gives a detailed picture of the evolution of the products along the reactor and allows us to monitor the effects of temperature and pressure.
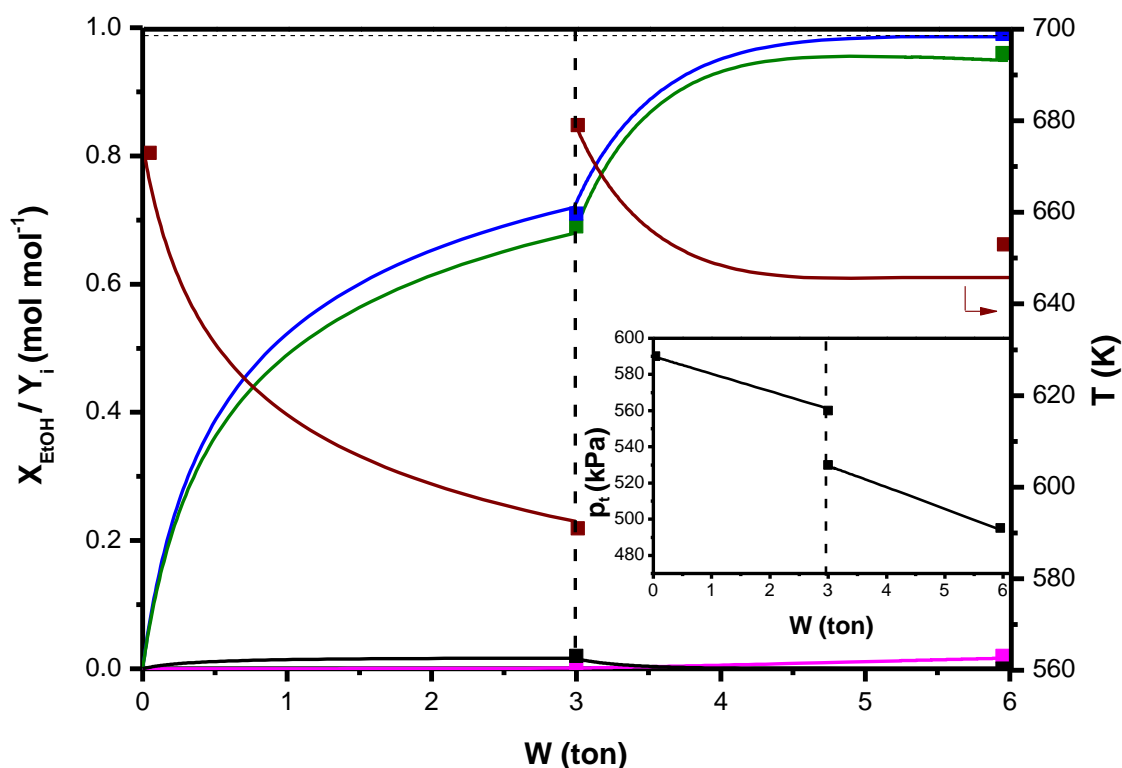
Figure 7-5: Ethanol conversion (X_{EtOH}, blue), ethene, diethyl ether and butene yield (green: Y_{C2H4}; black: Y_{DEE}; magenta; Y_{C4H8}) and temperature profiles (T) as function of catalyst mass. Inset shows the pressure drop (p_t) as function of catalyst mass. Calculated by integration of eqs. (7-5), (7-6), (7-7) and (7-12) and simultaneously solving eqs. (7-26) and (7-28) with the corresponding net production rates as defined in eq. (7-27) with parameters taken from Table 7-2 and the experimental conditions given in Table 7-3. Symbols indicate the experimental points given in Table 7-4.

A monotonous decrease of the temperature with increasing catalyst mass is observed in Figure 7-5. This means that the monomolecular pathway (eq 3-22)) is the most dominant along the entire reactor axis. After the first bed, the temperature of the outlet flow is increased via interstage heating prior to sending the effluent to the subsequent bed. Although the temperature shows good agreement at the end of the first bed, a discrepancy is observed in the second bed between the simulated and the experimentally observed temperature. A total temperature drop of 116 K is simulated while only a temperature drop of 107 K is observed. This can be compared to the total maximum adiabatic temperature drop as calculated by:

$$\Delta T_{ad,max} = \frac{F_{EtOH}^0(-\Delta H_r^0)}{G\,c_p} \tag{7-31}$$

This maximum adiabatic temperature drop was found to be 119 K and is closer to the simulated temperature drop than the experimentally observed temperature drop. Also the pressure drop was described adequately as shown as inset in Figure 7-5.

The catalyst effectiveness factor along the first reactor bed is shown in Figure 7-6 and was found to increase from 0.21 to 0.42. A concentration profile along the dimensionless catalyst pellet diameter is shown as inset. It can be observed that severe diffusion limitations exists.
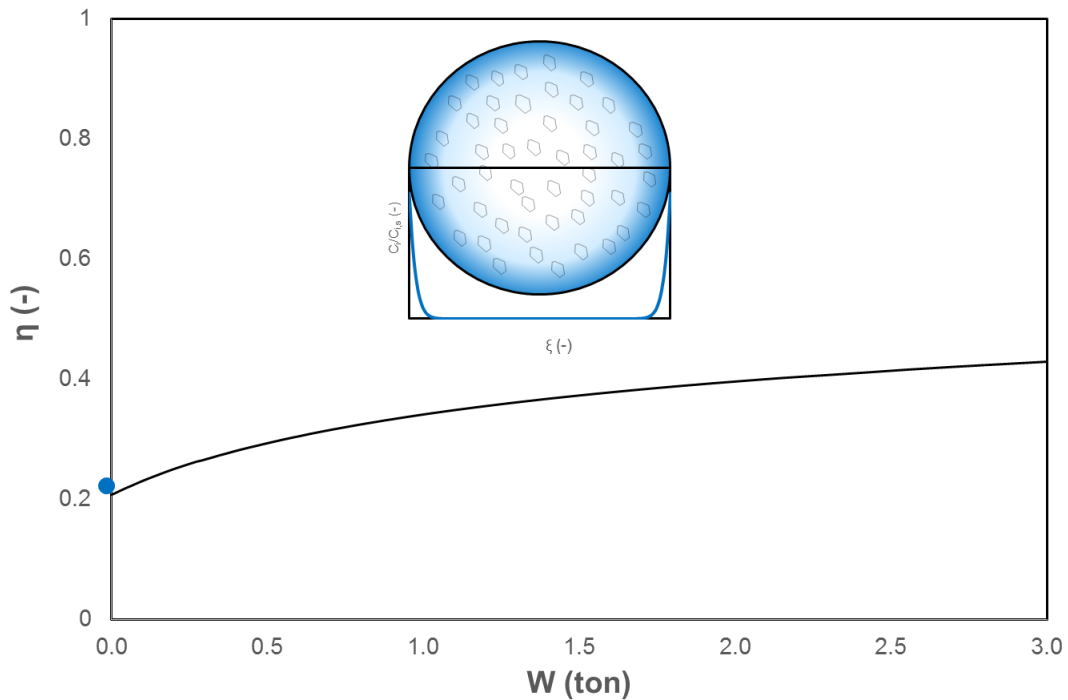
Figure 7-6: Catalyst effectiveness factor, as calculated by eq (7-21), as function of catalyst mass. The inset shows the relative concentration profile along the dimensionless catalyst pellet diameter. Calculated by integration of eqs. (7-5), (7-6), (7-7) and (7-12) and simultaneously solving eqs. (7-26) and (7-28) with the corresponding net production rates as defined in eq. (7-27) with parameters taken from Table 7-2 and the experimental conditions given in Table 7-3.

7.5   Optimization of an industrial ethanol dehydration reactor

As a good agreement between the model and the experimentally observed values is achieved, the model can now be utilized to investigate and optimize the industrial ethanol dehydration reactor. One of the key process parameters for industrial operation will be the amount of water added to the feed and the operating temperature. The ethanol content in the fermentation broth depends on the type of yeast used and is typically around 15 wt% and thus water removal via distillation can be considered.

The effect of ethanol content of the feed mixture on the maximum adiabatic temperature drop is illustrated in Figure 7-7. The higher the ethanol content, the higher the maximum adiabatic temperature drop along the reactor. This is related to changes in the mixture heat capacity due to changing feed composition. At 673 K, pure ethanol feed would result in a total temperature drop of 400 K while the aqueous conditions studied in this work, only amounted to a temperature drop of 119 K. As heat is consumed along the reactor with increasing ethanol conversion due to the endothermicity of the monomolecular ethanol dehydration, a higher water content allows for higher heat storage that can be utilized in the course of the reaction. At low ethanol content, the temperature effect on the maximum adiabatic temperature drop can be neglected. A substantial difference, however, at high ethanol content can be observed: a temperature difference of 70 K is calculated between 573 K and 773 K for a feed with no additional water. Other effects of high water content that have been reported are inhibition and diluting effects [36, 37].
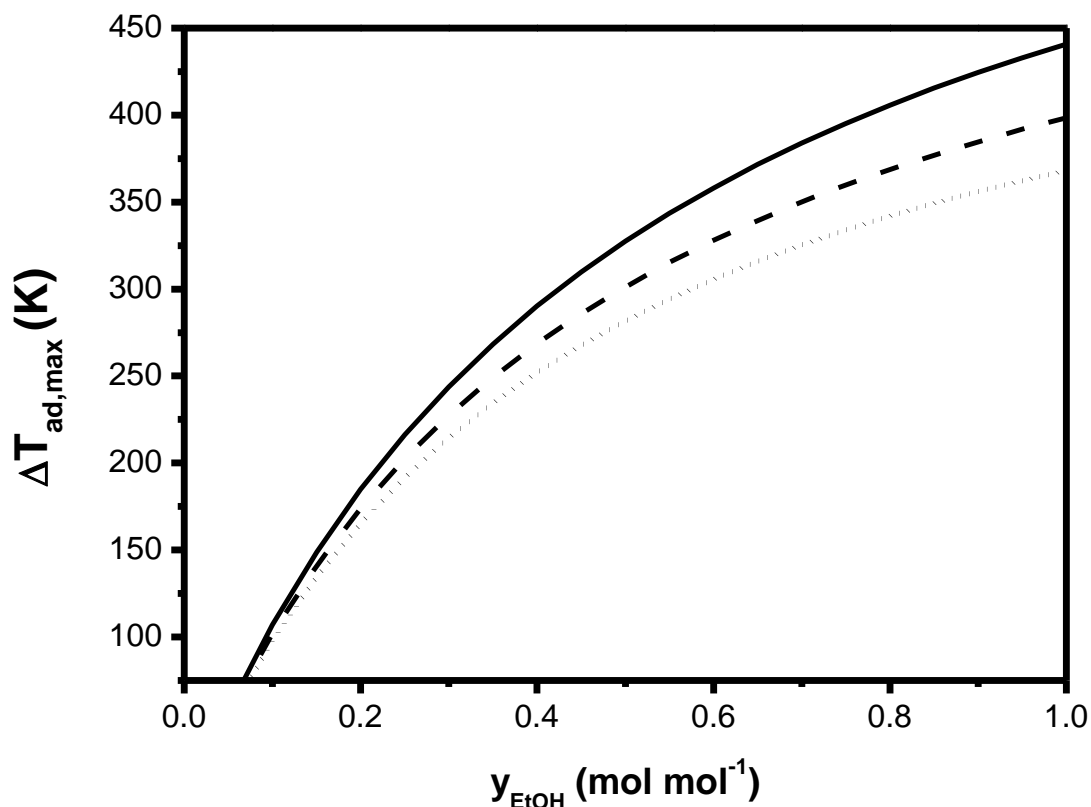
Figure 7-7: Maximum adiabatic temperature drop *as* function of molar ethanol fraction for three different temperatures (full line: 573 K, dashed line: 673 K, dotted line: 773 K) and the process conditions taken from Table 7-3.

The effect of varying water content on conversion, ethene yield and outlet temperature of the first reactor is shown in Figure 7-8. The highest conversion and ethene yield was obtained at the lowest ethanol content as can be seen in Figure 7-8. This low ethanol content also results in the lowest temperature drop as expected from Figure 7-7. As can be seen from the simulations, increasing the water content in the feed would result in even higher conversions and more efficient use of the industrial reactor. However, this can only be assessed when only the size and cost of the other equipment (compressors,...) is taken into account.
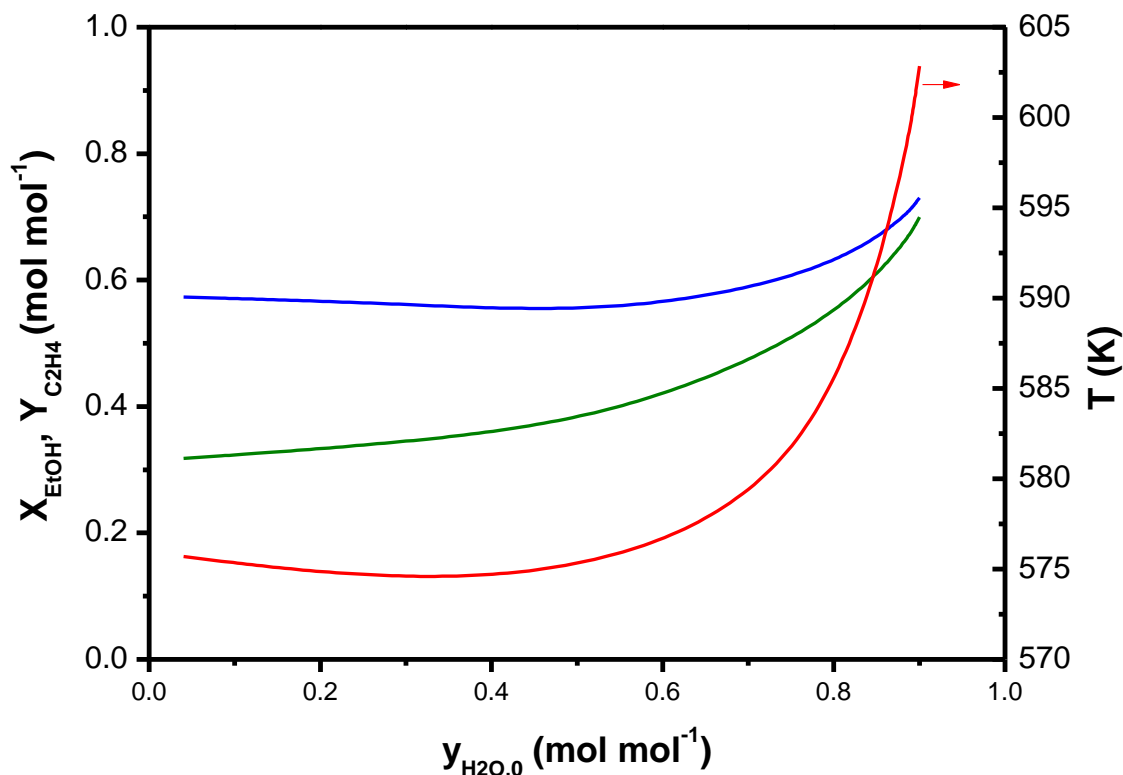
Figure 7-8: Ethanol conversion (X_{EtOH}, blue), ethene yield (Y_{EtOH}, green), outlet temperature (T, red) of the first reactor as function of water inlet content. Calculated by integration of eqs. (7-5), (7-6), (7-7) and (7-12) and simultaneously solving eqs. (7-26) and (7-28) with the corresponding net production rates as defined in eq. (7-27) with parameters taken from Table 7-2 and the experimental conditions given in Table 7-3.

Decreasing the water content, results in less conversion of ethanol and remarkably also less ethene yield. At high water content the ratio between ethene yield and ethanol conversion is close to one while increasing the water content decreases this ratio. Diethyl ether is produced instead in higher quantities which thus lowers the production of ethene. Higher ethanol partial pressure thus favor the formation of diethyl ether and decreases the selectivity to ethene. Dimerization of ethene to 1-butene was not observed in none of the case studies. The temperature drop observed in the reactor is not so pronounced as seen in Figure 7-7 which is related to conversion of ethanol to diethyl ether which is slightly exothermic. Minimizing the temperature drop due to high water content, will automatically result in higher conversion as can be seen from the figure.

The simulations are in line with patent literature where they claim the necessity of introducing a heating fluid in the reactor when working with pure ethanol feed. It has been claimed, for instance, propose the use of either water vapor obtained from inside or outside the process or recycling of a portion of the effluent of the dehydration reactor, i.e., ethene that is produced [2]. The latter is not advisable as introduction of ethene influences the thermodynamic equilibrium of the dehydration reaction and ethene participates in the subsequent conversion to higher hydrocarbons which will increase the yield of secondary products.

7.6   Conclusions

A fully ab initio derived reaction network for ethanol dehydration on H-ZSM-5 was used to simulate an industrial multi-bed adiabatic reactor. Internal transport limitations inside the catalyst pellet were explicitly accounted for, while no external transport limitations nor internal heat transport limitations were observed at the conditions investigated in this work. Good agreement was found with experimental results reported in patent literature, i.e., temperature, pressure and outlet flow rates. The industrial reactor model developed in this work based on ab initio calculated reaction and equilibrium coefficients can be of importance for the design, optimization and control of industrial alcohol conversion processes as illustrated by a design case in which the water content of the feed was varied. It was illustrated that it is not beneficial to utilize feeds with high ethanol content as it results in lower conversion and ethene yield. Furthermore a bigger temperature drop over the catalyst bed is observed. It is better to use a highly dilute feed for the operation of the industrial ethanol dehydration reactor. Of course, in order to properly assess the optimal configuration and feedstock properties, investment and operating costs of the total facility should be taken into account.

7.7　References

[1] E.G. Derouane, J.B. Nagy, P. Dejaifve, J.H.C. Vanhooff, B.P. Spekman, J.C. Vedrine, C. Naccache, Elucidation of Mechanism of Conversion of Methanol and Ethanol to Hydrocarbons on a New Type of Synthetic Zeolite, Journal of Catalysis, 53 (1978) 40-55.

[2] H.V.V. Barrocas, J.B. de Castro M. da Silva, R.C. de Assis, Process for preparing ethene, in, US 4232179 A, 1980.

[3] Atol: polymer grade bio-ethylene by dehydration of 1G and 2G renewable ethanol, (http://www.axens.net/product/technology-licensing/20080/atol.html), accessed on 2/5/2016

[4] B. Jiang, X. Feng, L. Yan, Y. Jiang, Z. Liao, J. Wang, Y. Yang, Methanol to Propylene Process in a Moving Bed Reactor with Byproducts Recycling: Kinetic Study and Reactor Simulation, Industrial & Engineering Chemistry Research, 53 (2014) 4623-4632.

[5] W. Jae Lee, G.F. Froment, Ethylbenzene Dehydrogenation into Styrene: Kinetic Modeling and Reactor Simulation, Industrial & Engineering Chemistry Research, 47 (2008) 9183-9194.

[6] G.F. Froment, G.A. Depauw, V. Vanrysselberghe, Kinetic Modeling and Reactor Simulation in Hydrodesulfurization of Oil Fractions, Industrial & Engineering Chemistry Research, 33 (1994) 2975-2988.

[7] N.V. Dewachtere, F. Santaella, G.F. Froment, Application of a single-event kinetic model in the simulation of an industrial riser reactor for the catalytic cracking of vacuum gas oil, Chemical Engineering Science, 54 (1999) 3653-3660.

[8] M.K. Sabbe, K.M. Van Geem, M.F. Reyniers, G.B. Marin, First Principle-Based Simulation of Ethane Steam Cracking, AIChE Journal, 57 (2011) 482-496.

[9] C.J.H. Jacobsen, S. Dahl, A. Boisen, B.S. Clausen, H. Topsøe, A. Logadottir, J.K. Nørskov, Optimal Catalyst Curves: Connecting Density Functional Theory Calculations with Industrial Reactor Design and Catalyst Selection, Journal of Catalysis, 205 (2002) 382-387.

[10] M.K. Sabbe, G. Canduela-Rodriguez, M.-F. Reyniers, G.B. Marin, DFT-based modeling of benzene hydrogenation on Pt at industrially relevant coverage, Journal of Catalysis, 330 (2015) 406-422.

[11] S.M. Alwahabi, G.F. Froment, Conceptual Reactor Design for the Methanol-to-Olefins Process on SAPO-34, Industrial & Engineering Chemistry Research, 43 (2004) 5112-5122.

[12] T.-Y. Park, G.F. Froment, Analysis of Fundamental Reaction Rates in the Methanol-to-Olefins Process on ZSM-5 as a Basis for Reactor Design and Operation, Industrial & Engineering Chemistry Research, 43 (2004) 682-689.

[13] Y.-Q. Zhuang, X. Gao, Y.-p. Zhu, Z.-h. Luo, CFD modeling of methanol to olefins process in a fixed-bed reactor, Powder Technology, 221 (2012) 419-430.

[14] Y. Zhao, H. Li, M. Ye, Z. Liu, 3D Numerical Simulation of a Large Scale MTO Fluidized Bed Reactor, Industrial & Engineering Chemistry Research, 52 (2013) 11354-11364.

[15] G.T. Kokotailo, S.L. Lawton, D.H. Olson, D.H. Olson, W.M. Meier, Structure of Synthetic Zeolite ZSM-5, Nature, 272 (1978) 437-438.

[16] P.B. Weisz, C.D. Prater, Interpretation of Measurements in Experimental Catalysis, in: V.I.K. W.G. Frankenburg, E.K. Rideal (Eds.) Advances in Catalysis, Academic Press, 1954, pp. 143-196.

[17] G.F. Froment, J. De Wilde, K.B. Bischoff, Chemical reactor analysis and design, 3rd ed., Wiley, Hoboken, N.J., 2011.

[18] R.C. Reid, J.M. Prausnitz, T.K. Sherwood, The properties of gases and liquids, 3d ed., McGraw-Hill, New York, 1977.

[19] R.E. Hicks, Pressure Drop in Packed Beds of Spheres, Industrial & Engineering Chemistry Fundamentals, 9 (1970) 500-502.

[20] D.P. Haughey, G.S.G. Beveridge, Structural properties of packed beds — A review, The Canadian Journal of Chemical Engineering, 47 (1969) 130-140.

[21] C.H. Bosanquet, British TA Report BR-507, 1944

[22] J.C. Maxwell, On the Dynamical Theory of Gases, Philosophical Transactions of the Royal Society of London, 157 (1867) 49-88.

[23] J. Stefan, Über das Gleichgewicht un die Bewegung, insbesondere die Diffusion von Gasgemengen., Sitzungsberichte Akad Wiss Wien, 63 (1871) 63-124.

[24] C. Wilke, Diffusional properties of multicomponent gases, Chemical Engineering Progress, 46 (1950) 95-104.

[25] J. Solsvik, H.A. Jakobsen, Modeling of multicomponent mass diffusion in porous spherical pellets: Application to steam methane reforming and methanol synthesis, Chemical Engineering Science, 66 (2011) 1986-2000.

[26] J. Solsvik, H.A. Jakobsen, Multicomponent mass diffusion in porous pellets: Effects of flux models on the pellet level and impacts on the reactor level. Application to methanol synthesis, The Canadian Journal of Chemical Engineering, 91 (2013) 66-76.

[27] J.W. Thybaut, G.B. Marin, Single-Event MicroKinetics: Catalyst design for complex reaction networks, Journal of Catalysis, 308 (2013) 352-362.

[28] E.N. Fuller, Schettle.Pd, J.C. Giddings, A New Method for Prediction of Binary Gas-Phase Diffusion Coeffecients, Industrial and Engineering Chemistry, 58 (1966) 19-&.

[29] R.C. Reid, J.M. Prausnitz, B.E. Poling, The properties of gases and liquids, 4th ed., McGraw-Hill, New York, 1987.

[30] M.-F. Reyniers, G.B. Marin, Experimental and Theoretical Methods in Kinetic Studies of Heterogeneously Catalyzed Reactions, Annual Review of Chemical and Biomolecular Engineering, 5 (2014) 563-594.

[31] K. Alexopoulos, M. John, K. Van der Borght, V. Galvita, M.-F. Reyniers, G.B. Marin, DFT-based microkinetic modeling of ethanol dehydration in H-ZSM-5, Journal of Catalysis, 339 (2016) 173-185.

[32] R. Johansson, S.L. Hruby, J. Rass-Hansen, C.H. Christensen, The Hydrocarbon Pool in Ethanol-to-Gasoline over HZSM-5 Catalysts, Catalysis Letters, 127 (2009) 1-6.

[33] F.F. Madeira, N.S. Gnep, P. Magnoux, H. Vezin, S. Maury, N. Cadran, Mechanistic insights on the ethanol transformation into hydrocarbons over HZSM-5 zeolite, Chemical Engineering Journal, 161 (2010) 403-408.

[34] A.T. Aguayo, A.G. Gayubo, A. Atutxa, M. Olazar, J. Bilbao, Catalyst deactivation by coke in the transformation of aqueous ethanol into hydrocarbons. Kinetic modeling and acidity deterioration of the catalyst, Industrial & Engineering Chemistry Research, 41 (2002) 4216-4224.

[35] V. Coupard, N. Touchais, S. Fleurier, H.G. Penas, P. De Smedt, W. Vermeiren, C. Adam, D. Minoux, Process for dehydration of dilute ethanol into ethylene with low energy consumption without recycling of water, in, US 20130090510 A1, 2013.

[36] C.B. Phillips, R. Datta, Production of ethylene from hydrous ethanol on H-ZSM-5 under mild conditions, Industrial & Engineering Chemistry Research, 36 (1997) 4466-4475.

[37] Y.C. Zhi, H. Shi, L.Y. Mu, Y. Liu, D.H. Mei, D.M. Camaioni, J.A. Lercher, Dehydration Pathways of 1-Propanol on HZSM-5 in the Presence and Absence of Water, Journal of the American Chemical Society, 137 (2015) 15781-15794.

Chapter 8

Conclusions and perspectives

Alcohol conversion is an interesting route for the sustainable production of biochemicals. Most attention so far has been given to methanol-to-olefins, but (bio)ethanol conversion is gaining interest rapidly due to a growing environmental awareness. Ethanol as a feedstock has been used for almost hundred years, primarily focusing on the production of ethene. Historically, alumina and silica-alumina were used as catalyst for the ethanol dehydration reaction, but research has shifted towards zeolites as they are active at lower temperatures and allow more flexibility to tune the product distribution based on shape selectivity and confinement effects. Zeolites also offer the possibility to produce interesting chemicals such as propene and aromatics. The drawback however is the occurrence of unwanted secondary reactions, such as coke formation and less hydrothermal stability at elevated temperatures.

In this work, a novel methodology is presented, i.e. *information-driven catalyst design*, where the primary focus is to maximize the information obtained from experimental testing. Catalyst optimization solely based on experimental trial-and-error has reached its limits: the lack of fundamental insights in the relevant phenomena hinders the development of novel and improved catalyst formulations. *Information-driven catalyst design* is particularly interesting for reactions for which small catalyst improvements will lead to a high profit increase. The methodology consists of detailed mechanistic investigation on the one hand and rapid catalyst testing on the other hand, exploiting the benefits of high-throughput experimentation. Both features can subsequently be combined into a microkinetic model for *in silico* catalyst optimization.

An in-depth mechanistic insight of ethanol conversion should facilitate its industrial implementation as it gains insight in the effect of process conditions and the occurrence and importance of specific reactions. The tools for elucidation of the reaction mechanism employed in this work are continuous flow and transient experiments, complemented with UV/VIS characterization of the catalyst, and comparison to the results of microkinetic simulations using ab initio calculated equilibrium and rate coefficients. Ethanol dehydration to ethene is mechanistically decoupled from the production of higher hydrocarbons due to complete surface coverage during ethanol dehydration. This prevents C_{3+} hydrocarbon formation before ethanol conversion is complete. Moreover, the production of higher hydrocarbons from ethanol was found to exhibit an autocatalytic behavior. Three routes for the production of hydrocarbons from ethene are identified involving different types of surface species: the dimerization of ethene to butene and two routes involving surface species labeled as aliphatic and aromatic.

A detailed experimental study on the dehydration of ethanol on H-ZSM-5 was conducted and it was found that high temperature and high conversion favour the formation of ethene at the expense of di-ethyl ether. Water was found to have no effect on the conversion of ethanol. Good agreement was found between the experimental data and the results from microkinetic simulations based on ab initio parameters. The comparison of H-ZSM-5 to other types of commercially interesting zeolites shows that the catalytic performance of H-ZSM-5 is among the highest of those included in the study, along with H-MOR and H-BETA, and thus justifies the interest in H-ZSM-5 as an industrial catalyst for ethanol dehydration. A correlation was found between the NH_3 desorption energy as determined via desorption experiments and the activity and selectivity to ethene of the different zeolites. A thorough investigation of this correlation via additional experimentation is required to fully understand this effect. Also confinement and shape selectivity should be examined in closer detail. An industrial reactor model for ethanol dehydration was developed and successfully validated against literature data. It was found that high water content is beneficial for high ethanol conversion and ethene yield.

Based on the experimental observations and the elucidated reaction network, a microkinetic model was proposed for the formation of higher hydrocarbons and the single-event methodology was applied to keep the number of adjustable parameters and computational effort within reasonable limits. This model was regressed to the experimental data to determine the unknown parameters. Only a limited number of adjustable parameters were present in the model, i.e. activation energies for ethylation and β-scission reaction, and the catalyst descriptors, i.e. the protonation enthalpies for primary, secondary and tertiary carbenium ions. All catalyst and kinetic descriptors were estimated significantly and with a sound physical meaning. A rate analysis at 573 K indicated the dimerization as the slowest step and thus responsible for the autocatalytic behavior. Catalyst optimization was attempted via metal modification of H-ZSM-5 with gallium, nickel and iron to result in effective tuning of the product selectivity. However, when comparing the effect of metal content at same conversion, no changes in selectivity was observed. Low metal content was found to have a positive effect on the concentration of acid sites and resulted in a higher activity.

The research into ethanol conversion to hydrocarbons has not yet reached its final destination. Further insights into the reaction mechanism via continuous flow experiments are possible by co-feeding one of the products, e.g. butene isomers or hexene isomers. More information, however, can be extracted via more sophisticated techniques such as Temporal Analysis of Products as already illustrated in this work. Future research should also focus more on extracting information related to diffusion and shape selective phenomena occurring inside the catalyst pores by comparing to other types of zeolites such as large pore zeolites (faujasites and beta zeolites). Steady State Isotopic Transient Kinetic Analysis (SSITKA) also holds opportunities as it allows to quantify the life time of species on the surface. Finally, using a recycle balance or a TEOM setup could provide invaluable information on the relationship between aromatic formation and the catalytic activity.

Ethanol dehydration is an ideal kinetic characterization reaction to assess the effect of zeolite structure on the chemical reaction. Establishing structure activity relationships, i.e. a relation between a structural parameter of the catalyst and the activity or selectivity, can help in

understanding the effect of acidity and confinement and formulate guidelines for further improvement of the catalysts. Ideally speaking, these relationships are also incorporated into the microkinetic models presented in this work. Eventually converting the optimal catalyst formulation into a lab procedure remains a challenge. The experimental efforts on catalyst optimization could be extended by further exploration of post-synthesis modification techniques, which allow to tailor the active site and the pore structure. Examples of these techniques are desilication, dealumination and atomic layer deposition. The former two allow to control the Si/Al ratio and are able to control the pore volume, which also has effect on the diffusion and shape selective phenomena occurring inside the crystallite.

Given the transition from conventional fossil to alternative fossil and renewable feedstocks, the *information-driven catalyst design* methodology should be expanded towards other processes such as glycerol hydrogenolysis and hydrodeoxygenation. These reactions are promising candidate reactions for further catalyst optimization, according to this proposed methodology. The complexity encountered in these processes requires a fundamental understanding to effectively optimize catalyst performance.

Appendix A

In this appendix, the chromatogram of a typical experiment for the conversion of ethanol to C_{3+} hydrocarbons is given. This experiment is conducted at 623K and 30 kPa ethanol with space time equal to 4.90 kg s mol^{-1}. The C_2 conversion in this experiment is 0.27. On the chromatogram, all peaks are identified up to C_5. For C_{6+} components, identification is difficult due to the high amount of double bound and structural isomers and hence these components are lumped. The absence of ethane and propane was determined using the microGC present at HTK-MI setup. The aromatics (benzene, toluene, xylene and ethylbenzene) were identified separately. FID calibration factors are used from Dietz et al. [1], except for the aromatics which are experimentally determined.

Figure A - 1: Typical GC chromatogram in ethanol conversion on H-ZSM- (T = 623 K, $p_{EtOH,0}$ = 30 kPa, W F^{-1} = 4.9 kg s mol^{-1})

(continued): **Figure A - 1: Typical GC chromatogram in ethanol conversion on H-ZSM- (T = 623 K, $p_{EtOH,0}$ = 30 kPa, W F^{-1} = 4.9 kg s mol^{-1})**

(continued): Figure A - 1: Typical GC chromatogram in ethanol conversion on H-ZSM- (T = 623 K, $p_{EtOH,0}$ = 30 kPa, W F^{-1} = 4.9 kg s mol^{-1})
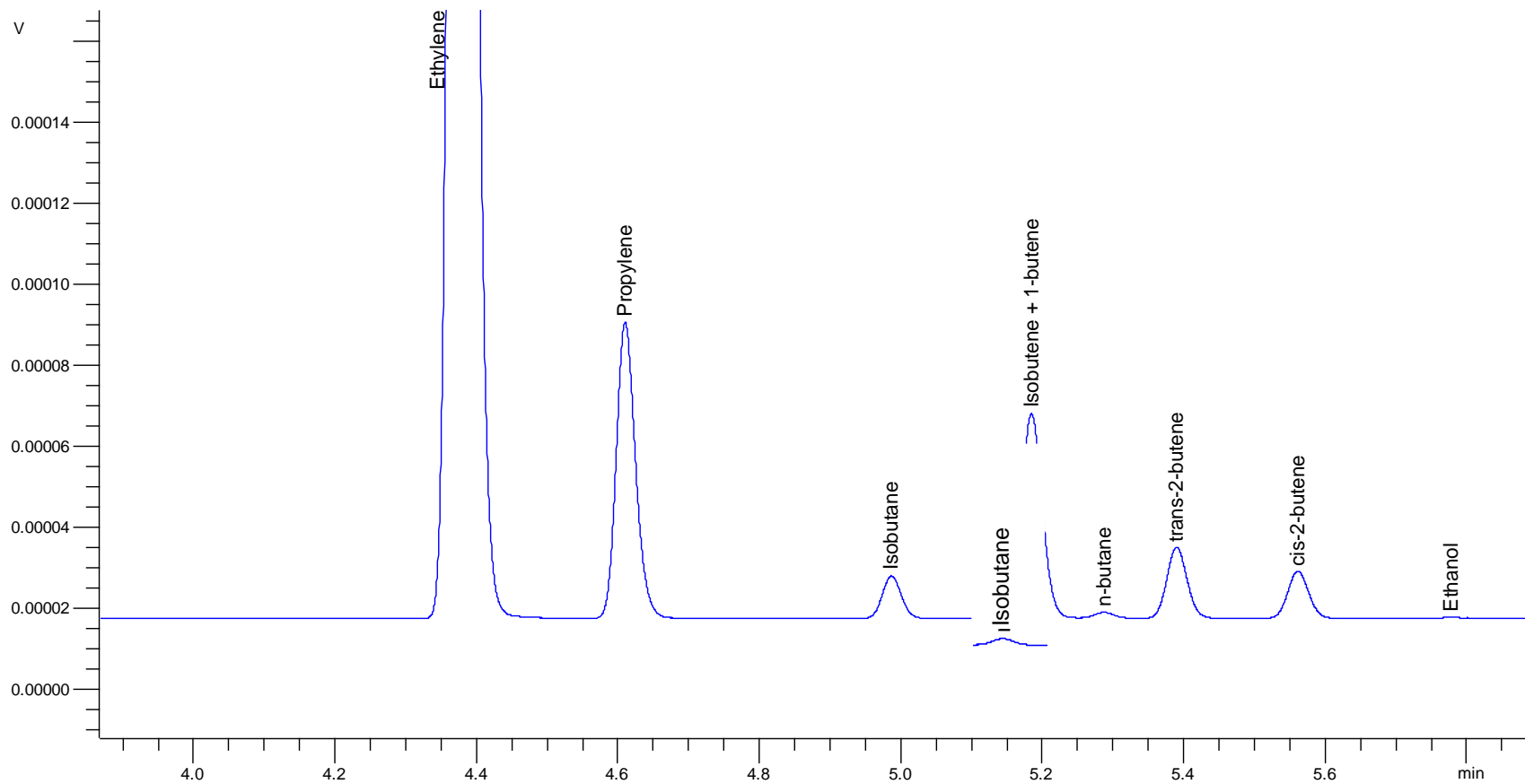
(continued): Figure A - 1: Typical GC chromatogram in ethanol conversion on H-ZSM- (T = 623 K, $p_{EtOH,0}$ = 30 kPa, W F^{-1} = 4.9 kg s mol^{-1})

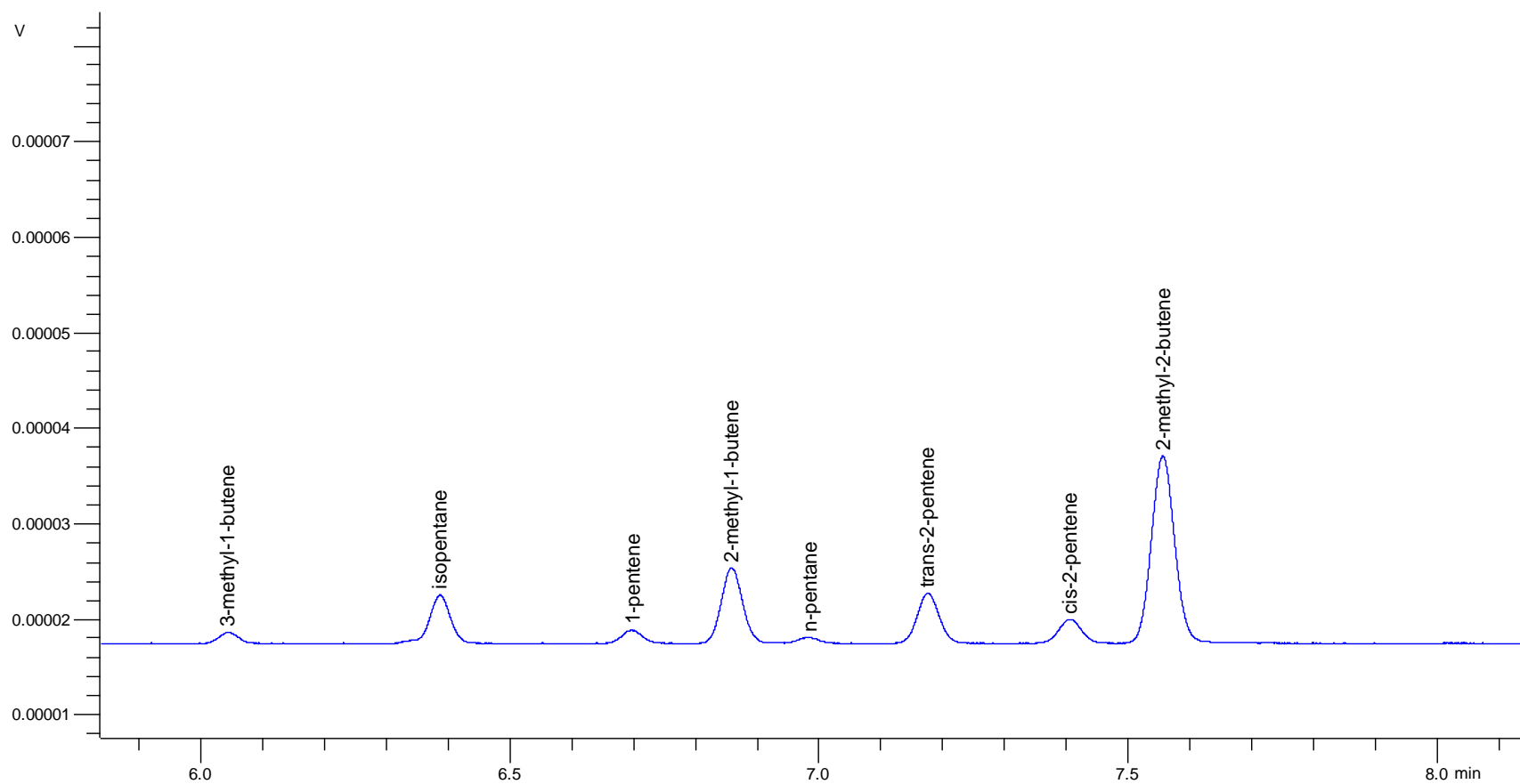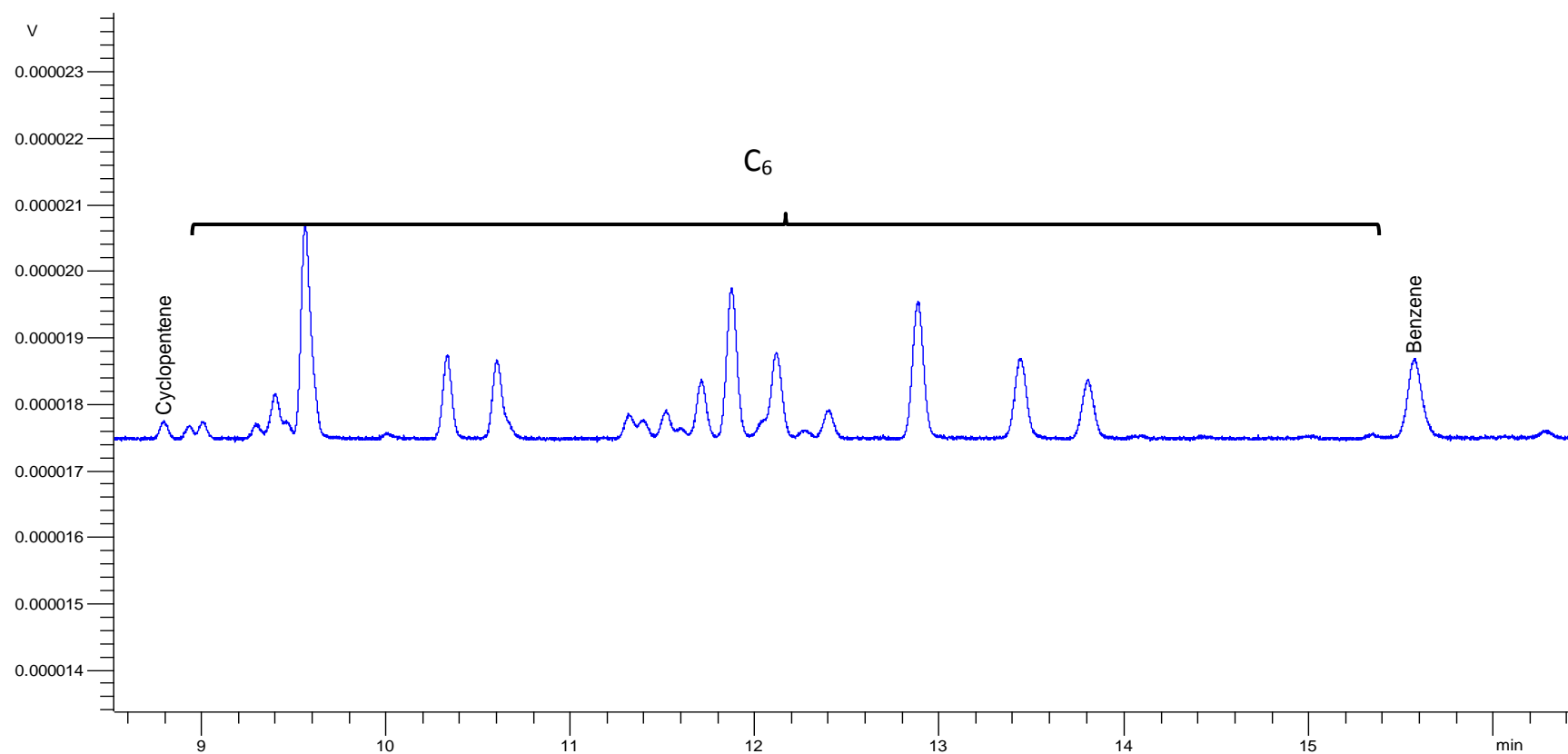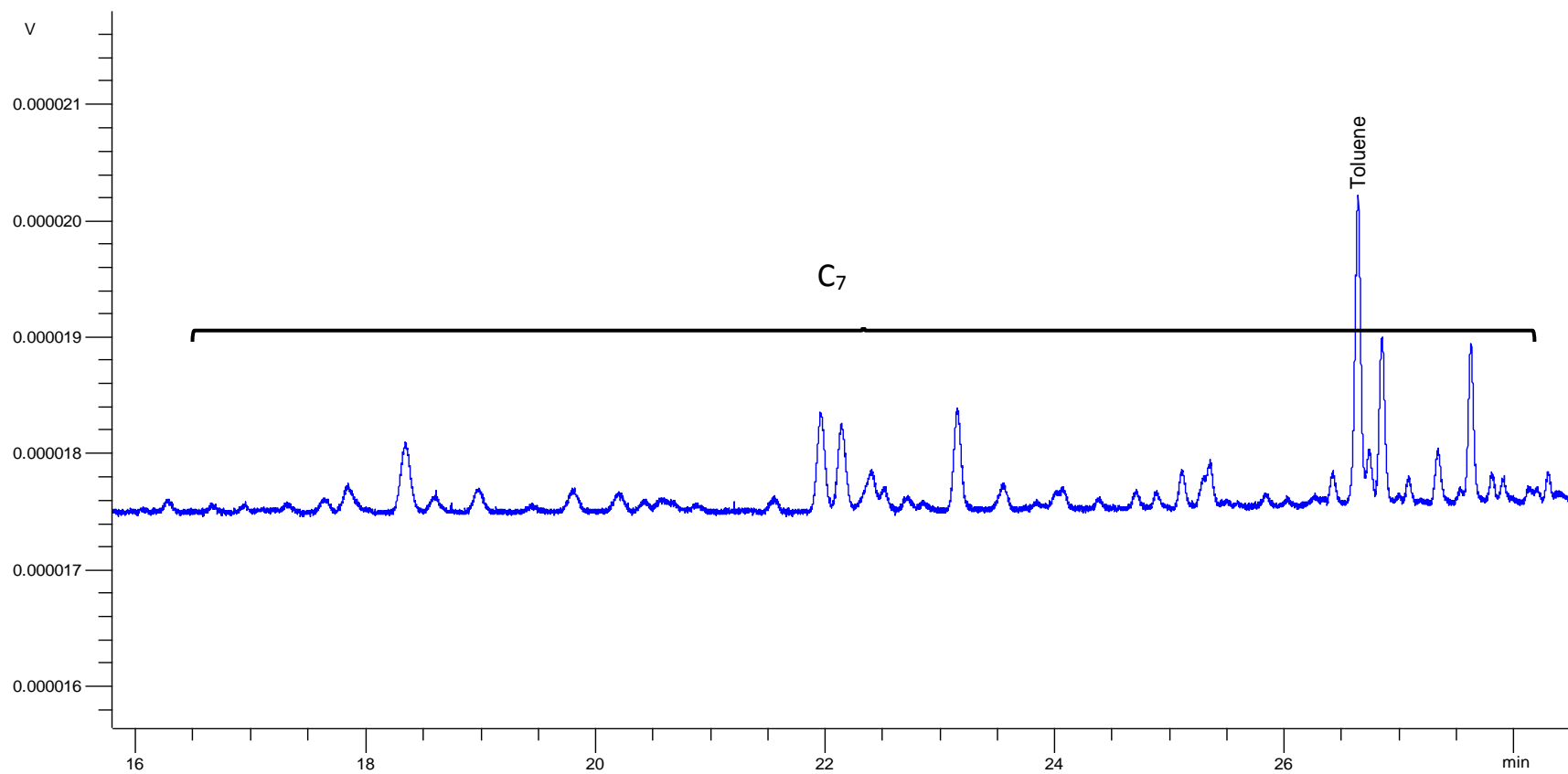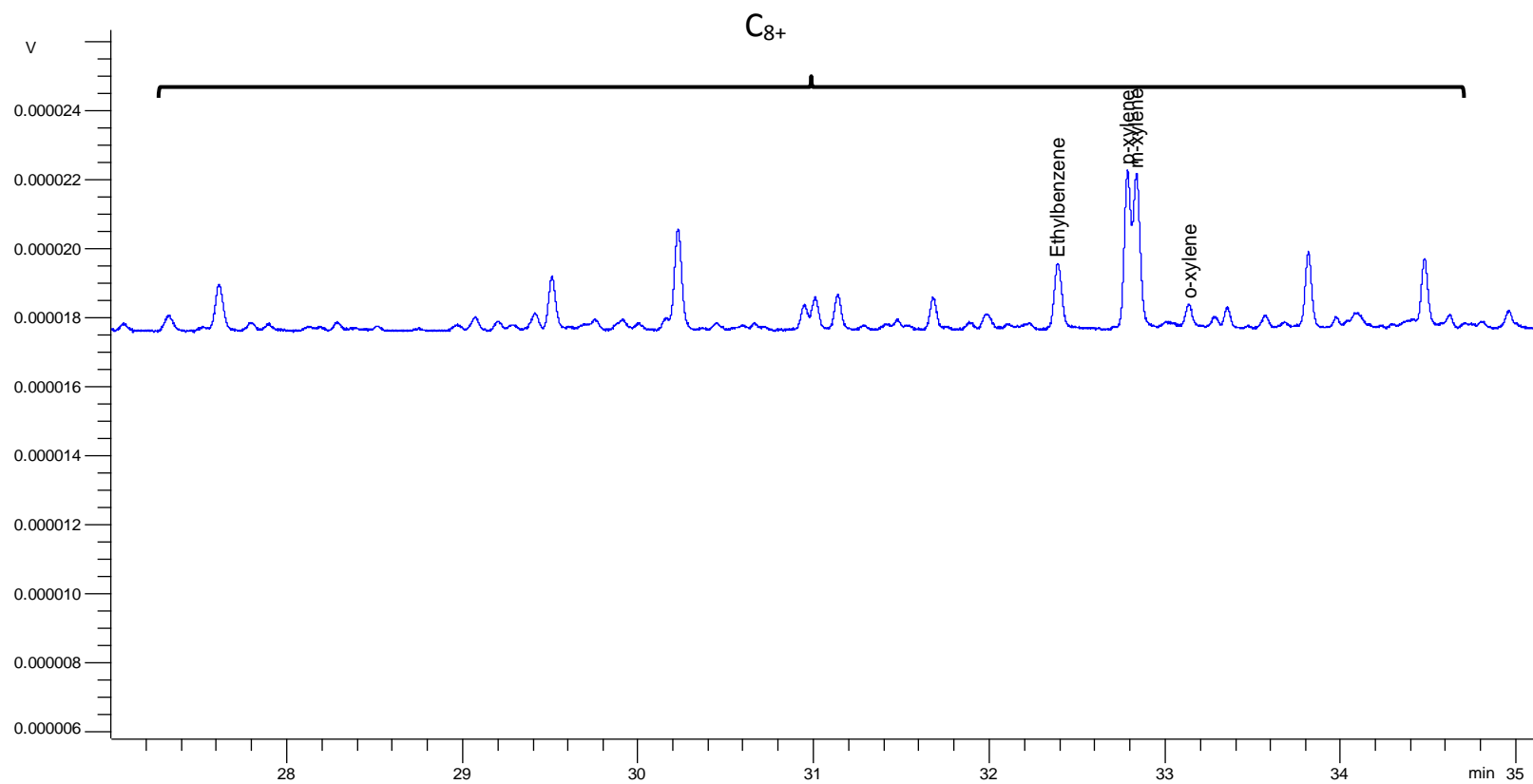(continued): Figure A - 1: Typical GC chromatogram in ethanol conversion on H-ZSM- (T = 623 K, $p_{EtOH,0}$ = 30 kPa, W F^{-1} = 4.9 kg s mol^{-1})

Table B - 2: Identified peaks for an ethanol/ethylene feed with the corresponding FID calibration factors.

Component	Retention time	Calibration factor
Methane	4.33	0.97
Ethylene	4.39	1.02
Propylene	4.63	1.00
Isobutane	5.00	1.00
Isobutene + 1-butene	5.20	1.00
n-butane	5.30	1.09
Trans-2-butene	5.41	1.00
Cis-2-butene	5.58	1.00
Ethanol	5.70	0.46
3-methyl-1-butene	6.06	1.00
Isopentane	6.41	1.05
1-pentene	6.72	1.00
2-methyl-1-butene	6.88	1.00
Diethyl ether	6.96	0.55
n-pentane	7.00	1.04
Trans-2-pentene	7.20	1.00
Cis-2-pentene	7.43	1.00
2-methyl-2-butene	7.58	1.00
Cyclopentene	8.89	1.00
C_6	8.89 – 16.00	1.00
C_7	16.00 – 26.00	1.00
C_{8+}	26.00 – 35.00	1.00
Benzene	15.58	1.198
Toluene	26.65	1.900
Ethyl-benzene	32.39	1.172
p-xylene	32.79	1.971
m-xylene	32.86	1.971
o-xylene	33.01	1.971

[1] W. Dietz, "Response factors for gas chromatographic analyses," *Journal of Chromatographic Science,* vol. 5, pp. 68-71, 1967.

Appendix B

In this appendix an overview is given of all the methods required to calculate the properties of pure components and mixtures as required in the reactor model for the simulation of an industrial ethanol dehydration reactor.

B.1 Pure component properties

B.1.1 Critical properties

Table B - 1 gives the pure components critical properties, i.e., critical temperature T_c, pressure p_c and volume V_c along with other properties such as molecular mass M_w, acentric factor ω, molar diffusion volumes for the Fuller-Schedding Giddings equation, and dipole moment μ.

Table B - 1:: Critical and other properties of ethanol, ethene, diethyl ether, water and 1-butene

	T_c [K]	p_c [10^5 Pa]	V_c [10^{-6} m³ mol^{-1}]	M_w [kg mol^{-1}]	ω [-]	μ [debye]
ethanol	513.9	61.4	167.1	0.046	0.6378	1.7
ethene	282.4	50.4	130.4	0.028	0.0882	0.0
diethyl ether	466.7	36.4	280.0	0.074	0.2800	1.3
Water	647.3	221.2	57.1	0.018	0.3852	1.8
1-butene	419.6	40.2	240	0.056	0.191	0.3

B.1.2 Heat capacity

The heat capacity of gases at a certain temperature T can be determined via:

$$c_p = A + B\,T + CT^2 + DT^3 \tag{B - 1}$$

The coefficients for equation (B - 1) can be found in Table B - 2.

Table B - 2: Coefficients for the determination of the heat capacity [in J mol^{-1} K^{-1})

	A	B	C	D
ethanol	9.014	0.214	-8.390 10^{-5}	1.373 10^{-9}
ethene	3.806	0.156	-8.348 10^{-5}	1.755 10^{-8}
diethyl ether	21.42	0.3359	-1.035 10^{-1}	-9.357 10^{-9}
water	32.24	0.0019	1.055 10^{-5}	-3.596 10^{-9}
1-butene				

B.1.3 Viscosity

The viscosity is expressed as:

$$\mu = \frac{40.785 F_{cm}(MT)^{1/2}}{V_c^{2/3}\Omega_v} \tag{B- 2}$$

Where μ is the viscosity, M the molecular mass, T the temperature, V_c the critical volume, Ω_v the viscosity integral calculated by:

$$\Omega_v = [A(T^*)^{-B}] + C[\exp(-DT^*)] + E[\exp(-FT^*)] \tag{B - 3}$$

in which T* = 1.2593 $T_{r,i}$, A = 1.16145, B = 0.14874, C= 0.52487, D=0.77320, E=2.16178, and F = 2.43787. The factor F_c accounts for molecular shape and polarity:

$$F_{cm} = 1 - 0.275\omega + 0.059035\mu_r^4 + \kappa \tag{B - 4}$$

Herein is ω the acentric factor and κ the association factor for correction for highly polar substances such as alcohols. For ethanol, this factor is 0.175. μ_r is a dimensionless dipole moment, defined as:

$$\mu_r = 131.3\frac{\mu}{(V_c T_c)^{1/2}} \tag{B - 5}$$

B.2 Mixing rules for properties

B.2.1 Molecular mass of mixtures

The molecular mass of a gas mixture, i.e., M_m, Yorizane[18] recommends the following rules:

$$M_m = \sum_{i=1}^{n_{comp}} y_i M_{w,i} \qquad \text{(B - 6)}$$

Where y_i is the molar fraction of component i in the gas phase and $M_{w,i}$ the molecular mass of component *i*.

B.2.2 Heat capacity of gas mixtures

Assuming an ideal gas or liquid mixture, heat capacity c_p of a gasmixture is given by:

$$c_p = \sum_{i=0}^{ncomp} y_i c_{p,i} \qquad \text{(B - 7)}$$

B.2.3 Viscosity of gas mixtures

Chung et al.[18] propose the following equation for the estimation of the mixture viscosity which corrects for the shape and the polarity:

$$\mu_m = \frac{26.69 F_{cm} (M_m T)^{1/2}}{\sigma_m^2 \Omega_v} \qquad \text{(B - 8)}$$

The mixing rules are:

$$\sigma_m^3 = \sum_i \sum_j y_i\, y_j \sigma_{ij}^3 \qquad \text{(B - 9)}$$

$$T_m^* = \frac{T}{\left(\frac{\epsilon}{k}\right)_m} \qquad \text{(B - 10)}$$

$$\left(\frac{\epsilon}{k}\right)_m = \frac{\sum_i \sum_j y_i\, y_j \frac{\epsilon_{ij}}{k} \sigma_{ij}^3}{\sigma_m^3} \qquad \text{(B - 11)}$$

$$M_m = \left[\frac{\sum_i \sum_j \ y_i \ y_j \frac{\epsilon_{ij}}{k} \sigma_{ij}^2 M_{ij}^{1/2}}{\left(\frac{\epsilon}{k}\right)_m \sigma_m^2} \right]^2$$
(B - 12)

$$\omega_m = \frac{\sum_i \sum_j \ y_i \ y_j \omega_{ij} \sigma_{ij}^3}{\sigma_m^3}$$
(B - 13)

$$\mu_m^4 = \sigma_m^3 \frac{\sum_i \sum_j \ y_i \ y_j \mu_i^2 \mu_j^2}{\sigma_{ij}^3}$$
(B - 14)

$$\kappa_m = \sum_i \sum_j y_i \ y_j \kappa_{ij}$$
(B - 15)

And the combining rules are:

$$\sigma_{ii} = \sigma_i = 0.809 \ V_{ci}^{1/3}$$
(B - 16)

$$\sigma_{ij} = \xi_i \ (\sigma_i \sigma_j)^{1/2}$$
(B - 17)

$$\frac{\epsilon_{ii}}{k} = \frac{\epsilon_i}{k} = \frac{T_{ci}}{1.2593}$$
(B - 18)

$$\frac{\epsilon_{ij}}{k} = \zeta_i \ \left(\frac{\epsilon_i}{k} \frac{\epsilon_j}{k}\right)^{1/2}$$
(B - 19)

$$\omega_{ii} = \omega_i$$
(B - 20)

$$\omega_{ij} = \frac{\omega_i + \omega_j}{2}$$
(B - 21)

$$\kappa_{ii} = \kappa_i$$
(B - 22)

$$\kappa_{ij} = \left(\kappa_i \kappa_j\right)^{1/2}$$
(B - 23)

$$M_{ij} = \frac{2 M_i M_j}{M_i + M_j}$$
(B - 24)

ξ_i and ζ_i are interaction parameters which are normally set equal to unity. The term F_{cm} is defined as:

$$F_{cm} = 1 - 0.275\omega_m + 0.059035\mu_{rm}^4 + \kappa_m \qquad \text{(B - 25)}$$

Where μ_{rm} is given by:

$$\mu_{rm} = \frac{131.3\mu_m}{(V_{cm}T_{cm})^{1/2}} \qquad \text{(B - 26)}$$

$$V_{cm} = \left(\frac{\sigma_m}{0.809}\right)^3 \qquad \text{(B - 27)}$$

$$T_{cm} = 1.2593\left(\frac{\epsilon}{k}\right)_m \qquad \text{(B - 28)}$$